UNIVERSITÀ DEGLI STUDI DI PADOVA

Centro Interdipartimentale di Studi e Attività Spaziali (CISAS)

DOTTORATO DI RICERCA IN SCIENZE, TECNOLOGIE E MISURE SPAZIALI

XXIV Ciclo

Sede Amministrativa: Università degli Studi di Padova

Indirizzo: Astronautica e Scienze da Satellite

Curriculum: Tecniche Spaziali per l'Osservazione della Terra

DETERMINATION OF THE OCEAN TIDE MODEL FROM LEO SATELLITE ORBITAL PERTURBATION ANALYSIS

DETERMINAZIONE DEL MODELLO DI MAREA OCEANICA DALL'ANALISI DELLE PERTURBAZIONI ORBITALI DI SATELLITI LEO

Dottoranda: Francesca Panzetta

Supervisore: Ch.mo Prof. Stefano Casotto
(Dipartimento di Fisica e Astronomia,
Università degli Studi di Padova)

Direttore della Scuola: Ch.mo Prof. Giampiero Naletto

Coordinatore dell'Indirizzo: Ch.mo Prof. Giampiero Naletto

31 Gennaio 2013

Acknowledgements

I want to thank the Prof. Casotto for many helpful discussions and valuable suggestions during these years.

Thanks are also due to the GOCE Italy group, coordinated by the Prof. Sansò, for the opportunity given to me to participate in a challenging Italian scientific project.

I am grateful to Massimo and Francesco for their precious contribution to this work and to all my friends for their moral support.

Thanks to my family which has been always to me in the difficult moments.

I especially want to thank the most important person of my life, Paolo, who has been always present, also on the other side of the world, and to whom this thesis is dedicated.

Theory is when we know everything but nothing works. Praxis is when everything works but we do not know why. We always end up by combining theory with praxis: nothing works and we do not know why.

Albert Einstein (1879-1955)

Abstract

The present study concerns the determination of ocean tide model parameters from GOCE orbital perturbation analysis. The GOCE satellite was launched by the European Space Agency in 2009 and is flying on a Sun-synchronous near circular orbit, at the very low altitude of about 250 km which makes it very sensitive to tidally induced orbit perturbations. The strategy adopted for analyzing GOCE GPS tracking data is the direct fully-dynamic approach, consisting in the GOCE precise orbit determination (POD) and accumulation of the normal equations for each orbital arc, followed by a multiarc solution for the estimation of the global ocean tide parameters.

The GOCE GPS observations are processed using the NAPEOS S/W system (ESA/ESOC), specific for satellite orbit determination and prediction, upgraded to inclusion of the partial derivatives with respect to the ocean tide parameters and the ocean tide model inversion capability.

A sensitivity study of the ocean tide perturbations on GOCE orbit was carried out using as a reference the FES2004 model, in order to define the set of tidal harmonic parameters affecting GOCE orbit. In particular, the secular rates of the GOCE angular elements are estimated through a linear least-square fit, being respectively $\dot{\omega} = -3.764817 \times 10^{-7}$ rad/s for the argument of perigee, $\dot{\Omega} = 2.022334 \times 10^{-7}$ rad/s for the longitude of ascending node and $\dot{M} = 1.167455 \times 10^{-3}$ rad/s for the mean anomaly.

From GOCE mean orbital characteristics, the spectral analysis of ocean tide perturbations in the radial, transverse and normal direction is performed using Kaula's linear satellite theory. Then, the perturbation statistics by coefficient is computed, obtaining a maximum RMS of about 1.323 m for the radial component, 363.136 m for the transverse component and 76.241 m for the normal component. The temporal aliasing problem is also accounted for the recovery of tidal parameters with GOCE and the principal alias periods are calculated for each tidal perturbation frequency, considering the length of the available GOCE data record. To fix a limit for the number of parameters to be estimated, three different cutoffs are applied to the RMS perturbation coefficients, respectively equal to 5 mm for the radial component, 2 cm for the transverse component and 1 cm for the normal component, both in the prograde and retrograde case. The total parameters to be estimated result to be 490.

GOCE data are processed to perform the fully-dynamic POD over daily orbital arcs from the 1st November 2009 until the 31st May 2011, but only arcs with a post-fit RMS of the GPS phase observations residuals lower than 8 mm are considered for the multiarc processing, for a total of 431 days.

The obtained preliminary results show the relative error of the estimated parameters with respect to the corresponding FES2004 parameters lower than 1 for about the 16% of the total, meaning that they are of the order of magnitude of the FES2004 parameters.

GOCE orbital data were reprocessed along the same period of the previous run, initializing the ocean tide model with the estimated parameters, if present, and maintaining otherwise the FES2004 parameters. The post-fit RMS of the GPS phase residuals obtained with the new ocean tide model has a mean value of 6.5 mm, and it is noteworthy that the difference between the

post-fit RMS obtained with the FES2004 model and that resulting from the new ocean tide model indicates a mean improvement of about 0.6 mm in for the 96% of the analyzed arcs and greater than 1 mm for the 16%, few days reach a difference of 2 mm.

Finally, the orbits obtained with the estimated parameters are compared with the orbits obtained employing the FES2004 model and the official GOCE Reduced-Dynamic PSO. The 3D RMS of the difference between the orbits computed using FES2004 and those recomputed with the new parameters shows a mean value of 2.5 cm, while the 3D RMS of the difference with respect to the official R/D PSO has a mean value of 4.9 cm. Moreover, the difference between the 3D RMS of the orbit residuals between the R/D PSO and the GOCE POD with FES2004 and the RMS of the difference between the GOCE R/D PSO and the GOCE POD with the new parameters results to have a mean improvement of 0.9 cm.

Further POD-Multiarc runs are certainly necessary, together with the refinement of the list of parameters to be estimated, removing excessively ill-estimated ocean tide parameters and introducing new parameters where appropriate. Indeed, the model parameter tuning and investigation is essential to adjust the best combination of parameters to be estimated. Moreover, an extension of the data set to much longer time-period should allow a substantial improvement of the obtained results. The task has proven very intensive and challenging, but the partial results obtained are encouraging and a motivation for future analysis.

Summary

For ten years, the three satellite gravity missions CHAMP, GRACE and GOCE are continuously improving our knowledge of the static and temporally changing Earth's gravity field, increasing spatial and temporal resolution to the extremely high level required by many geoscience applications, like Geodesy, Oceanography and Solid-Earth Physics. In particular, this study concerns the periodically variable part of the geopotential induced by the ocean tides and the estimation of the ocean tides parameters from GOCE orbital perturbation analysis.

Tides are periodical phenomena affecting both the solid Earth and oceans, caused by the differential gravitational attraction of external perturbing bodies on the Earth's surface, whose corresponding potential is named Tide-Generating Potential (TGP), and by their response to this potential. The TGP can be directly determined from the astronomical positions of the external perturbing bodies, its effect is also called direct tide and is the basis for the equilibrium tide theory. The equilibrium tide is the theoretical tide that would exist on an ideal perfectly rigid and non-rotating Earth (no effect of the Coriolis force), totally covered with oceans of uniform depth, where the response to the tide-generating forces is instantaneous and no dissipation is present. Obviously, the equilibrium tide does not represent the real tidal effect, being too small compared to the observed tide, however it is an important reference for tidal analysis, giving an order of magnitude of tidal phenomena. On the other hand, the real response of the solid Earth and oceans to the TGP, also called indirect tide, depends on the elastic properties of the Earth. The Laplace Tidal Equations (LTE) are introduced to explain the relations between the ocean, the solid Earth and the loading effects, in order to derive the fundamental equations of the ocean tide height field and the ocean tide potential.

The two main parameterizations of the ocean tide height field are presented. The classical spherical harmonic representation is characterized by a sum of partial tide heights each corresponding to a tidal frequency, while the response analysis assumes a transfer function or impulse response between the tidal forcing and the ocean tide height field, which is linear inside each tidal band. The cotidal and corange charts are reported for the main diurnal and semidiurnal tidal constituents (K_1, P_1, O_1, Q_1, M_2, S_2, K_2, N_2), to visualize the dynamic content of the ocean tide height induced by their tidal frequency. On the other hand, the development of a new computational algorithm for the accurate redetermination of the Groves and Reynolds orthotide coefficients is illustrated and the corresponding computational results are discussed within the orthotide formalism.

In order to estimate the ocean tide harmonic parameters, the lowest possible Earth orbit, GOCE orbit, was selected to obtain the largest possible tidal signal affecting a satellite. GOCE (Gravity field and steady-state Ocean Circulation Explorer) is a LEO satellite launched by the European Space Agency (ESA) on the 17th March 2009 and flying at the very low altitude of about 250 km in a nearly Sun-synchronous and nearly circular orbit with an inclination of about 96.7 deg. The main purposes of GOCE mission are to map the static part of Earth's gravity field with an unprecedented precision of 1 mGal = 10^{-5} m/s^2 and to model the geoid with an accuracy of 1-2 cm, at a spatial resolution of 100 km. To achieve these objectives, GOCE is

carrying onboard for the first time an Electrostatic Gravity Gradiometer (EGG) to measure the Earth's gravity gradient along three orthogonal directions and a Satellite-to-Satellite Tracking Instrument (SSTI) consisting of a GPS receiver. The spectral characteristics of the measurement types of these two instruments are complementary, but GOCE gradiometric measurements are only marginally sensitive to ocean tide effects, allowing to recover the short-wavelength part of the gravity field. For this reason, only GOCE GPS tracking data are used for the present work, being GOCE very sensitive to tidally induced orbit perturbations thanks to its extremely low altitude and so representing an excellent test-bed for the application of classical orbit perturbation analysis methods to recover tidal parameters.

Several analysis procedures were considered, but the direct numerical method was chosen, consisting in a fully-dynamic POD of GOCE, with the accumulation of the normal equations for each orbital arc, followed by a multiarc solution for the estimation of the global arc-independent ocean tide parameters. The tool selected to perform this type of analysis is ESA's NAPEOS s/w system, which provides the capabilities of orbit determination and prediction and parameter estimation. The estimation of ocean tide parameters, however, was not implemented in the system when it was acquired, so it was necessary to upgrade it with the entire implementation of the partial derivatives with respect to the ocean tide harmonic parameters and the extension of the structure for the inclusion of the ocean tide parameters characteristics: the tidal constituent, the harmonic type (C or S), the harmonic degree and order and the chirality (prograde or retrograde).

The principal task in order to accomplish the scientific objective of the study is the definition of the set of ocean tide harmonic parameters to which GOCE is more sensitive. Hence, a global and detailed sensitivity study of the ocean tide perturbations on GOCE orbit is carried out using as a reference the FES2004 model. First of all, the effect of various combinations of ocean tide constituents on GOCE orbit was evaluated over different time intervals and ocean tides accelerations acting on GOCE orbit were determined using different existent ocean tide models. Then, from the evolution of GOCE orbital elements available from a preliminary run of GOCE POD with NAPEOS, the GOCE mean orbital characteristics are estimated through a linear least-square fit and reported in Table 1.

Table 1. GOCE mean orbital elements and rates used for the spectral analysis of tidal perturbations on GOCE.

Element	Value
$\bar{a}$	6632.884525 km
$\bar{e}$	2.306273×10^{-3}
$\bar{i}$	1.686227 rad
ω_0	1.845595 rad
Ω_0	5.471748 rad
M_0	0.971383 rad
$\dot{\omega}$	-3.764817×10^{-7} rad/s
$\dot{\Omega}$	2.022334×10^{-7} rad/s
$\dot{M}$	1.167455×10^{-3} rad/s
Nodal Period	89.728100 min
Repeat Period	979 revs/61 nodal days

The analytical spectral analysis of the ocean tide perturbations affecting GOCE orbit in the radial, transverse and normal (RTN) directions up to degree and order 20 is computed using Kaula's linear satellite theory, together with the perturbation statistics by coefficient. The prograde amplitude spectra in RTN are reported respectively in Figure 1, 2, 3, while the RMS of the ocean tide perturbations accumulated over all the constituents in RTN is shown respectively in Figures 4, 5, 6, with a maximum RMS of about 1.323 m for the radial component, of 363.136 m for the transverse component and of 76.241 m for the normal component.

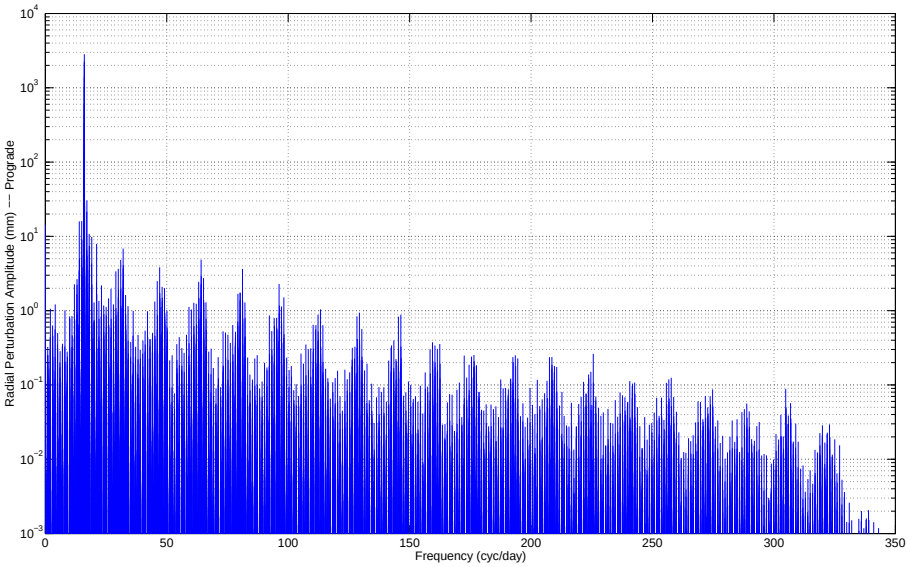

Figure 1. Amplitude spectrum of the radial prograde perturbation in position due to ocean tides.

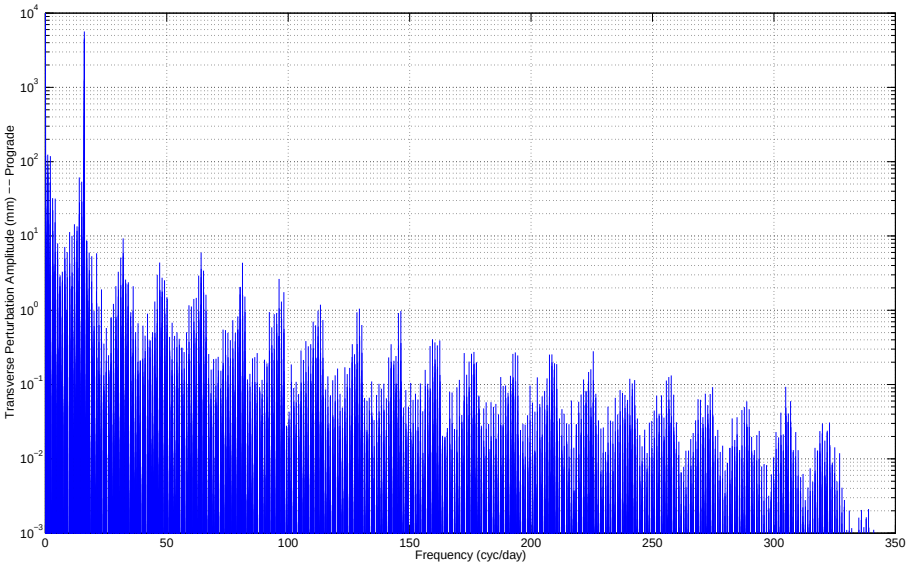

Figure 2. Amplitude spectrum of the transverse prograde perturbation in position due to ocean tides.

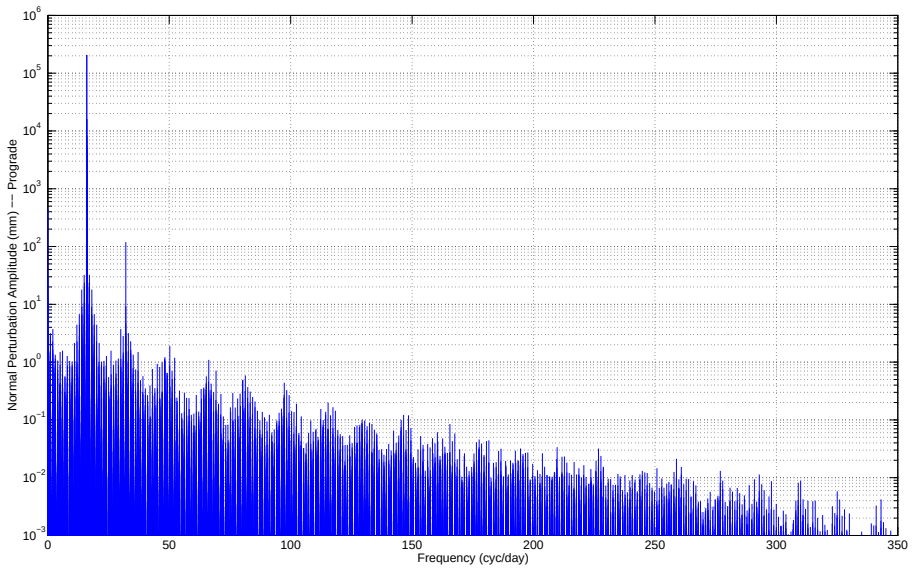

Figure 3. Amplitude spectrum of the normal prograde perturbation in position due to ocean tides.

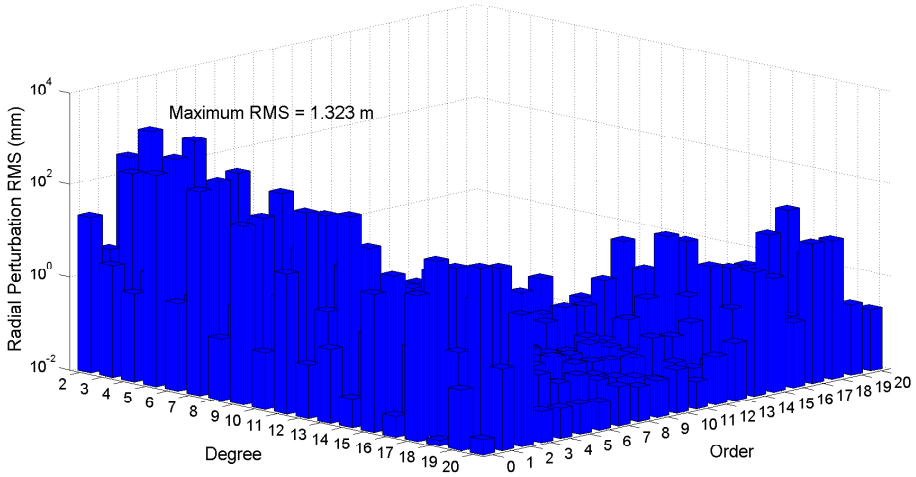

Figure 4. Accumulated RMS by coefficient of the radial perturbation in position due to ocean tides.

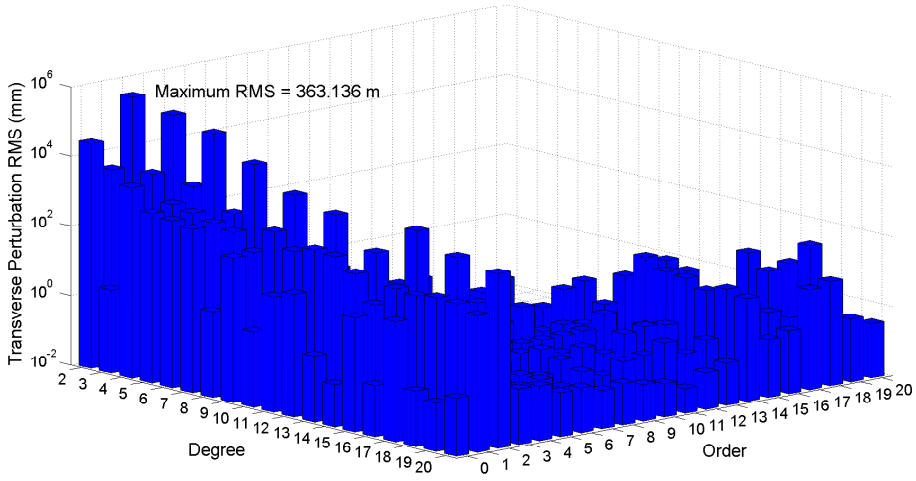

Figure 5. Accumulated RMS by coefficient of the transverse perturbation in position due to ocean tides.

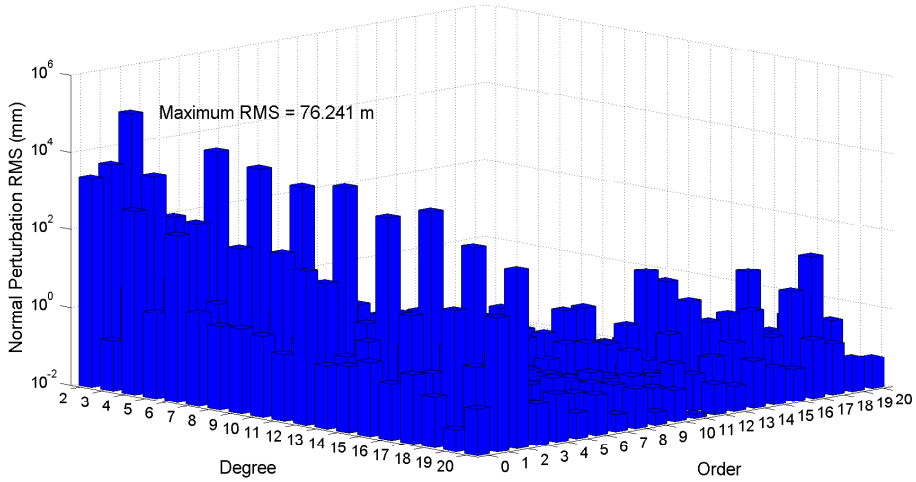

Figure 6. Accumulated RMS by coefficient of the normal perturbation in position due to ocean tides.

The temporal aliasing problem of the tidal perturbation frequencies strongly affects GOCE, because it samples the static gravity field and its time-varying part only along its orbital path, with a temporal resolution depending on its repeat period. Following closely a repeat period of 979 revolutions in 61 nodal days, the tidal frequencies as felt by GOCE are aliased to periods from 122 days (twice the orbit repeat period) to almost infinite. Unfortunately, GOCE is also a Sun-synchronous satellite, so it does not allow the complete estimation of the diurnal and semidiurnal solar tide constituents S_2 and S_1 which have original periods of exactly 12 h and 24 h, because it will always sample both these constituents at the same phase every day. In particular, during the spectral analysis, the principal alias periods were computed for all the ocean tide perturbation frequencies. Also the length of the GOCE data record is taken into account: for the available 400 days of measurements, the limit period beyond which GOCE is not able to solve for a parameter turns out to be approximately 200 days. The choice adopted consists in not estimating the coefficient (l, m), if the largest partial spectral amplitude, among all those contributing to the same pair (l, m), is aliased beyond 200 days.

Combining information deriving from the spectral analysis, the perturbation statistics by coefficient and the determination of ocean tide alias periods, the gridof the ocean tide parameters from harmonic degree 2 to 20 to be estimated from GOCE orbital data can be identified and consists of 490 parameters. It must be pointed out that the total number of parameters is limited by the application of three different cutoffs on the perturbation RMS by coefficient, respectively equal to 5 mm for the radial component, 2 cm for the transverse component and 1 cm for the normal component, both in the prograde and retrograde case.

GOCE orbital data were processed in daily arcs from the 1st November 2009, corresponding to the beginning of the operational phase, until the 31st May 2011, but only arcs with a post-fit RMS of the GPS phase observations residuals lower than 8 mm were considered for the multiarc processing, for a total of 431 days.

The obtained preliminary results show that the 56% of the total number of parameters has a difference below 1 cm from the FES2004 model, while the relative error of the estimated parameters with respect to the corresponding FES2004 parameters lower than 1 for about the 16% of the total, meaning that they are of the order of magnitude of the FES2004 parameters.

GOCE orbital data were reprocessed from the 1st November 2009 to the 31st May 2011, initializing the ocean tide model with the estimated parameters, if present, and maintaining otherwise the FES2004 parameters. The post-fit RMS of the GPS phase residuals obtained with the new ocean tide model has a mean value of 6.5 mm, and it is noteworthy that the difference between the post-fit RMS obtained with the FES2004 model and that resulting from the new ocean tide model indicates a mean improvement of about 0.6 mm in for the 96% of the analyzed arcs and greater than 1 mm for the 16%, while few days reach a difference of 2 mm (see Figure 6.8).

Finally, the orbit comparison shows that the 3D RMS of the difference between the orbits computed using FES2004 and those recomputed with the new parameters presents a mean value of 2.5 cm, the 3D RMS of the difference with respect to the official R/D PSO has a mean value of 4.9 cm. The difference between the 3D RMS of the orbit residuals between the R/D PSO and the GOCE POD with FES2004 and the RMS of the difference between the GOCE R/D PSO and the GOCE POD with the new parameters results to have a mean improvement of 0.9 cm (see Figure 6.11).

Further POD-Multiarc runs are certainly necessary, together with the refinement of the list of parameters to be estimated, removing excessively ill-estimated ocean tide parameters and introducing new parameters where appropriate. The model parameter tuning and investigation is essential to adjust the best combination of parameters to be estimated. Moreover, an extension of the data set to much longer time-period should allow a substantial improvement of the obtained results. Indeed, the task has proven very intensive and challenging, but the partial results obtained are encouraging and a motivation for future analysis.

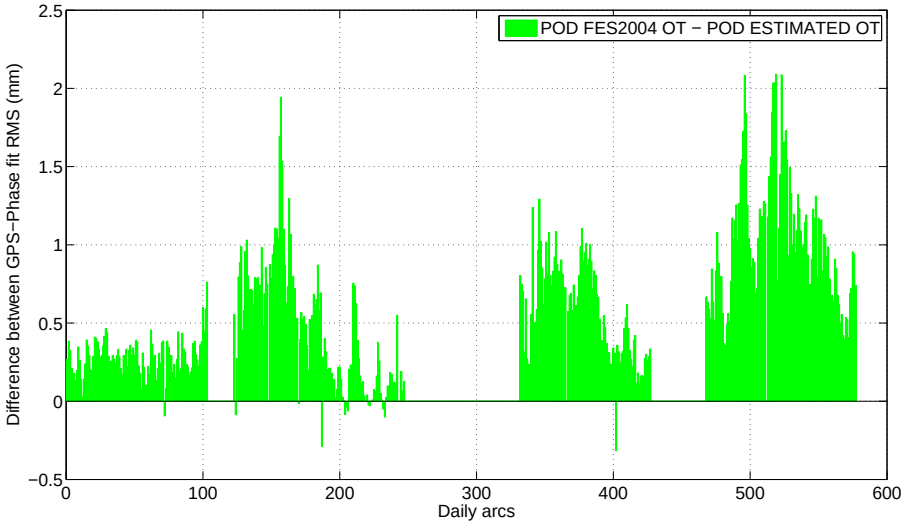

Figure 7. Difference between the fit RMS obtained using FES2004 model and the fit RMS obtained with the new estimated ocean tide parameters, instead of the corresponding FES2004 parameters.

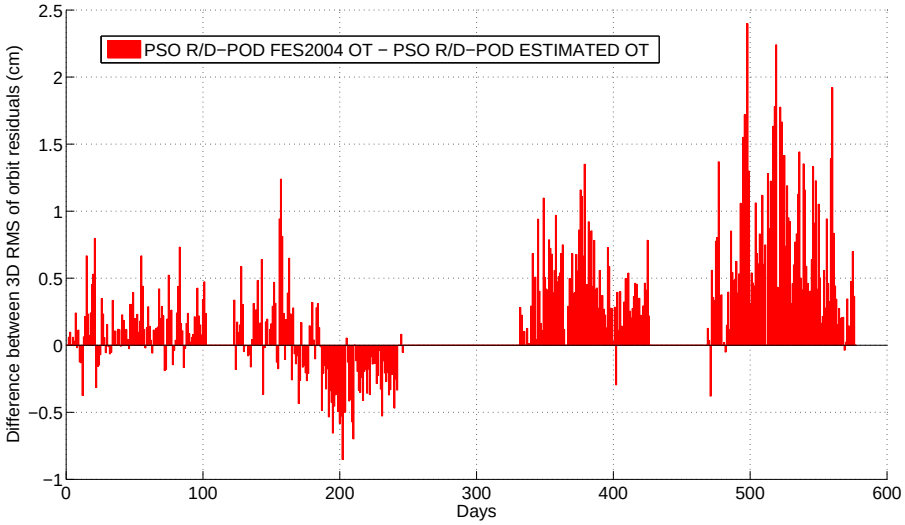

Figure 8. Difference between the 3D RMS of the differences between R/D PSO and the GOCE orbits estimated with FES2004 and the RMS of the difference between the GOCE R/D PSO and the orbits recomputed with the new parameters.

The structure of the thesis is the following. In Chapter 1, a background of the main space geodetic techniques is briefly presented to introduce the three measurement concepts characterizing the new generation of satellite gravity missions CHAMP, GRACE and GOCE.

In Chapter 2 the theory and the mathematical development regarding the tidal force is illustrated.

In Chapter 3 the ocean tide height parameterizations are described, the main being the classical harmonic representation and the convolution formalism, including the response method and the orthotide method.

In Chapter 4 two strategies for the processing of GOCE orbital data are explained, the fundamental one being the direct numerical fully-dynamic approach, consisting in performing the fully-dynamic precise orbit determination of GOCE, and the alternative being a first-order approach, consisting in determining the corrections to the tidal parameters of the reference model used through a least-square differential correction of the GPS phase observation residuals.

In Chapter 5 a sensitivity analysis of the ocean tide perturbations on GOCE is performed, computing the analytical spectral analysis and the statistics perturbation by coefficient of radial, transverse and normal perturbations on GOCE; alias periods of each tidal term are also calculated and the list of ocean tide parameters to be estimated with the multiarc approach is defined.

In Chapter 6 the processing of GOCE orbital data is presented and the preliminary results of the ocean tide parameter estimation are discussed, showing the comparison with official reduced-dynamic PSO and orbits computed with the reference FES2004 ocean tide model.

In Chapter 7 the conclusions are reported.

Riassunto

Da dieci anni, le missioni gravimetriche satellitari CHAMP, GRACE e GOCE stanno continuamente migliorando la nostra conoscenza del campo gravitazionale terrestre, sia della sua componente statica che tempo variabile, aumentando la risoluzione spaziale e temporale fino ai livelli estremamente elevati richiesti da molte applicazioni geoscientifiche, come la Geodesia, l'Oceanografia e la Fisica della Terra solida. In particolare, il presente lavoro di ricerca si concentra sulla parte periodicamente variabile del geopotenziale indotta dalle maree oceaniche e riguarda la stima dei parametri di marea oceanica dall'analisi delle perturbazioni orbitali di GOCE.

Le maree sono fenomeni periodici che interessano sia la Terra solida che gli oceani. Sono causate dall'attrazione gravitazionale differenziale sulla superficie della Terra da parte dei corpi perturbativi esterni, il cui potenziale corrispondente è chiamato Potenziale Generatore di Marea (TGP, Tide-Generating Potential), e dalla conseguente risposta della superficie terrestre a questo potenziale. Il TPG può essere direttamente determinato dalle posizioni astronomiche dei corpi perturbativi esterni, il cui effetto è chiamato marea diretta ed è alla base della teoria della marea di equilibrio. La marea di equilibrio, infatti, è la marea teorica che esisterebbe in una Terra ideale perfettamente rigida e non rotante (nessun effetto della forza di Coriolis), totalmente coperta di oceani aventi una profondità uniforme, dove la risposta alle forze generatrici di marea sia istantanea e non sia presente dissipazione. Ovviamente, la marea di equilibrio non rappresenta la marea reale, essendo troppo piccola rispetto alle marea osservata, tuttavia è un importante riferimento per l'analisi dei fenomeni mareali, in quanto contribuisce a darne un ordine di grandezza. Invece, la vera risposta della Terra solida e degli oceani al TPG, chiamata anche marea indiretta, dipende dalle proprietà elastiche della Terra. Le Equazioni Mareali di Laplace (LTE, Laplace Tidal Equations) sono introdotte per spiegare le relazioni tra gli oceani, la Terra solida e l'effetto di carico degli oceani sulla terra solida (marea di loading), in modo da derivare le equazioni fondamentali del campi di altezza di marea oceanica e del potenziale di marea oceanica.

Vengono descritte quindi le due principali parametrizzazioni del campo di altezza di marea oceanica. La rappresentazione classica in armoniche sferiche è caratterizzata da una somma di altezze di marea parziali, ciascuna corrispondente a una frequenza di marea, mentre l'analisi della risposta (Response Method) assume l'esistenza di una funzione di trasferimento o una risposta impulsiva tra le forze di marea e il campo di altezza di marea oceanica che è lineare all'interno di ciascuna banda mareale.

Le mappe cotidali e di corange sono riportate per le principali costituenti di marea diurne e semidiurne (K_1, P_1, O_1, Q_1, M_2, S_2, K_2, N_2), e sono utili per visualizzare il contenuto dinamico dell'altezza di marea oceanica indotto dalla loro frequenza. Inoltre, viene illustrato lo sviluppo un nuovo algoritmo di calcolo per la rideterminazione accurata dei coefficienti di ortomarea di Groves e Reynolds e i corrispondenti risultati numerici ottenuti sono discussi all'interno del formalismo delle ortomaree.

Per stimare i parametri armonici di marea oceanica si è deciso di utilizzare il satellite attualmente posto sull'orbita più bassa attorno alla Terra, ovvero GOCE, così da ottenere sulla sua

perturbazione d'orbita i segnali di marea più ampi possibili. GOCE (Gravity field and steady-state Ocean Circulation Explorer) è un satellite LEO che è stato lanciato dall'Agenzia Spaziale Europea (ESA, European Space Agency) il 17 marzo 2009 e orbita ad un'altezza di circa 250 km, su un'orbita eliosincrona quasi circolare, avente un'inclinazione di circa 96.7 gradi. Gli obiettivi principali di GOCE sono la mappatura della parte statica del campo gravitazionale terrestre con una precisione senza precedenti pari a 1 mGal (10^{-5} m/s^2) e il modellamento del geoide con una accuratezza di 1-2 cm, entrambi con una risoluzione spaziale di 100 km. Per raggiungere questi obiettivi, GOCE trasporta a bordo per la prima volta un Gradiometro Gravitazionale Elettrostatico (EGG, Electrostatic Gravity Gradiometer) per misurare il gradiente di gravità lungo tre direzioni ortogonali e uno strumento per l'inseguimento d'orbita da satellite a satellite (SSTI), costituito da un ricevitore GPS. Le caratteristiche spettrali di questi due tipi di misure sono complementari. Tuttavia, le misure gradiometriche di GOCE permettono di ricostruire la parte del campo gravitazionale a bassa frequenza, e sono solo marginalmente sensibili agli effetti delle maree oceaniche. Per questa ragione, in questo lavoro verranno utilizzati solamente i dati del ricevitore GPS di GOCE, in quanto GOCE è particolarmente sensibile alle perturbazioni orbitali indotte dalle maree per via della sua altitudine estremamente bassa che lo rende un eccellente banco di prova per l'applicazione del metodo classico dell'analisi delle perturbazioni orbitali per la stima dei parametri di marea.

Per il processamento dei dati orbitali di GOCE, sono state considerate diverse procedure di analisi, ma alla fine è stato scelto l'approccio numerico diretto, che consiste in una determinazione orbitale precisa di GOCE totalmente dinamica con l'accumulazione delle equazioni normali per ogni arco orbitale, seguiti da una soluzione multiarco per la stima dei parametri di marea oceanica globali.. Lo strumento scelto per eseguire questa analisi è il software NAPEOS sviluppato e mantenuto dall'ESA, che permette la determinazione e predizione orbitale e la stima di parametri. La stima dei parametri di marea oceanica, tuttavia, non era già presente in NAPEOS ed è stata implementata solo dopo aver acquisito il sistema. E stato necessario aggiornare NAPEOS con implementazione completa delle derivate parziali rispetto ai parametri di marea oceaniche ed estendere le sue strutture dati per l'inclusione delle caratteristiche dei parametri: la costituenti di marea, il tipo armonico (C or S), l'ordine e il grado armonici e la chiralità (prograda o retrogada).

Il compito fondamentale per raggiungere gli obiettivi scientifici di questo studio è la definizione di un set di parametri di marea oceanica verso i quali GOCE è maggiormente sensibile. A tale scopo, è stato effettuato uno studio dettagliato della sensibilità dell'orbita di GOCE alle perturbazioni di marea oceanica, portato avanti usando come modello di riferimento il FES2004. Innanzitutto, è stato valutato l'effetto delle varie combinazioni delle costituenti delle maree oceaniche sull'orbita di GOCE su differenti intervalli di tempo. Poi le accelerazioni delle maree oceaniche agenti sull'orbita di GOCE sono state determinate usando differenti modelli esistenti di marea oceanica. Quindi, a partire dall'evoluzione degli elementi orbitali di GOCE resa disponibile grazie a una POD preliminare di GOCE con NAPEOS, sono state stimate le caratteristiche orbitali medie di GOCE (riportate in Tabella 2) tramite un fit lineare ai minimi quadrati.

Utilizzando la teoria lineare di Kaula, è stata effettuata l'analisi spettrale analitica delle perturbazioni delle maree oceaniche agenti sull'orbita di GOCE nelle direzioni radiale, trasversa e normale (RTN) fino a ordine e grado 20, assieme alla statistica delle perturbazioni per coefficiente. Gli spettri delle ampiezze prograde nel sistema RTN sono mostrati rispettivamente nelle Figure 9, 10, 11, mentre l'RMS delle perturbazioni di marea accumulato su tutte le costituenti nel sistema RTN è mostrato rispettivamente nelle Figure 12, 13, 14, in cui è possibile notare un RMS massimo per la componente radiale di 1.323 m, per la trasversa di 363.136 m e per la normale di 76.241 m.

GOCE risente del problema dell'aliasing temporale delle frequenze di perturbazione mareale, in quanto campiona il campo gravitazionale statico e la parte tempo-variante solamente lungo il percorso della sua orbita, con una risoluzione temporale che dipende dal suo periodo di ripetizione

Table 2. Elementi orbitali medi di GOCE e loro variazioni utilizzati per l'analisi spettrale delle perturbazioni mareali su GOCE.

Elemento	**Valore**
$\bar{a}$	6632.884525 km
$\bar{e}$	2.306273×10^{-3}
$\bar{i}$	1.686227 rad
ω_0	1.845595 rad
Ω_0	5.471748 rad
M_0	0.971383 rad
$\dot{\omega}$	-3.764817×10^{-7} rad/s
$\dot{\Omega}$	2.022334×10^{-7} rad/s
$\dot{M}$	1.167455×10^{-3} rad/s
Nodal Period	89.728100 min
Repeat Period	979 revs/61 nodal days

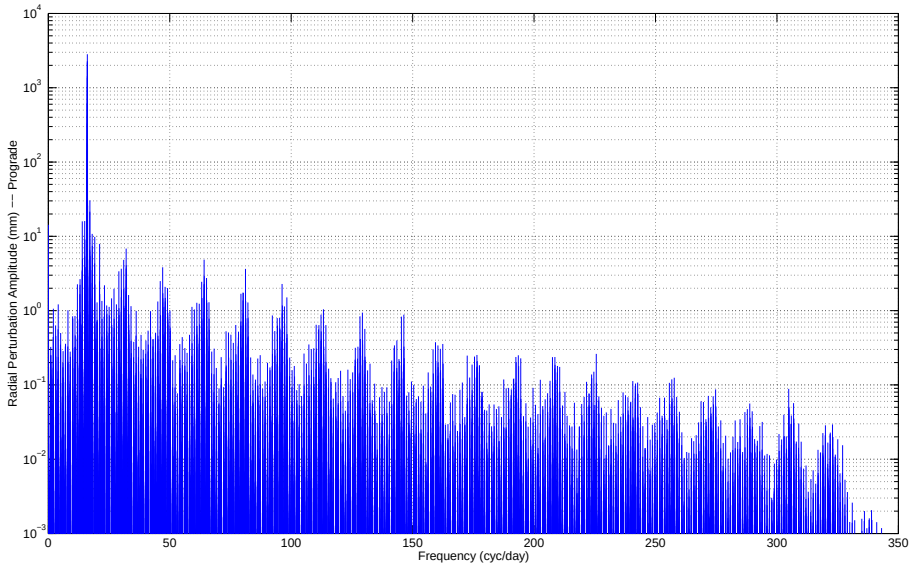

Figure 9. Spettro d'ampiezza della perturbazione prograda radiale in posizione dovuta alle maree oceaniche.

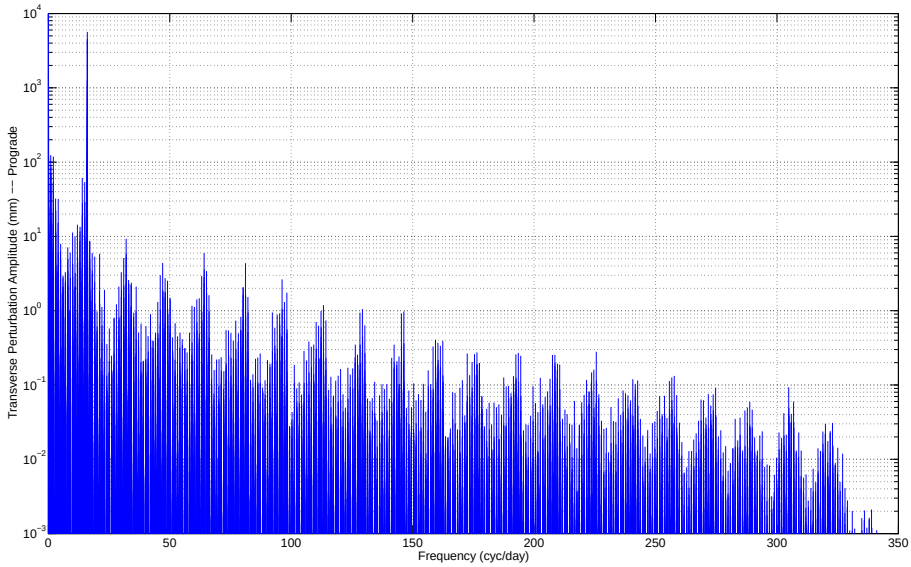

Figure 10. Spettro d'ampiezza della perturbazione prograda trasversa in posizione dovuta alle maree oceaniche.

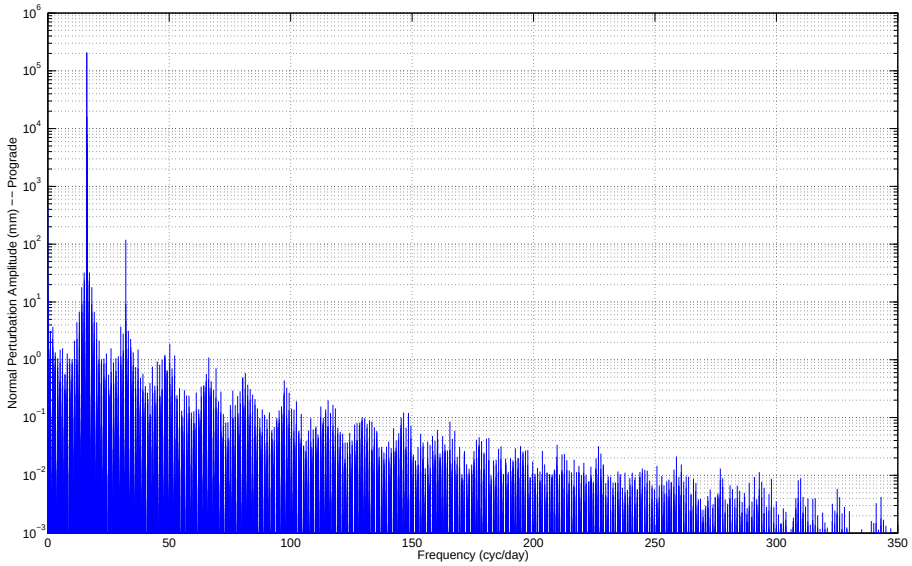

Figure 11. Spettro d'ampiezza della perturbazione prograda normale in posizione dovuta alle maree oceaniche.

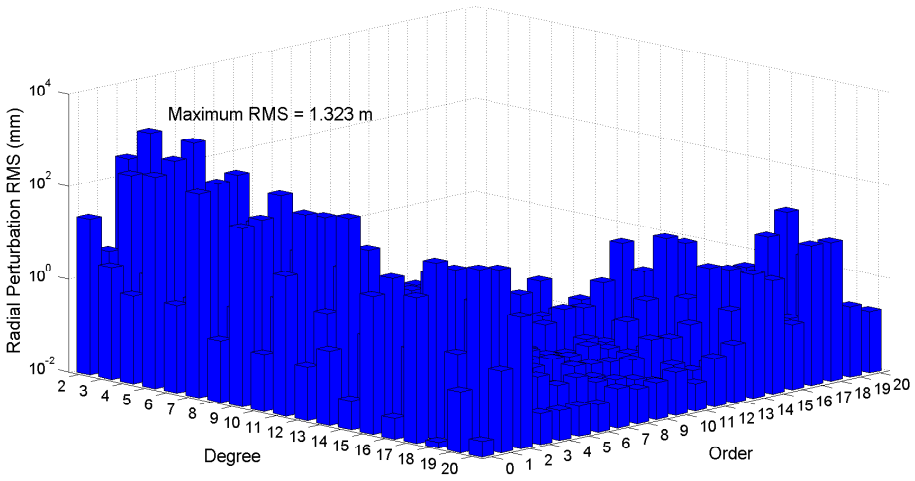

Figure 12. RMS accumulato per coefficiente sulle costituenti dovuto alla perturbazione radiale delle maree oceaniche in posizione.

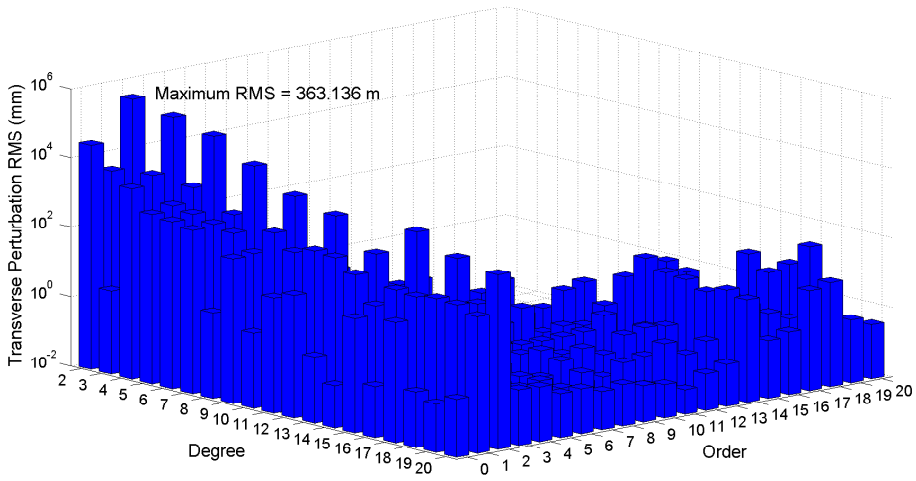

Figure 13. RMS accumulato per coefficiente sulle costituenti dovuto alla perturbazione trasversa delle maree oceaniche in posizione.

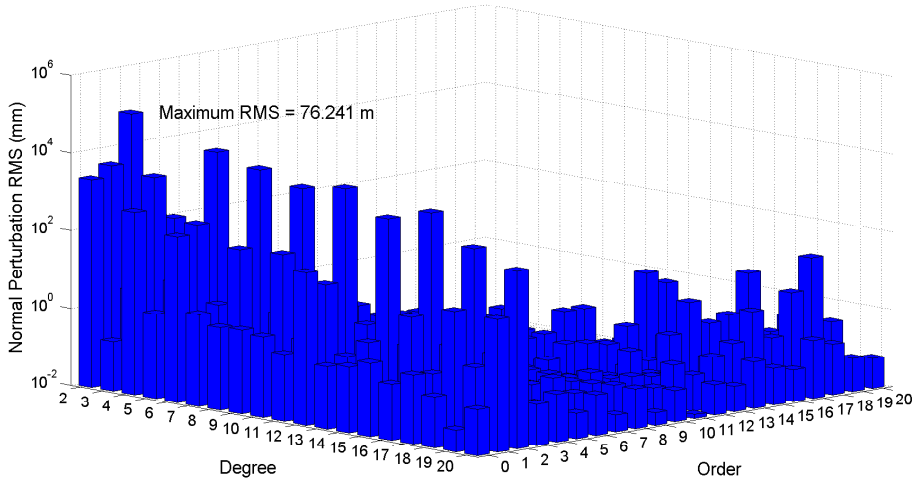

Figure 14. RMS accumulato per coefficiente sulle costituenti dovuto alla perturbazione normale delle maree oceaniche in posizione.

della traccia a terra. Seguendo da vicino un periodo di ripetizione di 979 rivoluzioni in 61 giorni nodali, il campionamento di GOCE causa aliasing delle frequenze mareali aventi un periodo inferiore a 122 giorni (due volte il periodo di ripetizione dell'orbita), le quali verrano spostate a periodi più lunghi, compresi tra 122 giorni e diversi anni. Sfortunatamente GOCE è un satellite in orbita eliosicnrona e pertanto non permette la stima completa delle costituenti delle maree solari diurne e semidiurne S_2 and S_1, aventi periodi di esattamente 12 e 24 ore, dato che campiona entrambe queste costituenti alla stessa fase ogni giorno. In particolare, durante l'analisi spettrale, sono stati calcolati i principali periodi di aliasing per tutte le frequenze di perturbazione delle maree oceaniche. Si è tenuto conto anche della durata del set di dati GOCE a disposizione: visti i 400 giorni di misure a disposizione, il limite oltre il quale GOCE non è più capace di stimare un parametro è di circa 200 giorni. Si è scelto di non stimare i coefficienti (l, m) se la più grande ampiezza parziale dello spettro, tra tutte quelle che contribuiscono alla stessa coppia (l, m), ha un periodo di aliasing di oltre i 200 giorni.

Combinando le informazioni derivanti dall'analisi spettrale, dalla statistica delle perturbazioni per coefficiente e dalla determinazione dei periodi di aliasing delle maree oceaniche, si può identificare la griglia dei parametri di marea oceanica da grado 2 fino a 20 che devono essere stimati con i dati orbitali di GOCE. Si tratta in tutto di 490 parametri. Il numero totale di parametri da stimare è limitato applicando un valore di soglia sugli RMS delle perturbazioni per coefficiente, rispettivamente di 5 mm per la componente radiale, 2 cm per la trasversa e 1 cm per la normale, sia nel caso prograde che retrograde.

I dati orbitali di GOCE sono stati processati suddividendoli in archi giornalieri dal 1 novembre 2009 (l'inizio della fase operativa) al 31 maggio 2011. Per l'analisi multiarco sono stati considerati solamente gli archi con un RMS di post-fit dei residui di fase GPS inferiore a 8 mm, per un totale di 431 giorni.

I risultati preliminari ottenuti mostrano che il 56% del numero totale di parametri differisce dai parametri del FES2004 per meno di 1 cm, mentre l'errore relativo dei parametri stimati rispetto ai corrispettivi parametri del FES2004 è inferiore a 1 per circa il 16% del totale, indicando che sono dello stesso ordine di grandezza dei parametri del FES2004.

Infine, i dati orbitali di GOCE sono stati riprocessati dal primo novembre 2009 al 31 maggio 2011, inizializzando il modello di marea oceanica con i parametri stimati, se presenti, mantenendo altrimenti i parametri del FES2004. L'RMS di post-fit dei residui degli osservabili di fase GPS ottenuti con il nuovo modello di marea oceanica ha un valore medio di 6.5 mm, ed è da notare come la differenza tra l'RMS post-fit ottenuto con il FES2004 e l'RMS risultante dal nuovo modello di marea oceanica mostra un miglioramento di circa 0.6 mm per il 96% degli archi analizzati e superiore a 1 mm per il 16%, mentre per alcuni archi raggiunge una differenza di 2 mm (si veda Figura 15).

Concludendo, il confronto delle orbite mostra che l'RMS 3D delle differenze tra le orbite calcolate usanto il FES2004 e quelle ricalcolate con i nuovi parametri mostra un valore medio di 2.5 cm, mentre l'RMS 3D delle differenze rispetto alle PSO a dinamica ridotta (R/D Precise Science Orbit) ufficiali ha un valore medio di 4.9 cm. Le differenze tra l'RMS 3D dei residui orbitali tra la PSO e la POD di GOCE con il FES2004 e l'RMS dei residui orbitali tra la PSO di GOCE e la POD di GOCE con i nuovi parametri mostra un miglioramento in media di circa 0.9 cm (si veda Figura 16).

Certamente, si rendono necessari ulteriori esecuzioni dei processi di POD e Multiarco, assieme al raffinamento della lista dei parametri da stimare, andando a rimuovere quelli eccessivamente mal stimati e introducendo opportunamente nuovi parametri. Inoltre, un'estensione del set di dati di GOCE su un periodo più lungo dovrebbe consentire un sostanziale miglioramento dei risultati. Infatti, sebbene il compito sia stato estremamente complicato e serrato, i risultati preliminari ottenuti sono motivo di incoraggiamento per ulteriori analisi.

La struttura di questa tesi è la seguente. Nel Capitolo 1 verrà presentato lo stato dell'arte delle principali tecniche di geodesia spaziale, per introdurre i tre concetti di misure che caratterizzano

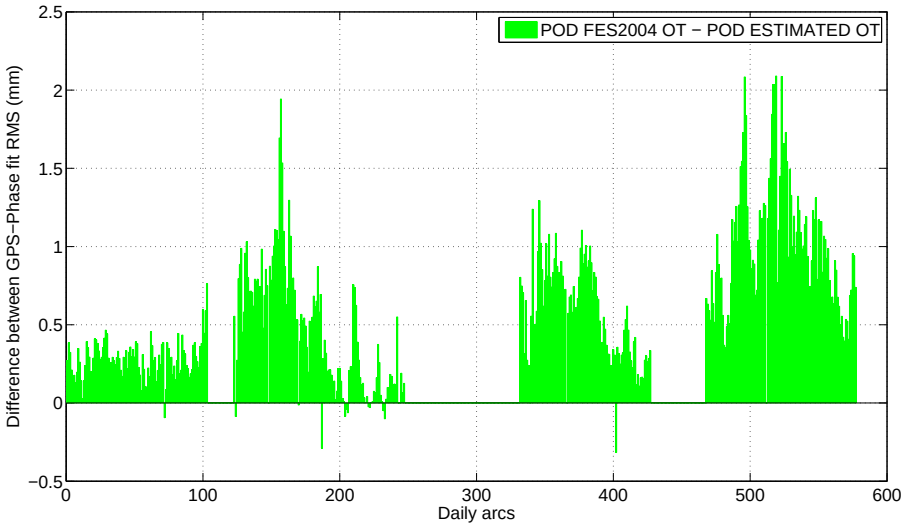

Figure 15. Differenze tra l'RMS del fit ottenuto usando il FES2004 e l'RMS del fit ottenuto con i nuovi parametri di marea oceanica, invece dei corrispondenti parametri del FES2004.

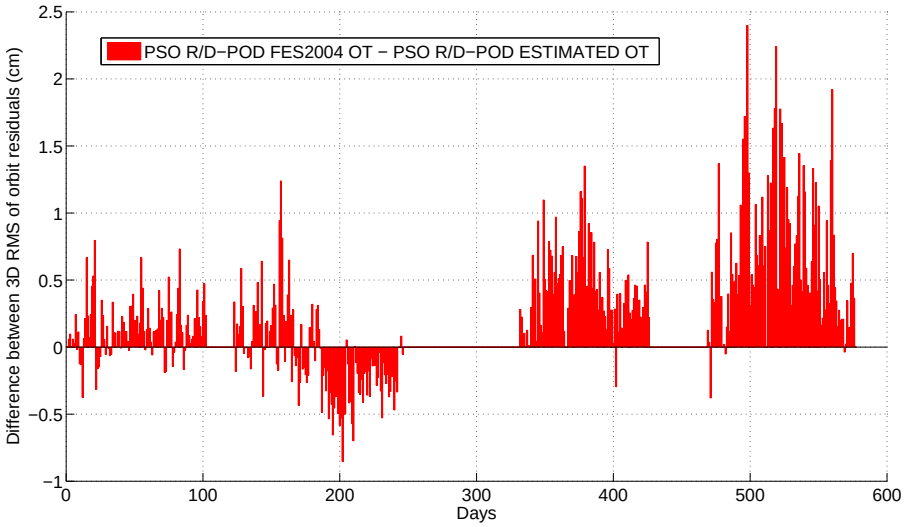

Figure 16. Differenze tra gli RMS 3D.

le nuove generazioni di missioni gravimetriche spaziali, CHAMP, GRACE e GOCE.

Nel Capitolo 2 verranno illustrate la teoria e lo sviluppo matematico riguardanti la forza mareale.

Nel Capitolo 3 saranno descritte le parametrizzazioni delle altezze di marea oceanica, soffermandosi in particolare sulla classica rappresentazione in armoniche e sul formalismo della convoluzione, il quale include il metodo di risposta e i metodo delle ortomaree.

Nel Capitolo 4 verranno spiegate due strategie per l'analisi dei dati orbitali di GOCE, dove l'approccio fondamentale è quello numerico diretto pienamente dinamico, consistente nell'eseguire la determinazione orbitale di GOCE totalmente dinamica. Il metodo alternativo è un approccio del primo ordine, dove si determinano le correzioni ai parametri mareali del modello di riferimento attraverso una correzione differenziale ai minimi quadrati dei residui delle osservazioni di fase GPS.

Nel Capitolo 5 verrà eseguita l'analisi della sensitività delle perturbazioni dei parametri di marea su GOCE, calcolando l'analisi spettrale analitica e la statistica delle perturbazioni per coefficiente delle perturbazioni radiali, trasverse e normali su GOCE; verranno inoltre calcolati i periodi di aliasing di ciascun termine mareale e definita la lista dei parametri di marea da stimare con l'approccio multiarco.

Nel Capitolo 6 verrà presentata l'analisi dei dati orbitali di GOCE e saranno discussi i risultati preliminari della stima dei parametri di marea oceanica, mostrando i confronti con le orbite PSO ufficiali a dinamica ridotta e le orbite determinate con il modello di marea oceanica di riferimento, il FES2004.

Nel Capitolo 7 saranno riportate le conclusioni.

Acronyms

ASI	Agenzia Spaziale Italiana (Rome, Italy)
CHAMP	CHAllenging Minisatellite Payload
CNES	Centre National d'Etudes Spatiales (Paris, France)
CTE	Cartwright-Taylor-Edden
DGFI	Deutsches Geodätisches Forschungsinstitut (Munich, Germany)
DORIS	Doppler Orbitography and Radio-positioning Integrated by Satellite
ECM	Earth's Center of Mass
EGG	Electrostatic Gravity Gradiometer
EOP	Earth Orientation Parameters
ESA	European Space Agency
GLONASS	GLObal NAvigation Satellite System
GMST	Greenwich Mean Sidereal Time
GMT	Generic Mapping Tools
GOCE	Gravity field and steady-state Ocean Circulation Explorer
GPS	Global Positioning System
GRACE	Gravity Recovery And Climate Experiment
GSFC	Goddard Space Flight Center (Greenbelt, Maryland, USA)
IERS	International Earth Rotation Service
IGS	International GPS Service
JPL	Jet Propulsion Laboratory (Pasadena, California, USA)
LAGEOS	LAser GEOdynamics Satellite
LAGRANGE	Laben GNSS Receiver for Advanced Navigation, Geodesy and Experiments
LEO	Low Earth Orbit
LLR	Lunar Laser Ranging
LOD	Length Of Day
NAPEOS	NAvigation Package for Earth Observation Satellites
NASA	National Aeronautics and Space Administration
NTDF	NAPEOS Tracking Data Format
PGR	Post-Glacial Rebound
POD	Precise Orbit Determination
RINEX	Receiver-INdependent EXchange format
RMS	Root Mean Square
RSS	Root Sum Square
SLR	Satellite Laser Ranging
SNREI	Spherical Non-Rotating Elastic Isotropic
SP3	Standard Product # 3
SST-hl	Satellite-to-Satellite Tracking high-low
STARLETTE	Satellite de Taille Adaptée avec Réflecteurs Laser por les ETudes de la TErre

TGP	Tide Generating Potential
TT	Terrestrial Time
UT1	Universal Time
VLBI	Very Long Baseline Interferometry

Contents

List of Figures

List of Tables

Chapter 1

The new generation of gravity missions

In this chapter, a background of the main space geodetic techniques is briefly presented in order to illustrate in more details the three different measurement concepts characterizing the new generation of satellite gravity missions CHAMP, GRACE and GOCE. Finally, the improvements obtainable in the future satellite gravity missions from formation flying technologies are discussed.

1.1 Introduction

Since the beginning of the space age, the determination of the Earth's gravity field has always been one of the main interests of the earth-science community. The gravitational force is responsible for many dynamic processes happening within the Earth's interior and on its surface, such as mantle convection, ocean and atmosphere circulation, solid Earth and ocean tides, ice distribution and sea-level change, post-glacial rebound and tectonic motions. All of these processes affect the distribution of mass on the Earth and produce temporal variations in the gravitational field, so an accurate gravity recovery is a necessary prerequisite for applications in different scientific disciplines, like oceanography, glaciology, geophysics and climatology and plays a dominant role in geodesy, the science concerned with the study of the shape and size of the Earth, its gravity field, its orientation in space and the variations of these quantities over time.

The roots of satellite geodesy can be dated in 1802, when Laplace determined the dynamical flattening of the Earth from the motion of the lunar node, treating the Moon as an artificial satellite. In the pre-satellite era the knowledge of the Earth's gravity field was based on terrestrial and airborne measurements and it was available with high accuracy only in few areas of the world.

Only by means of satellites, the knowledge of the Earth's gravity field can be achieved globally, homogeneously and within a reasonable time period. The proper era of satellite geodesy started with the launch of the first artificial satellite, Sputnik-1 (URSS), on 4 October 1957 and with the important geodetic result of the determination of the Earth's flattening as $f = 1/298.3$ from tracking observations of Sputnik-2 (URSS) and Explorer-1 (NASA) in 1958.

The development of new technologies, relying on precise distance or phase measurements transmitted or reflected from extraterrestrial objects, such as quasars, the Moon or artificial satellites, has enhanced knowledge of the global Earth's gravity field and the geoid[1]. In particular, space geodesy has become a dialectic science, in the sense that the geopotential models are better known by the accurate orbit determination satellites and, at the same time, the position of satellites is better localized by improved potential models. Nowadays, four main space geodetic techniques can be classified (Schubert, 2007):

- Very Long Baseline Interferometry (VLBI), a radio measurement system that determines the difference in arrival times of radio signals by cross-correlation; in particular, VLBI

[1] The geoid is the equipotential surface corresponding to the mean sea level of an hypothetical ocean at rest.

measurements are made at two high frequencies, about 2.3 GHz and 8 GHz, and are affected by a propagation delay due to the ionosphere that can be removed by a dual-frequency correction; typically, observations are made in sessions with a duration of about 24 hours; VLBI is sensitive to processes changing the relative position of the radio telescopes with respect to the source, such as solid Earth tides or tectonic motions; it is mostly used for accurate measurements of polar motion and UT1;

- Satellite and Lunar Laser Ranging (SLR and LLR), optical systems measuring the time of flight required for laser pulses to travel from a ground laser transmitter to a satellite equipped with retro-reflectors and to return back; this time is then converted into a distance measurement between the satellite and the observing station with an accuracy of 1-10 mm. Like the previous technique, SLR is sensitive to processes that change the distance between the satellite and the observing site and can be used to determine the temporal variations of the Earth's gravity field and the location of the Earth's centre of mass. LLR is similar to SLR except that retro-reflectors are located on the Moon and consequently the received signal is much weaker, needing more powerful laser and detection systems;

- Doppler Orbitography and Radio-positioning Integrated by Satellite (DORIS), a radio system developed by the Centre National d'Etudes Spatiales (CNES) and used since 1990. It consists of more than 50 transmitting beacons globally distributed on the Earth's surface and receivers located onboard artificial satellites, with the aim to provide precise ground location and precise orbit determination, in particular tracking satellites for radar altimetry applications. DORIS uses a dual-frequency Doppler tracking that allows to correct for ionospheric effects and operates by accurately measuring the Doppler shift of the two separate signals (2036.25 MHz and 401.25 MHz) transmitted from ground stations and received onboard the satellites. These measurements allow to derive the velocity of the satellites on their orbits and are processed to determine the precise satellite positions and other quantities, such as the Earth Orientation Parameters (EOP);

- Global Navigation Satellite Systems (GPS, GLONASS), radio systems providing inexpensive, highly accurate, global and continuous positioning measurements. GNSS systems consist of constellations of transmitting satellites and a ground network of receivers. They can be used for a large variety of applications in the fields of navigation, geodesy and timing, in particular for satellite POD and Earth gravity field improvement.

In recent decades a wide variety of satellite mission have been planned for geodetic applications by combining the space-based techniques described above and among them we illustrate the most relevant. LAGEOS-1 (LAser GEOdynamics Satellite) and LAGEOS-2, launched respectively by NASA in 1976 and by NASA/ASI in 1992, were passive spherical satellites placed at an altitude of 5900 km and covered with 426 corner-cube retro-reflectors used to reflect laser beams transmitted from ground stations (see Figure 1.1). LAGEOS-1 was the first spacecraft dedicated exclusively to high-precision laser ranging: by measuring the round trip time of flight of the laser beam, the distance between the satellites and the ground station could be accurately determined, allowing to calculate station position to within 1-3 cm. These satellites were designed to be as heavy as possible to minimize the effects of non-gravitational forces, to contain as many retro-reflectors as possible and to minimize the effects of solar radiation pressure; moreover the materials were chosen to reduce the effects of the Earth's magnetic field on their orbits. Due to their characteristics, LAGEOS satellites were used mainly for orbit determination and gravity field recovery purposes.

Also STARLETTE (Satellite de Taille Adaptée avec Réflecteurs Laser por les ETudes de la TErre) and Stella, launched by CNES respectively in 1975 and 1993, are passive spherical bodies covered with 60 retro-reflectors (see Figure 1.1). Their small size compared to their mass allows their use mainly to determine the gravitational attraction than other forces such as the

atmospheric drag or the solar radiation pressure. In particular Starlette is very sensitive to zonal variations in the gravity field, more than the LAGEOS, while Stella is mainly used for gravity field recovery.

The altimetry mission TOPEX/Poseidon, launched by NASA/CNES in 1992 and ended in 2005, provided information about ocean topography, ocean circulation and their interaction with the atmosphere with unprecedented accuracy employing three independent geodetic techniques (SLR, DORIS and GPS) to determine the satellite altitude.

ERS-2 (European Remote Sensing) satellite was launched by ESA in 1995 and was equipped with a radar altimeter to measure ocean surface temperature and winds and a sensor for atmospheric ozone research.

Figure 1.1. On the left: artistic picture of LAGEOS 1 (GSFC web site http://library01.gsfc.nasa.gov/); on the right: artistic picture of Starlette and Stella (GSFC web site http://ilrs.gsfc.nasa.gov/).

Jason-1, launched by NASA/CNES in 2001 as follow-on to the highly successful TOPEX/Poseidon mission, is a microwave altimeter used primarily for ocean studies.

ENVISAT (ENVIronmental SATellite), launched by ESA in 2002, successor to ERS-2, carries both a radar altimeter and a DORIS tracking receiver to provide continuous observation and monitoring of the Earth's land, atmosphere, oceans and ice caps.

ICESat (Ice, Cloud and land Elevation Satellite), launched by NASA in 2003, is a laser altimeter used primarily for polar ice-sheet studies. The laser altimeter measures height from the spacecraft to the ice sheet with an precision of better than 10 cm. The height measurements coupled with the radial orbit positions, provided by a combination of satellite laser ranging and GPS data, allows the determination of topography.

1.2 Complementary satellite gravity missions

Before the launch of the first satellite, the knowledge of the Earth's gravity field was based only on terrestrial and airborne observations allowing high accurate measurements in few regions of the world, while in others there were even no gravity data.

In the last ten years, the more stringent requirements of precision necessary for various scientific disciplines have motivated the planning of three dedicated satellite gravity missions (CHAMP, GRACE, GOCE), with the aim to improve accuracy and spatial resolution of the Earth's gravity field models. Three different measurement concepts of the Earth's gravity field have been realized (see Figure 1.2):

- high-low satellite-to-satellite tracking (SST-hl), employed by CHAMP mission, in which the LEO satellite orbit is continuously determined by GNSS systems and the 3D accelerometer onboard the satellite allows to obtain the accelerations caused by the Earth's gravity field, corresponding to the first derivatives of the gravitational potential;

- low-low satellite-to-satellite tracking (SST-ll), employed by GRACE mission, that measures the difference between the accelerations acting on the two LEO satellites, in such a way

that the effects of non gravitational accelerations, as atmospheric drag and solar radiation pressure, can be eliminated;

- Satellite Gravity Gradiometry (SGG), employed by GOCE mission, that determines the local gravity gradient by measuring the differences in acceleration of two masses within a single spacecraft, corresponding to the second derivative of the gravitational potential.

The fundamental parameter that determines the sensitivity with respect to the spatial scales of the Earth's gravitational potential is the distance between the test masses (Hofmann-Wellenhof & Moritz, 2005). In practice, the case of SST-hl consists in an acceleration determination over an almost infinite baseline corresponding to the distance between the satellite and the Earth; SST-ll consists in an acceleration difference determination over a long baseline corresponding to the distance between the two LEO satellites; SGG consists in an acceleration gradient determination over an almost zero baseline realized by the gradiometer axes. Consequently, while the low-low SST provides accurate long and mid wavelength model, the gravity gradiometry provides accurate short wavelength model, thus GRACE and GOCE missions are complementary to each other.

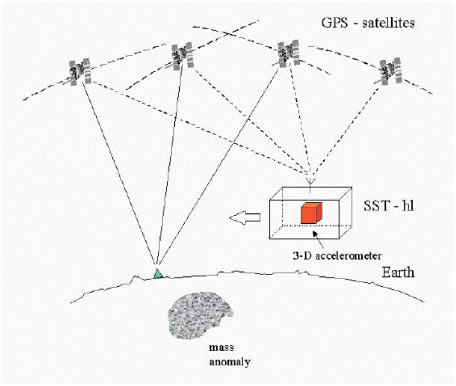

(a) SST-hl

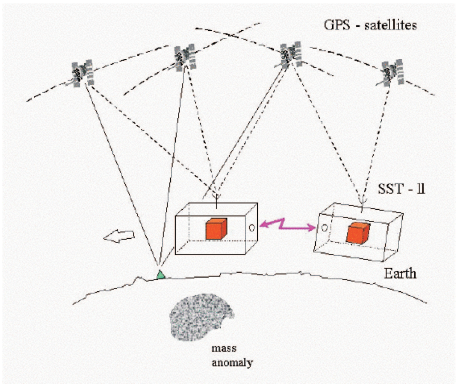

(b) SST-ll

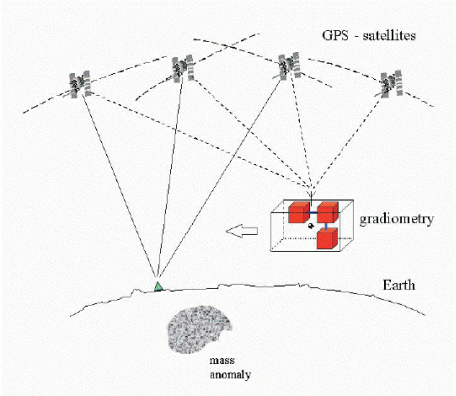

(c) SGG

Figure 1.2. Measurement concepts of three different satellite gravity missions (ESA SP-1233(1), 1999).

The purpose of these three measurement concepts is to counteract the natural attenuation of the gravitational field with altitude by differential measurement, where the gravitational sensitivity increases with decreasing distance between the test masses. Finally, it must be noticed that high resolutions require relatively low satellite orbits, while the determination of temporally varying phenomena improves as the time span of the measurements increases.

1.2.1 CHAMP

CHAMP (CHAllenging Minisatellite Payload) (Reigber, 1998) is a German mission under the leadership of the GFZ in Potsdam and with the partnership of NASA, CNES and AFRL (Air Force Research Laboratories, USA). The satellite was launched in 2000 from Plesetzk, Russia, onto an almost circular, near polar orbit, with an average altitude of 450 km. Although the design lifetime of the satellite system was 5 years, CHAMP is currently collecting data used for many scientific applications, such as GPS radio occultation.

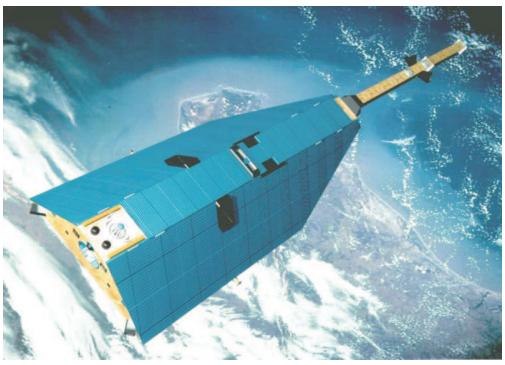

Figure 1.3. Artistic picture of CHAMP (GFZ web site http://op.gfz-potsdam.de/champ/).

The primary objectives of CHAMP are the mapping of the global static Earth's gravity field together with the recovering of the global magnetic field and the profiling of the ionosphere and the troposphere (see Figure 1.3). The main instruments to achieve the mission goals are:

- a dual-frequency GPS receiver (provided by NASA/JPL), to determine the satellite orbit;
- a three-axis accelerometer (provided by CNES), to measure the non-gravitational accelerations acting on the satellite which are mainly due to atmospheric drag, solar radiation pressure, Earth albedo radiation and attitude maneuvers. Using these measurements allows to generate a dynamic orbit of the LEO without modeling the non-gravitational forces which is very helpful for gravity field recovery. A cold gas propulsion system has been employed in order to control the attitude and to perform orbit change maneuvers; the attitude of the spacecraft is not stable over a long time period due to the design of the satellite. The attitude is corrected by thruster pulses of the cold gas propulsion system, which may happen between 70 and 200 times per day;
- a laser retro-reflector array for SLR measurements. The SLR technique is a completely independent technique to determine precise orbits for the LEO. SLR observations are accurate at the cm level, unambiguous and free of atmospheric propagation effects due to water vapor. This is why the SLR technique is very useful for calibrating the orbit resulting from the GPS tracking;
- a fluxgate magnetometer, to measure the vector components of the Earth's magnetic field.

1.2.2 GRACE

GRACE (Gravity Recovery And Climate Experiment), launched in 2002, may be considered as the follow-on of CHAMP mission. It is a joint project between NASA and DLR and consists of two Earth satellites (see Figure 1.4), following each other along the same orbital trajectory, with an along track relative distance of 220 km $\pm$ 50 km. The inclination of the orbit is about 89° to maximize the global coverage and the orbit altitude, initially 500 km, is decreasing to about 300 km. The main purpose of GRACE is the determination of the Earth's gravity field and its temporal variations. A K-Band Ranging (KBR) system is the fundamental instrument of

GRACE because it allows to measure the range and range-rate between the two spacecrafts with a precision of respectively 10 μm and 1 μm/s with a 5 s data sampling interval. This dual-band microwave link provides a new and independent observation type for mapping the gravity field of the Earth.

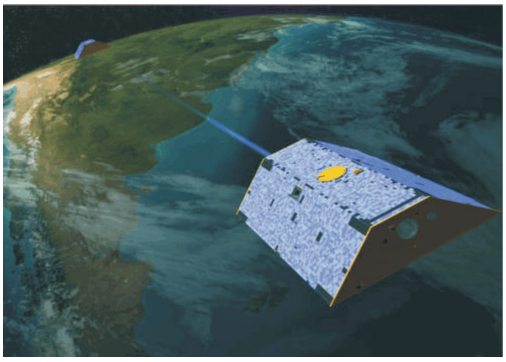

Figure 1.4. Artistic picture of GRACE (http://www.csr.utexas.edu/grace/).

The dual one-way K (24.5 GHz) and Ka (32.7 GHz) band microwave inter-satellite ranging system with a precision of 10 μm (Kim et al., 2001), the Ultra-Stable Oscillator (USO) accurate to within 70 ps for time-tagging, the 3-axis super-STAR accelerometers with a precision of $4{\times}10^{-12}$ m/s^2 (Davis et al., 1999; Perret et al., 2001) within the bandwidth of $2 \times 10^{-4} - 0.1$ Hz (Kang et al., 2006), and the dual-frequency 24-channel Blackjack GPS receivers comprise GRACE's instrument suite.

The orbits of the two satellites, sensing these effects at slightly different phases, will be perturbed differentially. This difference in perturbations is manifested in the intersatellite range changes. The GRACE microwave ranging instrument will provide very accurate measurements of the range changes. By making these differential measurements enables significant improvement in the estimates of the higher resolution features of the Earth gravity field.

1.2.3 GOCE

GOCE (Gravity field and steady-state Ocean Circulation Explorer) was launched on 17 March 2009 (see Figure 1.5) as the first Earth Explorer core mission of the ESA Living Planet Program. GOCE is flying at the very low altitude of about 260 km on a dusk-dawn nearly Sun-synchronous and near circular orbit, inclined 96.5° with respect to the Earth's equator. In particular, the dusk-dawn nearly Sun-synchronous orbit assures a stable energy supply from the solar panels, meaning that the orientation of the satellite orbital plane is constant relative to the direction to the Sun and the local time at the ascending node is 18 h, so the orbital plane remains approximately perpendicular towards the Sun direction. Moreover, GOCE is a very slim satellite with a cross-sectional area of 1.1 m^2, a length of 5.3 m and a weight of about 1050 kg.

The main purpose of GOCE is to map the static part of Earth's gravity field with an unprecedented precision of 1 mGal = 10^{-5} m/s^2 and to model the geoid with an accuracy of 1 cm, achieving these results at a spatial resolution of 100 km.

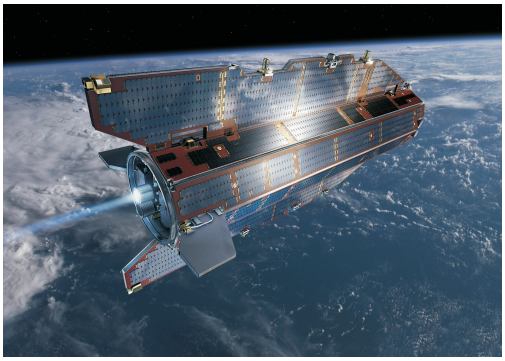

Figure 1.5. Artistic picture of GOCE (ESA web site http://www.esa.int/esaLP/).

The main scientific payload onboard GOCE is a three-axis Electrostatic Gravity Gradiometer (EGG), for the first time employed in a satellite mission. The EGG consists of three pairs of accelerometers along three spatial orthogonal directions and two accelerometers of the same pair are mounted at 50 cm distance to each other. The proof masses are made of platinum-rhodium alloy with a dimension of 4 cm by 4 cm by 1 cm. The principle of operation of an accelerometer is that a proof mass is floated in a small cage and is kept in the centre of the cage by electrostatic forces, representing the accelerations seen by the proof mass. The accelerations measured by each accelerometer can be as small as one part in 10,000,000,000,000 of the gravity acceleration on the Earth.

Because the accelerations of the masses is very weak and subject to noise or dissipative forces, the method of differential measurement is used. In fact, the difference in the accelerations of two accelerometers belonging to the same arm is measured, allowing to remove noise and disturbing forces that affect both accelerometers in the same manner. The remaining signal is the Earth's gravity gradient along the arm direction, in other words the second derivative of the gravitational potential, and it represents the basic scientific product of GOCE (ESA SP-1233(1), 1999). In particular, GOCE gradiometer has two ultra-sensitive axes and a less sensitive axis. It provides very sensitive measurements of the three linear and the three angular accelerations of the spacecraft, the three in-line gravity gradient components V_{xx}, V_{yy}, V_{zz} (X indicating the flight direction and Z pointing approximately radially away from the Earth) of the Earth gravity gradient tensor $\mathbf{V}_{ij}$ and of one off-diagonal gravity gradient term $\mathbf{V}_{xz}$ in the XZ plane to maximize the sensitivity of the determination of the angular accelerations about the Y-axis. The two remaining off-diagonal gravity gradient terms $\mathbf{V}_{xy}$ and $\mathbf{V}_{yz}$ are estimated with much lower sensitivity (ESA SP-1233(1), 1999). The result of a science measurement phase is a gravity gradient map covering our planet except for small areas around the poles. The gradiometer is used to recover the short-wavelength part of the gravity field: the measurement bandwidth covers the frequency range between 5 mHz and 100 mHz.

The average acceleration of two accelerometers in one arm is also measured. This average represents the external non-gravitational forces acting on the spacecraft, like atmospheric drag and solar radiation pressure. This information is used to command the electric ion propulsion engine to continuously compensate the atmospheric drag forces and torques and keep the satellite flying drag-free in the in-flight direction. The air density average value during the scientific mission is about 5.6×10^{-14} g/cm^3, corresponding to an altitude around 260 km. The varying thrust level when in drag-free mode is due to changes in the solar activity, which has increased significantly starting from March 2011, causing the average thrust level to jump from about 2.7 mN to 4 mN, with peaks of instantaneous thrust of 7.6 mN, not affecting, obviously, the GOCE altitude.

The second scientific payload of GOCE is the 12-channel LAGRANGE (Laben GNSS Receiver for Advanced Navigation, Geodesy and Experiments) GPS receiver, working on both L1 and L2 frequencies, with a sampling rate of 1 Hz. Satellite-to-Satellite-Tracking in high-low mode (SST-

hl) is used for the orbit determination and for retrieval of the long- and medium-wavelength part of the gravity field.

The techniques of gradiometry and SST-hl are complementary, allowing the recovery of the gravity field over all the spatial scales. The point of overlap between the gravity retrieval capabilities of SST-hl and gradiometry begins at around degree and order L = 15 (resolution of 1300 km) and ends at degree and order L = 60 (resolution of 330 km).

Finally, GOCE is carrying onboard a laser retro-reflector array, used for SLR measurements, providing mainly an independent validation of the GPS POD, star cameras for the attitude control and an ion thruster for the realization of a drag-free control of the satellite in along-track direction.

1.3 Future satellite gravity missions

Satellite gravity missions such as CHAMP, GRACE and GOCE, together with other complementary information, are continuously improving our knowledge of the static and temporally changing gravity field, increasing spatial and temporal resolution to a high level required by many geoscience applications. Despite the always better accuracy in the gravity field recovery, some intrinsic limitations remain unremovable in current gravity missions. The limited mission duration prevents from the possibility of a continuous monitoring of changes in Earth's gravity field and mass transport in the Earth system; moreover each mission provides observable having a proper directional sensitivity and consequently a non-isotropic error behavior.

Future satellite gravity missions will probably make use of the formation flying technologies to solve the non-isotropy problem and some other criticality. A satellite formation consists of a constellation of two or more satellites performing relative motion around a common center using an active control scheme to maintain their relative positions and velocities. GRACE also can be seen as the most simple type of formation, named leader-follower configuration, characterized by an along-track orientation, so its observable suffers from a weak information along the line-of-sight. On the other hand, in a generic formation with more than two satellites, the measure of the distances between the satellites includes information about the radial gravitational signal, while a relative inclination between the satellites can provide a cross-track gravitational information. A first fundamental advantage is that the observations in such formations are significantly richer in gravitational content, leading to a higher S/N ratio. Moreover the global information deriving from satellites flying in formation can drastically decrease the non-isotropy of the low-low satellite tracking observations and in particular the cross-track information may reduce the aliasing problem (Sneeuw & Schaub, 2004) because it allows to gain sensitivity in East-West direction. In practice, a formation with sufficiently many satellites could permit to determine the full tensor of gravity gradients. Furthermore, the GPS positioning of a satellite in a formation may be determined with a much higher accuracy than positioning of a single satellite. Finally formation flying presents the practical advantages of improving the mission survivability and reducing mission costs.

These future formation flying missions will probably make use of laser tracking and atomic interference metrology systems for measuring the variation of the satellite-satellite relative distance caused by external perturbations.

In 2004 Thales Alenia Space Italia (TAS-I) received by the European Space Agency (ESA) a contract for studying a new gravimetry mission, named Satellite-to-Satellite Interferometry (SSI), with the objective of monitoring the temporal variations of the Earth's gravity field at high resolution up to harmonic degree $n = 180 - 240$, as in GOCE and over a long period of time equal to 5-10 years, as in CHAMP and GRACE (Cesare et al., 2006). Changes in the relative spacing between two satellites produced by the geopotential is measured by a Michelson laser interferometer rather than a radio-frequency ranging system, in particular in any interferometric technique the phase of two different waves are compared as a measure of relative distance between

the sources. In the interferometric technique, optical frequencies presents some benefits with respect to the microwave frequencies: laser interferometry has an intrinsically higher resolution because changes in the spacing on the order of the wavelength are detected and this allows in principle to reconstruct the Earth's gravity field with a higher spatial resolution; another significant advantage of shorter wavelengths is the dramatic reduction in diffraction effects that scale as the wavelength.

A similar concept was also considered for the mission EX-5, planned by NASA as the follow-on to GRACE, which will map the Earth's variable gravity field using the Disturbance Reduction System (DRS), a technology that will enable spacecraft control with nanometer precision.

Another metrology system currently studied is the atom interferometry gravity gradiometer, which allows to make acceleration measurements on two vertically separated laser cooled ensembles of cesium atoms in free-fall using a pair of vertically propagating laser beams. The propagation axes of these laser beams are aligned to pass through both ensembles. The light-pulse atom interference method is used to measure the acceleration of each ensemble with respect to a reference frame defined by the phase fronts of the interrogating optical fields. The difference between the measured acceleration of each atom ensemble, divided by their separation, is a measure of the in-line component of the gravity gradient tensor, that characterizes the gravitational field inhomogeneity induced by non-uniform mass distributions (McGuirk et al., 2002).

Chapter 2

The tidal force

Tides are periodical phenomena affecting both the solid Earth and oceans, caused by the differential gravitational attraction of external perturbing bodies, mainly the Moon and the Sun, on the Earth's surface. The spherical harmonic representation of the geopotential is treated as an introduction to the mathematical development of the tide field. The tidal force acts both in a direct and indirect way. The tide-generating potential can be directly determined from the astronomical positions of the external perturbing bodies, its effect is also called direct tide and is the basis for the equilibrium tide theory. On the other hand, the real response of the solid Earth and oceans to this potential, also called indirect tide, depends on the elastic properties of the Earth.

2.1 Historical background

The first explanation of the ocean tide phenomenon can be found in Newton's gravitational theory in 1687. He described in his monograph *Philosophiae Naturalis Principia Mathematica* how the tides arise from the gravitational attraction of the Moon and the Sun on the Earth and set the basis for the equilibrium tide theory, resulting under certain idealized conditions. However, the problem of tide prediction has been considered and treated only after one hundred years.

In 1798 Laplace introduced the separation into tidal species (long period, diurnal and semidiurnal) visualizing the possibility of the harmonic method, not proceeding further with the development and formulated his tidal equations that can not be solved analytically and their numerical solutions depend on the bathymetry and the shape of the coastlines.

In 1867 Lord Kelvin introduced the harmonic method of tidal analysis and prediction, inventing in 1972 the tide-predicting machine.

In 1883 Darwin developed and systematized the harmonic method of tidal analysis based on fitting data from discrete tide gauges to known frequencies dependent on lunar and solar motion. In this way, knowledge of ocean tides was possible only near the coastlines, but not on a global scale. He also argued that for a perfectly rigid Earth, the observed amplitude of the ocean tide would equal the theoretical value. He applied it to observations of long periodic ocean tides, finding that the amplitude was only two-third of the theoretical tides, so concluding that the Earth is not completely rigid, but deformable. Moreover, Darwin introduced symbols to classify the main frequencies of the tidal spectrum, like the M_2 symbol, representing the most energetic tide caused by the Moon at a semidiurnal frequency.

In 1921 Doodson performed algebraically the first full expansion of the tide-generating potential from an analytical ephemeris up to 378 harmonics and introduced a nomenclature for each tidal constituent characterized by a sequence of six integer numbers, compactly called Doodson

number **k**, which are used to multiply six fundamental frequencies related to the Earth, Moon and Sun astronomical motions.

In 1966 Munk and Cartwright introduced the convolution method for tide prediction, called response method, defining the admittance function in the frequency domain which represents the linear response of the ocean to the tide-generating potential ([92] Munk & Cartwright, 1966).

Cartwright, Tayler and Edden in 1971-1973 computed the potential from more modern lunar ephemerides and then applied Fourier methods to analyze numerically the resulting series and get amplitudes for the various harmonics in units of length ([10] Cartwright & Tayler, 1971; [11] Cartwright & Edden, 1973). The tidal constituents of the TGP have been extended to 505 harmonics, which assumed the usual name of CTE representation.

In 1975 Groves and Reynolds defined an orthogonalized convolution method for tide prediction, called orthotide method ([51] Groves & Reynolds, 1975).

Büllesfeld in 1985 expanded the harmonic development to 656 terms.

In 1987 Tamura was the first to introduce tidal contributions coming from Jupiter and Venus and its harmonic expansion was extended to 1200 terms ([117] Tamura, 1987).

Xi in 1989 computed the tide-generating potential up to 2933 terms.

Hartmann and Wenzel in 1995 and Roosbeek in 1996 added arguments for Mars, Mercury and Saturn arriving to a total of 11 astronomic elements. Hartmann and Wenzel introduced 12935 lines ([53] Hartmann & Wenzel, 1994; [54] Hartmann & Wenzel, 1995), while Roosbeek used an analytical method and introduced about 6499 lines, also accounting for indirect lunar perturbations on the Sun ([102] Roosbeek, 1996).

Finally, the most recent tidal potential development is that of Kudryavtsev in 2004, who introduced 28806 harmonics ([69] Kudryavtsev, 2004).

2.2 The gravitational field of the Earth

The gravity potential W on a point at rest on the Earth's surface is the sum of the gravitational potential V and of the centrifugal potential C ([57] Hofmann-Wellenhof & Moritz, 2005)[1]

$$W = V + C = G \int\int\int_{V'} \frac{dM'}{d} + \frac{1}{2}\omega_e^2(x^2 + y^2), \tag{2.1}$$

where $G = 6.6672 \cdot 10^{-11}$ m^3/kg/s is the Newton gravitational constant, d is the distance between the mass element dM' and the attracted point $P(x, y, z)$, V' is the integration volume corresponding to the mass M_e, ω_e is the angular velocity of the Earth and (x^2+y^2) is the square of the distance to the rotational axis. The surfaces having a constant gravity potential are called equipotential surfaces

$$W = \text{constant} \tag{2.2}$$

and the particular equipotential surface W_0 to which the force of gravity is everywhere perpendicular, corresponding to the mean sea level of an hypothetical ocean at rest was proposed as the mathematical figure of the Earth by Gauss and was then called geoid. The gravity potential W satisfies the generalized Poisson equation

$$\nabla^2 W = \nabla^2 V + \nabla^2 C = -4\pi G\rho + 2\omega_e^2, \tag{2.3}$$

where ρ is the mass density of the Earth.

Moreover, a reference potential U, called normal potential, has been defined as the gravity potential associated with a best-fitting ellipsoid of revolution, the normal ellipsoid, rotating with

[1] In addition to the centrifugal acceleration, there is the Coriolis acceleration $\mathbf{a}_{Co} = -2\boldsymbol{\omega_e} \times \mathbf{v}$ which acts only on a moving body and is zero for a body at rest on the Earth.

the Earth[2]. The difference $T = W - U$ between the actual and the normal gravity potentials is known as the anomalous or disturbing potential and it excludes the centrifugal potential ([4] Barthelmes, 2009). The normal gravity potential accounts for approximately 99.9995% of the total potential ([107] Schubert, 2007).

Now we focus on the Earth's gravitational potential V, also called geopotential, in order to illustrate its mathematical modeling and its temporal variations, among which there are the periodic variations caused by ocean tides.

In general, the gravitational potential outside an extended body like the Earth, where $\rho = 0$, satisfies the Laplace equation

$$\nabla^2 V = 0, \tag{2.4}$$

whose solutions are solid spherical harmonics, representable as zonal, sectorial and tesseral harmonics (see Figure 2.1).

The inverse of the distance d between two points, respectively the field point $P(r, \lambda, \phi)$ at which the potential $V(r, \lambda, \phi)$ is to be determined and the source point $Q(r', \lambda', \phi')$ corresponding to the mass element dM', both defined by the spherical polar coordinates r (radius), λ (longitude) and ϕ (geocentric latitude[3]), can be expressed as a function of Legendre polynomials $P_l(\cos\psi)$

$$\frac{1}{d} = \frac{1}{r}\sum_{l=0}^{\infty}\left(\frac{r'}{r}\right)^l P_l(\cos\psi), \tag{2.6}$$

where ψ is the angle between the two radius vectors $\mathbf{r}$ and $\mathbf{r'}$ with $r' < r$, meaning that $P(r, \lambda, \phi)$ is a point outside the Brillouin sphere[4] of the body, so that the series converges. According to the addition theorem for spherical harmonics[5], the inverse of the distance is written as

$$\frac{1}{d} = \frac{1}{r}\sum_{l=0}^{\infty}\sum_{p=-l}^{l}\frac{4\pi}{2l+1}\left(\frac{r'}{r}\right)^l Y_{lp}(\lambda, \phi)Y_{lp}^*(\lambda', \phi'), \tag{2.8}$$

where $Y_{lp}(\theta, \phi)$ is a surface spherical harmonic and $*$ indicates the complex conjugate.

Thus, the static gravitational potential becomes

$$V(r, \lambda, \phi) = \frac{G}{r}\sum_{l=0}^{\infty}\sum_{p=-l}^{l}\frac{4\pi}{2l+1}Y_{lp}(\lambda, \phi)\int\int\int_{V'}\left(\frac{r'}{r}\right)^l Y_{lp}^*(\lambda', \phi')dM'. \tag{2.9}$$

Now we introduce the complex harmonic coefficients K_{lp} of the gravitational potential, called Stokes coefficients

$$K_{lp}^* = \frac{4\pi}{(2l+1)M_e a_e^l}\int\int\int_{V'} r'^l Y_{lp}^*(\lambda', \phi')dM', \tag{2.10}$$

[2]To completely determine the normal gravity potential U and the reference ellipsoid, four fundamental constants are necessary: the Earth's gravitational parameter GM_e, the semimajor axis a of the ellipsoid, the Earth's angular velocity ω_e and the Earth's flattening f or the second-degree zonal Stokes coefficient C_{20}.

[3]The geocentric latitude ϕ is related to the geodetic latitude ϕ_{geod} through the relation

$$\phi = \arctan[\tan\phi_{geod}(1-f)^2], \tag{2.5}$$

where f is the Earth's flattening.

[4]The Brillouin sphere is the sphere of minimum volume centered in the system origin and containing all the mass of the body, in practice it is the sphere outside which, the series converges.

[5]The addition theorem for spherical harmonics establishes that a Legendre polynomial can be expressed as

$$P_l(\cos\psi) = \frac{4\pi}{2l+1}\sum_{p=-l}^{l}Y_{lp}^*(\lambda', \phi')Y_{lp}(\lambda, \phi). \tag{2.7}$$

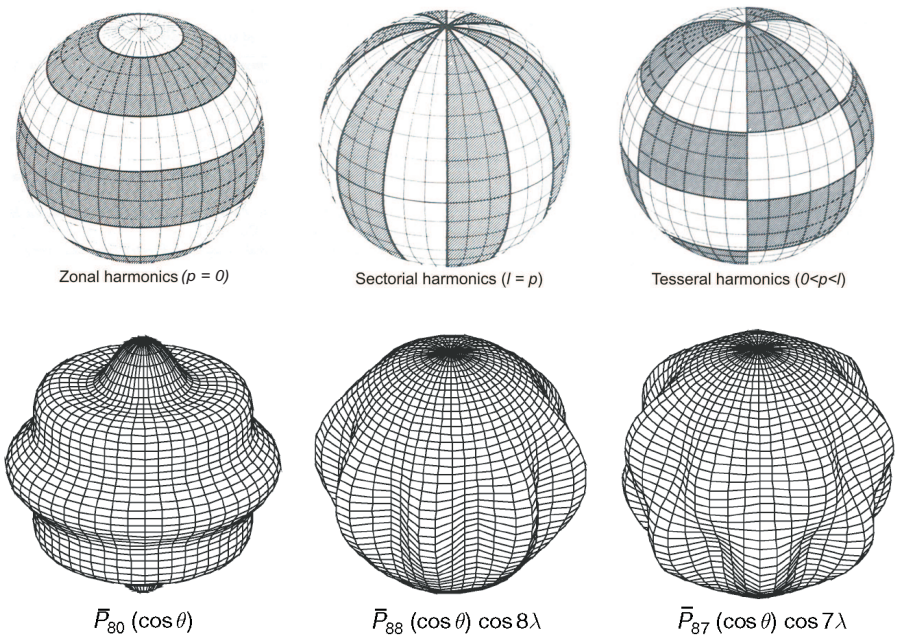

Figure 2.1. Top: zonal, sectorial and tesseral spherical harmonics of the gravitational potential; l and p are respectively the harmonic degree and order ([78] Lorenzini, 2006); bottom: examples of zonal, sectorial and tesseral harmonics on the sphere ([107] Schubert, 2007).

which are adimensional due to the scale factors of Earth mass M_e and Earth radius a_e. So the gravitational potential is developed as a Laplace series

$$V(r,\lambda,\phi) = \frac{GM_e}{r}\sum_{l=0}^{\infty}\sum_{p=-l}^{l}\left(\frac{a_e}{r}\right)^l K_{lp}^* Y_{lp}(\lambda,\phi). \tag{2.11}$$

Because the potential is a real value function, we express it as

$$V(r,\lambda,\phi) = \frac{GM_e}{r}\sum_{l=0}^{L}\sum_{p=0}^{l}\left(\frac{a_e}{r}\right)^l [C_{lp}\cos(p\lambda) + S_{lp}\sin(p\lambda)]P_{lp}(\sin\phi), \tag{2.12}$$

where C_{lp} and S_{lp} are the real Stokes coefficients of the static field and L is the maximum degree at which the harmonic series is truncated. If the Earth had a complete rotational symmetry and so all the longitudes were equivalent, the non-zonal terms ($p \neq 0$) would not be present in the harmonic development, because they depend on the longitude λ ([57] Hofmann-Wellenhof & Moritz, 2005). It is worth noting that the half-wavelength of a (l,p) harmonic in (2.12) is roughly $20,000/l$ km. Moreover, any (l,p) term decreases with increasing radius r as $(a_e/r)^{l+1}$, thus terms with small values of l (long wavelengths) are the least attenuated at the satellite altitude and so tend to be easily determined. At the same time, terms with $p = 0$ are better determined than terms with $p > 0$, because they do not depend on the longitude ([107] Schubert, 2007).

Stokes coefficients with degree $l = 0, 1$ require a discussion. The coefficient with degree and order zero C_{00} corresponds to the distribution of mass of the body and it is defined as $C_{00} = \frac{1}{M_e}\int\int\int_{V'} dM' = 1$, due to the choice of the mass M_e as normalizing factor in equation (2.10), so the first term of the geopotential harmonic series is the central Keplerian term. Moreover, if the coordinate system origin is the Earth's barycenter, the terms with degree $l = 1$ (dipole) vanish, because they are proportional to the center of mass of the body generating the potential, so $C_{10} = C_{11} = S_{11} = 0$. Thus, the perturbing (non-Keplerian and non-central) part of the gravitational potential is usually expanded from degree $l = 2$ (quadrupole). Among the perturbing coefficients,

$C_{20} \cong -0.0010827$ ([64] Kaula, 1966)[6] is related to the Earth's flattening and it is about 10^3 times greater than the other coefficients; C_{22} and S_{22} account for the equatorial ellipticity and C_{30} is the pear-shaped term ([64] Kaula, 1966).

In order to avoid problems in the numerical representation of the spherical harmonics, it is convenient to introduce the so called full normalization factor N_{lp}[7] ([64] Kaula, 1966)

$$N_{lp} = \sqrt{\frac{(2-\delta_{0p})(2l+1)(l-p)!}{(l+p)!}}, \tag{2.14}$$

which applies to both the Stokes coefficients and the associated Legendre functions and leads to their normalized form

$$\bar{C}_{lp} = \frac{C_{lp}}{N_{lp}}, \tag{2.15}$$

$$\bar{S}_{lp} = \frac{S_{lp}}{N_{lp}}, \tag{2.16}$$

$$\bar{P}_{lp} = N_{lp} P_{lp}. \tag{2.17}$$

Finally, the non-central static gravitational field of the Earth is given by

$$V(r,\lambda,\phi) = \frac{GM_e}{r}\left\{1 + \sum_{l=2}^{L}\sum_{p=0}^{l}\left(\frac{a_e}{r}\right)^l [\bar{C}_{lp}\cos(p\lambda) + \bar{S}_{lp}\sin(p\lambda)]\bar{P}_{lp}(\sin\phi)\right\}. \tag{2.18}$$

Besides the static geopotential, there is a time variable part due to the fact that the Earth is a dynamic system, having oceans and a fluid atmosphere, a continuously changing distribution of ice and snow, a rebound from glacial loading of the last ice age and mobile tectonic plates. These processes affect the distribution of mass of the Earth and produce changes in the Earth's gravity field on different spatial and temporal scales, ranging from hours to thousands of years, and conveniently modeled as variations of the standard normalized Stokes coefficients $\bar{C}_{lp}$ and $\bar{S}_{lp}$.

The main phenomena causing temporal variations of the Earth's gravity field, which in turn affect the motion of Earth orbiting satellites, can be classified as solid and ocean tides, atmospheric tides, pole tides, seasonal variations due to meteorological mass redistribution, long term variations due to post-glacial rebound (PGR).

Solid and ocean tides are periodic deformations induced in the solid Earth and in the oceans, arising from the gravitational attraction of external bodies, primarily the Sun and the Moon. Ocean tide phenomenon is the main topic of this work of research and will be treated in detail in the next sections.

Atmospheric tides consist in minor atmospheric oscillations on a global scale with typical periods of 12 and 24 hours and velocities between 5 m/s (in the troposphere) and 50 m/s (in the mesosphere), which can load the Earth enough to induce fluctuations in gravity. They are mainly due to air pressure changes caused by daily variations in solar irradiation, while, only in small measure, they can be driven by the gravitational attraction of the Sun and the Moon ([24] Chapman & Lindzen, 1970).

[6] The second degree zonal coefficient C_{20} is often substituted by $J_2 = -C_{20}$ in Geodesy applications.

[7] The ratio of factorials

$$f_{lp} = \frac{(l-p)!}{(l+p)!} \tag{2.13}$$

can be computed recursively for each degree l as follows

1. $f_{l0} = 1$,
2. $f_{lp} = \frac{f_{l,p-1}}{(l+p)(l-p+1)}$, $p = 1, 2, ..., l$.

Pole tides represent the response of the solid Earth and the ocean to variations in the centrifugal force, caused by changes in the direction of the Earth's spin axis relative to a point fixed on the Earth. In particular, pole tides primarily occur with a period of 433 days (about 14 months), called Chandler wobble, and annually, where the annual term is more important than the solar annual ocean tide *Sa* ([71] Lambeck, 1980). Both periods are long enough for the pole tide displacement to be considered in equilibrium with the forcing centrifugal potential. The maximum range of potential height is a few cm ([107] Schubert, 2007).

The dominant effect in seasonal variations is due to atmospheric mass transport associated with atmospheric disturbances and seasonal climatic variations, leading to atmospheric pressure fluctuations and variations in groundwater storage.

The post-glacial rebound is the isostatic adjustment of the crust and mantle that were depressed by the static weight of ice sheets during the last glacial period. Typical uplift rates of the crust are of the order of 1 cm/yr. It affects northern Europe (especially Scotland, Fennoscandia and northern Denmark), Siberia, Canada, parts of Patagonia and Antarctica and provides the main observational evidence for mantle viscosity ([71] Lambeck, 1980). The redistribution of lithospheric masses after the melting of the ice sheets contributes to a secular change in the gravity field: in particular, SLR data available since 1979 revealed a secular decrease in the Earth's oblateness, which is directly related to C_{20} and it is consistent with a migration of mass from low latitudes toward high latitudes ([107] Schubert, 2007). However, C_{20} has been increasing since 1997 ([28] Cox & Chao, 2002), implying a glacial and oceanic mass redistribution strong enough to reverse the negative trend due to the post-glacial rebound and probably caused by the rapid subpolar glacial melting and mass shifts in the Pacific and Indian oceans ([33] Dickey et al., 2002).

2.3 Tide-Generating Potential (TGP)

The tide-generating force $\mathbf{F}_{\mathrm{TGP}}$ is responsible for the deformation of the solid Earth and the oceans under the gravitational attraction of external perturbing bodies, so it is a conservative force. At the centers of mass of two extended spherically symmetric and non-rotating bodies in orbital motion around the common barycenter, the gravitational acceleration equals the orbital (centrifugal) acceleration. In particular, each point of a bodies executes the same circular motion, experiencing the same orbital acceleration, while the gravitational acceleration is not the same everywhere on the body. Thus, assuming the Earth as an extended and spherically symmetric body, a difference exists between the gravitational attraction $\mathbf{F}_{\mathrm{P}}$ of an external body at the point P on the Earth's surface and the attraction $\mathbf{F}_{\mathrm{ECM}}$ at the Earth's center of mass (ECM) and it represents the tide-generating force, defined as a differential force (see Figure 2.2)

$$\begin{aligned}\mathbf{F}_{\mathrm{TGP}}(\mathbf{r}_{\mathrm{P}}) =& \mathbf{F}_{\mathrm{P}}(\mathbf{r}_{\mathrm{P}}) - \mathbf{F}_{\mathrm{ECM}}(\mathbf{r}_{\mathrm{ECM}}) \\ =& \nabla_{\mathbf{r}_{\mathrm{P}}} V(\mathbf{r}_{\mathrm{P}}) - \nabla_{\mathbf{r}_{\mathrm{ECM}}} V(\mathbf{r}_{\mathrm{ECM}}) \\ =& \nabla_{\mathbf{r}_{\mathrm{P}}} [V(\mathbf{r}_{\mathrm{P}}) - W(\mathbf{r}_{\mathrm{P}})] \\ =& \nabla_{\mathbf{r}_{\mathrm{P}}} V_{\mathrm{TGP}}(\mathbf{r}_{\mathrm{P}}),\end{aligned} \tag{2.19}$$

where V_{TGP} is called tide-generating potential (TGP).

At the point directly under the perturbing body (the sub-body point) and at its antipode, the tide-generating force is oriented in opposite directions away from the Earth, giving origin to a double tidal bulge, which is slightly weaker at the antipode, because here the gravitational force of the external body is lower. It can be noticed that the tide-generating field becomes weaker and weaker within the Earth's surface, until it vanishes at the geocenter (see Figure 2.3). Moreover, tide-generating forces do not exercise an acceleration on the Earth, being symmetrical with respect to three orthogonal axes, so that the resultant is zero ([125] Wenzel, 1997).

However, at very high precision, it should be considered that assuming the orbital acceleration of the Earth equal to the gravitational attraction of the perturbing body at the geocenter is an

approximation, being valid only for a spherically symmetric Earth. The Earth's orbital motion is affected by the figure forces, resulting from the interaction between the non-spherical extended mass distribution of the Earth and the perturbing bodies, which are assumed to be point masses. In practice, the Earth's oblateness is responsible for the so called Earth's flattening effect[8] ([125] Wenzel, 1997) on the TGP, consisting of a small homogeneous field varying with time and superimposed on the conventional tide-generating force. In particular, the Earth's ellipticity contributes about ±3 ngal to the lunar tide-generating force, while its effect on the solar tide-generating force is negligible, because of the very small parallax[9] of the Sun ([30] Dahlen, 1993).

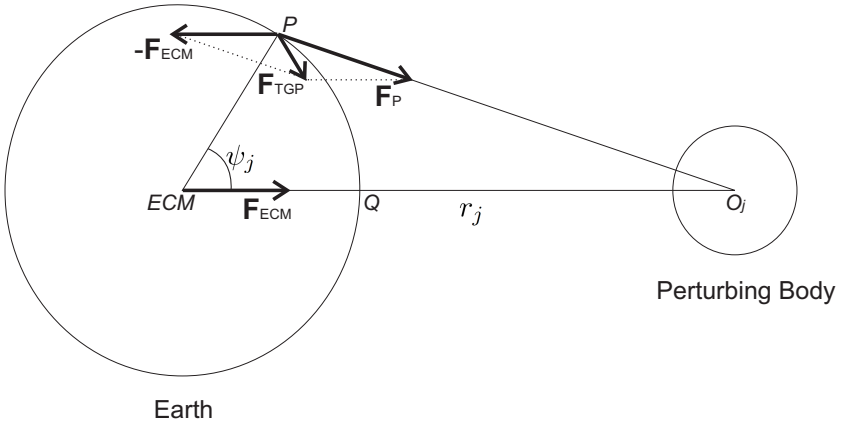

Figure 2.2. Geometry of the tide-generating force due to an external body acting on the Earth's surface.

The calculation of tidal phenomena requires a representation of the TGP, which is based on the relative positions of the external bodies (indicated with the subscript $j = 1, ..., J$) and it is defined as

$$V_{\mathrm{TGP}}(t, r, \lambda, \phi) = \sum_{j=1}^{J} \sum_{n=2}^{N} \frac{GM_j}{r_j} \left(\frac{r}{r_j}\right)^n P_n(\cos\psi_j), \tag{2.21}$$

where M_j is the mass of the perturbing body, ψ_j is the zenith angle between the vector to the observation point P with geocentric coordinates (r, λ, ϕ) and the vector to the external perturbing body O_j with geocentric coordinates (r_j, λ_j, ϕ_j). Hereinafter, the TGP is considered as calculated on the Earth's surface, so the radial coordinate is $r = a_e$ and can be dropped out from the variables in the parentheses. It can be noticed that the TGP coincides with the perturbing function of an external body acting on a particle on the Earth's surface.

Applying the addition theorem for spherical harmonics (2.7), the TGP becomes

$$V_{\mathrm{TGP}}(t, \lambda, \phi) = \sum_{j=1}^{J} \sum_{n=2}^{N} \sum_{m=-n}^{n} \frac{GM_j}{r_j} \left(\frac{a_e}{r_j}\right)^n \frac{4\pi(2-\delta_{0m})}{2n+1} \bar{Y}^*_{nm}(\lambda_j, \phi_j) \bar{Y}_{nm}(\lambda, \phi). \tag{2.22}$$

The normalized complex surface spherical harmonics are defined as

$$\bar{Y}_{nm}(\lambda_j, \phi_j) = N_{nm} P_{nm}(\sin\phi_j)\, \mathrm{e}^{\mathrm{i}\, m\lambda_j} = \bar{P}_{nm}(\sin\phi_j)\, \mathrm{e}^{\mathrm{i}\, m\lambda_j}, \tag{2.23}$$

[8] Including the Earth's flattening effect, the complete expression of the TGP becomes ([126] Wilhelm, 1983)

$$V_{\mathrm{TGP}}(t, r, \lambda, \phi) = \sum_{j=1}^{J} \frac{GM_j}{r_j} \left\{ \sum_{n=2}^{N} \left(\frac{r}{r_j}\right)^n P_n(\cos\psi_j) + \left(\frac{r}{r_j}\right) \sum_{n=2}^{N} J_n \left(\frac{a_e}{r_j}\right)^n \left[(n+1) P_n(\cos\theta_j) \cos\psi_j + \frac{dP_n(\cos\theta_j)}{d\theta_j} \sin\psi_j \cos z_j \right] \right\}, \tag{2.20}$$

where θ_j is the colatitude of the perturbing body and z_j is the angle $\widehat{Q}$ (see Figure 2.4).

[9] The parallax a_e/r is about 1/60 for the Moon and 1/23,000 for the Sun.

where N_{nm} is the ortho-normalization factor

$$N_{nm} = (-1)^m \sqrt{\frac{(2n+1)(n-m)!}{4\pi(n+m)!}}, \tag{2.24}$$

which includes the Condon-Shortley phase $(-1)^m$ and is different from the full normalization (2.14) applied to the geopotential spherical harmonics. The multiplicative term $(2-\delta_{0m})$ explicitly appears in expression (2.22) because it is not included in the ortho-normalization factor N_{nm}.

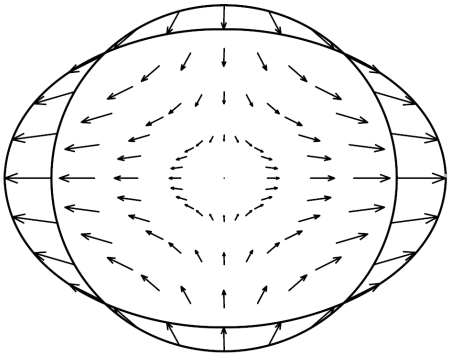

Figure 2.3. Field of the tide-generating forces acting on the Earth: the elliptical line shows the equipotential surface ([107] Schubert, 2007).

The TGP can be expressed according to the Cartwright-Tayler-Edden (CTE) convention ([10] Cartwright & Tayler, 1971; [11] Cartwright & Edden, 1973) in a compact form, separating the astronomical time-dependent part and the geographical part as follows

$$V_{\mathrm{TGP}}(t,\lambda,\phi) = g \sum_{n=2}^{N} \sum_{m=0}^{n} \bar{c}^{*}_{nm}(t) \bar{Y}_{nm}(\lambda,\phi), \tag{2.25}$$

where $g = GM/a_e^2$ is the gravity acceleration on the Earth's surface and $\bar{c}_{nm}(t) = \bar{a}_{nm}(t) + \mathrm{i}\,\bar{b}_{nm}(t)$ are the complex ortho-normalized coefficients of the TGP, time-dependent quantities with the dimension of a length in such a way that the term V_{TGP}/g represents the change in the geoid height due to the TGP. In particular, these harmonic coefficients $\bar{c}_{nm}(t)$ can be computed either through accurate ephemerides of celestial perturbing bodies as

$$\bar{c}_{nm}(t) = \sum_{j=1}^{J} \frac{GM_j}{gr_j} \left(\frac{a_e}{r_j}\right)^n \frac{4\pi(2-\delta_{0m})}{2n+1} \bar{P}_{nm}(\sin\phi_j)\, \mathrm{e}^{\mathrm{i}\, m\lambda_j} \tag{2.26}$$

or through the sum of tidal harmonics, obtained from analytical or numerical spectral analysis[10] of the TGP, as

$$\bar{c}_{nm}(t) = \sum_{\mathbf{k}} H_{\mathbf{k}}\, \mathrm{e}^{-\mathrm{i}[\Theta_{\mathbf{k}}(t) + \phi_{n\mathbf{k}}]}, \tag{2.27}$$

where, for each tidal constituent defined by the Doodson number $\mathbf{k}$ in (2.39) which is implicitly related to the order m, $H_{\mathbf{k}}$ is the CTE tidal amplitude in units of a length, $\Theta_{\mathbf{k}}(t)$ is the phase angle or Doodson argument and $\phi_{nk} = \frac{\pi}{2} \mod (n+m;2)$ is the phase correction necessary to account for the adopted CTE convention ([32] Desai and Yuan, 2006).

The spherical harmonic order m of the TGP expresses the longitude dependence and so the time dependence, being related to the variations of this potential during a daily rotation, so it

[10] TGP catalogues computed by analytical spectral analysis require analytical ephemerides of celestial perturbing bodies, while those computed by numerical spectral analysis require accurate numerical ephemerides of celestial perturbing bodies, like the JPL ephemerides ([125] Wenzel, 1997).

defines the tidal species: in particular $m = 0$ represents long period tidal waves, because their period is not a fraction of a day, while $m = 1, 2, 3, 4, ..., n$ corresponds respectively to diurnal, semidiurnal, terdiurnal, quaterdiurnal bands, etc., up to n band.

Because of the presence of the parallactic factor $(a_e/r_j)^n$, applications generally require only terms of the TGP with degree $n = 2$, which account for the 98% of the total potential ([125] Wenzel, 1997), so that the magnitude of the TGP is proportional to mass and distance of the external perturbing body as GM_j/r_j^3. Normalizing this quantity to make the value for the Moon equal to 1, the value for the Sun is 0.46, for Venus 5×10^{-5}, for Jupiter 6×10^{-6} and less for all other planets ([107] Schubert, 2007). Thus tides are dominated by the lunisolar component, nevertheless recent harmonic developments of the TGP also include planetary terms.

For the highest precision applications, it is necessary to consider also terms of the TGP due to the Moon with degree $n = 3$ and $n = 4$.

Table 2.1. List of the main TGP catalogues, with the number of tidal waves and the perturbing bodies considered.

TGP Catalogue	Number of Waves	Perturbing Bodies	Accuracy (nm/s^2)
Doodson (1921)	378	Moon, Sun	1.04080
Cartwright-Tayler-Edden (1973)	505	Moon, Sun	0.38440
Buellesfeld (1985)	656	Moon, Sun	0.24020
Tamura (1987)	1200	Moon, Sun, Venus, Jupiter	0.08340
Xi (1989)	2933	Moon, Sun, Venus, Jupiter	0.06420
Tamura (1993)	2060	Moon, Sun, Venus, Jupiter	0.03080
Hartmann-Wenzel (1995)	12935	Moon, Sun, Venus, Jupiter, Mars, Mercury, Saturn	0.00140
Roosbeek (1996)	6499	Moon, Sun, Venus, Jupiter Mars, Mercury, Saturn, lunar perturbations on the Sun	0.02000
Kudryavtsev (2004)	28806	Moon, Sun, Venus, Jupiter, Mars, Mercury, Saturn	0.00064

These developments are identified as TGP catalogues, which consist of tables containing amplitudes, phases and frequencies of tidal waves generated by the direct effect of celestial perturbing bodies and have the advantage of remaining valid for a long time. Among the available TGP catalogues, the most important are reported in Table 2.1 ([125] Wenzel, 1997), where, for each one, the number of tidal waves, the perturbing bodies and the accuracy are specified. Usually, the catalogues are distributed in the standard HW95 normalization and format ([54] Hartmann and Wenzel, 1995).

2.3.1 The equilibrium tide

The equilibrium tide is the theoretical tide that would exist on an ideal perfectly rigid and non-rotating Earth (no effect of the Coriolis force), totally covered with oceans of uniform depth, where the response to the tide-generating forces is instantaneous and no dissipation is present.

The equilibrium tide potential can be directly determined from the astronomical positions of the external perturbing bodies, so it coincides simply with the TGP. Considering only the TGP of degree $n = 2$ in (2.21), the equilibrium tide potential on the Earth's surface due to the perturbing body j results in

$$\begin{aligned} V^{(j)}_{2,\mathrm{TGP}}(t,\lambda,\phi) &= \frac{GM_j}{r_j}\left(\frac{a_e}{r_j}\right)^2 P_2(\cos\psi_j), \\ &= \frac{1}{2}\frac{GM_j}{r_j}\left(\frac{a_e}{r_j}\right)^2 (3\cos^2\psi_j - 1), \end{aligned} \tag{2.28}$$

where the expression of the second-degree Legendre polynomial $P_2(\cos\psi_j) = \frac{1}{2}(3\cos^2\psi_j - 1)$ has been substituted.

The trigonometric term function of the zenith angle ψ_j can be conveniently expressed through the geocentric spherical coordinates of the perturbing body j and the geographic coordinates of the observer

$$\cos\psi_j = \cos\theta\cos\theta_j + \sin\theta\sin\theta_j\cos(\lambda - \lambda_j), \tag{2.29}$$

$$= \cos\theta\sin\delta_j + \sin\theta\cos\delta_j\cos(\vartheta_g + \lambda - \alpha_j), \tag{2.30}$$

$$= \cos\theta\cos\delta_j + \sin\theta\cos\delta_j\cos H_j, \tag{2.31}$$

where ϕ and λ are respectively the latitude and the longitude of the observation point, θ_j and λ_j are the colatitude and the longitude of the body, δ_j and α_j are the declination and the right ascension of the body, ϑ_g is the Greenwich sidereal angle and H_j is the hour angle of the body (see Figure 2.4), satisfying the following relations

$$\theta_j = \frac{\pi}{2} - \delta_j, \tag{2.32}$$

$$\lambda_j = \alpha_j - \vartheta_g, \tag{2.33}$$

$$H_j = \lambda - \lambda_j. \tag{2.34}$$

Substituting the relation (2.31) into (2.28), the equilibrium tide potential (2.28) on the Earth's surface due to a celestial perturbing body j assumes the expression

$$\begin{aligned} V^{(j)}_{2,\mathrm{TGP}}(t,\lambda,\phi) = D_j\Big[&3(\sin^2\phi - \frac{1}{3})(\sin^2\delta_j - \frac{1}{3}) \\ &+ \sin(2\phi)\sin(2\delta_j)\cos H_j \\ &+ \cos^2\phi\cos^2\delta_j\cos(2H_j)\Big], \end{aligned} \tag{2.35}$$

where $D_j = \frac{3}{4}GM_j\frac{a_e^2}{r_j^3}$ is the so called Doodson tidal constant and it is 2.63 $\mathrm{m}^2/\mathrm{s}^2$ for the Moon and 1.21 $\mathrm{m}^2/\mathrm{s}^2$ for the Sun. In this way, the equilibrium tide potential depends on the latitude of the observer and the distance, the declination and the hour angle of the celestial body, with the latter three all being functions of time.

Laplace was the first to separate the equilibrium tide potential (2.35) according to three main tidal species, looking at the dependence on the hour angle H_j of the perturbing body. The first term in (2.35) corresponds to the first species tides, it does not depend on the hour angle, but on the declination cycle of the perturbing body as $\sin^2\delta_j$, so it has a long period temporal frequency of half month for the Moon and half year for the Sun. Moreover, it is a function of the latitude

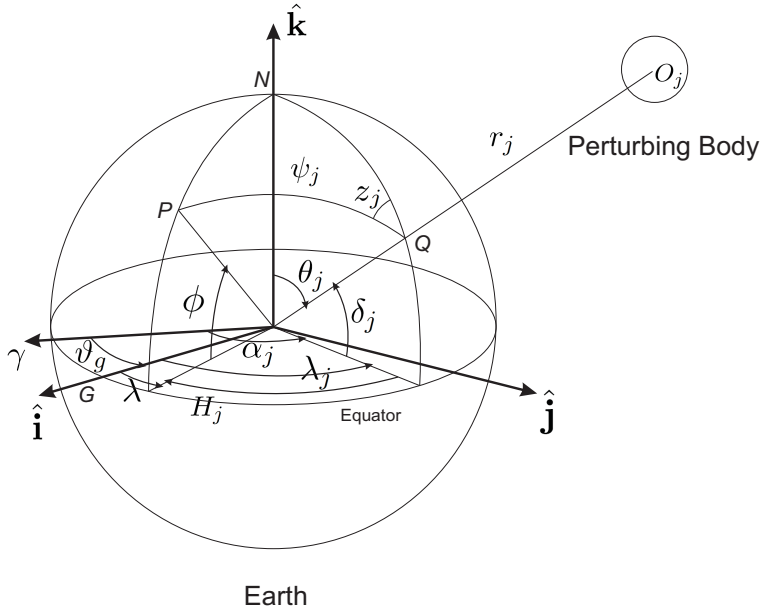

Figure 2.4. Geometry for the computation of the equilibrium tide potential at the observation point $P(\lambda, \phi)$ due to a celestial perturbing body: the geocentric spherical coordinates of the body are visualized, where $\hat{\mathbf{i}}$ axis points toward the Greenwich meridian indicated by G, $\hat{\mathbf{k}}$ points toward the North Pole indicated by N and $\hat{\mathbf{j}}$ completes the right-handed tern.

as $3\sin^2\phi - 1$, so it is a zonal term, with maximum amplitude at the poles and zero amplitude at latitude $\phi = \pm\, 35.26°$.

The second term in (2.35) is associated to the second species tides and it depends on $\cos H_j$, so it has a diurnal temporal frequency, with maximum amplitude at latitude $\phi = \pm\, 45°$ and zero amplitude at the equator and at the poles. These tides are modulated by periods of half declination cycle of the perturbing body, because of the factor $\sin(2\delta_j)$.

The third term in (2.35) is finally associated to the third species tides and it depends on $\cos(2H_j)$, so it has a semidiurnal temporal frequency, with maximum amplitude at the equator and zero amplitude at the poles. Also these tides are modulated by periods of half declination cycle of the perturbing body, because of the factor $\cos^2\delta_j$.

Considering only the zonal second-degree term of the TGP, the equilibrium tide height due to a perturbing body j is defined as the radial displacement of a particle on the Earth's surface

$$\begin{aligned}
\zeta_{2,\mathrm{EQ}}^{(j)} &= \frac{V_{2,\mathrm{TGP}}^{(j)}}{g} \\
&= \frac{1}{2}\frac{GM_j}{M_e}\frac{a_e^4}{r_j^3}(3\cos^2\psi_j - 1) \\
&= \frac{3}{4}\frac{GM_j}{M_e}\frac{a_e^4}{r_j^3}\left[\cos(2\psi_j) + \frac{1}{3}\right] \\
&= D_j M_e a_e^2\left[\cos(2\psi_j) + \frac{1}{3}\right],
\end{aligned} \tag{2.36}$$

where the maximum tide height happens for $\psi_j = 0, \pi$ (conjunction and opposition) and the minimum for $\psi_j = \pm\pi/2$ (quadrature). In particular, the relation $\zeta_{2,\mathrm{EQ}}^{(j),max} = -2\zeta_{2,\mathrm{EQ}}^{(j),min}$ exists between the maximum and the minimum equilibrium tide due to an external body, resulting in

$$\mathrm{Moon}\begin{cases} \zeta_{2,\mathrm{EQ}}^{(M),max} = 35.6 \quad \mathrm{cm} \\ \zeta_{2,\mathrm{EQ}}^{(M),min} = -17.8 \quad \mathrm{cm} \end{cases} \tag{2.37}$$

$$\text{Sun} \begin{cases} \zeta_{2,\text{EQ}}^{(S),max} = 16.4 \quad \text{cm} \\ \zeta_{2,\text{EQ}}^{(S),min} = -8.2 \quad \text{cm} \end{cases} \tag{2.38}$$

where, accounting for both lunar and solar contribution, the maximum equilibrium tide is 52 cm and the minimum is −26 cm, with a total excursion of about 78 cm. Moreover, it can be noticed that the ratio between the solar and the lunar equilibrium tides is about $\zeta_{2,\text{EQ}}^{(S)}/\zeta_{2,\text{EQ}}^{(M)} = 0.46$. This ratio is valid also for the maximum tidal acceleration exerted by the Moon and the Sun on the Earth, being about 1.2×10^{-6} m/s^2 for the Moon and 5.5×10^{-7} m/s^2 for the Sun. The effect of the other planets is much smaller, the largest being that of Venus, with a ratio of 0.000113 with respect to the Sun.

According to the equilibrium theory, the tide-raising body (Moon or Sun) would tend to draw the hypothetical ocean sphere covering the Earth into a prolate spheroid, stretched along the line joining the celestial body, thus generating two bulges of high water, one directly under the perturbing body and another one on the opposite side of the Earth, propagating around the Earth from east to west at a steady rate, keeping up with the relative position of the tide-raising body ([108] Schureman, 1940).

Tidal cycles are influenced by various astronomical parameters. The orbital inclination of the celestial body (Moon or Sun), and hence of the tidal bulges, on the Earth's equator implies changes in the declination of the tide-raising body, resulting in two unequal high tides and two unequal low tides per (lunar or solar) day. This phenomenon is known as the diurnal or declinational inequality of the semidiurnal tides and gives rise to the diurnal tides. At the equator the tidal ellipsoid, and so the semidiurnal tides, are quite symmetrical, the diurnal inequality is minimum and the tides are known as equatorial tides; on the other hand, when the declination of the celestial body is not equal to zero, the diurnal tides become stronger, these tides are called tropic tides and at the high latitudes in theory only one high and low tide would occur (see Figure 2.5).

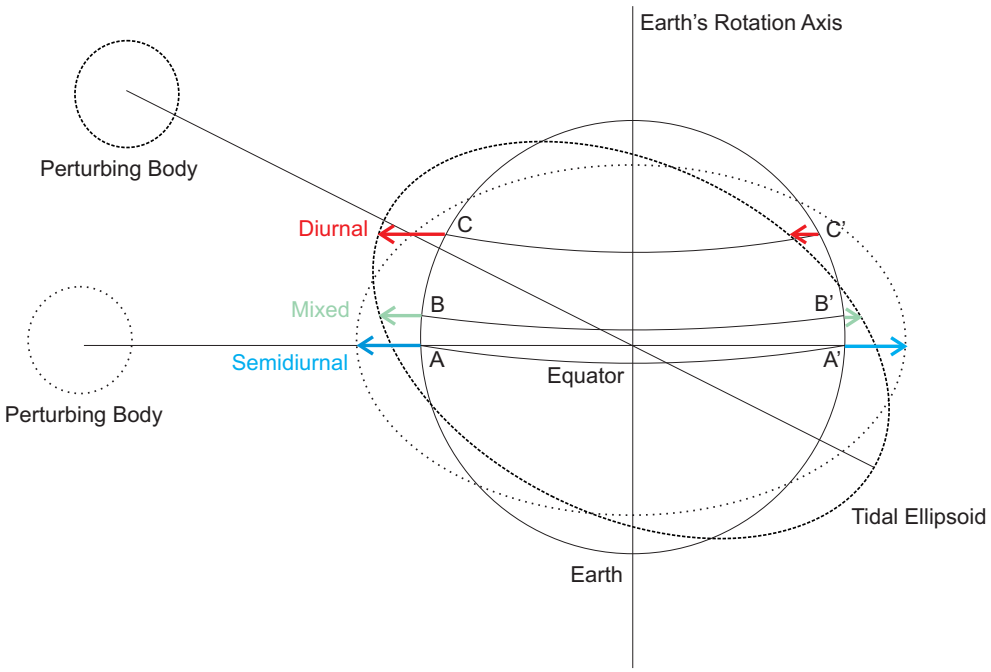

Figure 2.5. Geometric representation of the diurnal inequality: at the points A and A' on the equator the tidal bulges are quite symmetrical and the tides are semidiurnal, at the points B and B' away from the equator the tides are mixed, being two unequal high tides and two unequal low tides per tidal day, at the points C and C' at higher latitudes there is only one high and low tide per tidal day.

Also the relative positions of the Moon and the Sun affect the magnitude of the tide-generating force. When the Moon is aligned with the Sun (new Moon and full Moon), the two tide-raising

bodies create the highest and lowest tides of the year, called spring tides; while when the Moon and Sun are at right angles to each other (first and last Moon quarters), the tides are at their least and are called neap tides. Because during one month the spring and neap tides occur two times, their tidal period is close to two weeks.

The equilibrium tide does not represent the real tidal effect, being too small compared to the observed tide, however it is an important reference for tidal analysis, giving an order of magnitude of tidal phenomena.

2.3.2 The Doodson argument

Being the TGP a periodically varying function, it can be expressed through a Fourier series having many fundamental frequencies, instead of one single frequency, because tides are induced by different combinations of the astronomical motions of the Earth, the Moon, the Sun and the planets.

In 1921 Doodson first performed the harmonic development of the TGP as in (2.27) from an analytical ephemeris[11] and introduced a very efficient classification of tidal waves, consisting in a sequence of 6 digits, compactly named Doodson number $\mathbf{k}$ and defined as

$$\mathbf{k} = k_1(k_2+5)(k_3+5).(k_4+5)(k_5+5)(k_6+5), \tag{2.39}$$

where 5 is a bias added to avoid negative numbers and in the case that the biased numbers exceed 9, the notation adopts X for 10 and E for 11; without bias the Doodson number is called the CTE number. The integer number k_1 represents the spherical harmonic order of the TGP or the tidal species, the pair k_1 k_2 defines a tidal group and the tern k_1 k_2 k_3 defines a tidal constituent. For example, the principal lunar semidiurnal constituent M_2 is specified with the Doodson number 255.555 or the CTE number 200.000.

In 1995 Hartmann and Wenzel first extended the Doodson number to 11 digits, because they included contributions of the planets Mercury, Venus, Mars, Jupiter and Saturn.

The Doodson or astronomical argument $\Theta_{\mathbf{k}}(t)$ defined for a specified tidal constituent $\mathbf{k}$, accounts for the time variations of the TGP, representing the phase of the equilibrium tide at a given time and it can be expressed to the first order as

$$\Theta_{\mathbf{k}}(t) = \dot{\Theta}_{\mathbf{k}}(t-t_0) + \Theta_{\mathbf{k}}(t_0) \tag{2.40}$$

$$= 2\pi f_{\mathbf{k}}(t-t_0) + \Theta_{\mathbf{k}}(t_0), \tag{2.41}$$

where $\dot{\Theta}_{\mathbf{k}}$ is the Doodson frequency in rad/day, $f_{\mathbf{k}}$ is the frequency of the tidal constituent in cyc/day and t is the time expressed in mean solar days reckoned from a reference epoch t_0 (J2000 = 1 January 2000, 12 h).

The Doodson argument $\Theta_{\mathbf{k}}(t)$ can be considered as the angular position of a fictitious body responsible of the tidal forcing induced by the constituent, which is assumed to travel around the equator with an angular speed equal to that of the corresponding constituent (see Figure 2.6). In practice, the astronomical tide-generating potential or equilibrium tide is decomposed into an almost periodic (non-harmonic frequency spectrum) series of harmonic partial tides with each constituent featuring some property of the elliptic and inclined orbits of the Moon and Earth (Schwiderski, 1980).

The Greenwich phase lag $\Psi_{\mathbf{k}}(\phi,\lambda)$ is a constant over a geographic grid for a tidal constituent and physically can be interpreted as the angular difference between the equilibrium tide and the observed tide for that constituent (see Figure 2.6), so it measures the time delay (in radians,

[11] An analytical ephemeris is essentially an algebraic description of the motion of the body as a function of time. However, the most precise ephemerides are numerical, coming from numerical integration of the equations of motion, with parameters chosen to best fit some set of observational data. They have been used primarily to produce reference time series, basis for a harmonic expansion of the tidal potential. The first tidal computation program based directly on an astronomical ephemeris was that of Longman (1959).

degrees or time units) of the observed ocean tide with respect to the forcing equilibrium tide at the Greenwich meridian. The phase of the observed constituent is a function of the time origin adopted, while the Greenwich phase lag is independent (Schwiderski, 1980).

The Doodson argument is usually computed as a linear combination of the fundamental astronomical arguments related to the Earth-Moon-Sun and planetary motions

$$\Theta_{\mathbf{k}}(t) = k_1\tau + k_2 s + k_3 h + k_4 p + k_5 N' + k_6 p_s + \sum_{i=7}^{11} k_i L_i, \tag{2.42}$$

where τ is the mean lunar time[12] in angle units (Moon's hour angle plus 180° or 12 h), s is the mean longitude of the Moon (the speed of s is about 13 deg/day), h is the mean longitude of the Sun, p is the longitude of the lunar mean perigee, N' is the negative of the longitude of the lunar mean ascending node on the ecliptic, p_s is the longitude of the solar mean perigee and L_i with $i = 7, ..., 11$ are respectively the mean longitudes of Mercury, Venus, Mars, Jupiter and Saturn ([112] Simon et al., 1994). All the longitudes are measured along the ecliptic.

Similarly, the Doodson frequency $\dot{\Theta}_{\mathbf{k}}$ is expressed in terms of the secular rates of the fundamental astronomical arguments as

$$\dot{\Theta}_{\mathbf{k}} = k_1\dot{\tau} + k_2\dot{s} + k_3\dot{h} + k_4\dot{p} + k_5\dot{N}' + k_6\dot{p}_s + \sum_{i=7}^{11} k_i\dot{L}_i \tag{2.43}$$

and the sidereally demodulated Doodson frequency $\dot{\Theta}^*_{\mathbf{k}}$ is given by

$$\dot{\Theta}^*_{\mathbf{k}} = \dot{\Theta}_{\mathbf{k}} - k_1\dot{\theta}_g. \tag{2.44}$$

In Table 2.2 the fundamental arguments of the Earth, Sun and Moon motions are reported, together with their frequencies and periods ([83] Petit and Luzum, 2010; [107] Schubert, 2007).

Table 2.2. Fundamental astronomical arguments.

Symbol	Frequency (cyc/day)	Period	Argument
θ_g	1.0027379	23h 56m 4.2s	Greenwich sidereal angle
τ	0.9661368	24h 50m 28.3s	local mean lunar time
s	0.0366011	27.3216 d	Moon's mean longitude
h	0.0027379	365.2422 d	Sun's mean longitude
p	0.0003095	8.847 yr	longitude of Moon's perigee
N'	0.0001471	18.613 yr	the negative of the longitude of Moon's ascending node
p_s	0.0000001	20941 yr	longitude of Sun's perigee

These arguments are determined in terms of the four Brown's arguments (Melchior, 1970), measured along the ecliptic eastward from the Vernal equinox: l is the Moon's mean anomaly, l_p the Sun's mean anomaly, $F = (l - \Omega)$ the Moon's mean elongation from the node (being Ω the Moon's mean longitude of the ascending node) and D the Moon's mean elongation from the Sun.

In Table 2.3 a list is reported of 106 tidal constituents of the FES2004 ocean tide model (Lyard et al., 2006) and ordered from the highest to the lowest CTE amplitude; for each constituent the Doodson number and the Darwin symbol (if present) are also specified. General symbols like M and S refer to lunar and solar origin, while the subscripts 1 and 2 refer to diurnal and

[12] The computation of the argument τ requires to calculate the Greenwich Mean Sidereal Time (GMST), which in turn needs the transformation from Terrestrial Time (TT) to Universal Time (UT1). The remaining arguments in the Doodson relation are slowly varying angles.

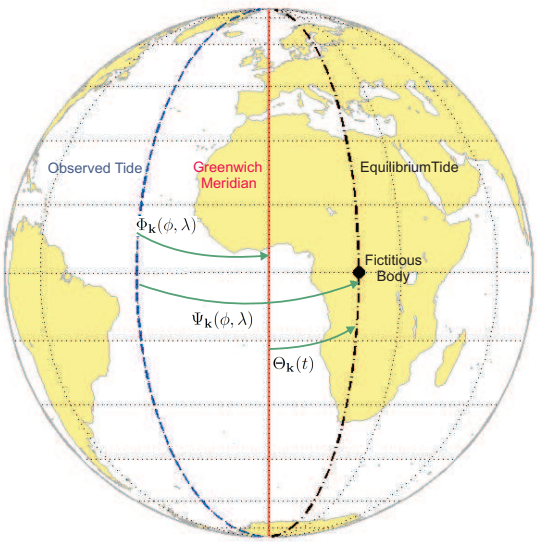

Figure 2.6. Geometry of the equilibrium tide, the observed tide and the Greenwich phase lag of a generic tide constituent.

semidiurnal species respectively. The eight largest tidal constituents together account for over 90% of the tidal signal ([35] Doodson, 1921) and they are the four semidiurnal waves M_2, N_2, S_2, K_2 and the four diurnal waves K_1, O_1, P_1, Q_1. If also the long period waves M_f, M_m, S_{sa} are considered, more than 95% of the tidal signal is characterized ([71] Lambeck, 1980).

In particular, M_2 is the principal lunar semidiurnal constituent, representing the rotation of the Earth with respect to the Moon with the period equal to half of the mean lunar day, while S_2 is the principal solar semidiurnal constituent, representing the rotation of the Earth with respect to the Sun with the period equal to half of the solar day. On the other hand, N_2 is a lunar elliptic semidiurnal constituent because it depends on the changes of distance and K_2 is a luni-solar declinational semidiurnal constituent because modulates the amplitude and frequency of M_2 and S_2 for the declinational effect of the Moon and Sun, respectively. Q_1 is a lunar elliptic diurnal constituent and modulates the amplitude and frequency of the declinational O_1. K_1 is a lunisolar diurnal constituent and, with O_1 lunar diurnal constituent, expresses the effect of the Moon's declination. They account for diurnal inequality and, at extremes, diurnal tides. With P_1 solar diurnal constituent, it expresses the effect of the Sun's declination. S_{sa} is the solar semiannual constituent and with S_a accounts for the nonuniform changes in the Sun's declination and distance, mostly reflecting yearly meteorological variations influencing sea level. M_m is a lunar monthly constituent, expressing the effect of irregularities in the monthly variation of the Moon's distance and therefore this period is also named as elliptic and it is equal to 27.555, called anomalistic month. Finally, M_f is a lunar fortnightly constituent and reflects the effect of departure from a sinusoidal declinational motion (associated with the variation of the Moon's monthly declination).

Table 2.3. List of 106 tidal constituents of the FES2004 ocean tide model, reported in decreasing order with respect to the CTE amplitude H_k.

Sequence Number	Doodson Number	Constituent Name	Number of Harmonic Terms	CTE Amplitude H_k (m)
1	255.555	M_2	3316	7.45648E-01
2	273.555	S_2	3304	2.94792E-01
3	165.555	K_1	3300	2.70864E-01
4	145.555	O_1	3237	1.90368E-01

Table 2.3 – Continued from previous page

Sequence Number	Doodson Number	Constituent Name	Number of Harmonic Terms	CTE Amplitude H_k (m)
5	245.655	N_2	3151	1.54442E-01
6	163.555	P_1	2616	8.36399E-02
7	275.555	K_2	2397	7.29849E-02
8	135.655	Q_1	956	2.53895E-02
9	165.565		952	2.37951E-02
10	145.545		887	2.29593E-02
11	237.555	μ_2	712	1.68275E-02
12	247.455	ν_2	701	1.64236E-02
13	255.545		637	1.49012E-02
14	275.565		446	1.14461E-02
15	235.755	$2N_2$	417	9.88063E-03
16	265.455	L_2	343	8.08723E-03
17	075.555	M_f	277	7.75071E-03
18	272.556	T_2	282	6.87847E-03
19	175.455	J_1	309	6.64132E-03
20	155.655	M_1	238	5.31897E-03
21	185.555	OO_1	137	2.96702E-03
22	065.455	M_m	100	2.85347E-03
23	057.555	S_{sa}	83	2.35406E-03
24	227.655	ϵ_2	96	2.19345E-03
25	055.565	LP	74	2.03640E-03
26	075.565		74	2.01380E-03
27	135.645		77	1.64369E-03
28	137.455	ρ_1	78	1.64273E-03
29	127.555	σ_1	68	1.48200E-03
30	185.565		67	1.35448E-03
31	245.645		56	1.12943E-03
32	125.755	$2Q_1$	50	1.09218E-03
33	285.455	η_2	45	9.45150E-04
34	165.545		48	9.09621E-04
35	155.455		45	8.74359E-04
36	263.655	λ_2	47	8.66789E-04
37	245.555	O_2	43	8.55173E-04
38	162.556	π_1	41	8.12688E-04
39	265.655		40	7.56314E-04
40	085.455	M_{tm}	25	6.14594E-04
41	265.555		28	5.01433E-04
42	225.855	$3N_2$	27	4.83850E-04
43	167.555	ϕ_1	22	4.46243E-04
44	183.555	SO_1	17	3.10721E-04
45	175.465		15	3.05464E-04
46	275.575		19	2.83920E-04
47	173.655	θ_1	13	2.71002E-04
48	274.554	R_2	17	2.49127E-04
49	254.556	α_2	17	2.48433E-04
50	155.665		11	2.47982E-04
51	155.555		11	2.38996E-04
52	157.455	χ_1	11	2.36000E-04

Table 2.3 – Continued from previous page

Sequence Number	Doodson Number	Constituent Name	Number of Harmonic Terms	CTE Amplitude H_k (m)
53	285.465		16	2.24067E-04
54	195.455	ν_1	13	2.09420E-04
55	147.555	τ_1	10	2.02425E-04
56	253.755	γ_2	14	1.89894E-04
57	265.665		15	1.88495E-04
58	256.554	β_2	14	1.87287E-04
59	063.655	MS_m	6	1.85589E-04
60	117.655		11	1.84777E-04
61	166.554	ψ_1	9	1.59933E-04
62	295.555		12	1.58304E-04
63	164.556	S_1	9	1.57183E-04
64	073.555	MS_f	5	1.51731E-04
65	085.465		5	1.37677E-04
66	238.554		10	1.30755E-04
67	217.755		9	1.24500E-04
68	056.554	S_a	4	1.18664E-04
69	295.565		9	1.08910E-04
70	137.445		7	9.24843E-05
71	229.455		7	8.90803E-05
72	195.465		7	8.73525E-05
73	185.355		6	8.25166E-05
74	065.555		3	8.23239E-05
75	127.545		5	6.97821E-05
76	153.655		5	6.91321E-05
77	235.655		5	6.52650E-05
78	185.575		5	6.40134E-05
79	145.755		5	6.28647E-05
80	075.355		2	5.37031E-05
81	125.745		4	5.02799E-05
82	145.535		4	4.72655E-05
83	246.654		4	4.53529E-05
84	175.555		4	4.45470E-05
85	075.575		1	3.90195E-05
86	083.655	MS_{tm}	1	3.65997E-05
87	065.445		1	3.49361E-05
88	065.465		1	3.46336E-05
89	244.656		3	3.28473E-05
90	155.445		3	3.16794E-05
91	248.454		3	3.16589E-05
92	219.555		3	3.09327E-05
93	093.555	MS_{qm}	1	3.08527E-05
94	065.655		1	2.84329E-05
95	058.554	S_{ta}	1	2.73742E-05
96	095.355		1	2.55593E-05
97	135.555		2	2.36545E-05
98	293.555		2	2.17076E-05
99	083.665		1	1.51239E-05
100	083.455		1	1.39139E-05

Table 2.3 – Continued from previous page

Sequence Number	Doodson Number	Constituent Name	Number of Harmonic Terms	CTE Amplitude H_k (m)
101	093.565		1	1.27040E-05
102	065.665		1	1.16454E-05
103	057.565	S_{saa}	1	1.16454E-05
104	115.855		1	1.07603E-05
105	095.365		1	1.05867E-05
106	163.545		1	1.04402E-05

2.4 The response of the Earth to the TGP

The Earth is not a homogeneous and perfectly rigid body, so it reacts to the astronomical forcing in a complex way. The response of the Earth to the TGP can be separated in deformations (solid and ocean tides), changes in the Earth's orientation in space (nutation and precession) and changes in the Earth's rotation rate [123, Wahr, 1981].

Ocean tides are generated by the same gravitational forces as Earth tides, the ability of the ocean to redistribute mass gives to ocean tides their own dynamics. Ocean tides have therefore the same spectrum as Earth tides but different amplitude and phase. Solid Earth tides are much easier to model than ocean tides because the Earth is more rigid than water and has a much simpler shape than the ocean basins.

First of all, the continents interrupt the propagation of the ocean tide waves and in shallow water the waves can not move fast enough to follow Sun and Moon: the response of the Earth to the TGP is not elastic and there is delay between the Earth's tidal bulge and the position of Sun and Moon. There are complicated mechanisms of energy dissipation in the interior of the Earth [70, Lambeck et al., 1974], causing a phase lag with respect to the TGP, thus tides in the real ocean are not in equilibrium with the tidal forcing. In fact, on the equator the tide should take one day to propagate around the Earth, but this would require a wave speed of about 460 m/s, which is only possible in an ocean about 22 km deep. So the tidal wave will follow the Moon or Sun with a time delay influenced by the bottom drag, slowing the progression of the wave.

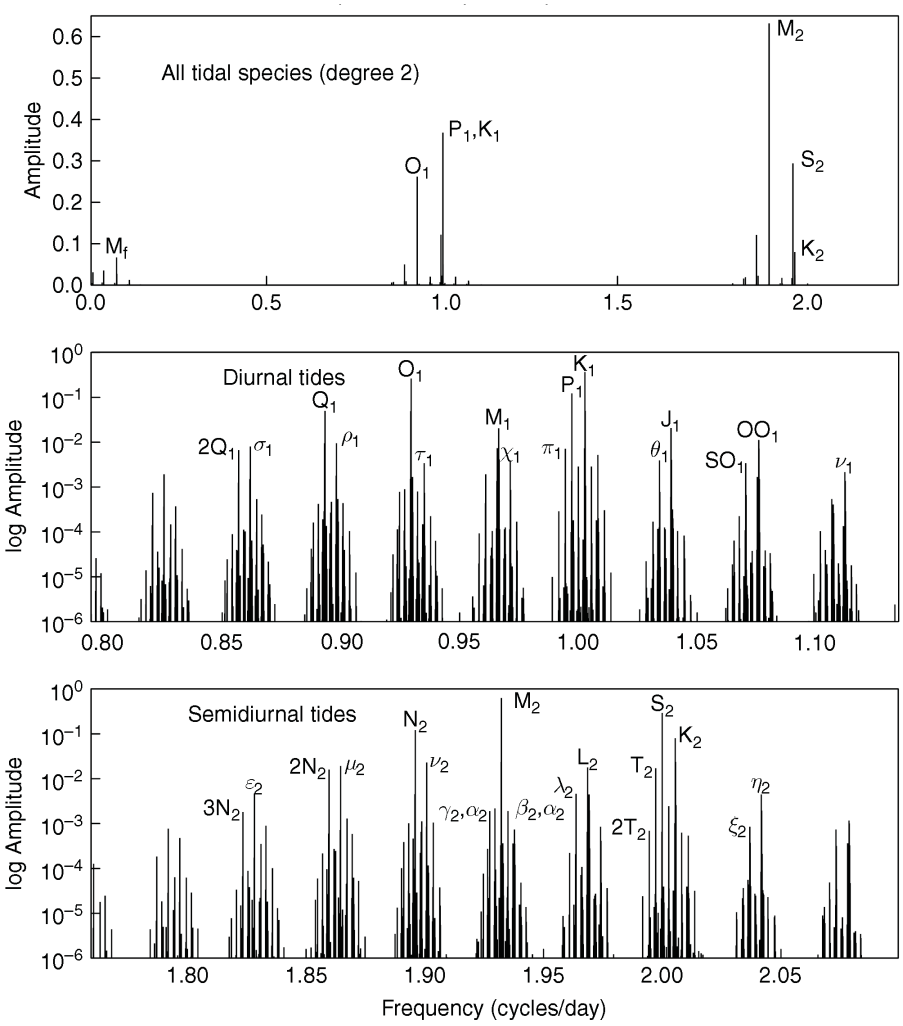

Figure 2.7. Spectrum of the TGP given by the amplitudes of the tidal harmonics, taken from Hartmann and Wenzel (1995), though normalized according to the convention of Cartwright and Tayler (1971). Figure reported by [107, Schubert, 2007].

Chapter 3

Parameterizations of the ocean tide height field

In this Chapter, the Laplace Tidal Equations (LTE) are introduced to explain the relations between the ocean, the solid Earth and the loading effects, in order to derive the fundamental equations of the ocean tide height field and the ocean tide potential. In particular, the ocean tide height can be expressed according to different parameterizations, the main being the classical spherical harmonic representation, characterized by a sum of partial tide heights each corresponding to a tidal frequency, and the response analysis, in which the transfer function or impulse response between the tidal forcing and the ocean tide height field is determined in each tidal band. As regards the harmonic representation, the cotidal and corange charts are reported for the main diurnal and semidiurnal tidal constituents (K_1, P_1, O_1, Q_1, M_2, S_2, K_2, N_2), to visualize the dynamic content of the ocean tide height induced by their tidal frequency. On the other hand, the development of a new algorithm for the accurate recomputation of the Groves and Reynolds orthotide coefficients is illustrated and the corresponding computational results are discussed within the orthotide formalism. Finally, a brief description of the existent ocean tide models and their general classification is provided.

3.1 The Laplace Tidal Equations (LTE)

As described in the previous Chapter, the equilibrium theory of tides introduced by Newton in 1687 provides the astronomical tide-generating potential, to which the ocean responds hydrodynamically in a complex way. Laplace in 1775 was the first to formulate the hydrodynamical equations of ocean tidal motions, the so called Laplace Tidal Equations (LTE)

$$\frac{\partial u}{\partial t} = 2\omega v \sin\phi + \frac{1}{R_e}\frac{\partial}{\partial \phi}[\Delta V_{\mathrm{TP}} - g(\zeta + \zeta^b)], \tag{3.1}$$

$$\frac{\partial v}{\partial t} = -2\omega u \sin\phi + \frac{1}{R_e \cos\phi}\frac{\partial}{\partial \lambda}[\Delta V_{\mathrm{TP}} - g(\zeta + \zeta^b)], \tag{3.2}$$

$$\frac{\partial \zeta}{\partial t} + \frac{1}{R_e \cos\phi}\left[\frac{\partial}{\partial \phi}(hv) + \frac{\partial}{\partial \phi}(hu\cos\phi)\right] = 0, \tag{3.3}$$

where (ϕ, λ) are latitude and longitude, ΔV_{TP} is the total tidal potential, $u(\phi, \lambda, t)$ and $v(\phi, \lambda, t)$ are respectively the east and north fluid velocities and ζ is the measured ocean tide height[1],

[1]The LTE are based on the assumption of an incompressible and single-layer ocean subject only to linearized inertial, potential, and Coriolis forces generated by the TGP. However, since the oceanic tidal motion is highly turbulent, the velocities $u(\phi, , t)$ and the tidal height ζ must be averaged [109, Schwiderski, 1980].

defined by the difference between the geocentric ocean surface tide ζ^s over the geoid and the bottom tide ζ^b as

$$\zeta = \zeta^s + \zeta^b. \tag{3.4}$$

The relations between the different tidal surfaces are well explained in Figure 3.1. In particular, a satellite altimeter measures the height of the instantaneous ocean surface relative to a reference ellipsoid, leading to a direct measurement of the geocentric or altimetric tide, denoted at a given latitude and longitude at any epoch by ζ^a. In turn, the altimetric tide is related to the true or bottom-relative ocean tide ζ as

$$\zeta^a - \zeta^{et} = \zeta + \zeta^{ol}. \tag{3.5}$$

The difference between the altimetric and the Earth tides is also called elastic ocean tide [39, Eanes and Bettadpur, 1995].

On the other hand, the ocean bottom tide height ζ^b (or seafloor tide) is given by the contributions from the solid Earth tide ζ^{et} and the ocean loading tide ζ^{ol} as

$$\zeta^b = \zeta^{et} + \zeta^{ol}. \tag{3.6}$$

It is important to notice that assuming linearity of the ocean's response, every ocean tide constituent is hydrodynamically decoupled from all others and can be constructed independently from the others. Hence the LTE and aforementioned relations are also valid for a single constituent **k**.

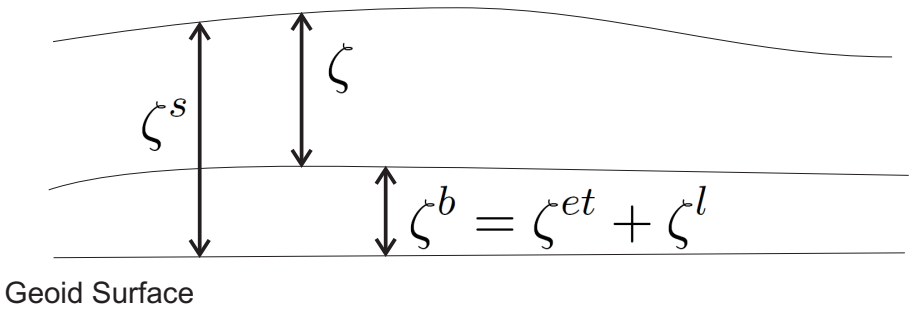

Figure 3.1. Geometric visualization of the measured ocean tide ζ, defined by the difference between the geocentric ocean surface tide ζ^s and the bottom tide ζ^b [110, Schwiderski, 1980].

The surface ocean loading displacement ζ^{ol}_m of a mass element m can be expressed as function of the adimensional ocean loading Love number h'_n

$$\zeta^{ol}_m = \frac{mR_e}{M_e} \sum_{n=0}^{\infty} h'_n P_n(\sin\psi) \tag{3.7}$$

and integrating over $m = \rho_w Re^2 \zeta d\sigma$, we obtain the surface displacement due to the ocean loading as

$$\zeta^{ol} = \frac{\rho_w R_e^3}{M_e} \int\int_{\Sigma} \zeta \sum_{n=0}^{\infty} h'_n P_n(\sin\psi) d\sigma \tag{3.8}$$

$$= \sum_{n=0}^{\infty} \frac{3}{2n+1} \frac{\rho_w}{\rho_e} h'_n \zeta_n, \tag{3.9}$$

being $d\sigma$ the solid angle element, ρ_e the Earth's density and ρ_w the mean density of the sea water.

From the expressions of the body tide and ocean loading tide, the geocentric tide results

$$\zeta^s = h_n \frac{V_{\mathrm{TGP}}}{g} + \sum_{n=0}^{\infty} \left[1 + \frac{3}{2n+1} \frac{\rho_w}{\rho_e} h'_n \right] \zeta_n. \tag{3.10}$$

In conclusion, the solid Earth tide potential is

$$\Delta U_n = \sum_{n=0}^{\infty} k_n V_{\mathrm{TGPn}}, \tag{3.11}$$

the ocean tide potential $_\zeta$ on the Earth's surface is given by

$$U_\zeta = g \sum_{n=0}^{\infty} \frac{3}{2n+1} \frac{\rho_w}{\rho_e} \zeta_n \tag{3.12}$$

and the potential correction due to the ocean loading tide is

$$U_\zeta = \sum_{n=0}^{\infty} k'_n U_{\zeta n}. \tag{3.13}$$

3.2 The harmonic representation

Every harmonic component of the equilibrium tide generates through the ocean's response an ocean partial tide of identical frequency, differing only in the amplitude and phase (Schwiderski, 1980). Hence, in the classical harmonic representation, the total tide height field $\zeta(\phi, \lambda, t)$ can be expressed as the sum of hundreds of partial tides $\zeta_{\mathbf{k}}(\phi, \lambda, t)$, each corresponding to a specified constituent $\mathbf{k}$ as

$$\zeta(\phi, \lambda, t) = \sum_{\mathbf{k}} \zeta_{\mathbf{k}}(\phi, \lambda, t). \tag{3.14}$$

In particular, each partial tide can be written as

$$\zeta_{\mathbf{k}}(\phi, \lambda, t) = Z_{\mathbf{k}}(\phi, \lambda) \cos[\Theta_{\mathbf{k}}(t) + \chi_{\mathbf{k}} - \Psi_{\mathbf{k}}(\phi, \lambda)], \tag{3.15}$$

where $Z_{\mathbf{k}}(\phi, \lambda)$ and $\Psi_{\mathbf{k}}(\phi, \lambda)$ are respectively amplitude and phase[2] of the tidal constituent at a specified geographic location, while the temporal part is represented by the Doodson argument $\Theta_{\mathbf{k}}(t)$ and $\chi_{\mathbf{k}}$ is the Doodson-Warburg phase correction, reported by the IERS TN32 Standards [82, McCarthy and Petit, 2003] and added because it is a convention to have cosine terms and positive amplitudes (see Table 3.1).

Tidal Band	$H_{\mathbf{k}} > 0$	$H_{\mathbf{k}} < 0$
Long Period	π	0
Diurnal	$\pi/2$	$-\pi/2$
Semidiurnal	0	π

Table 3.1. Doodson-Warburg phase correction (McCarthy & Petit, 2003): the phase changes depending on the sign of the Cartwright-Tayler-Edden amplitude $H_{\mathbf{k}}$ (m) for a specified constituent $\mathbf{k}$.

[2]The Greenwich phase of the ocean partial tide, which measures the retardation time (in radians, degrees, or time units) of the oceanic tide $\zeta_{\mathbf{k}}$, relative to the forcing equilibrium tide at Greenwich meridian $\lambda = 0$ (Schwiderski, 1980).

3.2.1 Schwiderski notation

The tide height can be written in complex form, separating the geographic part from the temporal part as

$$\zeta^c_{\mathbf{k}}(\phi,\lambda,t) = \zeta^s_{\mathbf{k}}(\phi,\lambda)\,\mathrm{e}^{[\Theta_{\mathbf{k}}(t)+\chi_{\mathbf{k}}]}, \tag{3.16}$$

where $\zeta^s_{\mathbf{k}}(\phi,\lambda)$ is the static tide height depending only on the geographic location and defined as

$$\zeta^s_{\mathbf{k}}(\phi,\lambda) = Z_{\mathbf{k}}(\phi,\lambda)\cos\Psi_{\mathbf{k}}(\phi,\lambda) - \mathrm{i}\,Z_{\mathbf{k}}(\phi,\lambda)\sin\Psi_{\mathbf{k}}(\phi,\lambda). \tag{3.17}$$

The spherical harmonic analysis of the in-phase and quadrature components of the static tide height gives

$$Z_{\mathbf{k}}(\phi,\lambda)\cos[\Psi_{\mathbf{k}}(\phi,\lambda)] = \sum_{n=0}^{N}\sum_{m=0}^{n}[a^{\mathbf{k}}_{nm}\cos(m\lambda) + b^{\mathbf{k}}_{nm}\sin(m\lambda)]P^m_n(\sin\phi), \tag{3.18}$$

$$Z_{\mathbf{k}}(\phi,\lambda)\sin[\Psi_{\mathbf{k}}(\phi,\lambda)] = \sum_{n=0}^{N}\sum_{m=0}^{n}[c^{\mathbf{k}}_{nm}\cos(m\lambda) + d^{\mathbf{k}}_{nm}\sin(m\lambda)]P^m_n(\sin\phi), \tag{3.19}$$

and allows to obtain the harmonic coefficients $a^{\mathbf{k}}_{nm}, b^{\mathbf{k}}_{nm}, c^{\mathbf{k}}_{nm}, d^{\mathbf{k}}_{nm}$.

Thus, the static tide height becomes

$$\begin{aligned}\zeta^s_{\mathbf{k}}(\phi,\lambda) =& Z_{\mathbf{k}}(\phi,\lambda)\cos\Psi_{\mathbf{k}}(\phi,\lambda) - \mathrm{i}\,Z_{\mathbf{k}}(\phi,\lambda)\sin\Psi_{\mathbf{k}}(\phi,\lambda) \\ =& \sum_{n=0}^{N}\sum_{m=0}^{n}[a^{\mathbf{k}}_{nm}\cos(m\lambda) + b^{\mathbf{k}}_{nm}\sin(m\lambda) - \mathrm{i}\,c^{\mathbf{k}}_{nm}\cos(m\lambda) - \mathrm{i}\,d^{\mathbf{k}}_{nm}\sin(m\lambda)]P^m_n(\sin\phi)\end{aligned} \tag{3.20}$$

After some algebraic manipulations we can express the trigonometric terms $\cos(m\lambda) \pm \mathrm{i}\sin(m\lambda)$ according to the Euler notation $\mathrm{e}^{\pm\mathrm{i}\,m\lambda}$ obtaining

$$\begin{aligned}a^{\mathbf{k}}_{nm}\cos(m\lambda) =& \frac{1}{2}[a^{\mathbf{k}}_{nm}\cos(m\lambda) + \mathrm{i}\,a^{\mathbf{k}}_{nm}\sin(m\lambda) + a^{\mathbf{k}}_{nm}\cos(m\lambda) - \mathrm{i}\,a^{\mathbf{k}}_{nm}\sin(m\lambda)] \\ =& \frac{1}{2}\sum_{+}^{-} a^{\mathbf{k}}_{nm}\,\mathrm{e}^{\pm\mathrm{i}\,m\lambda},\end{aligned} \tag{3.21}$$

$$\begin{aligned}b^{\mathbf{k}}_{nm}\sin(m\lambda) =& \frac{1}{2}[b^{\mathbf{k}}_{nm}\sin(m\lambda) + \mathrm{i}\,b^{\mathbf{k}}_{nm}\cos(m\lambda) + b^{\mathbf{k}}_{nm}\sin(m\lambda) - \mathrm{i}\,b^{\mathbf{k}}_{nm}\cos(m\lambda)] \\ =& \frac{1}{2}\sum_{+}^{-} \mp\mathrm{i}\,b^{\mathbf{k}}_{nm}\,\mathrm{e}^{\pm\mathrm{i}\,m\lambda},\end{aligned} \tag{3.22}$$

$$\begin{aligned}-\mathrm{i}\,c^{\mathbf{k}}_{nm}\cos(m\lambda) =& \frac{1}{2}[-\mathrm{i}\,c^{\mathbf{k}}_{nm}\cos(m\lambda) + c^{\mathbf{k}}_{nm}\sin(m\lambda) - \mathrm{i}\,c^{\mathbf{k}}_{nm}\cos(m\lambda) - c^{\mathbf{k}}_{nm}\sin(m\lambda)] \\ =& \frac{1}{2}\sum_{+}^{-} -\mathrm{i}\,c^{\mathbf{k}}_{nm}\,\mathrm{e}^{\pm\mathrm{i}\,m\lambda},\end{aligned} \tag{3.23}$$

$$\begin{aligned}-\mathrm{i}\,d^{\mathbf{k}}_{nm}\sin(m\lambda) =& \frac{1}{2}[-\mathrm{i}\,d^{\mathbf{k}}_{nm}\sin(m\lambda) + d^{\mathbf{k}}_{nm}\cos(m\lambda) - d^{\mathbf{k}}_{nm}\cos(m\lambda) - \mathrm{i}\,d^{\mathbf{k}}_{nm}\sin(m\lambda)] \\ =& \frac{1}{2}\sum_{+}^{-} \mp d^{\mathbf{k}}_{nm}\,\mathrm{e}^{\pm\mathrm{i}\,m\lambda}\,.\end{aligned} \tag{3.24}$$

Substituting these relations into the equation (3.20) yields

$$\zeta^s_{\mathbf{k}}(\phi,\lambda) = \sum_{n=0}^{N}\sum_{m=0}^{n}\sum_{+}^{-}[(a^{\mathbf{k}}_{nm} \mp d^{\mathbf{k}}_{nm}) - \mathrm{i}(c^{\mathbf{k}}_{nm} \pm b^{\mathbf{k}}_{nm})]P^m_n(\sin\phi)\,\mathrm{e}^{\pm\mathrm{i}\,m\lambda} \tag{3.25}$$

and so the the complex and the real tide heights, defined respectively by the equation (3.16) and (3.15), become

$$\zeta^c_{\mathbf{k}}(\phi,\lambda,t) = \frac{1}{2}\sum_{n=0}^{N}\sum_{m=0}^{n}\sum_{+}^{-}[(a^{\mathbf{k}}_{nm} \mp d^{\mathbf{k}}_{nm}) - \mathrm{i}(c^{\mathbf{k}}_{nm} \pm b^{\mathbf{k}}_{nm})]P^m_n(\sin\phi)\,\mathrm{e}^{\mathrm{i}[\Theta_{\mathbf{k}}(t)+\chi_{\mathbf{k}}\pm m\lambda]}, \tag{3.26}$$

$$\begin{aligned}\zeta_{\mathbf{k}}(\phi,\lambda,t) =& \frac{1}{2}\sum_{n=0}^{N}\sum_{m=0}^{n}\sum_{+}^{-}[(a^{\mathbf{k}}_{nm} \mp d^{\mathbf{k}}_{nm})\cos(\Theta_{\mathbf{k}}(t)+\chi_{\mathbf{k}}\pm m\lambda)\\ &+ (c^{\mathbf{k}}_{nm} \pm b^{\mathbf{k}}_{nm})\sin(\Theta_{\mathbf{k}}(t)+\chi_{\mathbf{k}}\pm m\lambda)]P^m_n(\sin\phi).\end{aligned} \tag{3.27}$$

We can introduce the following relation

$$\hat{C}^{\mathbf{k}\pm}_{nm}\sin\varepsilon^{\mathbf{k}\pm}_{nm} = \frac{1}{2}(a^{\mathbf{k}}_{nm} \mp d^{\mathbf{k}}_{nm}), \tag{3.28}$$

$$\hat{C}^{\mathbf{k}\pm}_{nm}\cos\varepsilon^{\mathbf{k}\pm}_{nm} = \frac{1}{2}(c^{\mathbf{k}}_{nm} \pm b^{\mathbf{k}}_{nm}), \tag{3.29}$$

where $\hat{C}^{\mathbf{k}\pm}_{nm}$ and $\varepsilon^{\mathbf{k}\pm}_{nm}$ are constant in time and space and are respectively amplitude and phase of the prograde and retrograde wave of the constituent $\mathbf{k}$. In particular the harmonic coefficients are explicitly calculated as

$$a^{\mathbf{k}}_{nm} = \hat{C}^{\mathbf{k}+}_{nm}\sin\varepsilon^{\mathbf{k}+}_{nm} + \hat{C}^{\mathbf{k}-}_{nm}\sin\varepsilon^{\mathbf{k}-}_{nm}, \tag{3.30}$$

$$b^{\mathbf{k}}_{nm} = \hat{C}^{\mathbf{k}+}_{nm}\cos\varepsilon^{\mathbf{k}+}_{nm} - \hat{C}^{\mathbf{k}-}_{nm}\cos\varepsilon^{\mathbf{k}-}_{nm}, \tag{3.31}$$

$$c^{\mathbf{k}}_{nm} = \hat{C}^{\mathbf{k}+}_{nm}\cos\varepsilon^{\mathbf{k}+}_{nm} + \hat{C}^{\mathbf{k}-}_{nm}\cos\varepsilon^{\mathbf{k}-}_{nm}, \tag{3.32}$$

$$d^{\mathbf{k}}_{nm} = \hat{C}^{\mathbf{k}-}_{nm}\sin\varepsilon^{\mathbf{k}-}_{nm} - \hat{C}^{\mathbf{k}+}_{nm}\sin\varepsilon^{\mathbf{k}+}_{nm}, \tag{3.33}$$

The direct relations to obtain phase $\varepsilon^{\mathbf{k}\pm}_{nm}$ and amplitude $C^{\mathbf{k}\pm}_{nm}$ from these coefficients are

$$\hat{C}^{\mathbf{k}+}_{nm} = \sqrt{(\hat{C}^{\mathbf{k}+}_{nm}\cos\varepsilon^{\mathbf{k}+}_{nm})^2 + (\hat{C}^{\mathbf{k}+}_{nm}\sin\varepsilon^{\mathbf{k}+}_{nm})^2}, \tag{3.34}$$

$$\hat{C}^{\mathbf{k}-}_{nm} = \sqrt{(\hat{C}^{\mathbf{k}-}_{nm}\cos\varepsilon^{\mathbf{k}-}_{nm})^2 + (\hat{C}^{\mathbf{k}-}_{nm}\sin\varepsilon^{\mathbf{k}-}_{nm})^2}, \tag{3.35}$$

$$\varepsilon^{\mathbf{k}+}_{nm} = \arctan\left(\frac{\hat{C}^{\mathbf{k}+}_{nm}\sin\varepsilon^{\mathbf{k}+}_{nm}}{\hat{C}^{\mathbf{k}+}_{nm}\cos\varepsilon^{\mathbf{k}+}_{nm}}\right), \tag{3.36}$$

$$\varepsilon^{\mathbf{k}-}_{nm} = \arctan\left(\frac{\hat{C}^{\mathbf{k}-}_{nm}\sin\varepsilon^{\mathbf{k}-}_{nm}}{\hat{C}^{\mathbf{k}-}_{nm}\cos\varepsilon^{\mathbf{k}-}_{nm}}\right). \tag{3.37}$$

Finally, the tide height of a specified constituent is given by

$$\zeta_{\mathbf{k}}(\phi,\lambda,t) = \sum_{n}\sum_{m}\sum_{+}^{-}\hat{C}^{\mathbf{k}\pm}_{nm}\sin[\Theta_{\mathbf{k}}(t)+\chi_{\mathbf{k}}\pm m\lambda+\varepsilon^{\mathbf{k}\pm}_{nm}]P^m_n(\sin\phi). \tag{3.38}$$

3.2.2 Lambeck and Ray notation

According to the Lambeck-Ray notation, the phase $\varepsilon^{\mathbf{k}\pm}_{nm}$ is replaced by the phase $\frac{\pi}{2} - \psi^{\mathbf{k}\pm}_{nm}$, thus the trigonometric relation in equation (3.38) can be developed using the fundamental expressions of sine and cosine

$$\sin(x \pm y) = \sin x\cos y \pm \cos x\sin y, \tag{3.39}$$

$$\cos(x \mp y) = \cos x\cos y \pm \sin x\sin y, \tag{3.40}$$

$$\sin(\frac{\pi}{2} - \theta) = \cos\theta, \tag{3.41}$$

$$\cos(\frac{\pi}{2} - \theta) = \sin\theta, \tag{3.42}$$

and becomes

$$\sin\left[\Theta_{\mathbf{k}}(t) + \chi_{\mathbf{k}} \pm m\lambda + \frac{\pi}{2} - \psi_{nm}^{\mathbf{k}\pm}\right] = \cos\left[\Theta_{\mathbf{k}}(t) + \chi_{\mathbf{k}} \pm m\lambda - \psi_{nm}^{\mathbf{k}\pm}\right]. \tag{3.43}$$

The phase according to the Lambeck-Ray notation is related to ours through the relation

$$\psi_{nm}^{\mathbf{k}\pm} = \frac{\pi}{2} - \varepsilon_{nm}^{\mathbf{k}\pm}. \tag{3.44}$$

Thus, the tide height related to a specified constituent is given by the following relation equivalent to the equation (3.38)

$$\zeta_{\mathbf{k}}(\phi,\lambda,t) = \sum_{n}\sum_{m}\sum_{+}^{-} \hat{C}_{nm}^{\mathbf{k}\pm}\cos[\Theta_{\mathbf{k}}(t) + \chi_{\mathbf{k}} \pm m\lambda - \psi_{nm}^{\mathbf{k}\pm}]P_n^m(\sin\phi). \tag{3.45}$$

Substituting equation (3.44) into (3.28) and (3.29) yields

$$\hat{C}_{nm}^{\mathbf{k}\pm}\cos\psi_{nm}^{\mathbf{k}\pm} = \frac{1}{2}(a_{nm}^{\mathbf{k}} \mp d_{nm}^{\mathbf{k}}), \tag{3.46}$$

$$\hat{C}_{nm}^{\mathbf{k}\pm}\sin\psi_{nm}^{\mathbf{k}\pm} = \frac{1}{2}(c_{nm}^{\mathbf{k}} \pm b_{nm}^{\mathbf{k}}), \tag{3.47}$$

and the harmonic coefficients are explicitly calculated as

$$a_{nm}^{\mathbf{k}} = \hat{C}_{nm}^{\mathbf{k}+}\cos\psi_{nm}^{\mathbf{k}+} + \hat{C}_{nm}^{\mathbf{k}-}\cos\psi_{nm}^{\mathbf{k}-}, \tag{3.48}$$

$$b_{nm}^{\mathbf{k}} = \hat{C}_{nm}^{\mathbf{k}+}\sin\psi_{nm}^{\mathbf{k}+} - \hat{C}_{nm}^{\mathbf{k}-}\sin\psi_{nm}^{\mathbf{k}-}, \tag{3.49}$$

$$c_{nm}^{\mathbf{k}} = \hat{C}_{nm}^{\mathbf{k}+}\sin\psi_{nm}^{\mathbf{k}+} + \hat{C}_{nm}^{\mathbf{k}-}\sin\psi_{nm}^{\mathbf{k}-}, \tag{3.50}$$

$$d_{nm}^{\mathbf{k}} = \hat{C}_{nm}^{\mathbf{k}-}\cos\psi_{nm}^{\mathbf{k}-} - \hat{C}_{nm}^{\mathbf{k}+}\cos\psi_{nm}^{\mathbf{k}+}. \tag{3.51}$$

The coefficients $a_{nm}^{\mathbf{k}}, b_{nm}^{\mathbf{k}}, c_{nm}^{\mathbf{k}}, d_{nm}^{\mathbf{k}}$ in Schwiderski and Casotto-Panzetta notation are equivalent to those in Lambeck-Ray notation: only the phase is different in the two notations.

3.2.3 Temporal variations of the Stokes coefficients due to ocean tides

The complex and real tide height field for a selected constituent are respectively given by

$$\zeta_{\mathbf{k}}^{c}(\phi,\lambda,t) = Z_{\mathbf{k}}(\phi,\lambda)\,\mathrm{e}^{\mathrm{i}[\Theta_{\mathbf{k}}(t)+\chi_{\mathbf{k}}-\Psi_{\mathbf{k}}(\phi,\lambda)]}, \tag{3.52}$$

$$\zeta_{\mathbf{k}}(\phi,\lambda,t) = Z_{\mathbf{k}}(\phi,\lambda)\cos[\Theta_{\mathbf{k}}(t) + \chi_{\mathbf{k}} - \Psi_{\mathbf{k}}(\phi,\lambda)]. \tag{3.53}$$

The static part $\zeta_{\mathbf{k}}^{S}(\phi,\lambda,t)$ of this tidal field can be expressed in two ways, according to whether or not the Doodson-Warburg phase correction $\chi_{\mathbf{k}}$ is included, as follows

$$\tilde{\zeta}_{\mathbf{k}}^{s}(\phi,\lambda) = Z_{\mathbf{k}}(\phi,\lambda)\,\mathrm{e}^{-\mathrm{i}[\Psi_{\mathbf{k}}-\chi_{\mathbf{k}}]}, \tag{3.54}$$

$$\zeta_{\mathbf{k}}^{s}(\phi,\lambda) = Z_{\mathbf{k}}(\phi,\lambda)\,\mathrm{e}^{-\mathrm{i}\,\Psi_{\mathbf{k}}}. \tag{3.55}$$

Starting from the equation (3.55) and performing the spherical harmonic analysis of the real and imaginary parts, we can obtain the spherical harmonic coefficients $a_{nm}^{\mathbf{k}}, b_{nm}^{\mathbf{k}}, c_{nm}^{\mathbf{k}}, d_{nm}^{\mathbf{k}}$

$$Z_{\mathbf{k}}(\phi,\lambda)\cos[\Psi_{\mathbf{k}}(\phi,\lambda)] = \sum_{n=0}^{N}\sum_{m=0}^{n}[a_{nm}^{\mathbf{k}}\cos(m\lambda) + b_{nm}^{\mathbf{k}}\sin(m\lambda)]P_n^m(\sin\phi), \tag{3.56}$$

$$Z_{\mathbf{k}}(\phi,\lambda)\sin[\Psi_{\mathbf{k}}(\phi,\lambda)] = \sum_{n=0}^{N}\sum_{m=0}^{n}[c_{nm}^{\mathbf{k}}\cos(m\lambda) + d_{nm}^{\mathbf{k}}\sin(m\lambda)]P_n^m(\sin\phi). \tag{3.57}$$

On the other hand, the equation (3.54) includes the Doodson-Warburg phase correction and consequently the spherical harmonic analysis of the real and imaginary parts yields different coefficients $A^{\mathbf{k}}_{nm}, B^{\mathbf{k}}_{nm}, C^{\mathbf{k}}_{nm}, D^{\mathbf{k}}_{nm}$

$$Z_{\mathbf{k}}(\phi,\lambda)\cos[\Psi_{\mathbf{k}}(\phi,\lambda)-\chi_{\mathbf{k}}] = \sum_{n=0}^{N}\sum_{m=0}^{n}[A^{\mathbf{k}}_{nm}\cos(m\lambda)+B^{\mathbf{k}}_{nm}\sin(m\lambda)]P^m_n(\sin\phi), \tag{3.58}$$

$$Z_{\mathbf{k}}(\phi,\lambda)\sin[\Psi_{\mathbf{k}}(\phi,\lambda)-\chi_{\mathbf{k}}] = \sum_{n=0}^{N}\sum_{m=0}^{n}[C^{\mathbf{k}}_{nm}\cos(m\lambda)+D^{\mathbf{k}}_{nm}\sin(m\lambda)]P^m_n(\sin\phi). \tag{3.59}$$

Developing the first arguments of the equations (3.58) and (3.59) using the equations (3.40) and (3.41), we obtain

$$\begin{aligned}
Z_{\mathbf{k}}(\phi,\lambda)\cos[\Psi_{\mathbf{k}}(\phi,\lambda)-\chi_{\mathbf{k}}] =& Z_{\mathbf{k}}(\phi,\lambda)[\cos\Psi_{\mathbf{k}}(\phi,\lambda)\cos\chi_{\mathbf{k}}+\sin\Psi_{\mathbf{k}}(\phi,\lambda)\sin\chi_{\mathbf{k}}] && (3.60)\\
=& \underline{Z_{\mathbf{k}}(\phi,\lambda)\cos\Psi_{\mathbf{k}}(\phi,\lambda)}\cos\chi_{\mathbf{k}}+\underline{Z_{\mathbf{k}}(\phi,\lambda)\sin\Psi_{\mathbf{k}}(\phi,\lambda)}\sin\chi_{\mathbf{k}}, && (3.61)\\
Z_{\mathbf{k}}(\phi,\lambda)\sin[\Psi_{\mathbf{k}}(\phi,\lambda)-\chi_{\mathbf{k}}] =& Z_{\mathbf{k}}(\phi,\lambda)[\sin\Psi_{\mathbf{k}}(\phi,\lambda)\cos\chi_{\mathbf{k}}-\cos\Psi_{\mathbf{k}}(\phi,\lambda)\sin\chi_{\mathbf{k}}], && (3.62)\\
=& \underline{Z_{\mathbf{k}}(\phi,\lambda)\sin\Psi_{\mathbf{k}}(\phi,\lambda)}\cos\chi_{\mathbf{k}}-\underline{Z_{\mathbf{k}}(\phi,\lambda)\cos\Psi_{\mathbf{k}}(\phi,\lambda)}\sin\chi_{\mathbf{k}}, && (3.63)
\end{aligned}$$

where the underlined terms are equal to first arguments of the equations (3.56) and (3.57). Substituting the second arguments of the equations (3.56) and (3.57) into the underlined terms of the equations (3.60) and (3.63) gives the following relations

$$\begin{aligned}
Z_{\mathbf{k}}(\phi,\lambda)\cos[\Psi_{\mathbf{k}}(\phi,\lambda)-\chi_{\mathbf{k}}] =& \sum_{n=0}^{N}\sum_{m=0}^{n}[a^{\mathbf{k}}_{nm}\cos(m\lambda)+b^{\mathbf{k}}_{nm}\sin(m\lambda)]P^m_n(\sin\phi)\cos\chi_{\mathbf{k}}+\\
&\sum_{n=0}^{N}\sum_{m=0}^{n}[c^{\mathbf{k}}_{nm}\cos(m\lambda)+d^{\mathbf{k}}_{nm}\sin(m\lambda)]P^m_n(\sin\phi)\sin\chi_{\mathbf{k}}\\
=&\sum_{n=0}^{N}\sum_{m=0}^{n}[a^{\mathbf{k}}_{nm}\cos\chi_{\mathbf{k}}\cos(m\lambda)+b^{\mathbf{k}}_{nm}\cos\chi_{\mathbf{k}}\sin(m\lambda)+\\
&c^{\mathbf{k}}_{nm}\sin\chi_{\mathbf{k}}\cos(m\lambda)+d^{\mathbf{k}}_{nm}\sin\chi_{\mathbf{k}}\sin(m\lambda)]P^m_n(\sin\phi)\\
=&\sum_{n=0}^{N}\sum_{m=0}^{n}[(a^{\mathbf{k}}_{nm}\cos\chi_{\mathbf{k}}+c^{\mathbf{k}}_{nm}\sin\chi_{\mathbf{k}})\cos(m\lambda)+\\
&(b^{\mathbf{k}}_{nm}\cos\chi_{\mathbf{k}}+d^{\mathbf{k}}_{nm}\sin\chi_{\mathbf{k}})\sin(m\lambda)]P^m_n(\sin\phi), && (3.64)\\
Z_{\mathbf{k}}(\phi,\lambda)\sin[\Psi_{\mathbf{k}}(\phi,\lambda)-\chi_{\mathbf{k}}] =& \sum_{n=0}^{N}\sum_{m=0}^{n}[c^{\mathbf{k}}_{nm}\cos(m\lambda)+d^{\mathbf{k}}_{nm}\sin(m\lambda)]P^m_n(\sin\phi)\cos\chi_{\mathbf{k}}-\\
&\sum_{n=0}^{N}\sum_{m=0}^{n}[a^{\mathbf{k}}_{nm}\cos(m\lambda)+b^{\mathbf{k}}_{nm}\sin(m\lambda)]P^m_n(\sin\phi)\sin\chi_{\mathbf{k}}\\
=&\sum_{n=0}^{N}\sum_{m=0}^{n}[c^{\mathbf{k}}_{nm}\cos\chi_{\mathbf{k}}\cos(m\lambda)+d^{\mathbf{k}}_{nm}\cos\chi_{\mathbf{k}}\sin(m\lambda)\\
&-a^{\mathbf{k}}_{nm}\sin\chi_{\mathbf{k}}\cos(m\lambda)-b^{\mathbf{k}}_{nm}\sin\chi_{\mathbf{k}}\sin(m\lambda)]P^m_n(\sin\phi)\\
=&\sum_{n=0}^{N}\sum_{m=0}^{n}[(c^{\mathbf{k}}_{nm}\cos\chi_{\mathbf{k}}-a^{\mathbf{k}}_{nm}\sin\chi_{\mathbf{k}})\cos(m\lambda)+\\
&(d^{\mathbf{k}}_{nm}\cos\chi_{\mathbf{k}}-b^{\mathbf{k}}_{nm}\sin\chi_{\mathbf{k}})\sin(m\lambda)]P^m_n(\sin\phi). && (3.65)
\end{aligned}$$

Finally we can explicitly write the harmonic coefficients $A^{\mathbf{k}}_{nm}, B^{\mathbf{k}}_{nm}, C^{\mathbf{k}}_{nm}, D^{\mathbf{k}}_{nm}$ as

$$A^{\mathbf{k}}_{nm} = a^{\mathbf{k}}_{nm}\cos\chi_{\mathbf{k}}+c^{\mathbf{k}}_{nm}\sin\chi_{\mathbf{k}}, \tag{3.66}$$

$$B_{nm}^{\mathbf{k}} = b_{nm}^{\mathbf{k}} \cos\chi_{\mathbf{k}} + d_{nm}^{\mathbf{k}} \sin\chi_{\mathbf{k}}, \tag{3.67}$$
$$C_{nm}^{\mathbf{k}} = c_{nm}^{\mathbf{k}} \cos\chi_{\mathbf{k}} - a_{nm}^{\mathbf{k}} \sin\chi_{\mathbf{k}}, \tag{3.68}$$
$$D_{nm}^{\mathbf{k}} = d_{nm}^{\mathbf{k}} \cos\chi_{\mathbf{k}} - b_{nm}^{\mathbf{k}} \sin\chi_{\mathbf{k}}. \tag{3.69}$$

This is the map from the harmonic coefficients $a_{nm}^{\mathbf{k}}$, $b_{nm}^{\mathbf{k}}$, $c_{nm}^{\mathbf{k}}$, $d_{nm}^{\mathbf{k}}$ to the coefficients $A_{nm}^{\mathbf{k}}, B_{nm}^{\mathbf{k}}$, $C_{nm}^{\mathbf{k}}$, $D_{nm}^{\mathbf{k}}$ including the Doodson-Warburg phase correction. The ocean tide height becomes

$$\begin{aligned}\zeta_{\mathbf{k}}(\phi,\lambda,t) = &\frac{1}{2}\sum_{n=0}^{N}\sum_{m=0}^{n}\sum_{+}^{-}[(A_{nm}^{\mathbf{k}} \mp D_{nm}^{\mathbf{k}})\cos(\Theta_{\mathbf{k}}(t) \pm m\lambda) \\ &+ (C_{nm}^{\mathbf{k}} \pm B_{nm}^{\mathbf{k}})\sin(\Theta_{\mathbf{k}}(t) \pm m\lambda)]P_n^m(\sin\phi).\end{aligned} \tag{3.70}$$

The inverse mapping is obtained resolving the two systems composed by the coupled equations (3.66)-(3.68) and (3.67)-(3.69)

$$a_{nm}^{\mathbf{k}} = A_{nm}^{\mathbf{k}} \cos\chi_{\mathbf{k}} - C_{nm}^{\mathbf{k}} \sin\chi_{\mathbf{k}}, \tag{3.71}$$
$$b_{nm}^{\mathbf{k}} = B_{nm}^{\mathbf{k}} \cos\chi_{\mathbf{k}} - D_{nm}^{\mathbf{k}} \sin\chi_{\mathbf{k}}, \tag{3.72}$$
$$c_{nm}^{\mathbf{k}} = C_{nm}^{\mathbf{k}} \cos\chi_{\mathbf{k}} + A_{nm}^{\mathbf{k}} \sin\chi_{\mathbf{k}}, \tag{3.73}$$
$$d_{nm}^{\mathbf{k}} = D_{nm}^{\mathbf{k}} \cos\chi_{\mathbf{k}} + B_{nm}^{\mathbf{k}} \sin\chi_{\mathbf{k}}. \tag{3.74}$$

Using the relations (3.28) and (3.29), it is possible to express the coefficients $A_{nm}^{\mathbf{k}}, B_{nm}^{\mathbf{k}}, C_{nm}^{\mathbf{k}}, D_{nm}^{\mathbf{k}}$ as functions of $\hat{C}_{nm}^{\mathbf{k}\pm}$, $\varepsilon_{nm}^{\mathbf{k}\pm}$ and $\chi_{\mathbf{k}}$ as follows

$$\frac{1}{2}(A_{nm}^{\mathbf{k}} \mp D_{nm}^{\mathbf{k}}) = \hat{C}_{nm}^{\mathbf{k}\pm}\sin\varepsilon_{nm}^{\mathbf{k}\pm}\cos\chi_{\mathbf{k}} + \hat{C}_{nm}^{\mathbf{k}\pm}\cos\varepsilon_{nm}^{\mathbf{k}\pm}\sin\chi_{\mathbf{k}} = C_{nm}^{\mathbf{k}\pm}, \tag{3.75}$$
$$\frac{1}{2}(C_{nm}^{\mathbf{k}} \pm B_{nm}^{\mathbf{k}}) = \hat{C}_{nm}^{\mathbf{k}\pm}\cos\varepsilon_{nm}^{\mathbf{k}\pm}\cos\chi_{\mathbf{k}} - \hat{C}_{nm}^{\mathbf{k}\pm}\sin\varepsilon_{nm}^{\mathbf{k}\pm}\sin\chi_{\mathbf{k}} = S_{nm}^{\mathbf{k}\pm}. \tag{3.76}$$

Thus, the ocean tide height can be written as

$$\begin{aligned}\zeta_{\mathbf{k}}(\phi,\lambda,t) = &\sum_{n=0}^{N}\sum_{m=0}^{n}\sum_{+}^{-}[(\hat{C}_{nm}^{\mathbf{k}\pm}\sin\varepsilon_{nm}^{\mathbf{k}\pm}\cos\chi_{\mathbf{k}} + \hat{C}_{nm}^{\mathbf{k}\pm}\cos\varepsilon_{nm}^{\mathbf{k}\pm}\sin\chi_{\mathbf{k}})\cos(\Theta_{\mathbf{k}}(t) \pm m\lambda) + \\ &(\hat{C}_{nm}^{\mathbf{k}\pm}\cos\varepsilon_{nm}^{\mathbf{k}\pm}\cos\chi_{\mathbf{k}} - \hat{C}_{nm}^{\mathbf{k}\pm}\sin\varepsilon_{nm}^{\mathbf{k}\pm}\sin\chi_{\mathbf{k}})\sin(\Theta_{\mathbf{k}}(t) \pm m\lambda)]P_n^m(\sin\phi) \\ = &\sum_{n=0}^{N}\sum_{m=0}^{n}\sum_{+}^{-}[C_{nm}^{\mathbf{k}\pm}\cos(\Theta_{\mathbf{k}}(t) \pm m\lambda) + S_{nm}^{\mathbf{k}\pm}\sin(\Theta_{\mathbf{k}}(t) \pm m\lambda)]P_n^m(\sin\phi).\end{aligned} \tag{3.77}$$

From these expressions, the coefficients $A_{nm}^{\mathbf{k}}, B_{nm}^{\mathbf{k}}, C_{nm}^{\mathbf{k}}, D_{nm}^{\mathbf{k}}$ can be explicitly derived as

$$A_{nm}^{\mathbf{k}} = (\hat{C}_{nm}^{\mathbf{k}+}\sin\varepsilon_{nm}^{\mathbf{k}+} + \hat{C}_{nm}^{\mathbf{k}-}\sin\varepsilon_{nm}^{\mathbf{k}-})\cos\chi_{\mathbf{k}} + (\hat{C}_{nm}^{\mathbf{k}+}\cos\varepsilon_{nm}^{\mathbf{k}+} + \hat{C}_{nm}^{\mathbf{k}-}\cos\varepsilon_{nm}^{\mathbf{k}-})\sin\chi_{\mathbf{k}}, \tag{3.78}$$
$$B_{nm}^{\mathbf{k}} = (\hat{C}_{nm}^{\mathbf{k}+}\cos\varepsilon_{nm}^{\mathbf{k}+} - \hat{C}_{nm}^{\mathbf{k}-}\cos\varepsilon_{nm}^{\mathbf{k}-})\cos\chi_{\mathbf{k}} - (\hat{C}_{nm}^{\mathbf{k}+}\sin\varepsilon_{nm}^{\mathbf{k}+} - \hat{C}_{nm}^{\mathbf{k}-}\sin\varepsilon_{nm}^{\mathbf{k}-})\sin\chi_{\mathbf{k}}, \tag{3.79}$$
$$C_{nm}^{\mathbf{k}} = (\hat{C}_{nm}^{\mathbf{k}+}\cos\varepsilon_{nm}^{\mathbf{k}+} + \hat{C}_{nm}^{\mathbf{k}-}\cos\varepsilon_{nm}^{\mathbf{k}-})\cos\chi_{\mathbf{k}} - (\hat{C}_{nm}^{\mathbf{k}+}\sin\varepsilon_{nm}^{\mathbf{k}+} + \hat{C}_{nm}^{\mathbf{k}-}\sin\varepsilon_{nm}^{\mathbf{k}-})\sin\chi_{\mathbf{k}}, \tag{3.80}$$
$$D_{nm}^{\mathbf{k}} = (\hat{C}_{nm}^{\mathbf{k}-}\sin\varepsilon_{nm}^{\mathbf{k}-} - \hat{C}_{nm}^{\mathbf{k}+}\sin\varepsilon_{nm}^{\mathbf{k}+})\cos\chi_{\mathbf{k}} + (\hat{C}_{nm}^{\mathbf{k}-}\cos\varepsilon_{nm}^{\mathbf{k}-} - \hat{C}_{nm}^{\mathbf{k}+}\cos\varepsilon_{nm}^{\mathbf{k}+})\sin\chi_{\mathbf{k}} \tag{3.81}$$

and

$$\hat{C}_{nm}^{\mathbf{k}\pm} = \sqrt{C_{nm}^{\mathbf{k}\pm 2} + S_{nm}^{\mathbf{k}\pm 2}}, \tag{3.82}$$
$$\varepsilon_{nm}^{\mathbf{k}\pm} = \arctan\left(\frac{C_{nm}^{\mathbf{k}\pm}}{S_{nm}^{\mathbf{k}\pm}}\right) - \chi_{\mathbf{k}}. \tag{3.83}$$

Developing the relation (3.77) we obtain

$$\begin{aligned}\zeta_{\mathbf{k}}(\phi,\lambda,t) =&\sum_{n=0}^{N}\sum_{m=0}^{n}\sum_{+}^{-}[C_{nm}^{\mathbf{k}\pm}\cos\Theta_{\mathbf{k}}(t)\cos(m\lambda)\mp C_{nm}^{\mathbf{k}\pm}\sin\Theta_{\mathbf{k}}(t)\sin(m\lambda)+\\ &S_{nm}^{\mathbf{k}\pm}\sin\Theta_{\mathbf{k}}(t)\cos(m\lambda)\pm S_{nm}^{\mathbf{k}\pm}\cos\Theta_{\mathbf{k}}(t)\sin(m\lambda)]P_n^m(\sin\phi)\\ =&\sum_{n=0}^{N}\sum_{m=0}^{n}\sum_{+}^{-}[(C_{nm}^{\mathbf{k}\pm}\cos\Theta_{\mathbf{k}}(t)+S_{nm}^{\mathbf{k}\pm}\sin\Theta_{\mathbf{k}}(t))\cos(m\lambda)+\\ &(\pm S_{nm}^{\mathbf{k}\pm}\cos\Theta_{\mathbf{k}}(t)\mp C_{nm}^{\mathbf{k}\pm}\sin\Theta_{\mathbf{k}}(t))\sin(m\lambda)]P_n^m(\sin\phi).\end{aligned}\tag{3.84}$$

The Stokes coefficients variations due to ocean tides, including ocean loading effects, are given in the unnormalized complex form by

$$\begin{aligned}\Delta K_{nm}(t) =&\Delta C_{nm}(t)-\mathrm{i}\,\Delta S_{nm}(t)\\ =&\sum_{\mathbf{k}}\frac{4\pi G\rho_w}{g}\frac{1+k'_n}{2n+1}\zeta_{nm}^{\mathbf{k}}(t),\end{aligned}\tag{3.85}$$

where $\zeta_{nm}^{\mathbf{k}}(t)$ are the complex unnormalized harmonic coefficients of the tide height at a specified frequency, and the complex form of the ocean tide generated potential is

$$\Delta V_{OT}^{C}(r,\lambda,\phi)=\frac{GM}{r}\sum_{n=2}^{N}\sum_{m=0}^{n}\left(\frac{a_e}{r}\right)^n\Delta K_{nm}^{*}(t)Y_n^m(\phi,\lambda).\tag{3.86}$$

The real unnormalized coefficients variations can be explicitly written as

$$\Delta C_{nm}(t)=\frac{4\pi G\rho_w}{g}\frac{1+k'_n}{2n+1}\sum_{\mathbf{k}}\sum_{+}^{-}[C_{nm}^{\mathbf{k}\pm}\cos\Theta_{\mathbf{k}}(t)+S_{nm}^{\mathbf{k}\pm}\sin\Theta_{\mathbf{k}}(t)],\tag{3.87}$$

$$\Delta S_{nm}(t)=\frac{4\pi G\rho_w}{g}\frac{1+k'_n}{2n+1}\sum_{\mathbf{k}}\sum_{+}^{-}[\pm S_{nm}^{\mathbf{k}\pm}\cos\Theta_{\mathbf{k}}(t)\mp C_{nm}^{\mathbf{k}\pm}\sin\Theta_{\mathbf{k}}(t)].\tag{3.88}$$

Including the full normalization factor into the factor F_{nm} defined as

$$F_{nm}=\frac{4\pi G\rho_w}{g}\frac{1+k'_n}{2n+1}\sqrt{\frac{(n+m)!}{(2-\delta_{0m})(2n+1)(n-m)!}}\tag{3.89}$$

and writing explicitly the relations (3.87) and (3.88), we obtain the fully-normalized Stokes coefficients variations due to ocean tides

$$\begin{aligned}\Delta\bar{C}_{nm}(t) =&F_{nm}\sum_{\mathbf{k}}[C_{nm}^{\mathbf{k}+}\cos\Theta_{\mathbf{k}}(t)+S_{nm}^{\mathbf{k}+}\sin\Theta_{\mathbf{k}}(t)+C_{nm}^{\mathbf{k}-}\cos\Theta_{\mathbf{k}}(t)+S_{nm}^{\mathbf{k}-}\sin\Theta_{\mathbf{k}}(t)]\\ =&F_{nm}\sum_{\mathbf{k}}[(C_{nm}^{\mathbf{k}+}+C_{nm}^{\mathbf{k}-})\cos\Theta_{\mathbf{k}}(t)+(S_{nm}^{\mathbf{k}+}+S_{nm}^{\mathbf{k}-})\sin\Theta_{\mathbf{k}}(t)],\end{aligned}\tag{3.90}$$

$$\begin{aligned}\Delta\bar{S}_{nm}(t) =&F_{nm}\sum_{\mathbf{k}}[S_{nm}^{\mathbf{k}+}\cos\Theta_{\mathbf{k}}(t)-C_{nm}^{\mathbf{k}+}\sin\Theta_{\mathbf{k}}(t)-S_{nm}^{\mathbf{k}-}\cos\Theta_{\mathbf{k}}(t)+C_{nm}^{\mathbf{k}-}\sin\Theta_{\mathbf{k}}(t)]\\ =&F_{nm}\sum_{\mathbf{k}}[(S_{nm}^{\mathbf{k}+}-S_{nm}^{\mathbf{k}-})\cos\Theta_{\mathbf{k}}(t)-(C_{nm}^{\mathbf{k}+}-C_{nm}^{\mathbf{k}-})\sin\Theta_{\mathbf{k}}(t)].\end{aligned}\tag{3.91}$$

Finally, comparing these relations to those of IERS-TN32 Standards (McCarthy & Petit, 2003), it can be noticed that the unnormalized prograde and retrograde harmonic coefficients $C_{nm}^{\mathbf{k}\pm}$ and $S_{nm}^{\mathbf{k}\pm}$ of the constituent $\mathbf{k}$ are

$$C_{nm}^{\mathbf{k}\pm}=C_{nm,IERS}^{\mathbf{k}\pm}$$

$$
\begin{aligned}
&= \frac{1}{2}(A^{\mathbf{k}}_{nm} \mp D^{\mathbf{k}}_{nm}) \\
&= \frac{1}{2}[(a^{\mathbf{k}}_{nm} \mp d^{\mathbf{k}}_{nm})\cos\chi_{\mathbf{k}} + (c^{\mathbf{k}}_{nm} \pm b^{\mathbf{k}}_{nm})\sin\chi_{\mathbf{k}}], \qquad (3.92)\\
S^{\mathbf{k}\pm}_{nm} &= S^{\mathbf{k}\pm}_{nm,IERS} \\
&= \frac{1}{2}(C^{\mathbf{k}}_{nm} \pm B^{\mathbf{k}}_{nm}) \\
&= \frac{1}{2}[(c^{\mathbf{k}}_{nm} \pm b^{\mathbf{k}}_{nm})\cos\chi_{\mathbf{k}} - (a^{\mathbf{k}}_{nm} \mp d^{\mathbf{k}}_{nm})\sin\chi_{\mathbf{k}}], \qquad (3.93)
\end{aligned}
$$

so that our harmonic coefficients $A^{\mathbf{k}}_{nm}, B^{\mathbf{k}}_{nm}, C^{\mathbf{k}}_{nm}, D^{\mathbf{k}}_{nm}$ are given by

$$
\begin{aligned}
A^{\mathbf{k}}_{nm} &= C^{\mathbf{k}+}_{nm} + C^{\mathbf{k}-}_{nm}, \qquad (3.94)\\
B^{\mathbf{k}}_{nm} &= S^{\mathbf{k}+}_{nm} - S^{\mathbf{k}-}_{nm}, \qquad (3.95)\\
C^{\mathbf{k}}_{nm} &= S^{\mathbf{k}+}_{nm} + S^{\mathbf{k}-}_{nm}, \qquad (3.96)\\
D^{\mathbf{k}}_{nm} &= C^{\mathbf{k}-}_{nm} - C^{\mathbf{k}+}_{nm}. \qquad (3.97)
\end{aligned}
$$

The ocean tide generated potential is given in the real form by

$$
\Delta V_{OT}(r,\lambda,\phi) = \frac{GM}{r}\sum_{n=2}^{N}\sum_{m=0}^{l}\left(\frac{a_e}{r}\right)^n \left[\Delta\bar{C}_{nm}(t)\cos(m\lambda) + \Delta\bar{S}_{nm}(t)\sin(m\lambda)\right]\bar{P}^m_n(\sin\phi). \qquad (3.98)
$$

3.2.4 Cotidal and corange charts

It is interesting to visualize the information content of the dynamic tide height at a certain frequency $\mathbf{k}$ through the corange and cotidal charts. The cotidal lines are those connecting geographic points with the same tidal phase $\Psi_{\mathbf{k}}(\varphi,\lambda)$ and so they are solutions of the equation

$$
\Psi_{\mathbf{k}}(\varphi,\lambda) = l\alpha,\ l = 1,2,...,360^\circ/\alpha, \qquad (3.99)
$$

where the phase varies from 0° to 360° (see Figure **??**).

On the other hand, corange lines are those connecting geographic points with the same corange, that corresponds to twice the tidal amplitude $Z_{\mathbf{k}}(\varphi,\lambda)$ and are given by the following equation

$$
2Z_{\mathbf{k}}(\varphi,\lambda) = C. \qquad (3.100)
$$

The cotidal lines meet at the amphidromic points characterized by a null tidal excursion for the considered constituent, around which the tide propagates in one tidal period and caused by the Coriolis force combined with continental coasts to produce standing waves. There are also anti-amphidromic points characterized by permanent high tide. Cotidal and corange lines would represent an orthogonal system if there were not tidal dissipation phenomena.

Charts with cotidal lines superimposed on the ocean tide height at a selected time are shown in Figures 3.2, 3.3, 3.4, 3.5, 3.6, 3.7, 3.8, 3.9, respectively for the eight main semidiurnal and diurnal tide constituents M_2, K_2, S_2, N_2, K_1, Q_1, P_1, O_1. The cotidal lines connecting points with the same tidal phase are represented with a color scale from green to pink, while low and high tides are respectively represented with a color scale from blue to red.

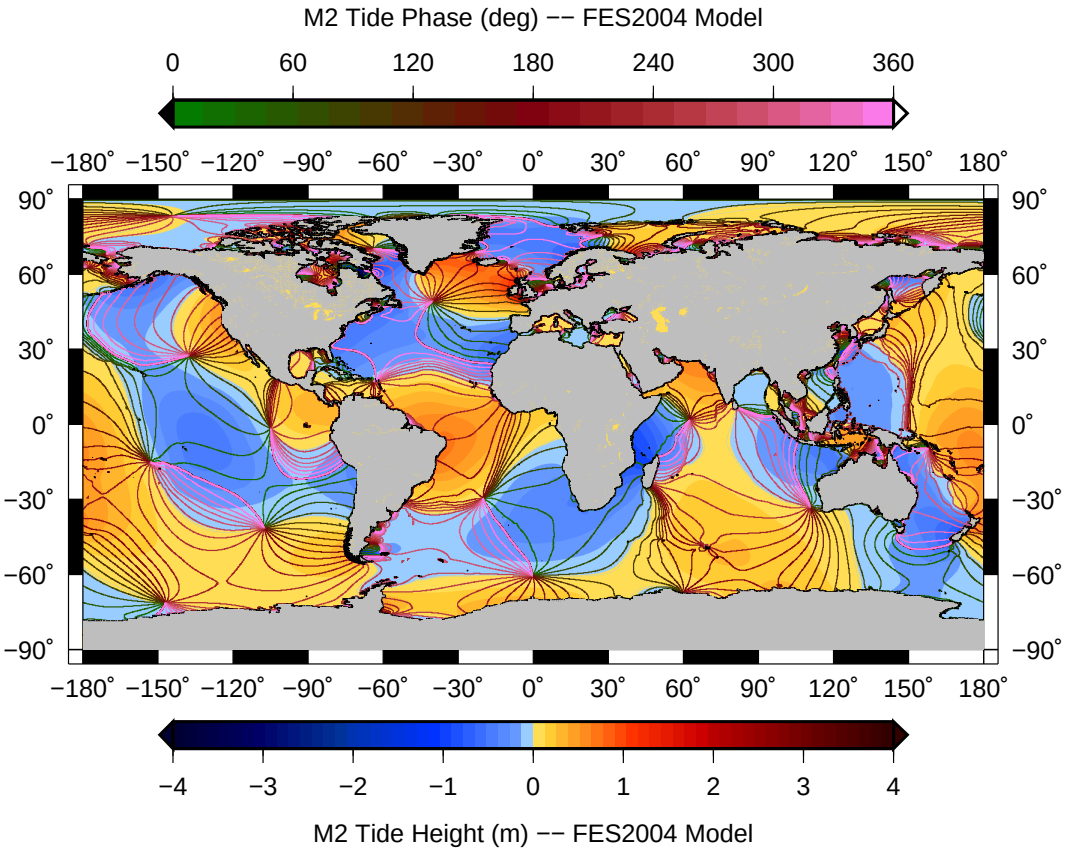

Figure 3.2. Cotidal and height chart of the M2 constituent of the FES2004 ocean tide model.

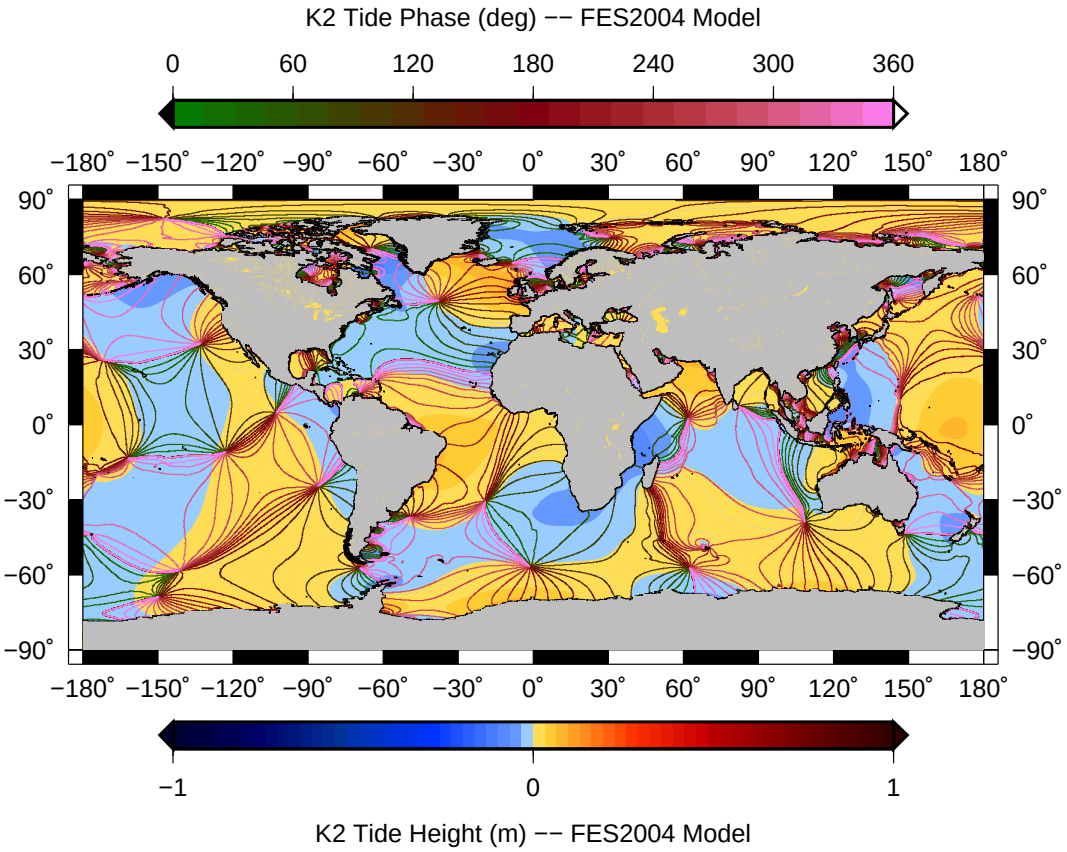

Figure 3.3. Cotidal and height chart of the K2 constituent of the FES2004 ocean tide model.

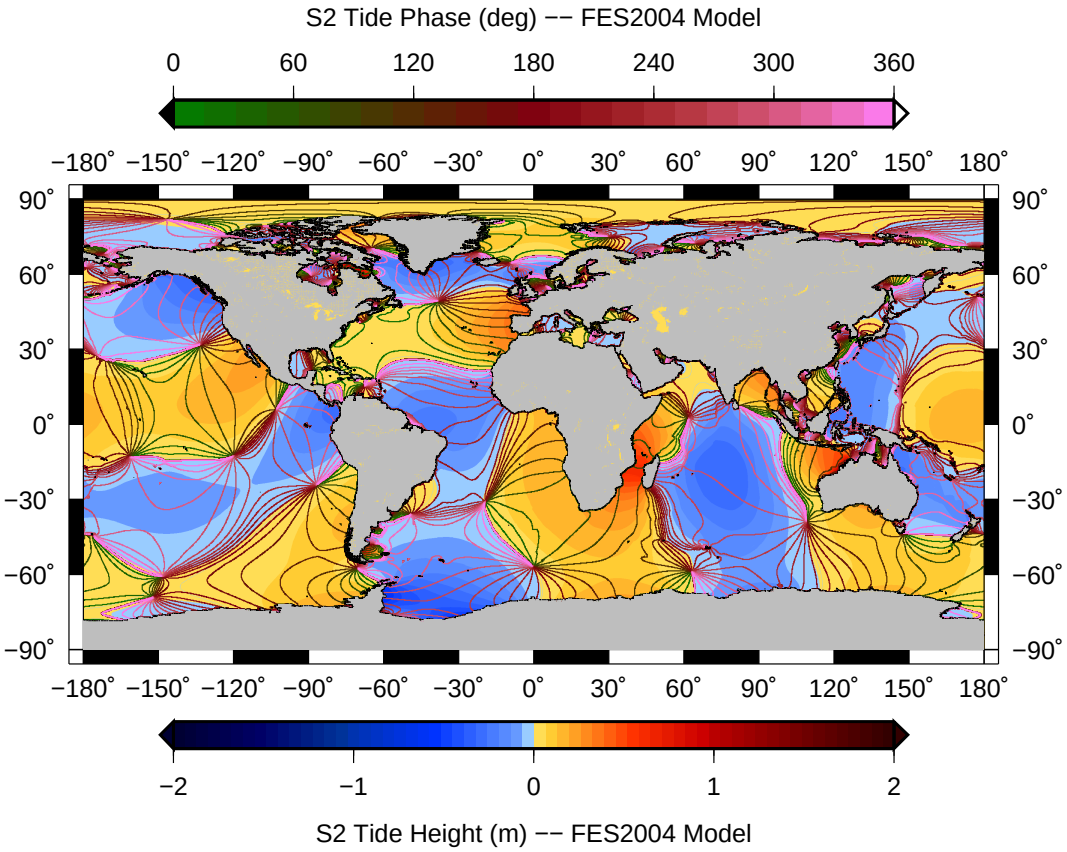

Figure 3.4. Cotidal and height chart of the S2 constituent using FES2004 ocean tide model.

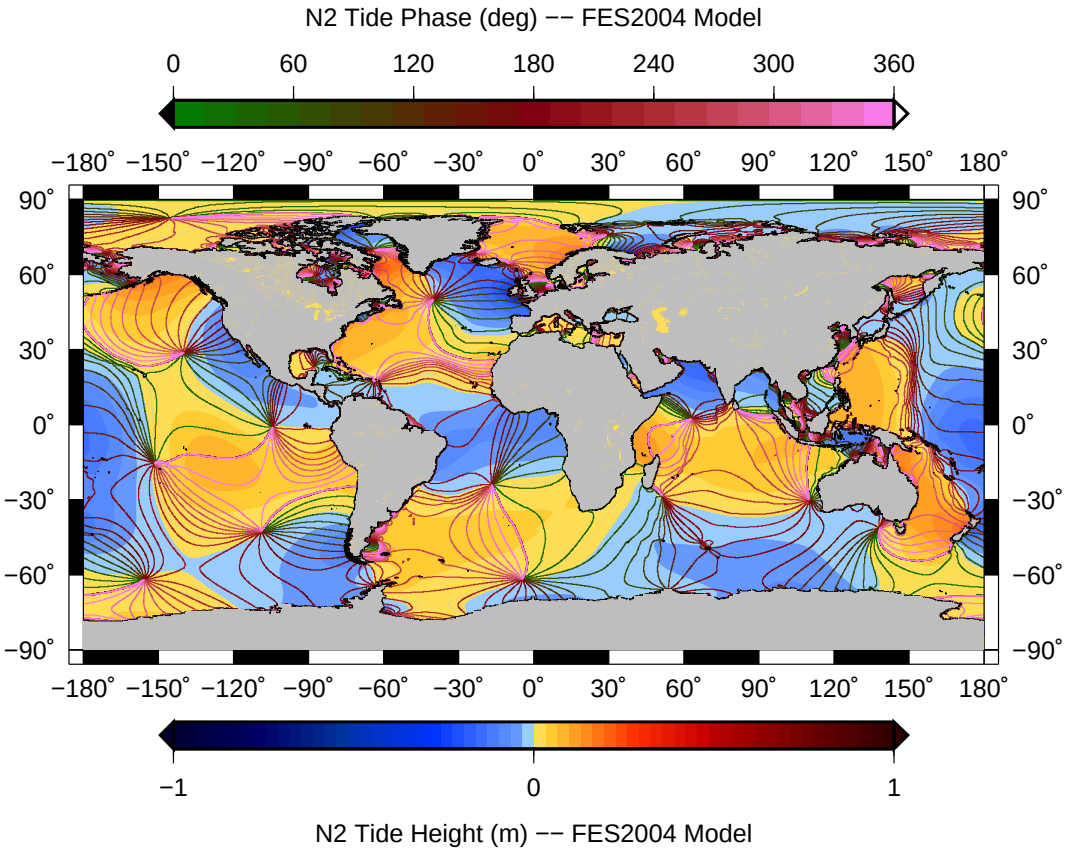

Figure 3.5. Cotidal and height chart of the N2 constituent using FES2004 ocean tide model.

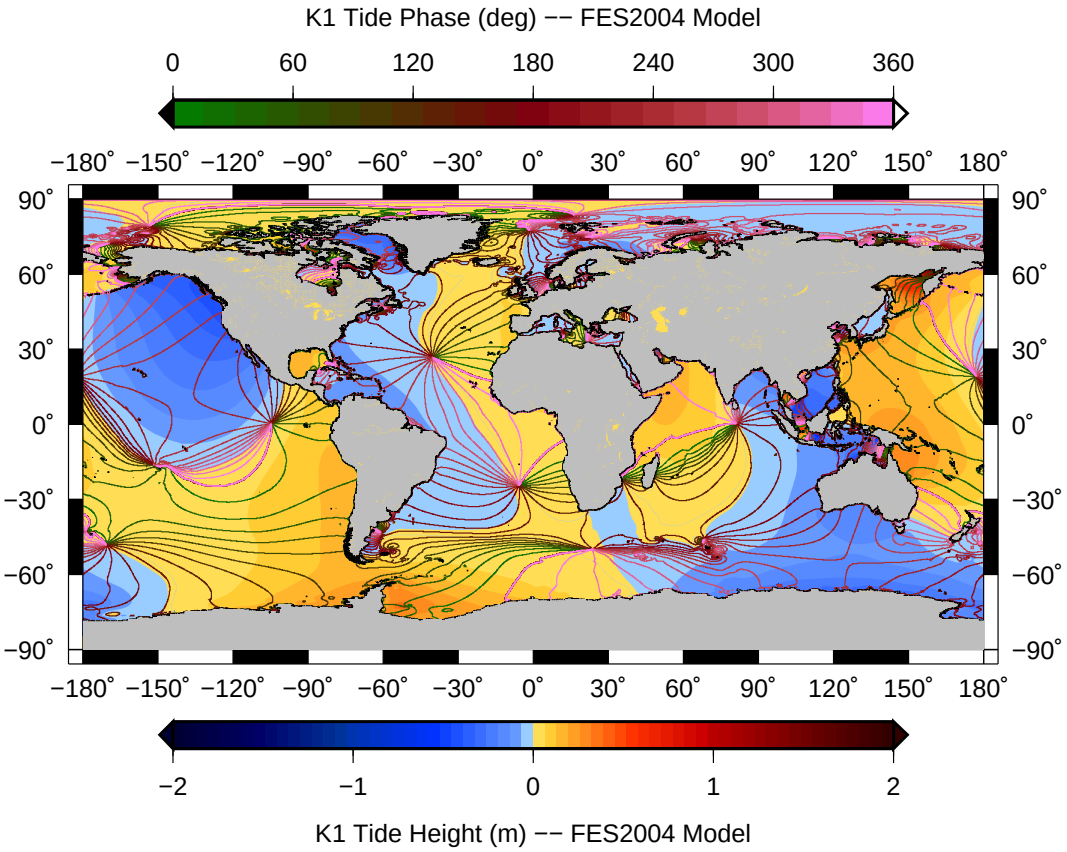

Figure 3.6. Cotidal and height chart of the K1 constituent using FES2004 ocean tide model.

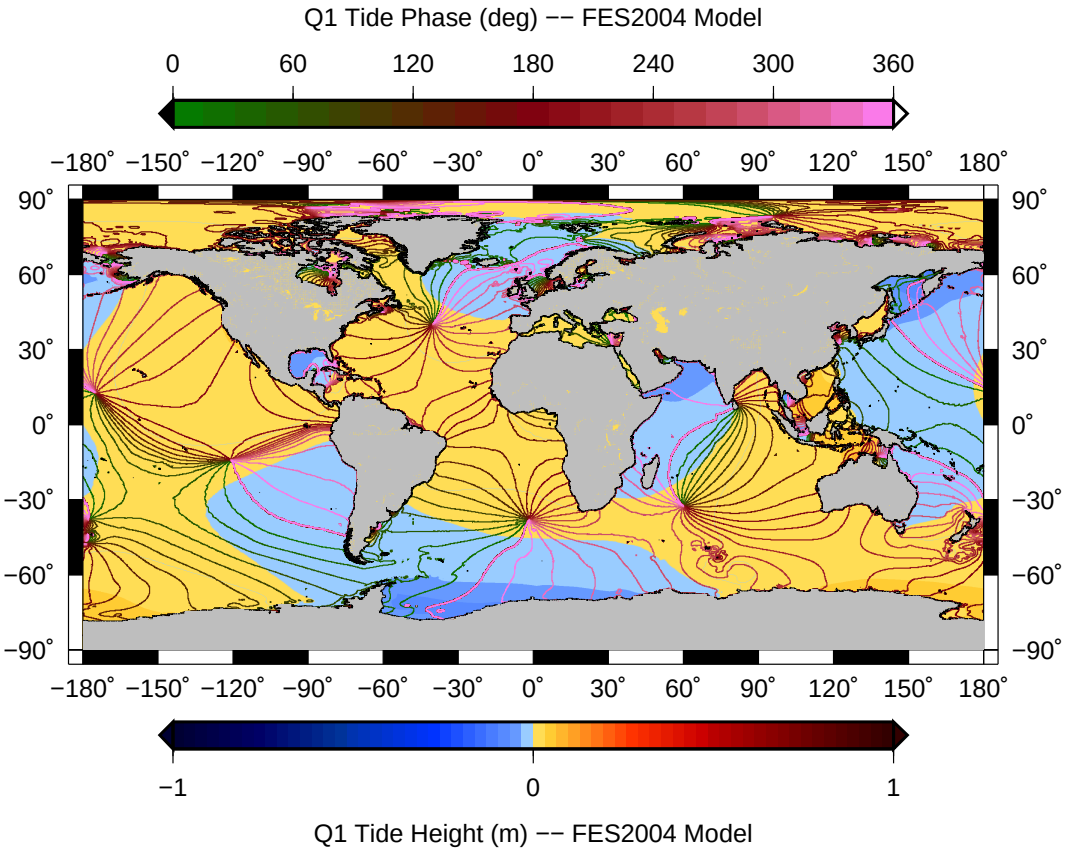

Figure 3.7. Cotidal and height chart of the Q1 constituent using FES2004 ocean tide model.

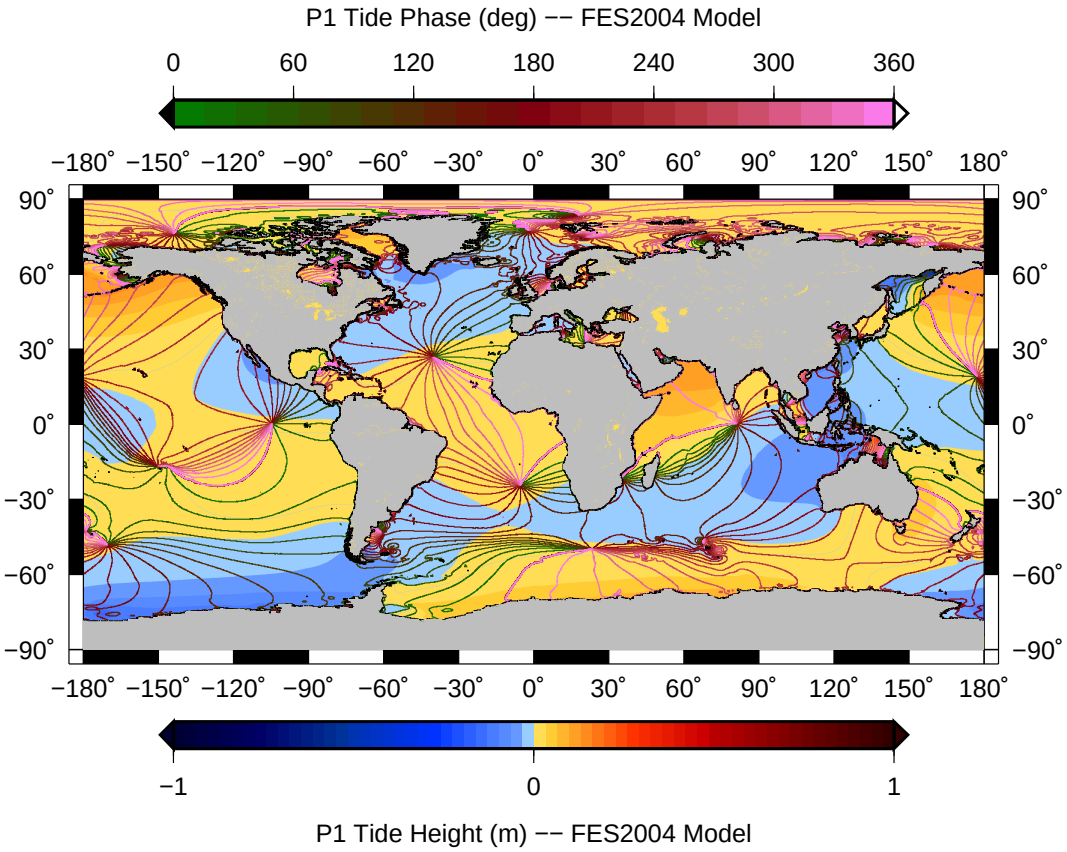

Figure 3.8. Cotidal and height chart of the P1 constituent using FES2004 ocean tide model.

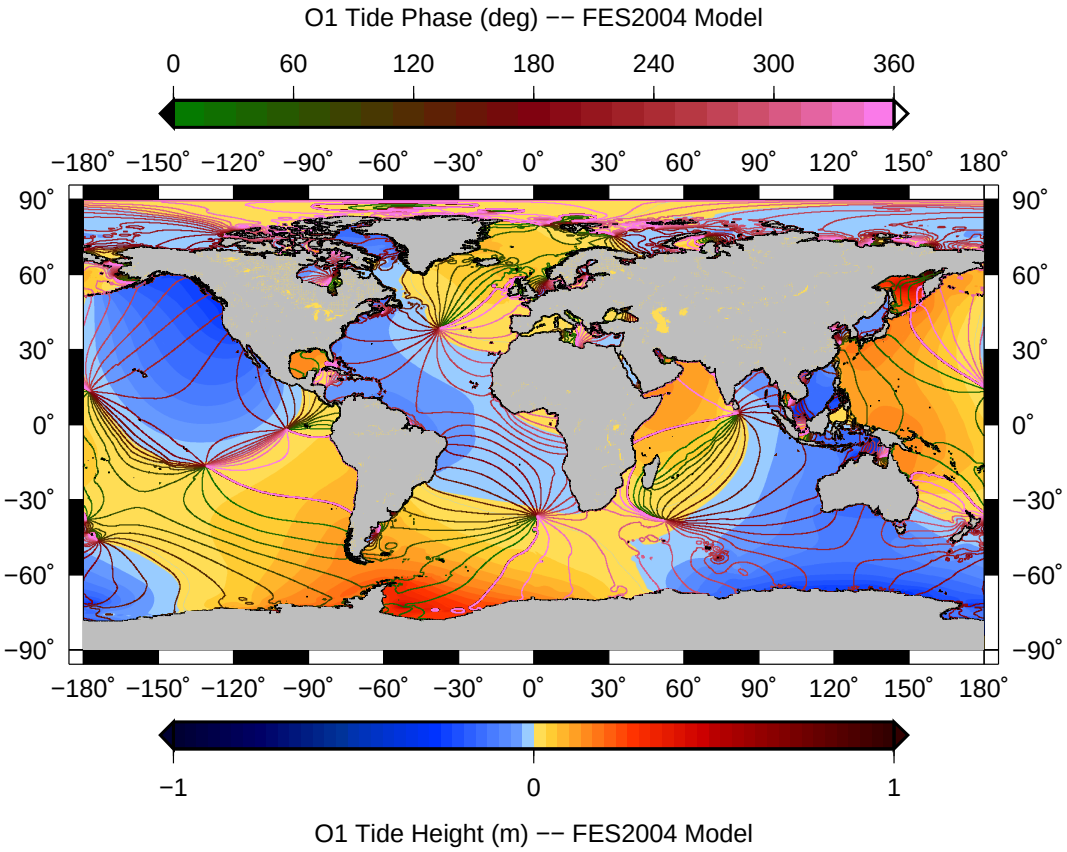

Figure 3.9. Cotidal and height chart of the O1 constituent using FES2004 ocean tide model.

Typically, an ocean tide model provides maps for only the largest tides or main waves. The spectrum of tidal geopotential perturbations can be completed by interpolation from the main waves to the smaller, secondary waves, using an assumption of linear variation of tidal admittance between closely spaced tidal frequencies (see the next Section).

3.3 The convolution formalism

In the convolution formalism, the ocean tide height field is obtained through a transfer function, or impulse response, from the tidal forcing in each tidal band. Munk and Cartwright (1966) first introduced the response method, taking advantage of the fact that the tidal admittance function is generally smooth inside each tidal band, in the sense that it is assumed to be a slowly varying function of frequency. An orthonormalized formulation of the response method was developed by Groves and Reynolds (1975), improving convergence and stability of the representation.

3.3.1 The response method

Instead of the sum of hundreds of tidal constituents, the response method [92, Munk and Cartwright, 1966] represents the total tide height $\zeta(\phi,\lambda,t)$ at a given time and location as a sum of partial tide heights, each arising from a tidal band defined by the order m ($m=0,1,2$ corresponds respectively to long period, diurnal and semidiurnal band) and expressed as a convolution of the TGP coefficients $c_{nm}(t)$ with appropriate weights for each band $g_s^m(\phi,\lambda)$

$$\zeta(\phi,\lambda,t) = \mathrm{Re}\sum_{l,m}\sum_{s=-S}^{S} g_s^m(\phi,\lambda)c_{nm}(t+s\Delta t), \tag{3.101}$$

where convenient values are $\Delta t = 2$ days [92, Munk and Cartwright, 1966] for the time lag and $S=1$ ([31] Desai and Wahr, 1995) for the number of lag. The main advantage of this method arise from the fact that the response of the ocean to the TGP is linear inside each tidal band. To pass from the time domain to the frequency domain is sufficient to apply a Fourier transform to the impulse response $g_s^m(\phi,\lambda)$, obtaining the response of the ocean $G_{\mathbf{k}}(\phi,\lambda)$ at a particular frequency $\mathbf{k}$: this complex function, called tidal admittance, has the fundamental property of being a generally a smooth function in each tidal band and it is defined by

$$G_{\mathbf{k}}(\phi,\lambda) = \sum_{s=-S}^{S} g_s^m(\phi,\lambda)e^{-\mathrm{i}\,\dot{\Theta}_{\mathbf{k}}s\Delta t}. \tag{3.102}$$

The admittance related to a specified band can be used to select the tide height at a particular frequency inside that band as follows

$$\zeta_{\mathbf{k}}(\phi,\lambda,t) = \mathrm{Re}[G^*_{\mathbf{k}}(\phi,\lambda)c_{nm}(t)], \tag{3.103}$$

moreover the real and imaginary parts of $G_{\mathbf{k}}(\phi,\lambda) = X_{\mathbf{k}}(\phi,\lambda) + \mathrm{i}\,Y_{\mathbf{k}}(\phi,\lambda)$ are useful to calculate the in-phase and quadrature amplitudes ($Z_{ph\mathbf{k}}(\phi,\lambda)$,$Z_{qu\mathbf{k}}(\phi,\lambda)$) of the tide height $\zeta_{\mathbf{k}}(\phi,\lambda,t)$ (Eanes and Bettadpur, 1995)

$$Z_{ph\mathbf{k}}(\phi,\lambda) = (-1)^m H_{\mathbf{k}} X_{\mathbf{k}}(\phi,\lambda), \tag{3.104}$$

$$Z_{qu\mathbf{k}}(\phi,\lambda) = -(-1)^m H_{\mathbf{k}} Y_{\mathbf{k}}(\phi,\lambda), \tag{3.105}$$

allowing to determine respectively the amplitude and phase of the tidal constituent

$$Z_{\mathbf{k}}(\phi,\lambda) = \sqrt{Z_{ph\mathbf{k}}(\phi,\lambda)^2 + Z_{qu\mathbf{k}}(\phi,\lambda)^2}, \tag{3.106}$$

$$\Psi_{\mathbf{k}}(\phi,\lambda) = \arctan\left(\frac{Z_{qu\mathbf{k}}(\phi,\lambda)}{Z_{ph\mathbf{k}}(\phi,\lambda)}\right). \tag{3.107}$$

3.3.2 The orthotides

The orthotide representation, firstly proposed by ([51] Groves and Reynolds, 1975), is based on the response method, but with orthogonality properties. According to this method the ocean tide height $\zeta(\phi, \lambda, t)$ at an epoch t, latitude ϕ and longitude λ can be expressed as the real part of a linear combination of complex nearly orthogonal functions of time $\zeta_i^m(t)$, called orthotides, multiplied by complex coefficients $z_i^m(\phi, \lambda) = u_i^m(\phi, \lambda) - \mathrm{i}\, v_i^m(\phi, \lambda)$, called orthoweights, dependent on the geographic location and defined for each tidal band indicated by the order m

$$\zeta(\phi, \lambda, t) = \mathrm{Re} \sum_m \sum_{i=0}^{I} z_i^m(\phi, \lambda) \zeta_i^m(t), \tag{3.108}$$

where I is the maximum orthotide order. Ideally, the orthoweights add some benefits with respect to the simple weights of the response method, in particular they are independent from each others, their magnitude decreases with increasing orthotide order (convergence) and their values are unique (stability) (Alcock and Cartwright, 1978).

The complex orthotides $\zeta_i^m(t)$ are given by a convolution between the complex harmonic coefficients $c_{nm}(t) = a_{nm}(t) + \mathrm{i}\, b_{nm}(t)$ of the TGP and the complex orthotide constants $W_{i,s}^m = U_{i,s}^m + \mathrm{i}\, V_{i,s}^m$ (tabulated for each band by Groves and Reynolds, 1975)

$$\zeta_i^m(t) = \sum_{s=-S}^{S} W_{i,s}^{m*} c_{nm}(t + s\Delta t), \tag{3.109}$$

where the symbol * denoted the complex conjugate.

It must be noticed that the orthotides $\zeta_i^m(t)$ are nearly orthogonal functions if averaged over a long time, in particular over at least 18.6 years, the period of the regression of the Moon's nodes. The reason for the orthotide basis to be only *nearly* orthonormal is that the fundamental astronomical frequencies appearing in the forcing function $c_{nm}(t)$ are incommensurable.

By substituting the equation (3.109) in (3.108) and thus multiplying the orthoweigths z_i^m for the orthotide constants $W_{i,s}^m$, the total tide height can be written analogously to the response method as a convolution sum

$$\zeta(\phi, \lambda, t) = \mathrm{Re} \sum_{l,m} \sum_{s=-S}^{S} w_s^m(\phi, \lambda) c_{nm}(t + s\Delta t), \tag{3.110}$$

where, for identity, $w_s^m(\phi, \lambda) = g_s^m(\phi, \lambda)$. For each tidal band m we can compute the spherical harmonic analysis of the convolution weights $w_s^m(\phi, \lambda)$ (Desai and Yuan, 2006) up to degree l and order p (not necessarily equal to the degree l and order m of the TGP development)

$$w_s^m(\phi, \lambda) = \sum_{l=0}^{\infty} \sum_{p=0}^{l} [\bar{D}_{lp}^m(s) \cos(p\lambda) + \bar{E}_{lp}^m(s) \sin(p\lambda)] \tag{3.111}$$

$$\cdot \bar{P}_{lp}(\sin\phi), \tag{3.112}$$

obtaining the complex fully-normalized spherical harmonic coefficients $\bar{D}_{lp}^m(s)$ and $\bar{E}_{lp}^m(s)$. The convolution between these harmonic coefficients and the tide-generating-potential coefficients $c_{nm}(t)$ produces the normalized harmonic coefficients $\bar{A}_{lp}^m(t)$ and $\bar{B}_{lp}^m(t)$ of the total ocean tide height in each tidal band (Desai and Yuan, 2006)

$$\begin{pmatrix} \bar{A}_{lp}^m(t) \\ \bar{B}_{lp}^m(t) \end{pmatrix} = \mathrm{Re} \sum_{s=-S}^{S} \begin{pmatrix} \bar{D}_{lp}^{m*}(s) \\ \bar{E}_{lp}^{m*}(s) \end{pmatrix} c_{nm}(t + s\Delta t). \tag{3.113}$$

Finally, the temporal variations of the Stokes coefficients of the geopotential due to ocean tides are given by the sum over contributions of each tidal band

$$\begin{pmatrix} \Delta\bar{C}_{lp}(t) \\ \Delta\bar{S}_{lp}(t) \end{pmatrix} = \sum_m \frac{4\pi G\rho_w}{g}\frac{1+k'_l}{2l+1}\begin{pmatrix} \bar{A}^m_{lp}(t) \\ \bar{B}^m_{lp}(t) \end{pmatrix}. \tag{3.114}$$

3.4 New algorithm to compute Groves and Reynolds orthotide coefficients

The orthotide coefficients of Groves and Reynolds (1975) are only available in the form of a table and no explicit algorithm was specified in the original paper. This contribution is an analysis of the orthotide approach and provides an explicit algorithm for the computation of the Groves and Reynolds basis functions.

A real orthotide $\zeta_n(t)$ of order n and tidal species s (omitted for simplicity from now on) can be expressed as

$$\zeta_n(t) = \sum_{k=-K}^{K} [U_{nk}a(t+k\Delta t) + V_{nk}b(t+k\Delta t)], \tag{3.115}$$

where $a(t+k\Delta t)$ and $b(t+k\Delta t)$ are the real and imaginary parts of the tide-generating potential coefficients of tidal species s and U_{nk} and V_{nk} are the *orthotide coefficients.* This equation, together with the orthonormality constraints

$$\langle \zeta_n(t)\zeta_m(t)\rangle = \delta_{nm}, \tag{3.116}$$

are the defining equations for the orthotides. The angle bracket operator $\langle\rangle$ is the time average operator.

The determination of the orthotide coefficients is based on the solution of a set of systems of equations like (3.116). The strategy is reminiscent of the Gram-Schmidt process of orthonormalization of a set of functions.

The analysis carried out in Appendix A shows that the maximum lag index K is a free parameter and its effective value is a function K_n of the orthotide order n given by

$$K_n = \lfloor (n+2)/4 \rfloor. \tag{3.117}$$

The Appendix A also shows that the number of non-zero orthotide coefficients at order n is

$$N_e = \left\lfloor \frac{n}{2} \right\rfloor + 1, \tag{3.118}$$

while the number of coefficients U_{nk} and the number of coefficients V_{nk} are given respectively by

$$N_U = \left\lfloor \frac{n+6}{4} \right\rfloor, \tag{3.119}$$

$$N_V = N_e - N_U. \tag{3.120}$$

The orthotide coefficients are then obtained as the solution of systems of $(n+1)$ equations the form

$$\begin{aligned} \delta_{nm} = \sum_{k=-K_n}^{K_n}\sum_{l=-K_m}^{K_m} & [(U_{nk}U_{ml} + V_{nk}V_{ml})\psi_{k-l} \\ & + (V_{nk}U_{ml} - U_{nk}V_{ml})\chi_{k-l}], \end{aligned} \tag{3.121}$$

successively for $n = 0, 1, ...$

Moreover, as shown in Appendix A, only even-order coefficients need be computed, and, among other things, that the symmetry relations

$$U_{n,-k} = (-1)^n U_{n,k}, \tag{3.122}$$
$$V_{n,-k} = -(-1)^n V_{n,k}. \tag{3.123}$$

hold. This implies that the orthotide (3.115) can now be written as

$$\begin{aligned}\zeta_n(t) &= U_{n0}a(t) + V_{n0}b(t) \\ &\quad + \sum_{k=1}^{K_n} U_{nk}\left[a(t+k\Delta t) + (-1)^n a(t-k\Delta t)\right] \\ &\quad + \sum_{k=1}^{K_n} V_{nk}\left[b(t+k\Delta t) - (-1)^n b(t-k\Delta t)\right].\end{aligned} \tag{3.124}$$

If we now also restrict both n and m to be even, system (3.121) takes the form

$$\begin{aligned}\delta_{nm} = {} & U_{n0}U_{m0}\psi_0 \\ & + \sum_{k=1}^{K_n} 2U_{m0}(U_{nk}\psi_k + V_{nk}\chi_k) \\ & + \sum_{l=1}^{K_m} 2U_{n0}(U_{ml}\psi_l + V_{ml}\chi_l) \\ & + \sum_{k=1}^{K_n}\sum_{l=1}^{K_m}[2U_{nk}U_{ml}(\psi_{k-l} + \psi_{k+l}) \\ & \qquad + 2V_{nk}V_{ml}(\psi_{k-l} - \psi_{k+l}) \\ & \qquad + 2U_{nk}V_{ml}(\chi_{k+l} - \chi_{k-l}) \\ & \qquad + 2V_{nk}U_{ml}(\chi_{k+l} + \chi_{k-l})].\end{aligned} \tag{3.125}$$

These are the N_e equations obtained for given n by letting m vary from 0 to n with step 2. In this context we will refer to m as the *secondary order.*

We can further proceed to discard the coefficients V_{iK_i} that have been eliminated by the analysis of Appendix B. Then the previous equation, restricted to m varying from 0 to $n-2$ with step 2, writes as

$$\begin{aligned}& U_{n0}U_{m0}\psi_0 + \sum_{l=1}^{K_m} 2U_{n0}U_{ml}\psi_l \\ & \quad + \sum_{l=1}^{N_{Vm}} 2U_{n0}V_{ml}\chi_l + \sum_{k=1}^{K_n} 2U_{m0}U_{nk}\psi_k \\ & \quad + \sum_{k=1}^{N_{Vn}} 2U_{m0}V_{nk}\chi_k \\ & \quad + \sum_{k=1}^{K_n}\sum_{l=1}^{K_m} 2U_{nk}U_{ml}(\psi_{k-l} + \psi_{k+l}) \\ & \quad + \sum_{k=1}^{N_{Vn}}\sum_{l=1}^{N_{Vm}} 2V_{nk}V_{ml}(\psi_{k-l} - \psi_{k+l})\end{aligned} \tag{3.126}$$

$$
\begin{aligned}
&+\sum_{k=1}^{K_n}\sum_{l=1}^{N_{V_m}} 2U_{nk}V_{ml}(\chi_{k+l}-\chi_{k-l})\\
&+\sum_{k=1}^{N_{V_n}}\sum_{l=1}^{K_m} 2V_{nk}U_{ml}(\chi_{k+l}+\chi_{k-l})=0,
\end{aligned}
$$

where N_{V_i} is the number of V coefficients that can be determined for even orthotide order i. In the particular case $n=m$, equation (3.125) simplifies instead to

$$
\begin{aligned}
&U_{n0}^2\psi_0+\sum_{k=1}^{K_n} 4U_{n0}U_{nk}\psi_k+\sum_{k=1}^{N_{V_n}} 4U_{n0}V_{nk}\chi_k\\
&+\sum_{k=1}^{K_n}\sum_{l=1}^{K_n} 2U_{nk}U_{nl}(\psi_{k-l}+\psi_{k+l})\\
&+\sum_{k=1}^{N_{V_n}}\sum_{l=1}^{N_{V_n}} 2V_{nk}V_{nl}(\psi_{k-l}-\psi_{k+l})\\
&+\sum_{k=1}^{K_n}\sum_{l=1}^{N_{V_n}} 2U_{nk}V_{nl}(\chi_{k+l}-\chi_{k-l})\\
&+\sum_{k=1}^{N_{V_n}}\sum_{l=1}^{K_n} 2V_{nk}U_{nl}(\chi_{k+l}+\chi_{k-l})=1.
\end{aligned}
\tag{3.127}
$$

The algebraic system formed by the $N_e-1=\lfloor n/2\rfloor$ equations (3.126) and the single equation (3.127) can now be solved to determine the orthotide coefficients at order n.

We proceed as follows. Rewrite Equation (3.126) by collecting each of the $\lfloor n/2\rfloor$ orthotide coefficients U_{n0}, U_{n1}, V_{n1}, U_{n2}, V_{n2}, ..., U_{nK_n}, $[V_{nK_n}]$.[3] Then

$$
\begin{aligned}
&U_{n0}\Big(U_{m0}\psi_0+\sum_{l=1}^{K_m} 2U_{ml}\psi_l+\sum_{l=1}^{N_{V_m}} 2V_{ml}\chi_l\Big)\\
&+U_{n1}\Big(2U_{m0}\psi_1+\sum_{l=1}^{K_m} 2U_{ml}(\psi_{1-l}+\psi_{1+l})\\
&+\sum_{l=1}^{N_{V_m}} 2V_{ml}(\chi_{1+l}-\chi_{1-l})\Big)\\
&+V_{n1}\Big(2U_{m0}\chi_1+\sum_{l=1}^{N_{V_m}} 2V_{ml}(\psi_{1-l}-\psi_{1+l})\\
&+\sum_{l=1}^{K_m} 2U_{ml}(\chi_{1-l}+\chi_{1+l})\Big)\\
&+U_{n2}\Big(2U_{m0}\psi_2+\sum_{l=1}^{K_m} 2U_{ml}(\psi_{2-l}+\psi_{2+l})\\
&+\sum_{l=1}^{N_{V_m}} 2V_{ml}(\chi_{2+l}-\chi_{2-l})\Big)\\
&+\quad\ldots
\end{aligned}
\tag{3.128}
$$

[3] Hereinafter, square brackets around a single quantity with index n indicate the empty set when the condition $n=4i-2$, for $i=1,2,...$ is met, according to the termination rule established in the analysis of Appendix B.

$$+ U_{nK}\Big(2U_{m0}\psi_K + \sum_{l=1}^{K_m} 2U_{ml}(\psi_{K-l} + \psi_{K+l}) + \sum_{l=1}^{N_{V_m}} 2V_{ml}(\chi_{K+l} - \chi_{K-l})\Big) + \Big[V_{nK}\Big(2U_{m0}\chi_K + \sum_{l=1}^{N_{V_m}} 2V_{ml}(\psi_{K-l} - \psi_{K+l}) + \sum_{l=1}^{K_m} 2U_{ml}(\chi_{K-l} + \chi_{K+l})\Big)\Big] = 0.$$

3.4.1 The computational algorithm

It is expedient at this point to introduce the auxiliary quantities A_m, B_{mk} and C_{mk} for order m defined as

$$A_m = U_{m0}\psi_0 + \sum_{l=1}^{K_m} 2U_{ml}\psi_l + \sum_{l=1}^{N_{V_m}} 2V_{ml}\chi_l, \tag{3.129}$$

$$B_{mk} = 2U_{m0}\psi_k + \sum_{l=1}^{K_m} 2U_{ml}(\psi_{k-l} + \psi_{k+l}) + \sum_{l=1}^{N_{V_m}} 2V_{ml}(\chi_{k+l} - \chi_{k-l}), \tag{3.130}$$

$$C_{mk} = 2U_{m0}\chi_k + \sum_{l=1}^{N_{V_m}} 2V_{ml}(\psi_{k-l} - \psi_{k+l}) + \sum_{l=1}^{K_m} 2U_{ml}(\chi_{k-l} + \chi_{k+l}), \tag{3.131}$$

so that the algebraic system (3.126) takes the simple form

$$A_m U_{n0} + \sum_{k=1}^{K_n} B_{mk}U_{nk} + \sum_{k=1}^{N_{V_n}} C_{mk}V_{nk} = 0, \tag{3.132}$$

for $m = 0, 2, ..., n-2$. Referring to Appendix B, it can be deduced that the blocks A_m are analytically zero except A_0, the blocks B_{mk} are analytically zero for $k = 1, 2..., \lfloor m/4 \rfloor$ and $m > 2$, the blocks C_{mk} are analytically zero for $k = 1, 2, ..., \lfloor (m-1)/4 \rfloor$ and $m > 4$.

At this point we consider U_{n0} as a parameter and each equation in (3.132) is solved for one of the $\lfloor n/2 \rfloor$ orthotide coefficients according to the sequence U_{n1}, V_{n1}, U_{n2}, V_{n2}, ..., U_{nK_n}, $[V_{nK_n}]$. This leads to writing the coefficients as

$$\begin{aligned}
U_{n1} &= U_{n1}\left(U_{n0}; V_{n1}, U_{n2}, V_{n2}, ..., U_{nK_n}, [V_{nK_n},]\right), \\
V_{n1} &= V_{n1}\left(U_{n0}; U_{n2}, V_{n2}, U_{n3}, ..., U_{nK_n}, [V_{nK_n},]\right), \\
U_{n2} &= U_{n2}\left(U_{n0}; V_{n2}, U_{n3}, V_{n3}, ..., U_{nK_n}, [V_{nK_n},]\right), \\
&\ldots = \ldots \\
U_{n,K_n-1} &= U_{n,K_n-1}\left(U_{n0}; V_{n,K_n-1}, U_{nK_n}, [V_{nK_n},]\right), \\
V_{n,K_n-1} &= V_{n,K_n-1}\left(U_{n0}; U_{nK_n}, [V_{nK_n},]\right), \\
U_{n,K_n} &= U_{n,K_n}\left(U_{n0}; [V_{nK_n},]\right),
\end{aligned} \tag{3.133}$$

$$V_{n,K_n} = [V_{n,K_n}(U_{n0})] .$$

The procedure that leads to this form calls for the expression of each coefficient of secondary order m^* to be immediately substituted into each subsequent occurrence of that coefficient in the expressions of coefficients of higher secondary orders $m > m^*$. This way the last expression can only depend on the single parameter U_{n0}. This leads to the general equations

$$U_{nk} = -T_k U_{n0} - \sum_{i=k+1}^{K_n} P_{ik} U_{ni} - \sum_{i=k}^{N_{V_n}} Q_{ik} V_{ni}, \tag{3.134}$$

$$V_{nk} = -Z_k U_{n0} - \sum_{i=k+1}^{K_n} R_{ik} U_{ni} - \sum_{i=k+1}^{N_{V_n}} S_{ik} V_{ni}, \tag{3.135}$$

where the functions T_k, P_{ik}, Q_{ik}, Z_k, R_{ik}, S_{ik} contain the blocks A_m, B_{mk}, C_{mk} with the order m directly expressed as a function of the lag index k and are given recursively as

$$T_k = \frac{-Z_{k-1}}{\frac{B_{4(k-1),k}}{C_{4(k-1),k-1}} - R_{k,k-1}}, \tag{3.136}$$

$$P_{ik} = \frac{\frac{B_{4(k-1),i}}{C_{4(k-1),k-1}} - R_{i,k-1}}{\frac{B_{4(k-1),k}}{C_{4(k-1),k-1}} - R_{k,k-1}}, \qquad i \neq 0, \tag{3.137}$$

$$Q_{ik} = \frac{\frac{C_{4(k-1),i}}{C_{4(k-1),k-1}} - S_{i,k-1}}{\frac{B_{4(k-1),k}}{C_{4(k-1),k-1}} - R_{k,k-1}}, \qquad i \neq 0, \tag{3.138}$$

$$Z_k = \frac{-T_k}{\frac{C_{2(2k-1),k}}{B_{2(2k-1),k}} - Q_{kk}}, \tag{3.139}$$

$$R_{ik} = \frac{\frac{B_{2(2k-1),i}}{B_{2(2k-1),k}} - P_{ik}}{\frac{C_{2(2k-1),k}}{B_{2(2k-1),k}} - Q_{kk}}, \qquad i \neq 0, \tag{3.140}$$

$$S_{ik} = \frac{\frac{C_{2(2k-1),i}}{B_{2(2k-1),k}} - Q_{ik}}{\frac{C_{2(2k-1),k}}{B_{2(2k-1),k}} - Q_{kk}}, \qquad i \neq 0, \tag{3.141}$$

except when $k = 1$, where the first three functions T_1, P_{i1} and Q_{i1} are

$$T_1 = \frac{A_0}{B_{01}}, \tag{3.142}$$

$$P_{i1} = \frac{B_{0i}}{B_{01}}, \qquad i \neq 0, \tag{3.143}$$

$$Q_{i1} = \frac{C_{0i}}{B_{01}} \qquad i \neq 0. \tag{3.144}$$

Note that (3.134) and (3.135) must be interpreted as providing the ordered list (3.133), i.e., the two equations are to be used severally in pairs. Also note that Equations (3.136)-(3.141) define the functions T_k, P_{ik}, Q_{ik}, Z_k, R_{ik}, S_{ik} in the form of one-step, mixed recurrence relations.

The system (3.134) and (3.135) can be solved by back substitution from either U_{nK_n} or V_{nK_n}, as provided by the last equation, in terms of the parameter U_{n0}. In fact, back substitution shows that the parameter U_{n0} is actually a *scaling* parameter, thus providing a solution for the scaled coefficients

$$\tilde{U}_{nk} = U_{nk}/U_{n0}, \tag{3.145}$$

$$\tilde{V}_{nk} = V_{nk}/U_{n0}, \tag{3.146}$$

for $k = 1, 2, ..., K_n$. The system then takes the form

$$\tilde{U}_{nk} = -T_k - \sum_{i=k+1}^{K_n} P_{ik}\tilde{U}_{ni} - \sum_{i=k}^{N_{Vn}} Q_{ik}\tilde{V}_{ni}, \tag{3.147}$$

$$\tilde{V}_{nk} = -Z_k - \sum_{i=k+1}^{K_n} R_{ik}\tilde{U}_{ni} - \sum_{i=k+1}^{N_{Vn}} S_{ik}\tilde{V}_{ni}, \tag{3.148}$$

for $k = 1, 2, ..., K_n$ and can be solved by back substitution from the last equation (which provides the last of either $\tilde{U}_{nK_n}$ or $\tilde{V}_{nK_n}$), thus providing $[\tilde{V}_{nK_n}]$, $\tilde{U}_{nK_n}$, $\tilde{V}_{n,K_n-1}$, ..., for the ordered sequence $k = K_n, K_n - 1, ..., 1$ of the lag index.

Now substitute these quantities in Equation (3.127), which can then be used to solve for the parameter U_{n0} as

$$U_{n0} = \frac{1}{\sqrt{R_n}}, \tag{3.149}$$

where the radicand R_n is given by

$$\begin{aligned} R_n = \psi_0 &+ \sum_{k=1}^{K_n} 4\tilde{U}_{nk}\psi_k + \sum_{k=1}^{N_{Vn}} 4\tilde{V}_{nk}\chi_k \\ &+ \sum_{k=1}^{K_n}\sum_{l=1}^{K_n} 2\tilde{U}_{nk}\tilde{U}_{nl}(\psi_{k-l} + \psi_{k+l}) \\ &+ \sum_{k=1}^{N_{Vn}}\sum_{l=1}^{N_{Vn}} 2\tilde{V}_{nk}\tilde{V}_{nl}(\psi_{k-l} - \psi_{k+l}) \\ &+ \sum_{k=1}^{K_n}\sum_{l=1}^{N_{Vn}} 2\tilde{U}_{nk}\tilde{V}_{nl}(\chi_{k+l} - \chi_{k-l}) \\ &+ \sum_{k=1}^{N_{Vn}}\sum_{l=1}^{K_n} 2\tilde{V}_{nk}\tilde{U}_{nl}(\chi_{k+l} + \chi_{k-l}). \end{aligned} \tag{3.150}$$

In the final step, Equations (3.145) and (3.146) are used to determine the remaining coefficients U_{nk} and V_{nk} for $k = 1, 2, ..., K_n$.

3.4.2 Example - Orthotide coefficients of order 8

It is useful to clarify the computational procedure developed in the previous section through an example. Consider the case of order $n = 8$. In this case Equation (3.132), for $m = 0, 2, 4, 6$ and $K_8 = 2$, can be used to generate a sequence of the type described by (3.133) according to the associated procedure. This leads to the expressions

$$\begin{aligned} U_{81} &= -\frac{A_0}{B_{01}}U_{80} - \frac{C_{01}}{B_{01}}V_{81} - \frac{B_{02}}{B_{01}}U_{82} - \frac{C_{02}}{B_{01}}V_{82}, \\ V_{81} &= -\frac{-\frac{A_0}{B_{01}}}{\left(\frac{C_{21}}{B_{21}} - \frac{C_{01}}{B_{01}}\right)}U_{80} - \frac{\left(\frac{B_{22}}{B_{21}} - \frac{B_{02}}{B_{01}}\right)}{\left(\frac{C_{21}}{B_{21}} - \frac{C_{01}}{B_{01}}\right)}U_{82} \\ &\quad - \frac{\left(\frac{C_{22}}{B_{21}} - \frac{C_{02}}{B_{01}}\right)}{\left(\frac{C_{21}}{B_{21}} - \frac{C_{01}}{B_{01}}\right)}V_{82}, \end{aligned}$$

$$U_{82} = -\frac{-\frac{\frac{A_0}{B_{01}}}{\left(\frac{C_{21}}{B_{21}}-\frac{C_{01}}{B_{01}}\right)}}{\frac{B_{42}}{C_{41}}-\frac{\left(\frac{B_{22}}{B_{21}}-\frac{B_{02}}{B_{01}}\right)}{\left(\frac{C_{21}}{B_{21}}-\frac{C_{01}}{B_{01}}\right)}}U_{80} - \frac{\frac{C_{42}}{C_{41}}-\frac{\left(\frac{C_{22}}{B_{21}}-\frac{C_{02}}{B_{01}}\right)}{\left(\frac{C_{21}}{B_{21}}-\frac{C_{01}}{B_{01}}\right)}}{\frac{B_{42}}{C_{41}}-\frac{\left(\frac{B_{22}}{B_{21}}-\frac{B_{02}}{B_{01}}\right)}{\left(\frac{C_{21}}{B_{21}}-\frac{C_{01}}{B_{01}}\right)}}V_{82},$$

$$V_{82} = -\frac{-\frac{\frac{A_0}{B_{01}}}{\left(\frac{C_{21}}{B_{21}}-\frac{C_{01}}{B_{01}}\right)}}{\frac{B_{42}}{C_{41}}-\frac{\left(\frac{B_{22}}{B_{21}}-\frac{B_{02}}{B_{01}}\right)}{\left(\frac{C_{21}}{B_{21}}-\frac{C_{01}}{B_{01}}\right)}}U_{80}, \tag{3.151}$$
$$\frac{C_{62}}{B_{62}}-\frac{\frac{C_{42}}{C_{41}}-\frac{\left(\frac{C_{22}}{B_{21}}-\frac{C_{02}}{B_{01}}\right)}{\left(\frac{C_{21}}{B_{21}}-\frac{C_{01}}{B_{01}}\right)}}{\frac{B_{42}}{C_{41}}-\frac{\left(\frac{B_{22}}{B_{21}}-\frac{B_{02}}{B_{01}}\right)}{\left(\frac{C_{21}}{B_{21}}-\frac{C_{01}}{B_{01}}\right)}}$$

which exhibit a high degree of redundancy due to the presence of repeated blocks at successive lag indices. In fact, simpler expressions can be found either through the introduction of the auxiliary quantities (3.137)-(3.141), or more directly from Equations (3.134) and (3.135) as

$$\begin{aligned} U_{81} &= -T_1U_{80} - Q_{11}V_{81} - P_{21}U_{82} - Q_{21}V_{82}, \\ V_{81} &= -Z_1U_{80} - R_{21}U_{82} - S_{21}V_{82}, \\ U_{82} &= -T_2U_{80} - Q_{22}V_{82}, \\ V_{82} &= -Z_2U_{80}. \end{aligned} \tag{3.152}$$

At this point we can solve this system parametrically in terms of U_{80} by back substitution to yield

$$\begin{aligned} \tilde{U}_{81} &= -T_1 - Q_{11}\tilde{V}_{81} - P_{21}\tilde{U}_{82} - Q_{21}\tilde{V}_{82}, \\ \tilde{V}_{81} &= -Z_1 - R_{21}\tilde{U}_{82} - S_{21}\tilde{V}_{82}, \\ \tilde{U}_{82} &= -T_2 - Q_{22}\tilde{V}_{82}, \\ \tilde{V}_{82} &= -Z_2, \end{aligned} \tag{3.153}$$

which can also be directly obtained from (3.147) and (3.148). We can then substitute into Equation (3.150) to get

$$\begin{aligned} R_8 = \psi_0 &+ 4\tilde{U}_{81}\psi_1 + 4\tilde{U}_{82}\psi_2 + 4\tilde{V}_{81}\chi_1 + 4\tilde{V}_{82}\chi_2 \\ &+ 2\tilde{U}_{81}^2(\psi_0+\psi_2) + 2\tilde{U}_{82}^2(\psi_0+\psi_4) \\ &+ 2\tilde{V}_{81}^2(\psi_0-\psi_2) + 2\tilde{V}_{82}^2(\psi_0-\psi_4) \\ &+ 4\tilde{U}_{81}\tilde{U}_{82}(\psi_1+\psi_3) + 4\tilde{V}_{81}\tilde{V}_{82}(\psi_1-\psi_3) \\ &+ 4\tilde{U}_{81}\tilde{V}_{82}(\chi_3+\chi_1) + 4\tilde{U}_{82}\tilde{V}_{81}(\chi_3-\chi_1) \\ &+ 4\tilde{U}_{81}\tilde{V}_{81}\chi_2 + 4\tilde{U}_{82}\tilde{V}_{82}\chi_4. \end{aligned} \tag{3.154}$$

Now the first coefficient U_{80} can be computed from (3.149) as $U_{80} = 1/\sqrt{R_8}$. Finally the remaining four coefficients are computed from Equations (3.145) and (3.146) as

$$\begin{aligned} U_{81} &= \tilde{U}_{81}U_{80}, \\ V_{81} &= \tilde{V}_{81}U_{80}, \\ U_{82} &= \tilde{U}_{82}U_{80}, \\ V_{82} &= \tilde{V}_{82}U_{80}. \end{aligned} \tag{3.155}$$

3.4.3 Orthotide coefficients to order 50

The algorithm developed to recompute the orthotide coefficients U_{nk} and V_{nk} has been implemented adopting a double precision for the floating point variables. Moreover, an orthonormality test has been performed to verify to which tolerance $\sigma_n m$ the equations (3.126) and (3.127) are satisfied up to a maximum orthotide order $N_{max} = 50$, using the orthotide coefficients determined with our algorithm.

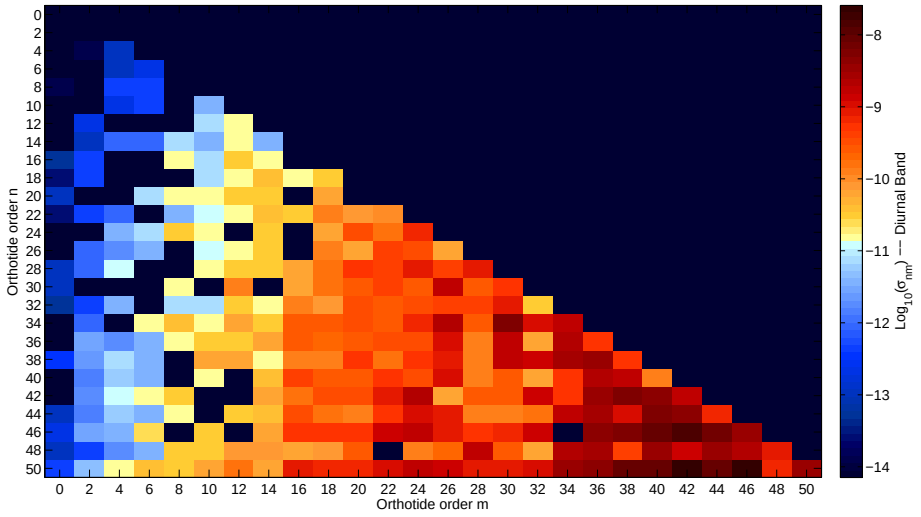

Figure 3.10. Logarithm of the error in the orthonormality test for products of diurnal even-order orthotides up to order 50.

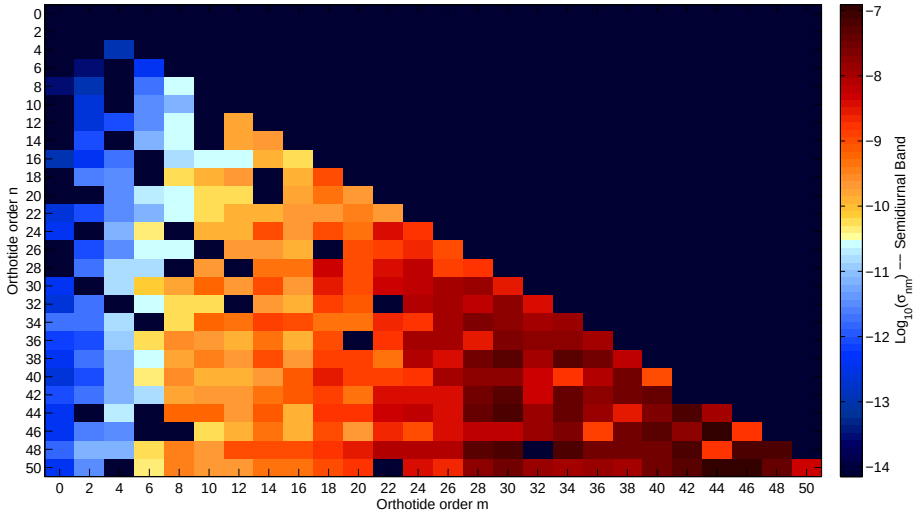

Figure 3.11. Logarithm of the error in the orthonormality test for products of semidiurnal even-order orthotides up to order 50.

First of all, the mean displaced products of the TGP coefficients have been recomputed adopting KSM03 tidal potential catalogue [69, Kudryavtsev, 2004], giving 28806 tidal constituents in HW95 normalization [?, Hartmann and Wenzel, 1995]. For this application, constituents with maximum degree p = 3 have been considered, among which 10885 are diurnal and 9539 are semidiurnal. The numerical results obtained from the computation of the mean displaced prod-

ucts are shown for the diurnal and semidiurnal bands in Table 1, with values in m^2 and rounded at the seventh significant digit.

Table 3.2. Diurnal and semidiurnal mean displaced products.

	Diurnal		Semidiurnal	
Lag k	ψ_k $(\mathbf{m}^{-1})$	χ_k $(\mathbf{m}^{-1})$	ψ_k $(\mathbf{m}^{-1})$	χ_k $(\mathbf{m}^{-1})$
0	0.1143485	0.0	0.2549553	0.0
1	0.1000269	-0.0267225	0.1807835	-0.1578598
2	0.0684872	-0.0311245	0.0139112	-0.2016354
3	0.0440198	-0.0091358	-0.1247702	-0.1048520
4	0.0438973	0.0232898	-0.1424478	0.0591261
5	0.0664914	0.0439981	-0.0345233	0.1783954
6	0.0945965	0.0406043	0.1231929	0.1785351
7	0.1082929	0.0176238	0.2287174	0.0634547
8	0.0978427	-0.0075126	0.2152325	-0.0923551
9	0.0697434	-0.0158238	0.0895000	-0.1886711
10	0.0429890	0.0007363	-0.0694914	-0.1592872
11	0.0368182	0.0327858	-0.1550701	-0.0174592
12	0.0564748	0.0585157	-0.1028699	0.1438360
13	0.0873914	0.0592547	0.0567200	0.2096154
14	0.1049500	0.0350730	0.2109848	0.1284920
15	0.0943468	0.0061111	0.2470939	-0.0418996
16	0.0632173	-0.0037733	0.1408460	-0.1773707
17	0.0347388	0.0134425	-0.0276157	-0.1843071
18	0.0284198	0.0449687	-0.1407011	-0.0651586
19	0.0463054	0.0688428	-0.1275794	0.0944714
20	0.0736908	0.0700231	-0.0029755	0.1903551
21	0.0903473	0.0494317	0.1507509	0.1635363
22	0.0836233	0.0224461	0.2353162	0.0314921
23	0.0565167	0.0090283	0.1940042	-0.1222688
24	0.0264741	0.0205810	0.0489067	-0.1958639
25	0.0142857	0.0510131	-0.1058212	-0.1342977
26	0.0287465	0.0793608	-0.1615129	0.0263523
27	0.0583619	0.0847097	-0.0735905	0.1749326
28	0.0788603	0.0632730	0.0980785	0.2029581
29	0.0725655	0.0325462	0.2292370	0.0892456
30	0.0431072	0.0171712	0.2266357	-0.0821998
31	0.0117786	0.0288222	0.0975010	-0.1894437
32	-0.0002620	0.0582372	-0.0640035	-0.1636997
33	0.0126984	0.0842585	-0.1504563	-0.0295939
34	0.0388940	0.0896280	-0.1102381	0.1220352
35	0.0583872	0.0717034	0.0279525	0.1946226
36	0.0559964	0.0433609	0.1760089	0.1414443
37	0.0310607	0.0249056	0.2372744	-0.0065104
38	-0.0011210	0.0307941	0.1661635	-0.1541010
39	-0.0187223	0.0584787	0.0046657	-0.1988349
40	-0.0094706	0.0883754	-0.1370553	-0.1036557
41	0.0185199	0.0978098	-0.1559570	0.0681095
42	0.0418485	0.0793484	-0.0358008	0.1933618
43	0.0404604	0.0475282	0.1366140	0.1816770

Table 3.2 – Continued from previous page

	Diurnal		Semidiurnal	
Lag k	ψ_k ($\mathbf{m}^{-1}$)	χ_k ($\mathbf{m}^{-1}$)	ψ_k ($\mathbf{m}^{-1}$)	χ_k ($\mathbf{m}^{-1}$)
44	0.0139775	0.0270259	0.2376658	0.0443857
45	-0.0188116	0.0326615	0.2003948	-0.1182421
46	-0.0357635	0.0589241	0.0573575	-0.1957011
47	-0.0276524	0.0861275	-0.0923376	-0.1423031
48	-0.0029309	0.0953453	-0.1528841	0.0021151
49	0.0193326	0.0804811	-0.0876962	0.1440920
50	0.0218727	0.0515142	0.0625617	0.1925220

The orthotide coefficients recomputed with our algorithm up to order $n = 50$ are listed in Table **??** for both diurnal and semidiurnal band, with numerical values up to the seventh significant digit in m^{-1}.

Figure 3.10 and Figure 3.11 illustrate the logarithm of the errors obtained in testing the orthonormality relation δ_{nm} for products of even-order orthotides up to order 50. It can be noticed that the orthonormality conditions are satisfied with a precision $\geq 10^{-9}$ for the diurnal band and $\geq 10^{-8}$ for the semidiurnal band up to orthotide order 24. Errors increase with the increase of the order n, because the orthotide coefficients of a specified order depend on the coefficients of the previous orders and so the numerical errors accumulate during the computation.

3.5 Global ocean tide models

Global ocean tide models are fundamental for many scientific disciplines. In particular, tides are considered as a noise or a correction to be removed from satellite gravity records and from the sea level observed by altimeters in order to study other oceanic phenomena such as ocean currents, wind driven water, water exchanges, etc. On the other hand, ocean tides represent a signal for applications concerning the evaluation of gravitational perturbations acting on an Earth orbiting satellite, for the accurate computation of ocean tide loading deformation and station displacements and to study the braking of the Earth's rotation by tidal dissipation into the oceans.

In general, it is possible to classify the global ocean tide models into three categories **??**Kantha, 2000]Kantha:

- models based on the analysis of altimetric data to extract various tidal signals,
- purely hydrodynamic models computed without any data assimilation,
- dynamical models with assimilation from observed tidal data (altimeter and coastal and pelagic tide gauges).

In Table 3.3 the main global ocean tide models are reported according to the previous classification, with their angular resolution.

A global ocean tide model can be compared with data from the global network of tide gauges at fixed stations, offering the only source of historical, precise, long-term accurate records of the ocean tide height. Major conclusions from tide gauge data have been that global sea level has risen approximately 10-25 cm during the past century.

Table 3.3. Classification of the main global ocean tide models and their angular resolution.

General Category	Ocean Tide Model	Angular Resolution
Analysis of altimetric data	CSR3.0 (Eanes and Bettadpur, 1995)	0.5°×0.5°
	CSR4.0 (Eanes and Bettadpur, 1999)	0.5°×0.5°
	GOT00 (Ray, 2000)	0.5°×0.5°
	GOT4.7 (Ray, 2000)	
	DTU10 (Cheng and Andersen, 2010)	0.125°×0.25°
	EOT11a (Bosch and Savcenko, 2011)	
	OSU12	
Purely hydrodynamic	FES95.2 (Le Provost et al., 1994)	0.5°×0.5°
Dynamical with data assimilation	ORI96 (Matsumoto et al., 1995)	0.5°×0.5°
	NAO99 (Matsumoto et al., 2000)	0.5°×0.5°
	SCW80 (Schwiderski, 1980)	1°×1°
	TPXO6 (Egbert and Erofeeva, 2002)	0.25°×0.25°
	TPXO7.2	0.25°×0.25°
	FES2004 (Lyard et al., 2006)	0.125°×0.25°
	FES2012	0.125°×0.25°

Chapter 4

Processing strategies of GOCE orbital data for ocean tide parameter estimation

Due to its 250 km altitude, GOCE is the most sensitive satellite to ocean tide perturbations and represents a test-bed for the application of classical orbit perturbation analysis methods to recover tidal parameters. Among the several processing strategies that can be adopted, the fundamental one is the direct numerical fully-dynamic approach, consisting in performing the fully-dynamic precise orbit determination of GOCE, accumulating the normal equations for each orbital arc and estimating the global ocean tide parameters through a multiarc solution.

The ESA's NAPEOS S/W system has been identified as the tool to perform this type of analysis, providing orbit determination/prediction and parameter estimation capabilities. However, it was necessary to upgrade the system with the implementation of the partial derivatives allowing for the ocean tide coefficient estimation process. As an alternative, a first-order approach is considered, consisting in determining the corrections to the tidal parameters of the reference model used through a least-square differential correction of the GPS phase observation residuals. The partial derivatives with respect to the ocean tide parameters according to the two main parameterizations are finally developed and reported.

4.1 The estimation problem

If at some time t_0 the satellite state vector $\mathbf{X}$ is known ($\mathbf{X}_0$) and the forces acting on the satellite are known, then the satellite equations of motion can be integrated to determine the state vector of the satellite at any future time. However, the initial state vector in never known exactly. Moreover, certain force models require physical parameters that are known only approximately, for example the satellite drag coefficient in aerodynamical forces, or the coefficients of the spherical harmonic expansion representation of the terrestrial gravity field. This is also the case with geophysical parameters that affect indirectly the equations of motion (like earth rotation and polar motion). Consequently, to determine the position of the satellite at a future time it is necessary that observations of the satellite are taken and used to obtain a better estimate of the satellite trajectory. The observational data, which will be subject to both systematic and random errors, will usually consist of measurements such as range, range-rate (Doppler), azimuth, elevation or some other observable quantity. These measurements have to be corrected with models which are imperfect (e.g. tropospheric correction) and are usually taken from stations whose earth-fixed coordinates are not exactly known.

The problem of determining the best estimate of the satellite state vector (and optionally other parameters and geophysical and geodetic quantities) is referred to as statistical orbit determination. Sometimes the main interest is focused on the estimation of the geophysical and

geodetic quantities themselves: this field is called space geodesy. Another variation of the problem is simulation and covariance analysis in which orbit determination strategies for a future mission are studied in terms of coverage, accuracy requirements and weighting of tracking data, orbit determination accuracy expectation, optimal arc-length, etc.

The problem can be generalized as follows: given an initial state vector at time t_0 and the initial values of parameters to be estimated (not necessarily at t_0), together with their a-priori covariance matrix, and given a set of real or simulated observations (not necessarily after t_0) also with their initial covariance matrix, find the "best" estimate of the state vector at a future time and of the rest of the parameters, together with an a-posteriori parameter and observation covariance matrix. So, in matrix notation the a-priori values are

$$\mathbf{X}_0 = \begin{bmatrix} x_0 \\ y_0 \\ z_0 \\ \dot{x}_0 \\ \dot{y}_0 \\ \dot{z}_0 \\ \alpha_1 \\ \vdots \\ \alpha_k \end{bmatrix}, \quad \mathbf{P}_0 = \begin{bmatrix} \sigma_{11}^2 & \sigma_{12} & \dots & \sigma_{1n} \\ \sigma_{21} & \sigma_{22}^2 & \dots & \sigma_{2n} \\ \vdots & \vdots & \ddots & \vdots \\ \sigma_{n1} & \sigma_{n2} & \dots & \sigma_{nn}^2 \end{bmatrix} \tag{4.1}$$

$$\mathbf{Y}_0 = \begin{bmatrix} y_1 \\ y_2 \\ \vdots \\ y_m \end{bmatrix}, \quad \mathbf{Q}_0 = \begin{bmatrix} \sigma_1^2 & 0 & \dots & 0 \\ 0 & \sigma_2^2 & \dots & 0 \\ \vdots & \vdots & \ddots & \vdots \\ 0 & 0 & \dots & \sigma_m^2 \end{bmatrix}, \tag{4.2}$$

$\mathbf{X}_0$ being the matrix of estimated parameters or extended initial state vector (n is the total number of estimated parameters). $\mathbf{P}_0$ is the a-priori covariance matrix of the parameters in $\mathbf{X}_0$. σ_{ii}^2 is the a-priori variance of parameter i, σ_{ij} is the a-priori covariance of parameters i and j, which is an indicator of their correlation or interdependence. For a mathematical definition of these statistical concepts see RD-12. $\mathbf{Y}$ is the matrix containing the observations (m is the total number of observations, $m > n$) and $\mathbf{Q}_0$ is the observation a-priori covariance matrix. We will assume here that the observations are a-priori not correlated, i.e. matrix $\mathbf{Q}_0$ is diagonal; this is not necessarily true, but it is in general not easy to find an a-priori estimation of the observation covariance. Let's call $\hat{X}(t)$ the best estimate of the extended state vector at time t, which is what we are trying to solve. By far the most widely-used criterion to obtain in practice the "best" estimate or solution is to minimize the sum of the square of the weighted residual observation errors, that is, the square of the difference between the observation and the expected value computed from an observation model (computed observation), multiplied by a factor (weight) according to the observation importance and expected accuracy. These methods are called least-square estimators, see RD-9, RD-20, RD-21, RD-25, and RD-29. In practice, observations are computed by evaluating the satellite state vector at the observation time and finding a geometric/kinematic relationship between the satellite position/velocity and the magnitude which is observed. We can then assume that the computed observations are a function of $\mathbf{X}(t)$, and define the residual observation vector as

$$\boldsymbol{\varepsilon} = \begin{bmatrix} y_1 - f_1\left(\hat{\mathbf{X}}(t_1)\right) \\ y_2 - f_2\left(\hat{\mathbf{X}}(t_2)\right) \\ \vdots \\ y_m - f_m\left(\hat{\mathbf{X}}(t_m)\right) \end{bmatrix} \tag{4.3}$$

The quantity to be minimized (i.e. the sum of the square of the weighted residual observation errors) is called the *loss function* and can be expressed as

$$J = \boldsymbol{\varepsilon}^T \mathbf{Q}_0^{-1} \boldsymbol{\varepsilon}, \tag{4.4}$$

$\mathbf{Q}_0^{-1}$ being the *weight matrix*. The weight matrix is necessary not only to give more importance to the most accurate observations but also to avoid adding magnitudes of different units (e.g. ranges and velocities). If the measurements are uncorrelated then $\mathbf{Q}_0^{-1}$ is diagonal

$$Q_0^{-1} = \begin{bmatrix} \sigma_1^{-2} & 0 & \dots & 0 \\ 0 & \sigma_2^{-2} & \dots & 0 \\ \vdots & \vdots & \ddots & \vdots \\ 0 & 0 & \dots & \sigma_m^{-2} \end{bmatrix} \tag{4.5}$$

The loss function described in Equation 4.4 can be modified to account for the uncertainties of the a-priori values of the estimated parameters (see RD-26). This leads to the definition

$$J = \boldsymbol{\varepsilon}^T \mathbf{Q}_0^{-1} \boldsymbol{\varepsilon} + \Psi, \tag{4.6}$$

where Ψ uses in some way (see below) information on the covariance of $\hat{\mathbf{X}}$. The problem is then to find the $\hat{\mathbf{X}}$ which minimize J. There are two major classes of least-squares estimators: batch and sequential (see RD-9, RD-20, RD-25, and RD-30). A *batch* estimator updates the *extended state vector* $\mathbf{X_0}$ (and optionally $\mathbf{P}_0$ and $\mathbf{Q}_0$) iteratively after a high enough number of observations (which define the estimation arc) has been collected after the epoch t_0. Once the process has converged to a best estimate of $\mathbf{X_0}$, $\hat{\mathbf{X}}_\mathbf{0}$, the satellite state vector can be propagated to any future time using as initial values the ones from $\hat{\mathbf{X}}_\mathbf{0}$. In a *sequential* estimator the observations are processed as soon as they are received, and the extended state vector $\mathbf{X}$ and its covariance matrix $\mathbf{P}$ are propagated/updated with every new observation or small set of observations. The main application of these estimators is the operational real-time orbit determination. Batch methods is described in the following Section.

4.2 Batch estimation

The objective is to find a best estimate of $\mathbf{X_0}$, (and optionally of $\mathbf{P_0}$ and $\mathbf{Q_0}$). We have seen that the computed observations can be expressed as a geometric/kinematic function of the satellite state vector at the time of the observation. As long as the satellite state vector can be propagated to any time from the initial state vector, the computed observations are a function of the time. The residual observation matrix can then be written as

$$\boldsymbol{\varepsilon}\left(\hat{\mathbf{X}}_0\right) = \begin{bmatrix} y_1 - f_1\left(\hat{\mathbf{X}}_0, t_1\right) \\ y_2 - f_2\left(\hat{\mathbf{X}}_0, t_2\right) \\ \vdots \\ y_m - f_m\left(\hat{\mathbf{X}}_0, t_m\right) \end{bmatrix} \tag{4.7}$$

Let's define in this case the loss function in Equation 4.6 as:

$$J\left(\hat{\mathbf{X}}_0\right) = \boldsymbol{\varepsilon}^T \mathbf{Q}_0^{-1} \boldsymbol{\varepsilon} + \hat{\mathbf{X}}_0^T \mathbf{P}_0^{-1} \hat{\mathbf{X}}_0, \tag{4.8}$$

where

$$\Delta\hat{\mathbf{X}}_0 = \hat{\mathbf{X}}_0 - \mathbf{X}_0. \tag{4.9}$$

An $\hat{\mathbf{X}}_0$ has to be found which minimizes the loss function $J\left(\hat{\mathbf{X}}_0\right)$. This is achieved by differentiating Equation 4.8 with respect to the estimated parameters $\hat{\mathbf{X}}_0$ and setting the resulting expression to zero. The problem has to be linearized in order to be solved. Let's assume that the difference between $\hat{\mathbf{X}}_0$ and $\mathbf{X}_0$ ($\Delta\hat{\mathbf{X}}_0$) is small (i.e. the initial values of the estimated parameters are a good enough approximation of the optimal ones). Then the computed observations can be expressed as their first order Taylor expansion around $\mathbf{X}_0$.

$$f_i\left(\hat{\mathbf{X}}_0, t_i\right) = f_i\left(\mathbf{X}_0, t_i\right) + \sum_{j=1}^{n} \frac{\partial f_i}{\partial \beta_j}\left(\hat{\beta}_j - \beta_j\right). \tag{4.10}$$

where the betas are all the estimated parameters, i.e. the elements of the $\mathbf{X}_0$ vector. The residuals can be expressed then as

$$\boldsymbol{\varepsilon}\left(\hat{\mathbf{X}}_0\right) = \begin{bmatrix} y_1 - f_1\left(\mathbf{X}_0, t_1\right) \\ y_2 - f_2\left(\mathbf{X}_0, t_2\right) \\ \vdots \\ y_m - f_m\left(\mathbf{X}_0, t_m\right) \end{bmatrix} - \mathbf{F}\left(\hat{\mathbf{X}}_0 - \mathbf{X}_0\right). \tag{4.11}$$

F is the *matrix of observation equation coefficients*, which contains the partial derivatives of the computed observations with respect to the estimated parameters

$$\mathbf{F} = \begin{bmatrix} \frac{\partial f_1}{\partial x_0} & \frac{\partial f_1}{\partial y_0} & \frac{\partial f_1}{\partial z_0} & \frac{\partial f_1}{\partial \dot{x}_0} & \frac{\partial f_1}{\partial \dot{y}_0} & \frac{\partial f_1}{\partial \dot{z}_0} & \frac{\partial f_1}{\partial \alpha_1} & \cdots & \frac{\partial f_1}{\partial \alpha_k} \\ \frac{\partial f_2}{\partial x_0} & \frac{\partial f_2}{\partial y_0} & \frac{\partial f_2}{\partial z_0} & \frac{\partial f_2}{\partial \dot{x}_0} & \frac{\partial f_2}{\partial \dot{y}_0} & \frac{\partial f_2}{\partial \dot{z}_0} & \frac{\partial f_2}{\partial \alpha_1} & \cdots & \frac{\partial f_2}{\partial \alpha_k} \\ \vdots & \vdots & \vdots & \vdots & \vdots & \vdots & \vdots & \ddots & \vdots \\ \frac{\partial f_m}{\partial x_0} & \frac{\partial f_m}{\partial y_0} & \frac{\partial f_m}{\partial z_0} & \frac{\partial f_m}{\partial \dot{x}_0} & \frac{\partial f_m}{\partial \dot{y}_0} & \frac{\partial f_m}{\partial \dot{z}_0} & \frac{\partial f_m}{\partial \alpha_1} & \cdots & \frac{\partial f_m}{\partial \alpha_k} \end{bmatrix}. \tag{4.12}$$

Substituting Equation 4.11 in Equation 4.8 and differentiating with respect to $\hat{\mathbf{X}}_0$ leads to the following iterative algorithm (called **normal equations**)

$$\hat{\mathbf{X}}_0^{k+1} = \hat{\mathbf{X}}_0^{k} + \left(\mathbf{P}_0^{-1} + \mathbf{F}^T\mathbf{Q}_0^{-1}\mathbf{F}\right)^{-1}\left(\Delta\mathbf{Y}^k + \mathbf{P}_0^{-1}\left(\mathbf{X}_0 - \hat{\mathbf{X}}_0^{k}\right)\right). \tag{4.13}$$

$\hat{\mathbf{X}}_0^k$ is the estimation on iteration k (equal to $\mathbf{X}_0$ on the first iteration), $\Delta\mathbf{Y}^k$ is the observation residual matrix calculated propagating $\hat{\mathbf{X}}_0^k$

$$\Delta\mathbf{Y}^k = \begin{bmatrix} y_1 - f_1\left(\hat{\mathbf{X}}_0^k, t_1\right) \\ y_2 - f_2\left(\hat{\mathbf{X}}_0^k, t_2\right) \\ \vdots \\ y_m - f_m\left(\hat{\mathbf{X}}_0^k, t_m\right) \end{bmatrix}. \tag{4.14}$$

The matrix

$$\mathbf{N} = \mathbf{P}_0^{-1} + \mathbf{F}^T\mathbf{Q}_0^{-1}\mathbf{F} \tag{4.15}$$

is called the **normal matrix**. It can be shown that the inverse of the normal matrix N is the best estimation of the covariance matrix of the estimated parameters, that is

$$\hat{\mathbf{P}}_0 = \mathbf{N}^{-1} = \left(\mathbf{P}_0^{-1} + \mathbf{F}^T\mathbf{Q}_0^{-1}\mathbf{F}\right)^{-1}. \tag{4.16}$$

4.3 Fully-dynamic approach: multiarc solution

To estimate ocean tide parameters assuring a clear separation of periodic effects, it necessary to process a long time period of data, so it is not possible to execute a single run of orbit determination. It is necessary to split the procedure into multiple similar procedures, also thanks to the linearity of the system of equations. In the multi-arc technique, the dynamical set of parameters is separated into two classes: arc-dependent parameters, which are constant along the duration of the single arc (such as the satellite state vector at the epoch or the orbital elements the epoch); arc-independent parameters, which are global constants along all the arcs (such as geodetic parameters, in particular tidal parameters).

The linearized observation equation is

$$\mathbf{Y} = A\mathbf{X} + \mathbf{e} \tag{4.17}$$

where $\mathbf{Y}$ is vector containing observations residuals, $\mathbf{X}$ is the vector containing the corrections to the complete state vector in order to nullify the discrepancy vector $\mathbf{e}$. The least-square estimate is

$$\hat{\mathbf{X}} = \left(\mathbf{A}^T\mathbf{W}\mathbf{A}\right)^{-1}\mathbf{A}^T\mathbf{W}\mathbf{Y} = \mathbf{N}^{-1}\mathbf{s}, \tag{4.18}$$

where

$$\mathbf{N} = \mathbf{A}^T\mathbf{W}\mathbf{A}, \tag{4.19}$$

$$\mathbf{s} = \mathbf{A}^T\mathbf{W}\mathbf{Y}, \tag{4.20}$$

This is the approach applied in a single arc solution with the orbital determination program BAHN when an unconstrained solution is required. If however Equation 4.17 is taken to represent the measurement equation of many single arc, a partitioning of the state vector into arc-independent parameters $\mathbf{X}_1$ and arc-dependent parameters

$$\mathbf{X}_2 = \{\mathbf{X}_{2,1}, \mathbf{X}_{2,2}, \ldots, \mathbf{X}_{2,n}\} \tag{4.21}$$

implies a measurement matrix having the structure

$$\mathbf{A} = \begin{bmatrix} \mathbf{A}_{11} & \mathbf{A}_{12,1} & \mathbf{0} & \ldots & \mathbf{0} \\ \mathbf{A}_{21} & \mathbf{0} & \mathbf{A}_{12,2} & \ldots & \mathbf{0} \\ \vdots & \vdots & \vdots & \ddots & \vdots \\ \mathbf{A}_{n1} & \mathbf{0} & \mathbf{0} & \ldots & \mathbf{A}_{12,n} \end{bmatrix} \tag{4.22}$$

giving a (symmetric) normal matrix $\mathbf{N}$ of the form

$$\mathbf{N} = \begin{bmatrix} \mathbf{N}_{11} & \mathbf{N}_{12,1} & \mathbf{N}_{12,1} & \ldots & \mathbf{N}_{12,n} \\ \mathbf{N}_{21,1} & \mathbf{N}_{22,1} & \mathbf{0} & \ldots & \mathbf{0} \\ \mathbf{N}_{21,2} & \mathbf{0} & \mathbf{N}_{22,2} & \ldots & \mathbf{0} \\ \vdots & \vdots & \vdots & \ddots & \vdots \\ \mathbf{N}_{21,n} & \mathbf{0} & \mathbf{0} & \ldots & \mathbf{N}_{22,n} \end{bmatrix} \tag{4.23}$$

This structure allows the solution to be written in the form of matrices of much smaller dimension. The estimate of the *arc-independent* parameters is ??Kaula, 1966]Kaula1966

$$\hat{\mathbf{X}}_1 = \mathbf{\Xi}\left(\mathbf{s}_1 - \sum_{j=1}^{n}\mathbf{N}_{12,j}\mathbf{N}_{22,j}^{-1}\mathbf{s}_{2,j}\right), \tag{4.24}$$

where $\boldsymbol{\Xi}$ is defined as

$$\boldsymbol{\Xi} = \left[\mathbf{N}_{11} - \sum_{j=1}^{n} \mathbf{N}_{12,j} \mathbf{N}_{22,j}^{-1} \mathbf{N}_{21,j} \right]^{-1} . \tag{4.25}$$

The estimate of the *arc-dependent* parameters of the k^{th} arc is

$$\hat{\mathbf{X}}_{2,k} = \mathbf{N}_{22,j}^{-1} \left(\mathbf{s}_{2,k} - \mathbf{N}_{21,k} \hat{\mathbf{X}}_1 \right). \tag{4.26}$$

The vector $\mathbf{s}$ in Equation 4.20 has been decomposed into

$$\mathbf{s}_1 = \sum_{j=1}^{n} \mathbf{A}_{j1}{}^T \mathbf{W}_j \mathbf{Y}_j, \tag{4.27}$$

$$\mathbf{s}_{2,k} = \mathbf{A}_{12,k}{}^T \mathbf{W}_k \mathbf{Y}_k, \tag{4.28}$$

where $\mathbf{Y}_j$ is the vector of measurements from the j^{th} arc. It is supposed that the weighted matrix $\mathbf{W}$ is selected such that $\mathbf{W} = \text{diag}\{\mathbf{W}_1, \ldots, \mathbf{W}_n\}$, where

$$\mathbf{W}_k^{-1} = D\{\mathbf{Y}_k\}. \tag{4.29}$$

Here $D\{\mathbf{Y}_k\}$ denotes the covariance of $\mathbf{Y}_k$, i.e. the expectation of $\mathbf{Y}_k \mathbf{Y}_k^T$

$$D\{\mathbf{Y}_k\} = E\{\mathbf{Y}_k \mathbf{Y}_k^T\} = \int \mathbf{Y}_k \mathbf{Y}_k^T p(\mathbf{Y}_k)\, d\mathbf{Y}_k, \tag{4.30}$$

where $p(\mathbf{Y}_k)$ is the probability density function of $\mathbf{Y}_k$. The joint covariance of two vectors $C\{\mathbf{Y}_k, \mathbf{Y}_l\}$ is defined in an analogous way. It is assumed that the measurements of each arc are uncorrelated with those of any other arc. It follows that

$$D\{\mathbf{s}_1\} = \sum_{j=1}^{n} \mathbf{A}_{j1}{}^T \mathbf{W}_j \mathbf{A}_{j1} = \mathbf{N}_{11} \tag{4.31}$$

$$C\{\mathbf{s}_{2,i}, \mathbf{s}_{2,j}\} = \mathbf{A}_{12,j}{}^T \mathbf{W}_j \mathbf{A}_{12,j} \delta_{ij} = \mathbf{N}_{22,j} \delta_{ij} \tag{4.32}$$

$$C\{\mathbf{s}_1, \mathbf{s}_{2,j}\} = \mathbf{A}_{j1}{}^T \mathbf{W}_j \mathbf{A}_{12,j} = \mathbf{N}_{12,j} \tag{4.33}$$

where $\delta_{ij} = 1$ if $i = j$ and $\delta_{ij} = 0$ otherwise. From Equations 4.24, 4.31 and 4.33, it can be seen that the covariance of the arc-independent parameters is given by

$$D\left\{\hat{\mathbf{X}}_1\right\} = \boldsymbol{\Xi}. \tag{4.34}$$

Moreover, since from Equations 4.24, 4.27 and 4.28

$$C\left\{\mathbf{s}_{2,k}, \hat{\mathbf{X}}_1\right\} = \left[\mathbf{N}_{12,k} - \mathbf{N}_{12,k} \mathbf{N}_{22,k}^{-1} \mathbf{N}_{22,k}\right]^T \boldsymbol{\Xi}^T = 0, \tag{4.35}$$

the covariance of the arc-dependent parameters of the k^{th} arc is

$$D\left\{\hat{\mathbf{X}}_{2,k}\right\} = \mathbf{N}_{22,k}^{-1} + \mathbf{N}_{22,k}^{-1} \mathbf{N}_{21,k}\, \boldsymbol{\Xi}\, \mathbf{N}_{21,k}^T \mathbf{N}_{22,k}^{-1}. \tag{4.36}$$

Finally, the joint covariance between the arc-independent parameters $\hat{\mathbf{X}}_1$ and the arc-dependent parameters of the k^{th} arc is

$$C\left\{\hat{\mathbf{X}}_1, \hat{\mathbf{X}}_{2,k}\right\} = -\boldsymbol{\Xi}\, \mathbf{N}_{21,k}^T \mathbf{N}_{22,k}^{-1}. \tag{4.37}$$

The FORTRAN program **MULTIARC** of NAPEOS has been modified to perform the calculation outlined in the Equations from 4.24 to 4.26 and 4.34, 4.34 and 4.37 for the solution and covariance of a selectable set of arc-dependent parameters for what concerns the ocean tides. In the following section the derivation of the partials computed for this implementation will be shown.

4.4 First-order approach: linear fit of GOCE GPS phase observation residuals

The GPS observables O (code pseudoranges, carrier phases, Doppler measurements) are generally non-linear functions of the state vectors $\mathbf{X}^t$ and $\mathbf{X}_r$, respectively of the transmitter (onboard the GPS satellite) and the receiver (onboard the LEO satellite), of kinematic parameters referring to the measure model and, implicitly, of dynamic parameters affecting the LEO satellite motion (Xu, 2003)

$$O = f(\mathbf{X}^t, \mathbf{X}_r, \delta t^t, \delta t_r, \delta_{ion}, \delta_{tro}, \delta_{tide}, \delta_{rel}, \delta_{mul}, N), \tag{4.38}$$

where the kinematic parameters are indicated and, in particular, δt^t and δt_r are respectively the clock errors of the transmitter and the receiver, δ_{ion} and δ_{tro} represent the ionospheric and tropospheric effects, δ_{tide} represents Earth tide and loading tide effects, δ_{rel} denotes relativistic effects, δ_{mul} denotes the multipath effects and N is the ambiguity.

Only if the force models are described perfectly by their dynamic parameters $\mathbf{P}$, at each instant t_i, the difference between the observations O_i and the computed quantities C_i will be zero, but this will never happen in practice, because the observations have errors and the models are inaccurate or incomplete, so that there will always be observation residuals $\Delta O_i = O_i - C_i \neq 0$.

If the observations ΔO_i are small, the non-linear problem can be approximated by a linear one and the observation functional O_i is expanded in a Taylor series up to the first order about the computed value C_i

$$O_i = C_i + \frac{\partial C_i}{\partial \mathbf{P}} \Delta \mathbf{P}, \tag{4.39}$$

where each observation is designed by subscript i.

We consider only GPS carrier phase observables ϕ_i because of their better resolution. The GPS phase residuals generated by NAPEOS with the reference force model represent our observations

$$O_i : \qquad \Delta\phi_i^{C/NAP} = \phi_i - \phi_i^{C/NAP}, \tag{4.40}$$

while the residuals generated by NAPEOS (or another software) with a different force model represent the computed observations

$$C_i : \qquad \Delta\phi_i^{C} = \phi_i - \phi_i^{C}. \tag{4.41}$$

Following the relation (4.39), we obtain our linearized observation equation

$$\Delta\phi_i^{C/NAP} = \Delta\phi_i^{C} + \frac{\partial \Delta\phi_i^{C}}{\partial \mathbf{P}} \Delta \mathbf{P} \tag{4.42}$$

that becomes

$$\Delta\phi_i^{C/NAP} = \Delta\phi_i^{C} + \frac{\partial (\phi_i - \phi_i^{C})}{\partial \mathbf{P}} \Delta \mathbf{P}, \tag{4.43}$$

where $\frac{\partial \phi_i}{\partial \mathbf{P}} = 0$, because the observables are constant. Finally, the linearized observation equation is

$$\Delta\phi_i^{C} = \Delta\phi_i^{C/NAP} + \frac{\partial \phi_i^{C}}{\partial \mathbf{P}} \Delta \mathbf{P} \tag{4.44}$$

and can be solved for the parameters $\Delta\mathbf{P}$ through a least-squares differential correction, in order to obtain $\Delta\phi_i^C = 0$. The corrections are then added to the reference tidal parameters $\mathbf{P}$ to obtain the first-order corrected parameters

$$\hat{\mathbf{P}} = \mathbf{P} + \Delta\mathbf{P}. \tag{4.45}$$

In equation (4.44), the partial derivatives of the computed phases with respect to the parameters must be expressed according to the chain rule as (Sansò & Rummel, 1989)

$$\frac{\partial \phi_i^{C}}{\partial \mathbf{P}} = \frac{\partial \phi_i^{C}}{\partial \mathbf{X}_r} \frac{\partial \mathbf{X}_r}{\partial \mathbf{P}}, \tag{4.46}$$

where $\mathbf{X}_r$ is the receiver state vector, because, in general, GPS observables do not depend explicitly on the dynamic parameters. In particular, the partials $\frac{\partial \phi_i^C}{\partial \mathbf{X}_r}$ represent the geometric part, while the partials $\frac{\partial \mathbf{X}_r}{\partial \mathbf{P}}$ represent the dynamic part.

The receiver state vector is defined by all the variables and the constant parameters describing the temporal variation of the dynamic system

$$\mathbf{X}_r = \begin{pmatrix} \mathbf{r} \\ \mathbf{v} \\ \mathbf{P} \end{pmatrix} \tag{4.47}$$

and its derivative as

$$\dot{\mathbf{X}}_r = \begin{pmatrix} \mathbf{v} \\ \mathbf{a} \\ \mathbf{0}_{q\times 1} \end{pmatrix}, \tag{4.48}$$

where $\mathbf{P}$ is a q-dimensional vector containing the dynamic parameters to be estimated, while $\mathbf{r}$, $\mathbf{v}$ and $\mathbf{a}$ are 3-dimensional vectors containing respectively position, velocity and acceleration of the receiver in the inertial geocentric system, so that the total dimension of the receiver state vector and of its derivative is $d = 6 + q$. In particular, the acceleration $\mathbf{a}$ is comprehensive of the entire adopted force model and can be expressed as the sum of different contributions

$$\mathbf{a} = \mathbf{a}_k + \mathbf{a}_p + \mathbf{a}_b + \mathbf{a}_{et} + \mathbf{a}_{ot} + \mathbf{a}_d + \mathbf{a}_s + \mathbf{a}_a, \tag{4.49}$$

where $\mathbf{a}_k$ is the keplerian acceleration, $\mathbf{a}_p$ is the perturbing part of the geopotential, $\mathbf{a}_b$ is the third-body acceleration, $\mathbf{a}_{et}$ and $\mathbf{a}_{ot}$ are terms due respectively to solid Earth tides and ocean tides, $\mathbf{a}_d$ represents the atmospheric drag, $\mathbf{a}_s$ is the solar radiation pressure acceleration and $\mathbf{a}_a$ is the Earth albedo pressure acceleration.

The partial derivatives $\frac{\partial \phi_i^C}{\partial \mathbf{X}_r}$, that are $\frac{\partial \phi_i^C}{\partial \mathbf{r}}$ and $\frac{\partial \phi_i^C}{\partial \mathbf{v}}$, are already implemented in NAPEOS and their numerical values can be printed on an output file.

On the other hand, the partials $\frac{\partial \mathbf{X}_r}{\partial \mathbf{P}}$ are called variational partials and are obtained integrating numerically the variational equations (Sansò & Rummel, 1989)

$$\frac{d}{dt}\left(\frac{\partial \mathbf{X}_r}{\partial \mathbf{P}}\right) = \frac{\partial \dot{\mathbf{X}}_r}{\partial \mathbf{P}} = \underbrace{\frac{\partial \dot{\mathbf{X}}_r}{\partial \mathbf{X}_r}\frac{\partial \mathbf{X}_r}{\partial \mathbf{P}}}_{\text{implicit}} + \underbrace{\left[\frac{\partial \dot{\mathbf{X}}_r}{\partial \mathbf{P}}\right]}_{\text{explicit}}, \tag{4.50}$$

which are within the numerical integration process of the state transition matrix $\mathbf{\Phi}(t, t_0)$

$$\dot{\mathbf{\Phi}}(t, t_0) = \mathbf{A}(t)\mathbf{\Phi}(t, t_0), \tag{4.51}$$

with initial conditions

$$\mathbf{\Phi}(t_0, t_0) = \mathbf{I}. \tag{4.52}$$

The matrix $\mathbf{A}(t)$, with dimension $d \times d$, contains the partial derivatives of the dynamic model and is explicitly defined as

$$\mathbf{A}(t) = \frac{\partial \dot{\mathbf{X}}_r}{\partial \mathbf{X}_r} = \begin{pmatrix} \frac{\partial \mathbf{v}}{\partial \mathbf{r}} & \frac{\partial \mathbf{v}}{\partial \mathbf{v}} & \frac{\partial \mathbf{v}}{\partial \mathbf{P}} \\ \frac{\partial \mathbf{a}}{\partial \mathbf{r}} & \frac{\partial \mathbf{a}}{\partial \mathbf{v}} & \frac{\partial \mathbf{a}}{\partial \mathbf{P}} \\ \mathbf{0}_{q\times 3} & \mathbf{0}_{q\times 3} & \mathbf{0}_{q\times q} \end{pmatrix} = \begin{pmatrix} \mathbf{0}_{3\times 3} & \mathbf{I}_{3\times 3} & \mathbf{0}_{3\times q} \\ A_{21} & A_{22} & A_{23} \\ \mathbf{0}_{q\times 3} & \mathbf{0}_{q\times 3} & \mathbf{0}_{q\times q} \end{pmatrix}. \tag{4.53}$$

The state transition matrix, having dimension $d \times d$, is defined as

$$\mathbf{\Phi}(t,t_0) = \frac{\partial \mathbf{X}_r}{\partial \mathbf{X}_{0r}} = \begin{pmatrix} \frac{\partial \mathbf{r}}{\partial \mathbf{r}_0} & \frac{\partial \mathbf{r}}{\partial \mathbf{v}_0} & \frac{\partial \mathbf{r}}{\partial \mathbf{P}_0} \\ \frac{\partial \mathbf{v}}{\partial \mathbf{r}_0} & \frac{\partial \mathbf{v}}{\partial \mathbf{v}_0} & \frac{\partial \mathbf{v}}{\partial \mathbf{P}_0} \\ \frac{\partial \mathbf{P}}{\partial \mathbf{r}_0} & \frac{\partial \mathbf{P}}{\partial \mathbf{v}_0} & \frac{\partial \mathbf{P}}{\partial \mathbf{P}_0} \end{pmatrix} = \begin{pmatrix} \Phi_{11} & \Phi_{12} & \Phi_{13} \\ \Phi_{21} & \Phi_{22} & \Phi_{23} \\ \mathbf{0}_{q\times 3} & \mathbf{0}_{q\times 3} & \mathbf{I}_{q\times q} \end{pmatrix} \tag{4.54}$$

where $\mathbf{X}_{0r}$ is the receiver initial state vector.

The system (4.51) is written explicitly as

$$\begin{pmatrix} \dot{\Phi}_{11} & \dot{\Phi}_{12} & \dot{\Phi}_{13} \\ \dot{\Phi}_{21} & \dot{\Phi}_{22} & \dot{\Phi}_{23} \\ \dot{\Phi}_{31} & \dot{\Phi}_{32} & \dot{\Phi}_{33} \end{pmatrix} = \begin{pmatrix} \mathbf{0}_{3\times 3} & \mathbf{I}_{3\times 3} & \mathbf{0}_{3\times q} \\ A_{21} & A_{22} & A_{23} \\ \mathbf{0}_{q\times 3} & \mathbf{0}_{q\times 3} & \mathbf{0}_{q\times q} \end{pmatrix} \cdot \begin{pmatrix} \Phi_{11} & \Phi_{12} & \Phi_{13} \\ \Phi_{21} & \Phi_{22} & \Phi_{23} \\ \mathbf{0}_{q\times 3} & \mathbf{0}_{q\times 3} & \mathbf{I}_{q\times q} \end{pmatrix}, \tag{4.55}$$

so the set of differential equations to be integrated is reduced to

$$\dot{\Phi}_{11} = \Phi_{21}, \tag{4.56}$$
$$\dot{\Phi}_{12} = \Phi_{22}, \tag{4.57}$$
$$\dot{\Phi}_{13} = \Phi_{23}, \tag{4.58}$$
$$\dot{\Phi}_{21} = A_{21}\Phi_{11} + A_{22}\Phi_{21}, \tag{4.59}$$
$$\dot{\Phi}_{22} = A_{21}\Phi_{12} + A_{22}\Phi_{22}, \tag{4.60}$$
$$\dot{\Phi}_{23} = A_{21}\Phi_{13} + A_{22}\Phi_{23} + A_{23}. \tag{4.61}$$

In conclusion, to proceed with the integration of the equations from (4.56) to (4.61) and then solve the variational equations in (4.50), allowing to calculate the phase partials in (4.46), it is necessary to compute the three blocks of partial derivatives

$$A_{21} = \frac{\partial \mathbf{a}}{\partial \mathbf{r}}, \tag{4.62}$$
$$A_{22} = \frac{\partial \mathbf{a}}{\partial \mathbf{v}}, \tag{4.63}$$
$$A_{23} = \frac{\partial \mathbf{a}}{\partial \mathbf{P}}. \tag{4.64}$$

Focusing on the computation of the phase partials with respect to the ocean tide parameters $\mathbf{P}_{ot}$, only the term of the acceleration due to ocean tides is considered and the blocks become

$$A_{21} = \frac{\partial \mathbf{a}_{ot}}{\partial \mathbf{r}}, \tag{4.65}$$
$$A_{22} = \mathbf{0}_{3\times 3}, \tag{4.66}$$
$$A_{23} = \frac{\partial \mathbf{a}_{ot}}{\partial \mathbf{P}_{ot}}, \tag{4.67}$$

where $A_{22} = \mathbf{0}_{3\times 3}$, because the ocean tide field is conservative and the tidal acceleration does not depend on the velocity, so the set of differential equations to be integrated is simplified to

$$\dot{\Phi}_{11} = \Phi_{21}, \tag{4.68}$$
$$\dot{\Phi}_{12} = \Phi_{22}, \tag{4.69}$$
$$\dot{\Phi}_{13} = \Phi_{23}, \tag{4.70}$$
$$\dot{\Phi}_{21} = A_{21}\Phi_{11}, \tag{4.71}$$

$$\dot{\Phi}_{22} = A_{21}\Phi_{12}, \tag{4.72}$$

$$\dot{\Phi}_{23} = A_{21}\Phi_{13} + A_{23}. \tag{4.73}$$

The ocean tide acceleration is the gradient of the ocean tide potential V_{ot}

$$\mathbf{a}_{ot} = \nabla V_{ot}, \tag{4.74}$$

which must be expressed as function of the tidal parameters we want to estimate.

The following paragraphs concern the calculation of the gradient of the ocean tide potential and of the partial derivatives corresponding to the blocks A_{21} and A_{23}. In particular, the partials of the block A_{23} will be derived with respect to two types of tidal parameters: the orthoweights and the harmonic coefficients.

4.5 Gradient of the ocean tide potential

The ocean tide potential is expressed in polar coordinates r, λ, ϕ, so its gradient is written according to the chain rule as

$$\begin{aligned}\mathbf{a}_{ot} =& \nabla V_{ot}(r,\lambda,\phi) = \left(\frac{\partial V_{ot}}{\partial \mathbf{r}}\right)^T \\ =& \left[\frac{\partial V_{ot}}{\partial r}\frac{\partial r}{\partial \mathbf{r}} + \frac{\partial V_{ot}}{\partial \phi}\frac{\partial \phi}{\partial \mathbf{r}} + \frac{\partial V_{ot}}{\partial \lambda}\frac{\partial \lambda}{\partial \mathbf{r}}\right]^T \\ =& \left(\frac{\partial r}{\partial \mathbf{r}}\right)^T \frac{\partial V_{ot}}{\partial r} + \left(\frac{\partial \phi}{\partial \mathbf{r}}\right)^T \frac{\partial V_{ot}}{\partial \phi} + \left(\frac{\partial \lambda}{\partial \mathbf{r}}\right)^T \frac{\partial V_{ot}}{\partial \lambda}.\end{aligned} \tag{4.75}$$

The partials of the potential with respect to the polar coordinates are given by

$$\frac{\partial V_{ot}}{\partial r} = -\frac{GM}{r^2}\sum_{l=0}^{\infty}\sum_{p=0}^{l}(l+1)\left(\frac{a}{r}\right)^l \left[\Delta\bar{C}_{lp}(t)\cos(p\lambda) + \Delta\bar{S}_{lp}(t)\sin(p\lambda)\right]\bar{P}_{lp}(\sin\phi), \tag{4.76}$$

$$\begin{aligned}\frac{\partial V_{ot}}{\partial \phi} =& \frac{GM}{r}\sum_{l=0}^{\infty}\sum_{p=0}^{l}\left(\frac{a}{r}\right)^l \left[\Delta\bar{C}_{lp}(t)\cos(p\lambda) + \Delta\bar{S}_{lp}(t)\sin(p\lambda)\right]\frac{\partial}{\partial\phi}\left[\bar{P}_{lp}(\sin\phi)\right] \\ =& \frac{GM}{r}\sum_{l=0}^{\infty}\sum_{p=0}^{l}\left(\frac{a}{r}\right)^l \left[\Delta\bar{C}_{lp}(t)\cos(p\lambda) + \Delta\bar{S}_{lp}(t)\sin(p\lambda)\right] \qquad (4.77) \\ & \cdot\left[-p\tan\phi\bar{P}_{lp}(\sin\phi) + \bar{P}_l^{p+1}(\sin\phi)\right], \qquad (4.78)\end{aligned}$$

$$\frac{\partial V_{ot}}{\partial \lambda} = \frac{GM}{r}\sum_{l=0}^{\infty}\sum_{p=0}^{l} p\left(\frac{a}{r}\right)^l \left[-\Delta\bar{C}_{lp}(t)\sin(p\lambda) + \Delta\bar{S}_{lp}(t)\cos(p\lambda)\right]\bar{P}_{lp}(\sin\phi). \tag{4.79}$$

The partials of the polar coordinates with respect to the position vector are obtain defining the Jacobian matrix of the transformation from polar coordinates to cartesian coordinates

$$\mathbf{F} = \begin{pmatrix} \frac{\partial r}{\partial \mathbf{r}} \\ \frac{\partial \phi}{\partial \mathbf{r}} \\ \frac{\partial \lambda}{\partial \mathbf{r}} \end{pmatrix} = \begin{pmatrix} \frac{\partial r}{\partial x} & \frac{\partial r}{\partial y} & \frac{\partial r}{\partial z} \\ \frac{\partial \phi}{\partial x} & \frac{\partial \phi}{\partial y} & \frac{\partial \phi}{\partial z} \\ \frac{\partial \lambda}{\partial x} & \frac{\partial \lambda}{\partial y} & \frac{\partial \lambda}{\partial z} \end{pmatrix}, \tag{4.80}$$

where the relations between the polar and the cartesian coordinates are

$$\begin{cases} r = & \sqrt{x^2+y^2+z^2} \\ \varphi = & \sin^{-1}\left(\frac{z}{r}\right) \\ \lambda = & \tan^{-1}\left(\frac{y}{x}\right), \end{cases} \tag{4.81}$$

allowing to explicit the partials of r as

$$\left(\frac{\partial r}{\partial \mathbf{r}}\right)^T = \begin{pmatrix} \frac{\partial r}{\partial x} \\ \frac{\partial r}{\partial y} \\ \frac{\partial r}{\partial z} \end{pmatrix} = \begin{pmatrix} \frac{x}{r} \\ \frac{y}{r} \\ \frac{z}{r} \end{pmatrix} = \frac{\mathbf{r}}{r}. \tag{4.82}$$

The partials of ϕ are

$$\frac{\partial \phi}{\partial x} = \frac{\partial}{\partial x}\sin^{-1}\left(\frac{z}{r}\right) = \frac{1}{\sqrt{1-\left(\frac{z}{r}\right)^2}}\frac{\partial}{\partial x}\left(\frac{z}{r}\right) = \frac{r}{\sqrt{x^2+y^2}}\left(-\frac{z}{r^3}x\right) = \frac{1}{\sqrt{x^2+y^2}}\left(-\frac{z}{r^2}x\right), \tag{4.83}$$

$$\frac{\partial \phi}{\partial y} = \frac{\partial}{\partial y}\sin^{-1}\left(\frac{z}{r}\right) = \frac{r}{\sqrt{x^2+y^2}}\left(-\frac{z}{r^3}y\right) = \frac{1}{\sqrt{x^2+y^2}}\left(-\frac{z}{r^2}y\right), \tag{4.84}$$

$$\frac{\partial \phi}{\partial z} = \frac{\partial}{\partial z}\sin^{-1}\left(\frac{z}{r}\right) = \frac{r}{\sqrt{x^2+y^2}}\left(\frac{r-z\frac{z}{r}}{r^2}\right) = \frac{1}{\sqrt{x^2+y^2}}\left(1-\frac{z}{r^2}z\right) = \frac{\sqrt{x^2+y^2}}{r^2}, \tag{4.85}$$

that in compact form are

$$\left(\frac{\partial \phi}{\partial \mathbf{r}}\right)^T = \frac{1}{(x^2+y^2)^{1/2}}\left[\left(\frac{\partial z}{\partial \mathbf{r}}\right)^T - \frac{z}{r^2}\mathbf{r}\right]. \tag{4.86}$$

Finally, the partials of λ are

$$\frac{\partial \lambda}{\partial x} = \frac{1}{1+\left(\frac{y}{x}\right)^2}\frac{\partial}{\partial x}\left(\frac{y}{x}\right) = \frac{x^2}{x^2+y^2}\left(-\frac{y}{x^2}\right) = -\frac{y}{x^2+y^2}, \tag{4.87}$$

$$\frac{\partial \lambda}{\partial y} = \frac{1}{1+\left(\frac{y}{x}\right)^2}\frac{\partial}{\partial y}\left(\frac{y}{x}\right) = \frac{x^2}{x^2+y^2}\left(\frac{x}{x^2}\right) = \frac{x}{x^2+y^2}, \tag{4.88}$$

$$\frac{\partial \lambda}{\partial z} = 0 \tag{4.89}$$

and in compact form

$$\begin{aligned}\left(\frac{\partial \lambda}{\partial \mathbf{r}}\right)^T &= \frac{1}{1+\left(\frac{y}{x}\right)^2}\left[\frac{\partial}{\partial \mathbf{r}}\frac{y}{x}\right] \\ &= \frac{1}{x^2+y^2}\left[x\left(\frac{\partial y}{\partial \mathbf{r}}\right)^T - y\left(\frac{\partial x}{\partial \mathbf{r}}\right)^T\right].\end{aligned} \tag{4.90}$$

4.6 Partials with respect to the receiver position vector

To compute the partials with respect to the receiver position vector, we have to apply the chain rule to the gradient of the potential, obtaining the following relation

$$\begin{aligned}\frac{\partial}{\partial \mathbf{r}}\left(\frac{\partial V}{\partial \mathbf{r}}\right)^T &= \frac{\partial}{\partial \mathbf{r}}\left[\left(\frac{\partial r}{\partial \mathbf{r}}\right)^T\frac{\partial V}{\partial r} + \left(\frac{\partial \phi}{\partial \mathbf{r}}\right)^T\frac{\partial V}{\partial \phi} + \left(\frac{\partial \lambda}{\partial \mathbf{r}}\right)^T\frac{\partial V}{\partial \lambda}\right] \\ &= \frac{\partial}{\partial \mathbf{r}}\left(\frac{\partial r}{\partial \mathbf{r}}\right)^T\frac{\partial V}{\partial r} + \frac{\partial}{\partial \mathbf{r}}\left(\frac{\partial \phi}{\partial \mathbf{r}}\right)^T\frac{\partial V}{\partial \phi} + \frac{\partial}{\partial \mathbf{r}}\left(\frac{\partial \lambda}{\partial \mathbf{r}}\right)^T\frac{\partial V}{\partial \lambda} \\ &\quad + \left(\frac{\partial r}{\partial \mathbf{r}}\right)^T\frac{\partial}{\partial \mathbf{r}}\frac{\partial V}{\partial r} + \left(\frac{\partial \phi}{\partial \mathbf{r}}\right)^T\frac{\partial}{\partial \mathbf{r}}\frac{\partial V}{\partial \phi} + \left(\frac{\partial \lambda}{\partial \mathbf{r}}\right)^T\frac{\partial}{\partial \mathbf{r}}\frac{\partial V}{\partial \lambda},\end{aligned} \tag{4.91}$$

which can be rewrite in a simpler form as

$$\begin{aligned}\frac{\partial}{\partial \mathbf{r}}\left(\frac{\partial V}{\partial \mathbf{r}}\right)^T =& \frac{\partial}{\partial \mathbf{r}}\left(\frac{\partial r}{\partial \mathbf{r}}\right)^T \frac{\partial V}{\partial r} + \frac{\partial}{\partial \mathbf{r}}\left(\frac{\partial \phi}{\partial \mathbf{r}}\right)^T \frac{\partial V}{\partial \phi} + \frac{\partial}{\partial \mathbf{r}}\left(\frac{\partial \lambda}{\partial \mathbf{r}}\right)^T \frac{\partial V}{\partial \lambda} \\ &+ \left(\frac{\partial r}{\partial \mathbf{r}}\right)^T \left[\frac{\partial^2 V}{\partial r^2}\frac{\partial r}{\partial \mathbf{r}} + \frac{\partial^2 V}{\partial r\,\partial \phi}\frac{\partial \phi}{\partial \mathbf{r}} + \frac{\partial^2 V}{\partial r\,\partial \lambda}\frac{\partial \lambda}{\partial \mathbf{r}}\right] \\ &+ \left(\frac{\partial \phi}{\partial \mathbf{r}}\right)^T \left[\frac{\partial^2 V}{\partial \phi\,\partial r}\frac{\partial r}{\partial \mathbf{r}} + \frac{\partial^2 V}{\partial \phi^2}\frac{\partial \phi}{\partial \mathbf{r}} + \frac{\partial^2 V}{\partial \phi\,\partial \lambda}\frac{\partial \lambda}{\partial \mathbf{r}}\right] \\ &+ \left(\frac{\partial \lambda}{\partial \mathbf{r}}\right)^T \left[\frac{\partial^2 V}{\partial \lambda\,\partial r}\frac{\partial r}{\partial \mathbf{r}} + \frac{\partial^2 V}{\partial \lambda\,\partial \phi}\frac{\partial \phi}{\partial \mathbf{r}} + \frac{\partial^2 V}{\partial \lambda^2}\frac{\partial \lambda}{\partial \mathbf{r}}\right]. \end{aligned} \tag{4.92}$$

Using the Jacobian matrix $\mathbf{F}$ and defining the matrix $\mathbf{E}$

$$\mathbf{E} = \begin{pmatrix} \frac{\partial^2 V}{\partial r^2} & \frac{\partial^2 V}{\partial r\,\partial \phi} & \frac{\partial^2 V}{\partial r\,\partial \lambda} \\ \frac{\partial^2 V}{\partial \phi\,\partial r} & \frac{\partial^2 V}{\partial \phi^2} & \frac{\partial^2 V}{\partial \phi\,\partial \lambda} \\ \frac{\partial^2 V}{\partial \lambda\,\partial r} & \frac{\partial^2 V}{\partial \lambda\,\partial \phi} & \frac{\partial^2 V}{\partial \lambda^2} \end{pmatrix}, \tag{4.93}$$

equivalent to the Hessian matrix of the potential in polar coordinates, we can rewrite the equation (4.92) in compact notation as

$$\frac{\partial}{\partial \mathbf{r}}\left(\frac{\partial V}{\partial \mathbf{r}}\right)^T = \frac{\partial}{\partial \mathbf{r}}\left(\frac{\partial r}{\partial \mathbf{r}}\right)^T \frac{\partial V}{\partial r} + \frac{\partial}{\partial \mathbf{r}}\left(\frac{\partial \phi}{\partial \mathbf{r}}\right)^T \frac{\partial V}{\partial \phi} + \frac{\partial}{\partial \mathbf{r}}\left(\frac{\partial \lambda}{\partial \mathbf{r}}\right)^T \frac{\partial V}{\partial \lambda} + \mathbf{F}^T\,\mathbf{E}\,\mathbf{F}\,. \tag{4.94}$$

The remaining partials that have to be computed are then

$$\frac{\partial^2 V}{\partial r^2} = \frac{GM}{r^3}\sum_{l=0}^{\infty}\sum_{p=0}^{l}(l+1)(l+2)\left(\frac{a}{r}\right)^l \left[\Delta\bar{C}_{lp}(t)\cos(p\lambda) + \Delta\bar{S}_{lp}(t)\sin(p\lambda)\right]\bar{P}_{lp}(\sin\phi)\,, \tag{4.95}$$

$$\frac{\partial^2 V}{\partial \lambda^2} = -\frac{GM}{r}\sum_{l=0}^{\infty}\sum_{p=0}^{l}p^2\left(\frac{a}{r}\right)^l \left[\Delta\bar{C}_{lp}(t)\cos(p\lambda) + \Delta\bar{S}_{lp}(t)\sin(p\lambda)\right]\bar{P}_{lp}(\sin\phi)\,, \tag{4.96}$$

$$\begin{aligned}\frac{\partial^2 V}{\partial \phi^2} &= \frac{GM}{r}\sum_{l=0}^{\infty}\sum_{p=0}^{l}\left(\frac{a}{r}\right)^l \left[\Delta\bar{C}_{lp}(t)\cos(p\lambda) + \Delta\bar{S}_{lp}(t)\sin(p\lambda)\right]\frac{\partial^2}{\partial \phi^2}\left[\bar{P}_{lp}(\sin\phi)\right] \\ &= \frac{GM}{r}\sum_{l=0}^{\infty}\sum_{p=0}^{l}\left(\frac{a}{r}\right)^l \left\{\begin{array}{c} \left[\Delta\bar{C}_{lp}(t)\cos(p\lambda) + \Delta\bar{S}_{lp}(t)\sin(p\lambda)\right]\times \\ \left\{\begin{array}{c} -\frac{l}{\cos^2\phi}\bar{P}_{lp}(\sin\phi) + p^2\tan^2\phi\,\bar{P}_{lp}(\sin\phi) \\ -(2p+1)\tan\phi\,\bar{P}_{lp+1}(\sin\phi) + \bar{P}_{lp+2}(\sin\phi) \end{array}\right\} \end{array}\right\}, \end{aligned} \tag{4.97}$$

$$\begin{aligned}\frac{\partial^2 V}{\partial r \partial \phi} &= -\frac{GM}{r^2}\sum_{l=0}^{\infty}\sum_{p=0}^{l}(l+1)\left(\frac{a}{r}\right)^l \left[\Delta\bar{C}_{lp}(t)\cos(p\lambda) + \Delta\bar{S}_{lp}(t)\sin(p\lambda)\right]\frac{\partial}{\partial \phi}\bar{P}_{lp}(\sin\phi) \\ &= -\frac{GM}{r^2}\sum_{l=0}^{\infty}\sum_{p=0}^{l}(l+1)\left(\frac{a}{r}\right)^l \left\{\begin{array}{c} \left[\Delta\bar{C}_{lp}(t)\cos(p\lambda) + \Delta\bar{S}_{lp}(t)\sin(p\lambda)\right]\times \\ \left[-q\tan\phi\,\bar{P}_{lp}(\sin\phi) + \bar{P}_{lp+1}(\sin\phi)\right] \end{array}\right\}, \end{aligned} \tag{4.98}$$

$$\frac{\partial^2 V}{\partial r \partial \lambda} = -\frac{GM}{r^2}\sum_{l=0}^{\infty}\sum_{p=0}^{l}p\,(l+1)\left(\frac{a}{r}\right)^l \left[-\Delta\bar{C}_{lp}(t)\sin p\lambda + \Delta\bar{S}_{lp}(t)\cos p\lambda\right]\bar{P}_{lp}(\sin\phi)\,, \tag{4.99}$$

$$\frac{\partial^2 V}{\partial\phi\partial\lambda} = \frac{GM}{r}\sum_{l=0}^{\infty}\sum_{p=0}^{l}\left(\frac{a}{r}\right)^l \left\{ \begin{array}{c} p\left[-\Delta\bar{C}_{lp}(t)\sin p\lambda + \Delta\bar{S}_{lp}(t)\cos p\lambda\right]\times \\ \left[-p\tan\phi\,\bar{P}_{lp}(\sin\phi) + \bar{P}_{lp+1}(\sin\phi)\right] \end{array} \right\}, \tag{4.100}$$

while for the partials with respect to the coordinates we have

$$\begin{aligned} \frac{\partial}{\partial\mathbf{r}}\left(\frac{\partial r}{\partial\mathbf{r}}\right)^T &= \frac{\partial}{\partial\mathbf{r}}\left(\frac{\mathbf{r}}{r}\right) = \frac{1}{r^2}\left[\frac{\partial\mathbf{r}}{\partial\mathbf{r}}\,r - \mathbf{r}\frac{\partial r}{\partial\mathbf{r}}\right] \\ &= \frac{1}{r^2}\left[\mathbf{I}\,r - \mathbf{r}\left(\frac{\mathbf{r}}{r}\right)^T\right] \\ &= \frac{1}{r}\left[\mathbf{I} - \frac{\mathbf{r}\mathbf{r}^T}{r^2}\right], \end{aligned} \tag{4.101}$$

$$\begin{aligned} \frac{\partial}{\partial\mathbf{r}}\left(\frac{\partial\phi}{\partial\mathbf{r}}\right)^T &= -\frac{1}{r^2}\frac{1}{(x^2+y^2)^{1/2}}\left[\mathbf{I}\,z + \mathbf{r}\frac{\partial z}{\partial\mathbf{r}} - 2\frac{z}{r^2}\mathbf{r}\mathbf{r}^T\right] \\ &\quad -\frac{1}{(x^2+y^2)^{3/2}}\left[\left(\frac{\partial z}{\partial\mathbf{r}}\right)^T - \mathbf{r}\frac{z}{r^2}\right]\left[x\frac{\partial x}{\partial\mathbf{r}} + y\frac{\partial y}{\partial\mathbf{r}}\right], \end{aligned} \tag{4.102}$$

$$\begin{aligned} \frac{\partial}{\partial\mathbf{r}}\left(\frac{\partial\lambda}{\partial\mathbf{r}}\right)^T &= \frac{1}{(x^2+y^2)}\left[\left(\frac{\partial y}{\partial\mathbf{r}}\right)^T\frac{\partial x}{\partial\mathbf{r}} - \left(\frac{\partial x}{\partial\mathbf{r}}\right)^T\frac{\partial y}{\partial\mathbf{r}}\right] \\ &\quad -\frac{2}{(x^2+y^2)^2}\left[\left(\frac{\partial y}{\partial\mathbf{r}}\right)^T x - \left(\frac{\partial x}{\partial\mathbf{r}}\right)^T y\right]\left[x\frac{\partial x}{\partial\mathbf{r}} + y\frac{\partial y}{\partial\mathbf{r}}\right], \end{aligned} \tag{4.103}$$

The matrices, in explicit form are

$$\frac{\partial}{\partial\mathbf{r}}\left(\frac{\partial r}{\partial\mathbf{r}}\right)^T = \frac{\partial}{\partial\mathbf{r}}\begin{pmatrix}\frac{\partial r}{\partial x}\\ \frac{\partial r}{\partial y}\\ \frac{\partial r}{\partial z}\end{pmatrix} = \begin{pmatrix}\frac{\partial^2 r}{\partial x^2} & \frac{\partial^2 r}{\partial y\partial x} & \frac{\partial^2 r}{\partial z\partial x}\\ \frac{\partial^2 r}{\partial x\partial y} & \frac{\partial^2 r}{\partial y^2} & \frac{\partial^2 r}{\partial z\partial y}\\ \frac{\partial^2 r}{\partial x\partial z} & \frac{\partial^2 r}{\partial y\partial z} & \frac{\partial^2 r}{\partial z^2}\end{pmatrix}, \tag{4.104}$$

$$\frac{\partial}{\partial\mathbf{r}}\left(\frac{\partial\phi}{\partial\mathbf{r}}\right)^T = \frac{\partial}{\partial\mathbf{r}}\begin{pmatrix}\frac{\partial\phi}{\partial x}\\ \frac{\partial\phi}{\partial y}\\ \frac{\partial\phi}{\partial z}\end{pmatrix} = \begin{pmatrix}\frac{\partial^2\phi}{\partial x^2} & \frac{\partial^2\phi}{\partial y\partial x} & \frac{\partial^2\phi}{\partial z\partial x}\\ \frac{\partial^2\phi}{\partial x\partial y} & \frac{\partial^2\phi}{\partial y^2} & \frac{\partial^2\phi}{\partial z\partial y}\\ \frac{\partial^2\phi}{\partial x\partial z} & \frac{\partial^2\phi}{\partial y\partial z} & \frac{\partial^2\phi}{\partial z^2}\end{pmatrix}, \tag{4.105}$$

$$\frac{\partial}{\partial\mathbf{r}}\left(\frac{\partial\lambda}{\partial\mathbf{r}}\right)^T = \frac{\partial}{\partial\mathbf{r}}\begin{pmatrix}\frac{\partial\lambda}{\partial x}\\ \frac{\partial\lambda}{\partial y}\\ \frac{\partial\lambda}{\partial z}\end{pmatrix} = \begin{pmatrix}\frac{\partial^2\lambda}{\partial x^2} & \frac{\partial^2\lambda}{\partial y\partial x} & \frac{\partial^2\lambda}{\partial z\partial x}\\ \frac{\partial^2\lambda}{\partial x\partial y} & \frac{\partial^2\lambda}{\partial y^2} & \frac{\partial^2\lambda}{\partial z\partial y}\\ \frac{\partial^2\lambda}{\partial x\partial z} & \frac{\partial^2\lambda}{\partial y\partial z} & \frac{\partial^2\lambda}{\partial z^2}\end{pmatrix}, \tag{4.106}$$

and the partials are

$$\frac{\partial^2 r}{\partial x^2} = \frac{1}{r}\left(1 - \frac{x^2}{r^2}\right), \qquad \frac{\partial^2 r}{\partial y^2} = \frac{1}{r}\left(1 - \frac{y^2}{r^2}\right), \qquad \frac{\partial^2 r}{\partial z^2} = \frac{1}{r}\left(1 - \frac{z^2}{r^2}\right), \tag{4.107}$$

$$\frac{\partial^2 r}{\partial x\partial y} = \frac{\partial^2 r}{\partial y\partial x} = -\frac{xy}{r^3}, \qquad \frac{\partial^2 r}{\partial z\partial y} = \frac{\partial^2 r}{\partial y\partial z} = -\frac{yz}{r^3}, \qquad \frac{\partial^2 r}{\partial z\partial x} = \frac{\partial^2 r}{\partial x\partial z} = -\frac{xz}{r^3}, \tag{4.108}$$

$$\frac{\partial^2\phi}{\partial x^2} = -\frac{1}{r^2}\left[\frac{1}{(x^2+y^2)^{1/2}}\left(z - 2\frac{z}{r^2}x^2\right) - \frac{zx^2}{(x^2+y^2)^{3/2}}\right], \tag{4.109}$$

$$\frac{\partial^2\phi}{\partial y^2} = -\frac{1}{r^2}\left[\frac{1}{(x^2+y^2)^{1/2}}\left(z - 2\frac{z}{r^2}y^2\right) - \frac{zy^2}{(x^2+y^2)^{3/2}}\right], \tag{4.110}$$

$$\frac{\partial^2\phi}{\partial x\partial y} = \frac{\partial^2\phi}{\partial y\partial x} = \frac{zxy}{r^2}\left[\frac{2}{r^2}\frac{1}{(x^2+y^2)^{1/2}} + \frac{1}{(x^2+y^2)^{3/2}}\right], \tag{4.111}$$

$$\frac{\partial^2\phi}{\partial z^2} = -\frac{1}{r^2}\frac{1}{(x^2+y^2)^{1/2}}\left(2z - 2\frac{z^3}{r^2}\right), \tag{4.112}$$

$$\frac{\partial^2\phi}{\partial x\partial z} = \frac{\partial^2\phi}{\partial z\partial x} = -\frac{1}{r^2}\frac{x}{(x^2+y^2)^{1/2}}\left(1 - 2\frac{z^2}{r^2}\right), \tag{4.113}$$

$$\frac{\partial^2\phi}{\partial y\partial z} = \frac{\partial^2\phi}{\partial z\partial y} = -\frac{1}{r^2}\frac{y}{(x^2+y^2)^{1/2}}\left(1 - 2\frac{z^2}{r^2}\right), \tag{4.114}$$

$$\frac{\partial^2\lambda}{\partial x^2} = \frac{2}{(x^2+y^2)^2}yx\,, \qquad \frac{\partial^2\lambda}{\partial y^2} = -\frac{2}{(x^2+y^2)^2}yx\,, \tag{4.115}$$

$$\frac{\partial^2\lambda}{\partial x\partial y} = \frac{\partial^2\lambda}{\partial y\partial x} = -\frac{1}{x^2+y^2} + \frac{2}{(x^2+y^2)^2}y^2\,, \tag{4.116}$$

$$\frac{\partial^2\lambda}{\partial z^2} = \frac{\partial^2\lambda}{\partial z\partial y} = \frac{\partial^2\lambda}{\partial y\partial z} = \frac{\partial^2\lambda}{\partial x\partial z} = \frac{\partial^2\lambda}{\partial z\partial x} = 0\,. \tag{4.117}$$

4.7 Partials with respect to the tidal parameters

Applying the chain rule we have

$$\frac{\partial}{\partial\mathbf{P}_{ot}}\left(\frac{\partial V_{ot}}{\partial\mathbf{r}}\right)^T = \frac{\partial}{\partial\mathbf{P}_{ot}}\left[\left(\frac{\partial r}{\partial\mathbf{r}}\right)^T\frac{\partial V_{ot}}{\partial r} + \left(\frac{\partial\phi}{\partial\mathbf{r}}\right)^T\frac{\partial V_{ot}}{\partial\phi} + \left(\frac{\partial\lambda}{\partial\mathbf{r}}\right)^T\frac{\partial V_{ot}}{\partial\lambda}\right] \tag{4.118}$$

$$= \left(\frac{\partial r}{\partial\mathbf{r}}\right)^T\frac{\partial^2 V_{ot}}{\partial\mathbf{P}_{ot}\partial r} + \left(\frac{\partial\phi}{\partial\mathbf{r}}\right)^T\frac{\partial^2 V_{ot}}{\partial\mathbf{P}_{ot}\partial\phi} + \left(\frac{\partial\lambda}{\partial\mathbf{r}}\right)^T\frac{\partial^2 V_{ot}}{\partial\mathbf{P}_{ot}\partial\lambda}. \tag{4.119}$$

The remaining partials that have to be computed are then

$$\frac{\partial^2 V_{ot}}{\partial\mathbf{P}_{ot}\partial r} = -\frac{GM}{r^2}\sum_{l=0}^{\infty}\sum_{p=0}^{l}(l+1)\left(\frac{a}{r}\right)^l\left[\frac{\partial\Delta\bar{C}_{lp}(t)}{\partial\mathbf{P}_{ot}}\cos(p\lambda) + \frac{\partial\Delta\bar{S}_{lp}(t)}{\partial\mathbf{P}_{ot}}\sin(p\lambda)\right]\bar{P}_{lp}(\sin\phi), \tag{4.120}$$

$$\frac{\partial^2 V_{ot}}{\partial\mathbf{P}_{ot}\partial\phi} = \frac{GM}{r}\sum_{l=0}^{\infty}\sum_{p=0}^{l}\left(\frac{a}{r}\right)^l\left[\frac{\partial\Delta\bar{C}_{lp}(t)}{\partial\mathbf{P}_{ot}}\cos(p\lambda) + \frac{\partial\Delta\bar{S}_{lp}(t)}{\partial\mathbf{P}_{ot}}\sin(p\lambda)\right]\frac{\partial}{\partial\phi}\left[\bar{P}_{lp}(\sin\phi)\right] \tag{4.121}$$

$$= \frac{GM}{r}\sum_{l=0}^{\infty}\sum_{p=0}^{l}\left(\frac{a}{r}\right)^l\left[\frac{\partial\Delta\bar{C}_{lp}(t)}{\partial\mathbf{P}_{ot}}\cos(p\lambda) + \frac{\partial\Delta\bar{S}_{lp}(t)}{\partial\mathbf{P}_{ot}}\sin(p\lambda)\right] \tag{4.122}$$

$$\cdot\left[-p\tan\phi\bar{P}_{lp}(\sin\phi) + \bar{P}_{lp+1}(\sin\phi)\right], \tag{4.123}$$

$$\frac{\partial^2 V_{ot}}{\partial\mathbf{P}_{ot}\partial\lambda} = \frac{GM}{r}\sum_{l=0}^{\infty}\sum_{p=0}^{l}p\left(\frac{a}{r}\right)^l\left[-\frac{\partial\Delta\bar{C}_{lp}(t)}{\partial\mathbf{P}_{ot}}\sin(p\lambda) + \frac{\partial\Delta\bar{S}_{lp}(t)}{\partial\mathbf{P}_{ot}}\cos(p\lambda)\right]\bar{P}_{lp}(\sin\phi). \tag{4.124}$$

The last partials that have to be computed are $\frac{\partial\Delta\bar{C}_{lp}(t)}{\partial\mathbf{P}_{ot}}$ and $\frac{\partial\Delta\bar{S}_{lp}(t)}{\partial\mathbf{P}_{ot}}$ which depend on the adopted ocean tide parameterization.

4.7.1 Partials with respect to the orthoweights

Using the orthotide parameterization, the vector of tidal parameters is defined as

$$\mathbf{P}_{ot} = \begin{pmatrix} u_i^m(\phi,\lambda) & v_i^m(\phi,\lambda) \end{pmatrix}, \tag{4.125}$$

where $u_i^m(\phi,\lambda)$ and $v_i^m(\phi,\lambda)$ are the orthoweights at order i and tidal band m, so we have to compute

$$\frac{\partial \Delta\bar{C}_{lp}(t)}{\partial \mathbf{P}_{ot}} = \begin{pmatrix} \frac{\partial \Delta\bar{C}_{lp}(t)}{\partial u_i^m} & \frac{\partial \Delta\bar{C}_{lp}(t)}{\partial v_i^m} \end{pmatrix}, \tag{4.126}$$

$$\frac{\partial \Delta\bar{S}_{lp}(t)}{\partial \mathbf{P}_{ot}} = \begin{pmatrix} \frac{\partial \Delta\bar{S}_{lp}(t)}{\partial u_i^m} & \frac{\partial \Delta\bar{S}_{lp}(t)}{\partial v_i^m} \end{pmatrix}. \tag{4.127}$$

The partials of the Stokes coefficient variations due to ocean tides with respect to the orthoweights at a specified order i and band m are

$$\frac{\partial \Delta\bar{C}_{lp}(t)}{\partial u_i^m(\phi,\lambda)} = \frac{4\pi G\rho_w}{g}\frac{1+k_l'}{2l+1} I \sum_{n=2}^{N}\sum_{m}\sum_{s=-S}^{S}[(U_{i,s}^m a_{nm}(t+s\Delta t) + V_{i,s}^m b_{nm}(t+s\Delta t)], \tag{4.128}$$

$$\frac{\partial \Delta\bar{C}_{lp}(t)}{\partial v_i^m(\phi,\lambda)} = \frac{4\pi G\rho_w}{g}\frac{1+k_l'}{2l+1} I \sum_{n=2}^{N}\sum_{m}\sum_{s=-S}^{S}[-V_{i,s}^m a_{nm}(t+s\Delta t) + U_{i,s}^m b_{nm}(t+s\Delta t)], \tag{4.129}$$

$$\frac{\partial \Delta\bar{S}_{lp}(t)}{\partial u_i^m(\phi,\lambda)} = \frac{4\pi G\rho_w}{g}\frac{1+k_l'}{2l+1} J \sum_{n=2}^{N}\sum_{m}\sum_{s=-S}^{S}[(U_{i,s}^m a_{nm}(t+s\Delta t) + V_{i,s}^m b_{nm}(t+s\Delta t)], \tag{4.130}$$

$$\frac{\partial \Delta\bar{S}_{lp}(t)}{\partial v_i^m(\phi,\lambda)} = \frac{4\pi G\rho_w}{g}\frac{1+k_l'}{2l+1} J \sum_{n=2}^{N}\sum_{m}\sum_{s=-S}^{S}[-V_{i,s}^m a_{nm}(t+s\Delta t) + U_{i,s}^m b_{nm}(t+s\Delta t)]. \tag{4.131}$$

4.7.2 Partials with respect to the harmonic coefficients

Using the harmonic parameterization, the vector of tidal parameters is

$$\mathbf{P}_{ot} = \begin{pmatrix} \tilde{C}_{lp}^{\mathbf{k}+} & \tilde{C}_{lp}^{\mathbf{k}-} & \tilde{S}_{lp}^{\mathbf{k}+} & \tilde{S}_{lp}^{\mathbf{k}-} \end{pmatrix}, \tag{4.132}$$

where the harmonic coefficients $\tilde{C}_{lp}^{\mathbf{k}+}, \tilde{C}_{lp}^{\mathbf{k}-}, \tilde{S}_{lp}^{\mathbf{k}+}, \tilde{S}_{lp}^{\mathbf{k}-}$ are defined for a tidal frequency $\mathbf{k}$, so we have to compute

$$\frac{\partial \Delta\bar{C}_{lp}(t)}{\partial \mathbf{P}_{ot}} = \begin{pmatrix} \frac{\partial \Delta\bar{C}_{lp}(t)}{\partial \tilde{C}_{lp}^{\mathbf{k}+}} & \frac{\partial \Delta\bar{C}_{lp}(t)}{\partial \tilde{C}_{lp}^{\mathbf{k}-}} & \frac{\partial \Delta\bar{C}_{lp}(t)}{\partial \tilde{S}_{lp}^{\mathbf{k}+}} & \frac{\partial \Delta\bar{C}_{lp}(t)}{\partial \tilde{S}_{lp}^{\mathbf{k}-}} \end{pmatrix}, \tag{4.133}$$

$$\frac{\partial \Delta\bar{S}_{lp}(t)}{\partial \mathbf{P}_{ot}} = \begin{pmatrix} \frac{\partial \Delta\bar{S}_{lp}(t)}{\partial \tilde{C}_{lp}^{\mathbf{k}+}} & \frac{\partial \Delta\bar{S}_{lp}(t)}{\partial \tilde{C}_{lp}^{\mathbf{k}-}} & \frac{\partial \Delta\bar{S}_{lp}(t)}{\partial \tilde{S}_{lp}^{\mathbf{k}+}} & \frac{\partial \Delta\bar{S}_{lp}(t)}{\partial \tilde{S}_{lp}^{\mathbf{k}-}} \end{pmatrix}. \tag{4.134}$$

The partials of the Stokes coefficient variations due to ocean tides with respect to the harmonic coefficients at a specified tidal frequency $\mathbf{k}$ are

$$\frac{\partial \Delta\bar{C}_{lp}(t)}{\partial \tilde{C}_{lp}^{\mathbf{k}+}} = F_{lp}\cos\Theta_{\mathbf{k}}(t), \tag{4.135}$$

$$\frac{\partial \Delta\bar{C}_{lp}(t)}{\partial \tilde{C}_{lp}^{\mathbf{k}-}} = F_{lp}\cos\Theta_{\mathbf{k}}(t), \tag{4.136}$$

$$\frac{\partial \Delta\bar{C}_{lp}(t)}{\partial \tilde{S}_{lp}^{\mathbf{k}+}} = F_{lp}\sin\Theta_{\mathbf{k}}(t), \tag{4.137}$$

$$\frac{\partial \Delta \bar{C}_{lp}(t)}{\partial \tilde{S}_{lp}^{\mathbf{k}-}} = F_{lp} \sin \Theta_{\mathbf{k}}(t), \tag{4.138}$$

$$\frac{\partial \Delta \bar{S}_{lp}(t)}{\partial \tilde{C}_{lp}^{\mathbf{k}+}} = -F_{lp} \sin \Theta_{\mathbf{k}}(t), \tag{4.139}$$

$$\frac{\partial \Delta \bar{S}_{lp}(t)}{\partial \tilde{C}_{lp}^{\mathbf{k}-}} = F_{lp} \sin \Theta_{\mathbf{k}}(t), \tag{4.140}$$

$$\frac{\partial \Delta \bar{S}_{lp}(t)}{\partial \tilde{S}_{lp}^{\mathbf{k}+}} = F_{lp} \cos \Theta_{\mathbf{k}}(t), \tag{4.141}$$

$$\frac{\partial \Delta \bar{S}_{lp}(t)}{\partial \tilde{S}_{lp}^{\mathbf{k}-}} = -F_{lp} \cos \Theta_{\mathbf{k}}(t). \tag{4.142}$$

Chapter 5

Sensitivity study of GOCE orbit to ocean tide perturbations

In this Chapter, a sensitivity study of ocean tide perturbations on GOCE orbit is presented. First of all, the effect of various combinations of ocean tide constituents on GOCE orbit was evaluated over different time intervals and ocean tides accelerations acting on GOCE orbit were determined using different existent ocean tide models. Then, a preliminary work was carried out to study the evolution of GOCE orbital elements along the precise estimated orbits covering the period of available data (1 November 2009 - 31 May 2011) and the secular rates of the GOCE angular elements (argument of perigee, longitude of ascending node, mean anomaly) were estimated through a linear least-square fit. Finally, the analytical spectral analysis of the ocean tide perturbations affecting GOCE orbit is presented using Kaula's linear satellite theory, which is necessary to define the set of ocean tide harmonic parameters to which GOCE is more sensitive, which will be estimated through a multiarc solution subsequent to the GOCE fully dynamic POD and accumulation of normal equations.

5.1 Evaluation of ocean tide effects on GOCE orbit

The effect of various combinations of ocean tide constituents on GOCE orbit was evaluated over 1 year, computing the difference between two orbits propagated with different force models. The initial state vector of GOCE was taken from the GOCE PSO of November 1, 2009 and two orbits were propagated: the first orbit was propagated with a force model comprehensive of the static gravity field (EIGEN-6C, 120x120) and the ocean tide field (FES2004, 50x50, for specified constituents); the second orbit was propagated with a force model including only the static gravity field (EIGEN-6C, 120x120).

The initial satellite state vector for the one-year forward propagation is taken from the GOCE official kinematic PSO solution of the 1 November 2009 at 00:00:00, while the initial satellite state vector for the 19-year backward propagation is taken from the GOCE official kinematic PSO solution of the 20 May 2011 at 00:00:00 ([8] Bock at al., 2011).

The results obtained for the different combinations of tidal constituents over 1 year are as follows:

- 106 constituents of the ocean tide field FES2004, 50x50, show a total position perturbation reaching a maximum of about 3000 m (see Figure 5.1);
- 8 main constituents $O1$, $P1$, $K1$, $Q1$, $N2$, $M2$, $K2$, $S2$ of the ocean tide field FES2004, 50x50, show a total effect of about 3000 m (see Figure 5.2);

- 6 main constituents $O1$, $P1$, $Q1$, $N2$, $M2$, $K2$ of the ocean tide field FES2004, 50x50 (the two resonant constituents $K1$ and $S2$ have been discarded), show a total effect of about 400 m (see Figure 5.3);
- 103 constituents of the ocean tide field FES2004, 50x50 (the three resonant constituents $K1$, $S1$ and $S2$ have been discarded), show a total effect of about 600 m (see Figure 5.4),
- the main constituent $M2$ of the ocean tide field FES2004, 50x50, shows a total effect of about 600 m (see Figure 5.5).

In addition, the two orbits were propagated backward over 19 years to cover the longest tidal period of 18.6 years regarding the lunar node regression due to the Sun perturbation. The first orbit includes 106 constituents of the ocean tide field (FES2004, 50x50). The difference between the orbits was computed and plotted in the RTN reference frame (see Figure 5.6), showing a maximum perturbation of about 140 km.

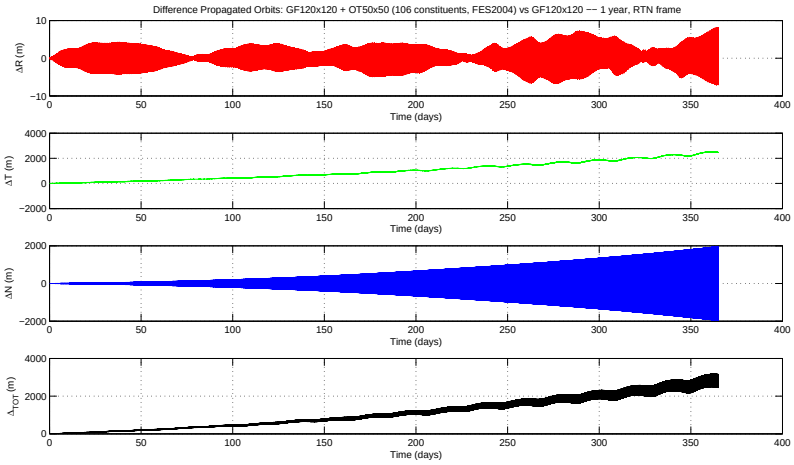

Figure 5.1. Difference between two GOCE orbits, one propagated with the gravity field and ocean tide field (106 constituents) and the other one propagated with only the gravity field over a period of 1 year. The maximum effect is about 3000 m.

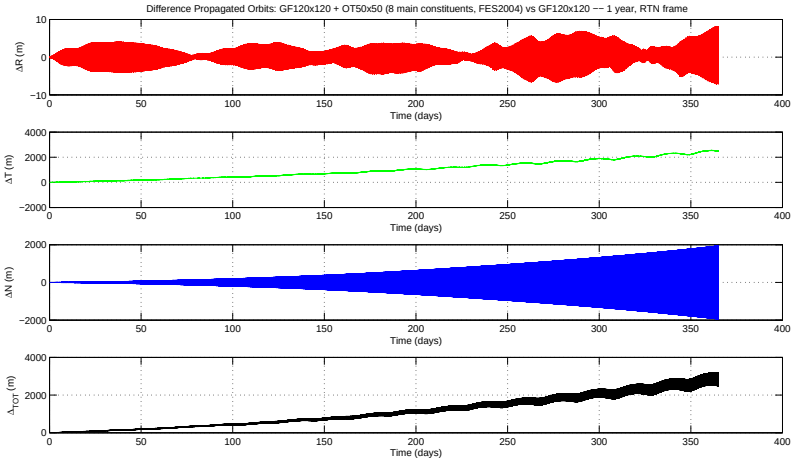

Figure 5.2. Difference between two GOCE orbits, one propagated with the gravity field and ocean tide field (8 main constituents) and the other one propagated with only the gravity field over a period of 1 year. The maximum effect is about 3000 m.

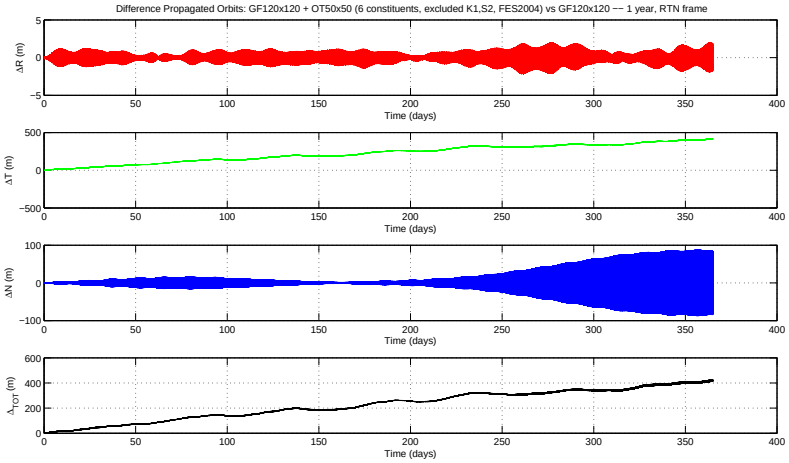

Figure 5.3. Difference between two GOCE orbits, one propagated with the gravity field and ocean tide field (6 main constituents, the resonant $K1$ and $S2$ are excluded) and the other one propagated with only the gravity field over a period of 1 year. The maximum effect is about 400 m.

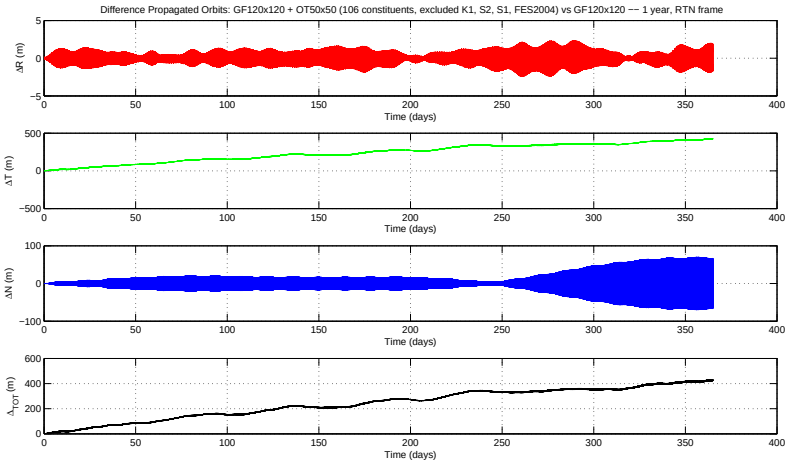

Figure 5.4. Difference between two GOCE orbits, one propagated with the gravity field and ocean tide field (103 constituents, the resonant $K1$, $S1$ and $S2$ are excluded) and the other one propagated with only the gravity field over a period of 1 year. The maximum effect is about 600 m.

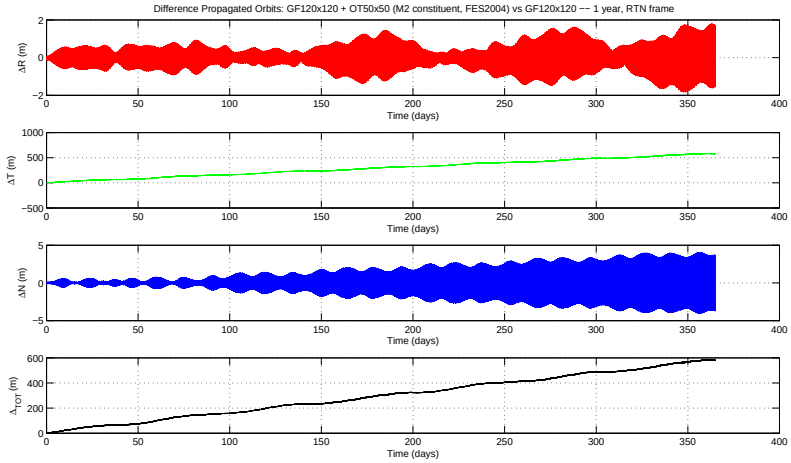

Figure 5.5. Difference between two GOCE orbits, one propagated with the gravity field and ocean tide field (only $M2$ constituent) and the other one propagated with only the gravity field over a period of 1 year. The maximum effect is about 600 m.

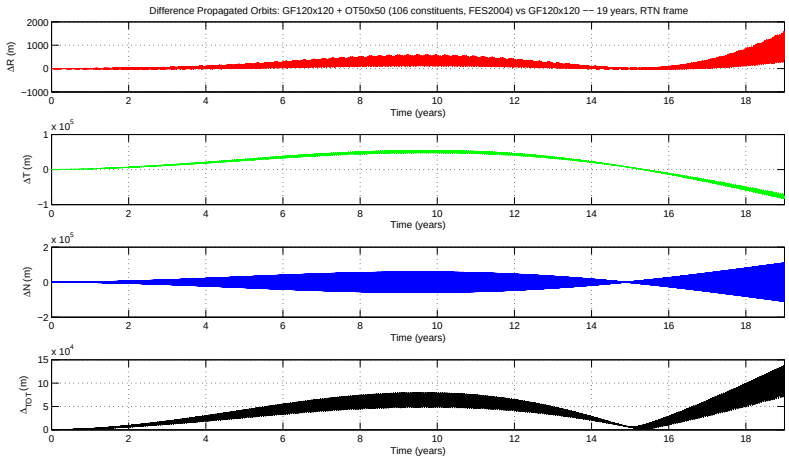

Figure 5.6. Difference between two GOCE orbits, one propagated with the gravity field and ocean tide field (106 constituents) and the other one propagated with only the gravity field over a period of 19 years. The maximum effect is about 140 km.

The effect of ocean tides on the GOCE orbit was also evaluated over different time intervals by fitting an orbit propagated with the static gravity field EIGEN-6C 120x120 ([50] Förste et al., 2011) and the ocean tide field FES2004 50x50 (106 constituents) ([79] Lyard et al., 2006) with an orbit including only the static gravity field EIGEN-6C 120x120. The fitted orbit is the orbit which best represents the propagated orbit, so the difference between these two orbits reflects the perturbation which can not be compensated by a force model including only the static gravity field, that is the ocean tide perturbation. The fit was performed choosing as initial epoch the middle of each considered time interval, in order to reduce the numerical effect due to the error propagation; moreover, only the initial satellite state vector was estimated during the fit process.

The initial satellite state vector for the propagation was taken from the GOCE official kinematic PSO solution of the 1 November 2009 at 00:00:00 ([8] Bock at al., 2011). The following programs of NAPEOS are used:

- PROPAG, to propagate the GOCE orbit for the considered time interval, including the static gravity field and the ocean tide field;
- TRACKSIM, to convert the format of the propagated orbit from sp3 file to NAPEOS Tracking Data Format (NTDF) file, a position observation file which can be read by BAHN;
- BAHN, to compute the fit, receiving in input the NTDF file and the propagated orbit and giving an sp3 file as output;
- ORBCOMP, to compute the statistic comparison between the propagated and the fitted orbit in RTN reference frame.

Results of the statistic comparison between the two orbits in RTN reference frame are reported in Table 5.1 and show a total RMS of the fit of 48.26 cm over one day, 19.98 m over one month and 131.90 m over one year. RMS of the orbit differences in RTN is computed as

$$RMS_{\Delta R} = \sqrt{\frac{\sum_1^{N_{tot}} \Delta R^2}{N_{tot}}}, \tag{5.1}$$

$$RMS_{\Delta T} = \sqrt{\frac{\sum_1^{N_{tot}} \Delta T^2}{N_{tot}}}, \tag{5.2}$$

$$RMS_{\Delta N} = \sqrt{\frac{\sum_1^{N_{tot}} \Delta N^2}{N_{tot}}}, \tag{5.3}$$

while the total RSS and RMS result from

$$RSS = \sqrt{(RMS_{\Delta R})^2 + (RMS_{\Delta T})^2 + (RMS_{\Delta N})^2}, \tag{5.4}$$

$$RMS = \sqrt{\frac{(RMS_{\Delta R})^2 + (RMS_{\Delta T})^2 + (RMS_{\Delta N})^2}{3}}. \tag{5.5}$$

Differences between the propagated and the fitted orbit are plotted in RTN reference frame for one day, one month and one year respectively in Figures 5.7, 5.8 and 5.9.

NAPEOS allows to include in the force model empirical accelerations, estimated in the radial, along-track and cross-track directions to compensate model omission errors. They consist of a combination of two periodic terms, function of the satellite argument of latitude $u = \omega + f$, and a constant one, as

$$\begin{aligned} \Delta\mathbf{a}_r &= (a_{r\,0} + a_{r\,c} \cos u + a_{r\,s} \sin u)\, \mathbf{u}_r \\ \Delta\mathbf{a}_a &= (a_{a\,0} + a_{a\,c} \cos u + a_{a\,s} \sin u)\, \mathbf{u}_a \\ \Delta\mathbf{a}_c &= (a_{c\,0} + a_{c\,c} \cos u + a_{c\,s} \sin u)\, \mathbf{u}_c. \end{aligned} \tag{5.6}$$

The corresponding nine parameters $(a_{r\,0}, a_{r\,c}, a_{r\,s}, a_{a\,0}, a_{a\,c}, a_{a\,s}, a_{c\,0}, a_{c\,c}, a_{c\,s})$ are called CPR because the period of these accelerations is one cycle per revolution.

To evaluate how much of the tidal signal is absorbed by CPR coefficients, another fit was performed including the static gravity field and the along- and cross-track CPR (see Table 5.2). Radial CPR is not considered because depends on the along-track CPR. This specific study is interesting in order to build a suitable setup in NAPEOS for GOCE POD and ocean tide parameter estimation through a multiarc solution. The goal is to obtain a good trade-off between the compensation of the model omission errors during the GOCE POD and the non-absorption of the tidal signal from which tidal parameters will be estimated.

Table 5.1. Statistic comparison between the propagated and the fitted orbit: RMS along the radial, transverse and normal directions, RSS and total RMS for one day, one month and one year. CPR are not included in the fitted orbit.

Time Interval	**RMS$_{\Delta R}$**	**RMS$_{\Delta T}$**	**RMS$_{\Delta N}$**	**RSS**	**RMS**
1 day	7.60 cm	82.52 cm	11.25 cm	83.59 cm	48.26 cm
1 month	8.71 m	31.68 m	10.90 m	34.61 m	19.99 m
1 year	31.33 m	112.18 m	196.53 m	228.45 m	131.90 m

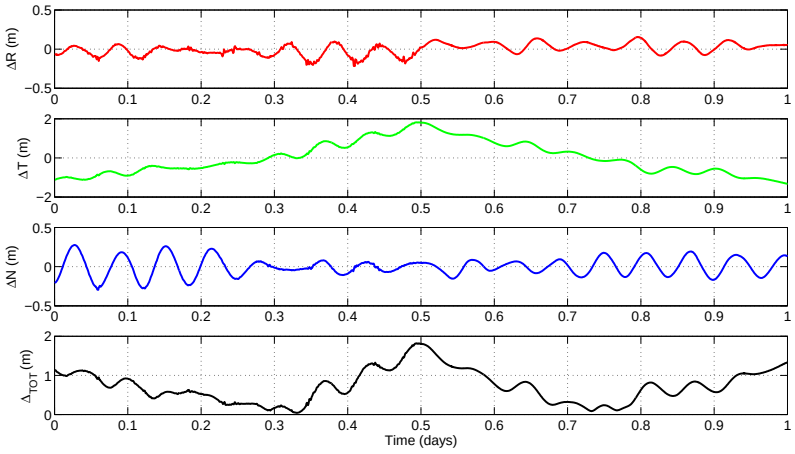

Figure 5.7. Difference between GOCE orbit propagated with gravity field and ocean tides and its fit with only the gravity field over a period of 1 day. Total RMS is of the order of 48.26 cm. CPR are not included in the fitted orbit.

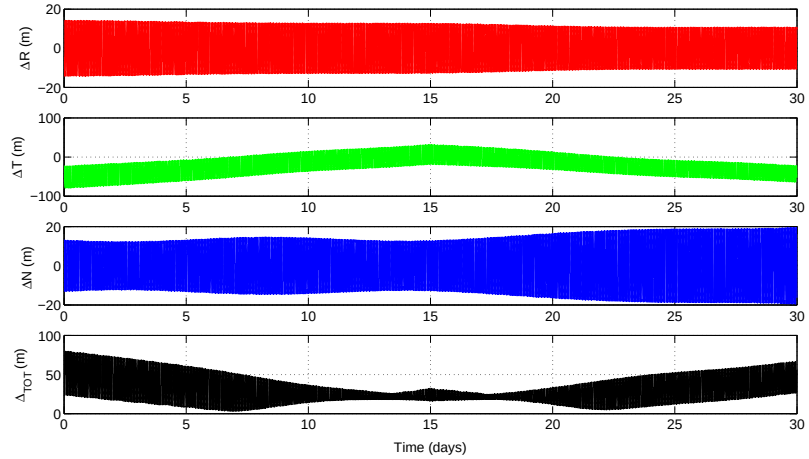

Figure 5.8. Difference between GOCE orbit propagated with gravity field and ocean tides and its fit with only the gravity field over a period of 1 month. Total RMS is of the order of 19.98 m. CPR are not included in the fitted orbit.

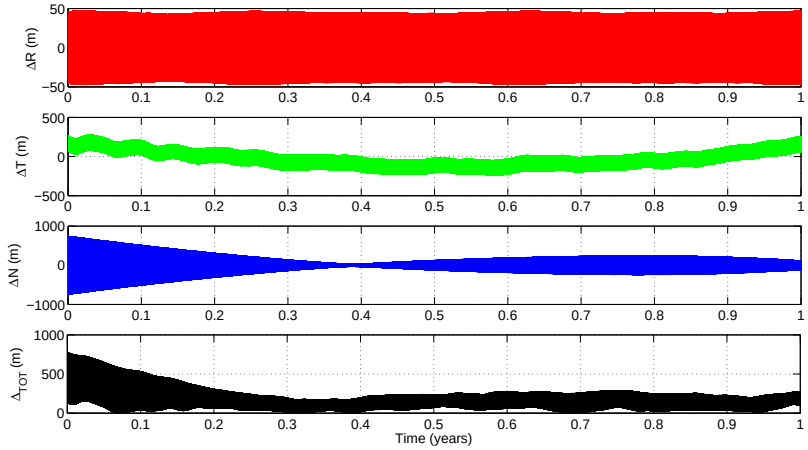

Figure 5.9. Difference between GOCE orbit propagated with gravity field and ocean tides and its fit with only the gravity field over a period of 1 year. Total RMS is of the order of 131.90 m. CPR are not included in the fitted orbit.

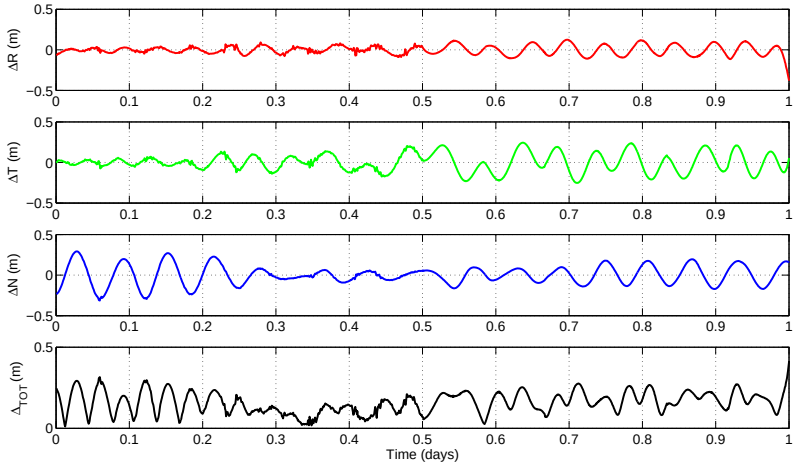

Figure 5.10. Difference between GOCE orbit propagated with gravity field and ocean tides and its fit with the gravity field and along-track CPR for 12 intervals over a period of 1 day. Total RMS is of the order of 9.90 cm.

Table 5.2. Statistic comparison between the propagated and the fitted orbit along the radial, transverse and normal directions, RSS and total RMS for one day, one month and one year. Along- and cross-track CPR (sine, cosine and constant coefficients) are included in the fitted orbit for different numbers of intervals over 1 day.

Time Interval	CPR Intervals	$\mathbf{RMS}_{\Delta R}$	$\mathbf{RMS}_{\Delta T}$	$\mathbf{RMS}_{\Delta N}$	RSS	RMS
	AT, 12 intervals	5.80 cm	11.04 cm	11.77 cm	17.14 cm	9.90 cm
1 day	CT, 12 intervals	18.48 cm	211.42 cm	3.48 cm	212.25 cm	122.55 cm
	AT+CT, 12 intervals	5.80 cm	11.04 cm	1.60 cm	12.57 cm	7.26 cm
	AT, 24 intervals	1.16 cm	1.08 cm	11.27 cm	11.38 cm	6.57 cm
1 day	CT, 24 intervals	24.24 cm	198.49 cm	4.55 cm	200.02 cm	115.48 cm
	AT+CT, 24 intervals	1.16 cm	1.08 cm	0.46 cm	1.65 cm	0.95 cm

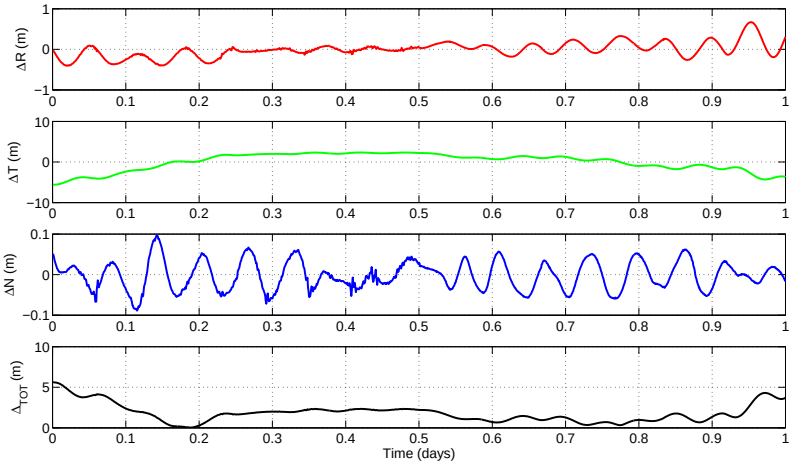

Figure 5.11. Difference between GOCE orbit propagated with gravity field and ocean tides and its fit with the gravity field and cross-track CPR for 12 intervals over a period of 1 day. Total RMS is of the order of 122.54 cm.

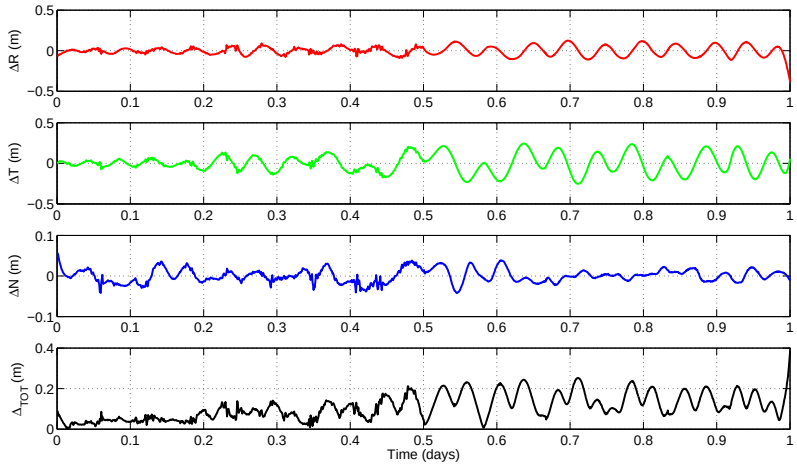

Figure 5.12. Difference between GOCE orbit propagated with gravity field and ocean tides and its fit with the gravity field, along- and cross-track CPR for 12 intervals over a period of 1 day. Total RMS is of the order of 7.26 cm.

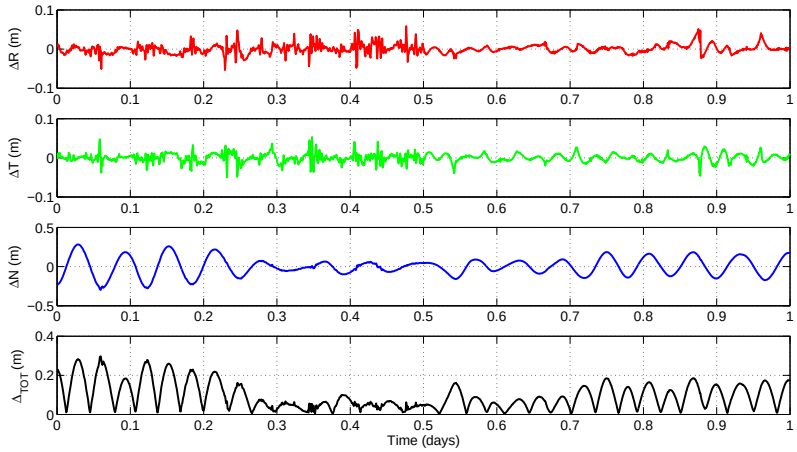

Figure 5.13. Difference between GOCE orbit propagated with gravity field and ocean tides and its fit with the gravity field and along-track CPR for 24 intervals over a period of 1 day. Total RMS is of the order of 6.54 cm.

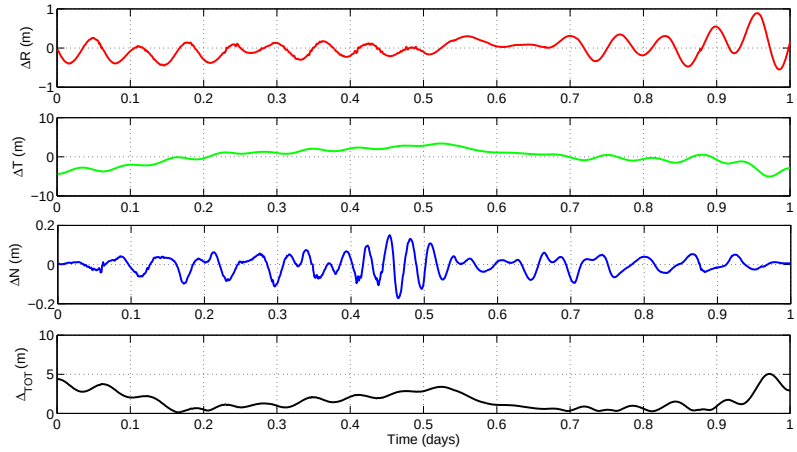

Figure 5.14. Difference between GOCE orbit propagated with gravity field and ocean tides and its fit with the gravity field and cross-track CPR for 24 intervals over a period of 1 day. Total RMS is of the order of 115.50 cm.

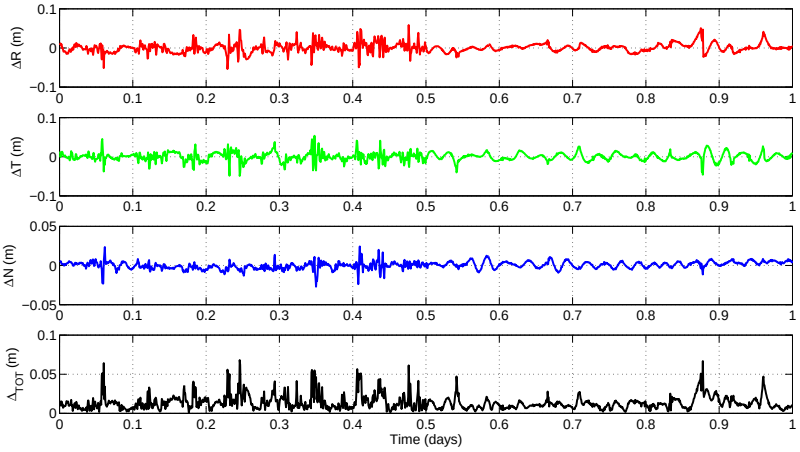

Figure 5.15. Difference between GOCE orbit propagated with gravity field and ocean tides and its fit with the gravity field, along- and cross-track CPR for 24 intervals over a period of 1 day. Total RMS is of the order of 0.95 cm.

5.2 Computation of ocean tide accelerations on GOCE orbit due to existent models

Accelerations due to ocean tides acting on GOCE orbit at a specified epoch were determined using different existent ocean tide models: FES2004, CSR 3.0, CSR 4.0, GOT00, TPXO6, SCW80, NAO99. As GOCE reference orbit we used kinematic orbits covering the period from 31 October 2009 to 11 January 2010 (72 days). The RMS of these accelerations are reported in Table 5.3 for each ocean tide model considered.

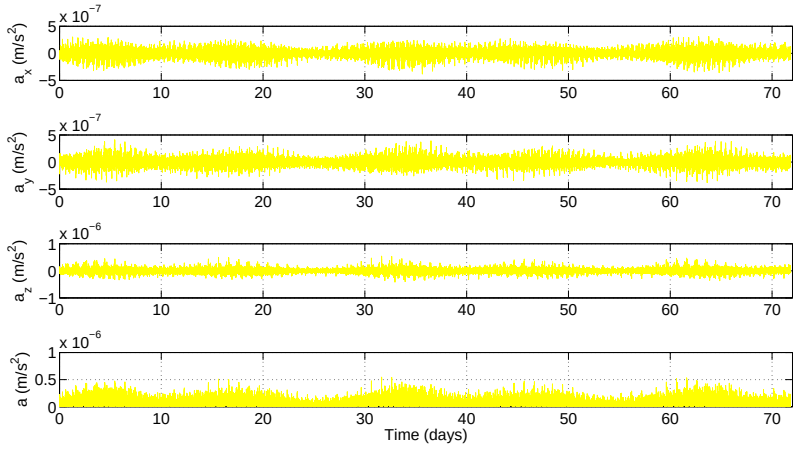

Figure 5.16. Ocean tide acceleration acting on GOCE orbit over a period of 72 days, computed using Schwiderski ocean tide model ([109], Schwiderski, 1980). The total RMS is 5.69×10^{-8} m/s^2.

Table 5.3. RMS of ocean tide accelerations due to different ocean tide models and affecting GOCE orbit, computed over the period from 31 October 2009 to 11 January 2010. For each model, maps of amplitude and phase were harmonically analyzed up to degree and order 50.

Ocean Tide Model	Angular Resolution	Tidal Constituents	Acceleration RMS
SCW80 (Schwiderski, 1980)	1°×1°	$Q_1, O_1, P_1, K_1, N_2, M_2, S_2, K_2, M_f$	5.69×10^{-8} m/s^2
CSR3.0 (Eanes and Bettadpur, 1995)	0.5°×0.5°	$Q_1, O_1, P_1, K_1, N_2, M_2, S_2, K_2$	5.72×10^{-8} m/s^2
CSR4.0 (Eanes and Bettadpur, 1999)	0.5°×0.5°	$Q_1, O_1, P_1, K_1, N_2, M_2, S_2, K_2$	5.74×10^{-8} m/s^2
GOT00 (Ray, 2000)	0.5°×0.5°	$Q_1, O_1, P_1, K_1, N_2, M_2, S_2, K_2$	5.69×10^{-8} m/s^2
NAO99 (Matsumoto et al., 2000)	0.5°×0.5°	$Q_1, O_1, P_1, K_1, N_2, M_2, S_2, K_2, M_f$	5.69×10^{-8} m/s^2
TPXO6 (Egbert and Erofeeva, 2002)	0.25°×0.25°	$Q_1, O_1, P_1, K_1, N_2, M_2, S_2, K_2, M_f$	5.69×10^{-8} m/s^2
FES2004 (Lyard et al., 2006)	0.125°×0.25°	$Q_1, O_1, P_1, K_1, S_1, N_2, M_2, S_2, K_2, 2N_2, M_f, M_m, M_{tm}, M_{Sqm}$	5.70×10^{-8} m/s^2

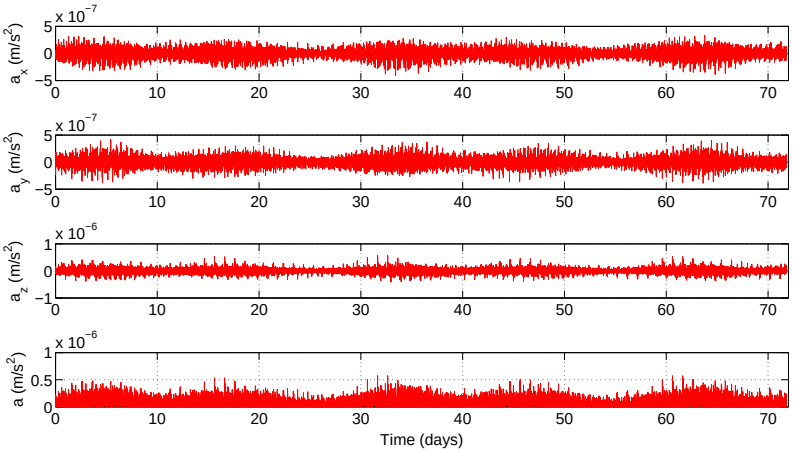

Figure 5.17. Ocean tide acceleration acting on GOCE orbit over a period of 72 days, computed using the CSR 3.0 ocean tide model ([39], Eanes and Bettadpur, 1995). The total RMS is 5.72×10^{-8} m/s^2.

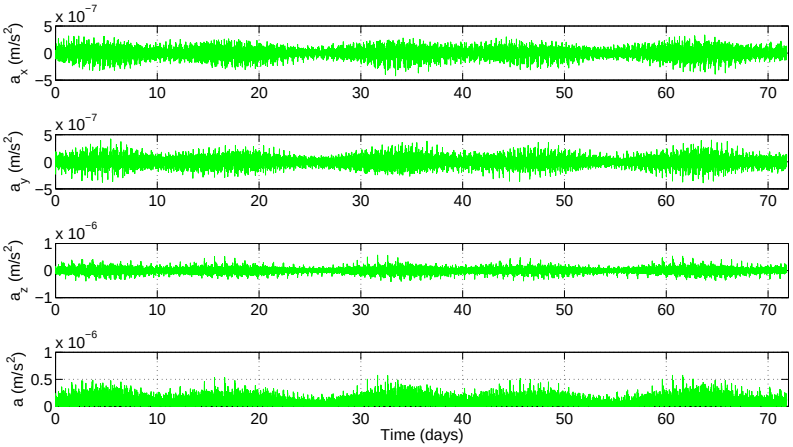

Figure 5.18. Ocean tide acceleration acting on GOCE orbit over a period of 72 days, computed using the CSR 4.0 ocean tide model ([39], Eanes and Bettadpur, 1995). The total RMS is 5.74×10^{-8} m/s^2.

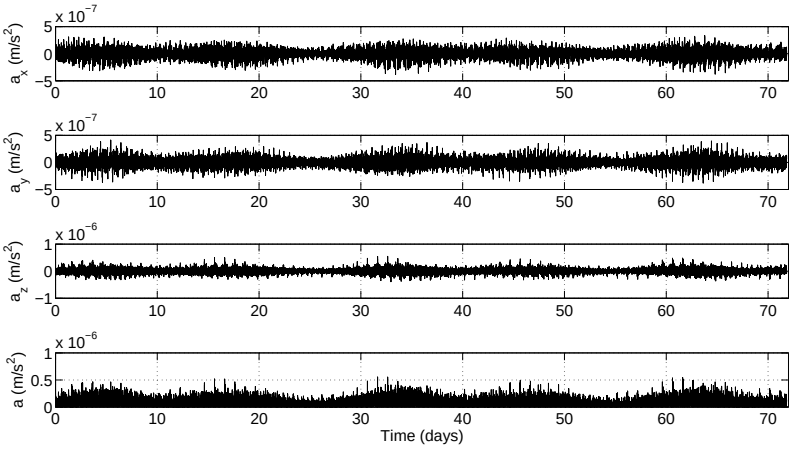

Figure 5.19. Ocean tide acceleration acting on GOCE orbit over a period of 72 days, computed using the GOT00 ocean tide model ([99], Ray, 1999). The total RMS is 5.69×10^{-8} m/s^2.

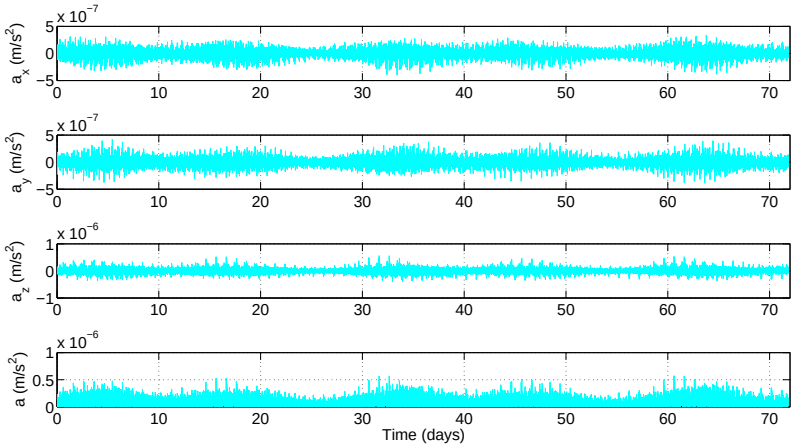

Figure 5.20. Ocean tide acceleration acting on GOCE orbit over a period of 72 days, computed using the NAO99 ocean tide model ([85], Matsumoto et al., 2000). The total RMS is 5.69×10^{-8} m/s^2.

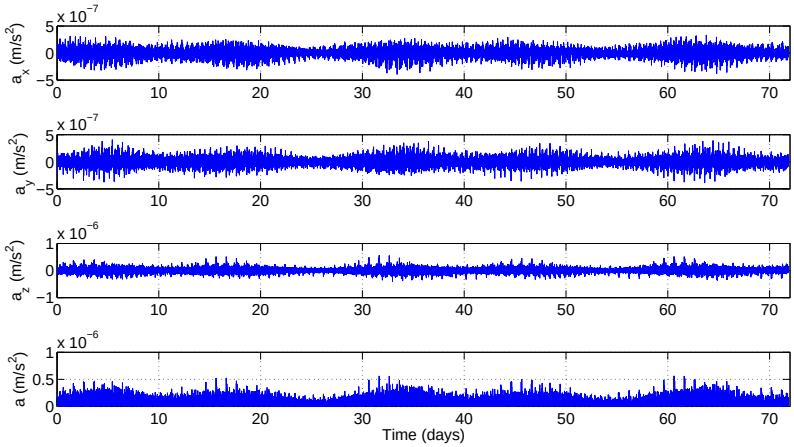

Figure 5.21. Ocean tide acceleration acting on GOCE orbit over a period of 72 days, computed using the TPXO6 ocean tide model ([40] Egbert and Erofeeva, 2002). The total RMS is 5.69×10^{-8} m/s^2.

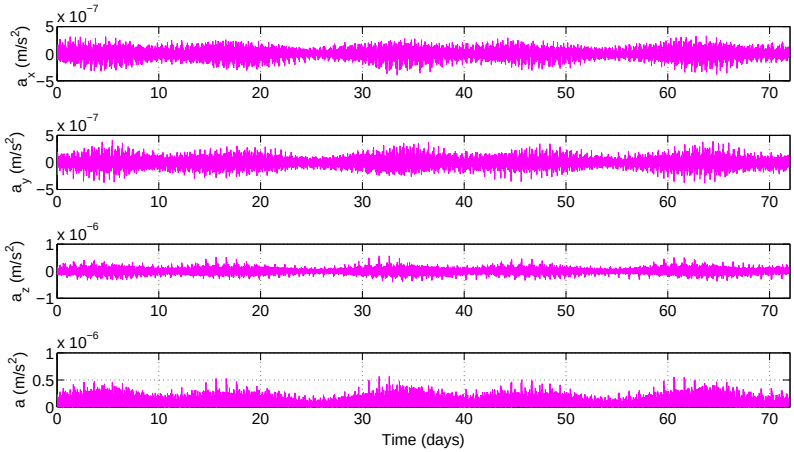

Figure 5.22. Ocean tide acceleration acting on GOCE orbit over a period of 72 days, computed using the FES2004 ocean tide model ([79] Lyard et al., 2006). The total RMS is 5.70×10^{-8} m/s^2.

5.3 Evolution of GOCE orbital elements

The natural evolution of GOCE orbital elements was analyzed along the period for which GOCE precise orbits were determined (1st November 2009 to 31st May 2011) as a preliminary study for the evaluation of ocean tide perturbations on the GOCE orbit. Figures 5.23, 5.24, 5.25, 5.27, 5.26, 5.28 and 5.29 show respectively the pattern of semimajor axis, eccentricity, inclination, longitude of ascending node, argument of perigee, mean anomaly and true anomaly.

In Figure 5.23, the changes of semimajor axis after the periods of missing data due to on-board failures can be observed: of particular significance were anomalies on the platform computers in 2010, leading to a prolonged interruption of the scientific mission.

The argument of perigee shows several numerical problems corresponding to low peaks of eccentricity of the order of 10^{-5}.

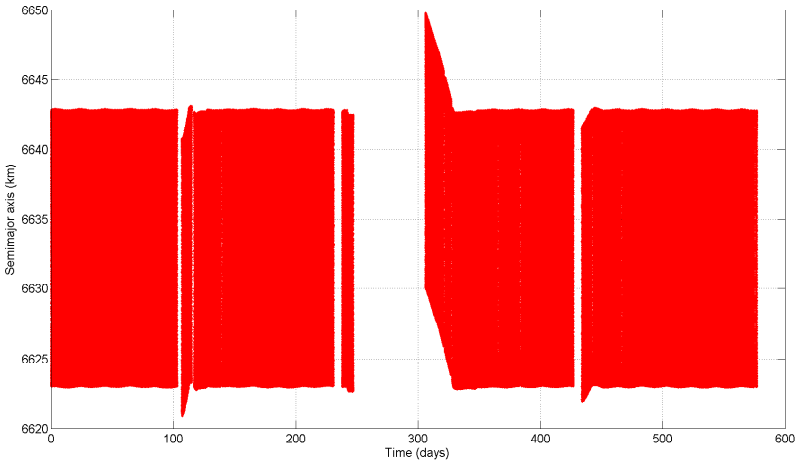

Figure 5.23. Evolution of the semimajor axis of GOCE orbit over the period 1st November 2009 - 31st May 2011. Units are kilometers.

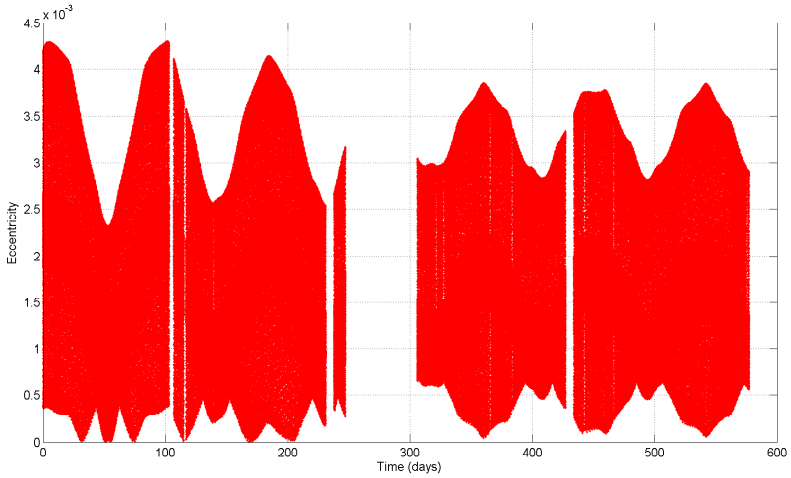

Figure 5.24. Evolution of the eccentricity of GOCE orbit over the period 1st November 2009 to 31st May 2011.

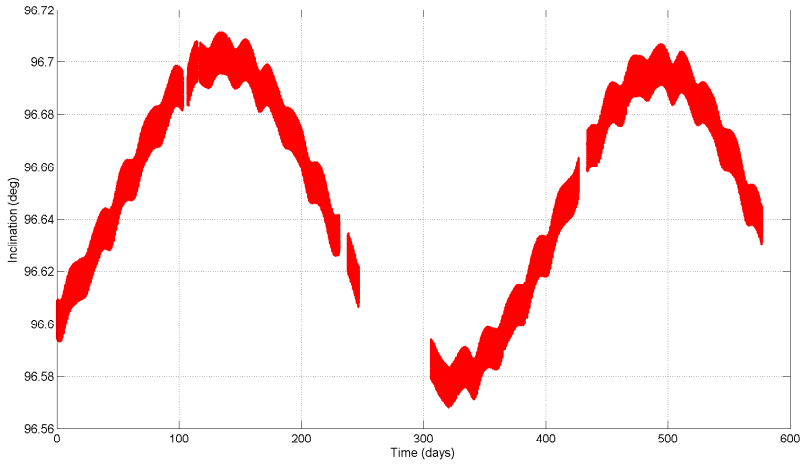

Figure 5.25. Evolution of the inclination of GOCE orbit over the period 1st November 2009 - 31st May 2011. Units are degrees.

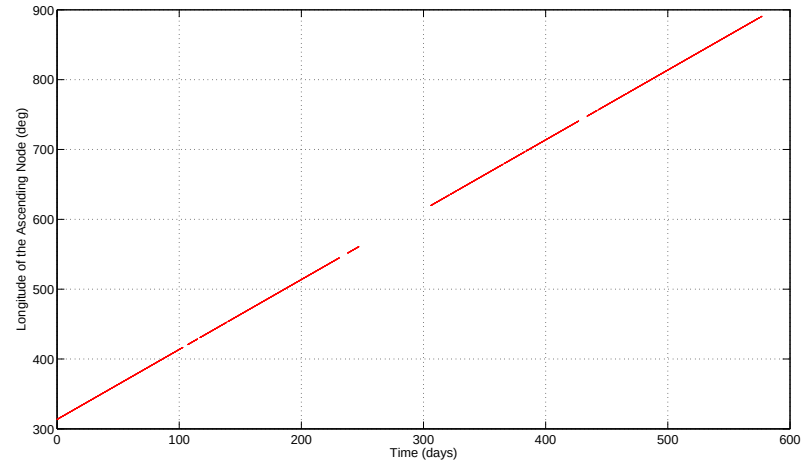

Figure 5.26. Evolution of the longitude of ascending node of GOCE orbit over the period 1st November 2009 - 31st May 2011. Units are degrees.

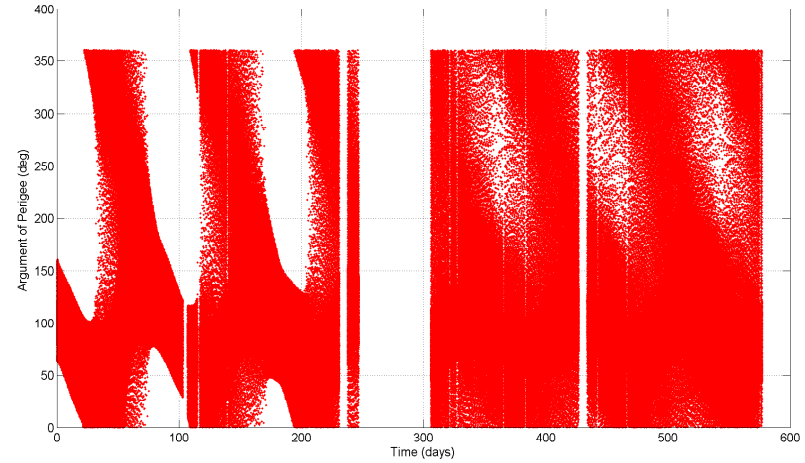

Figure 5.27. Evolution of the argument of perigee of GOCE orbit over the period 1st November 2009 - 31st May 2011. Units are degrees.

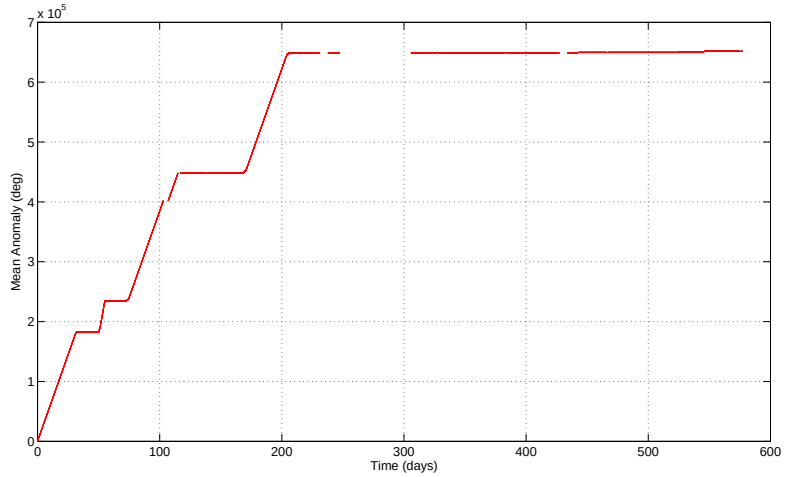

Figure 5.28. Evolution of the mean anomaly of GOCE orbit over the period 1st November 2009 - 31st May 2011. Units are degrees.

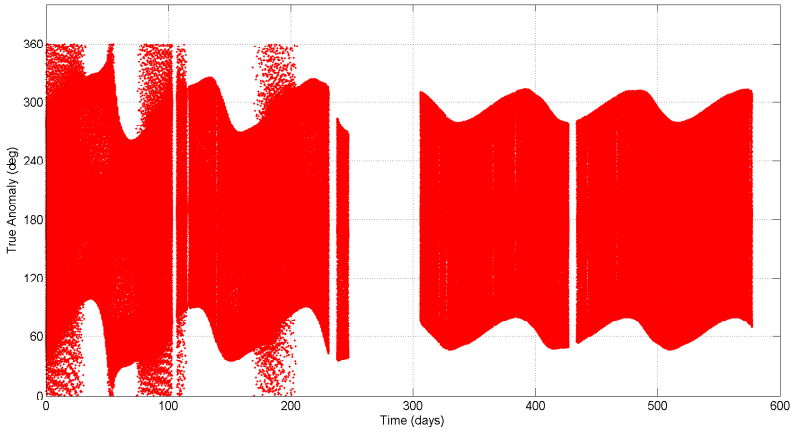

Figure 5.29. Evolution of the true anomaly of GOCE orbit over the period 1st November 2009 - 31st May 2011. Units are degrees.

5.4 Computation of the secular rates of GOCE angular elements

Considering the first 30 days of the GOCE precise estimated orbits (1st-30th November 2009), the secular rates of the angular elements of GOCE orbit (argument of perigee, longitude of ascending node, mean anomaly) were estimated through a linear least-square fit in order to account for the secular perturbations due to all the zonal terms C_{n0} of the geopotential. GOCE mean orbital characteristics are reported in Table 5.4.

Table 5.4. GOCE mean orbital elements and rates used for the spectral analysis of tidal perturbations on GOCE.

Element	Value
$\bar{a}$	6632.884525 km
$\bar{e}$	2.306273×10^{-3}
$\bar{i}$	1.686227 rad
ω_0	1.845595 rad
Ω_0	5.471748 rad
M_0	0.971383 rad
$\dot{\omega}$	-3.764817×10^{-7} rad/s
$\dot{\Omega}$	2.022334×10^{-7} rad/s
$\dot{M}$	1.167455×10^{-3} rad/s
Nodal Period	89.728100 min
Repeat Period	979 revs/61 nodal days

The obtained orbital rates lead to the ratio

$$\frac{\dot{M} + \dot{\omega}}{\dot{\theta}_g - \dot{\Omega}} = 16.049183, \tag{5.7}$$

which corresponds closely to the orbital resonance 16:1, so resonances will occur at orders m close to 16, 32, 48, 64, etc.

The nodal period N_p is given by

$$N_p = \frac{2\pi}{\dot{M} + \dot{\omega}} = 89.728053 \quad \text{min}, \tag{5.8}$$

while the nodal day[1] N_d is approximately equal to a solar day, because GOCE is a Sun-synchronous satellite

$$N_d = \frac{2\pi}{\omega_e - \dot{\Omega}} = 1.000043 \quad \text{days}. \tag{5.9}$$

Finally, the repeat period in solar days results form the multiplication between the nodal day and the repeat period T_{rp}^N in nodal days, which is 61 days for GOCE

$$T_rp = N_d T_{rp}^N = 61.002623 \quad \text{days}. \tag{5.10}$$

[1] A nodal day is the period between two consecutive passages of the ascending node of the satellite orbit over the same Earth-fixed meridian. In general, the precession of the ascending node is much slower than the Earth's rotation, so the nodal day differs slightly from a solar day; for a Sun-synchronous orbit a nodal day is equal to a solar day.

Figures 5.30, 5.31 and 5.32 show in blue the pattern of the angular element and in red the corresponding fit.

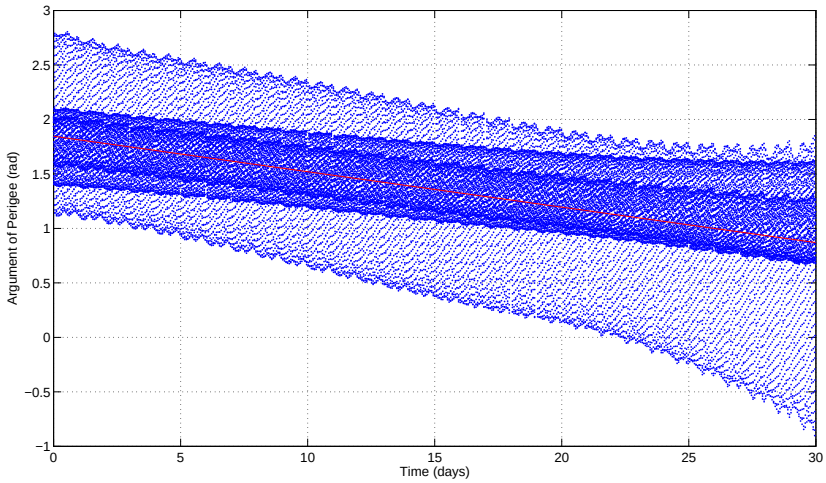

Figure 5.30. Fit of the argument of perigee.

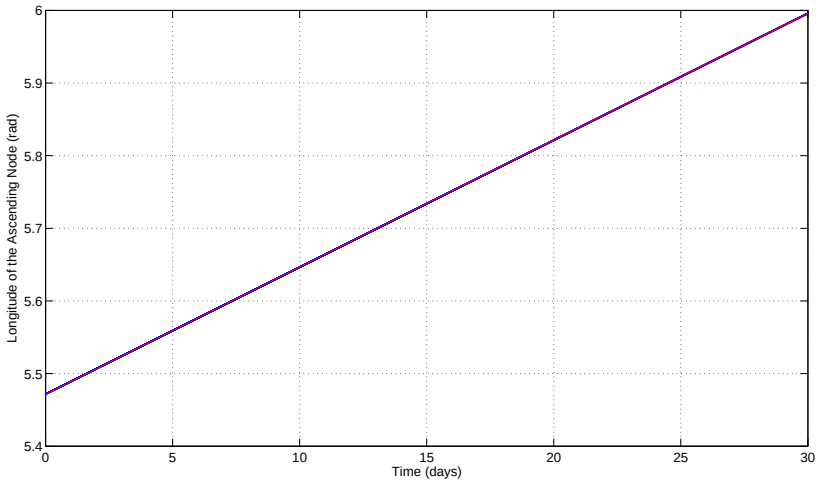

Figure 5.31. Fit of the ascending node.

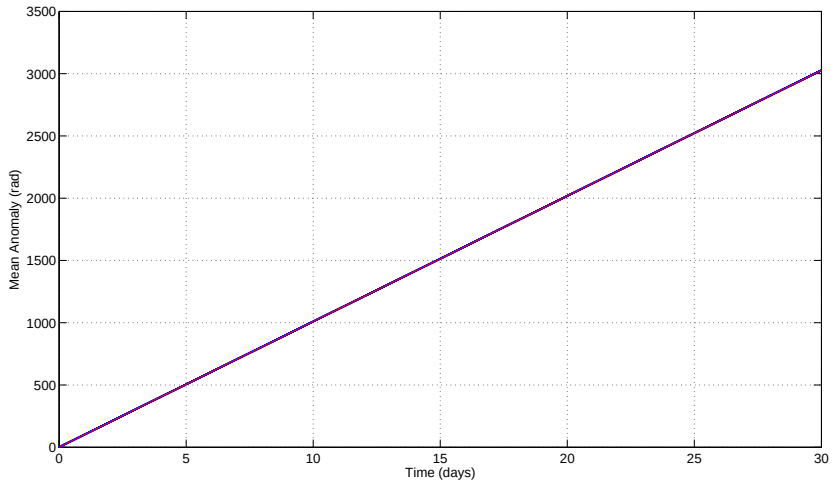

Figure 5.32. Fit of the mean anomaly.

5.5 Spectral analysis of ocean tide perturbations on GOCE

In order to identify a specific list of ocean tide parameters ($\bar{C}^{\pm}_{\mathbf{k}lm}, \bar{S}^{\pm}_{\mathbf{k}lm}$) to be estimated through a multiarc solution during the GOCE fully dynamic POD, it is necessary to evaluate the sensitivity of these parameters on GOCE orbit. An analytical method is used which determines the spectrum of ocean tide perturbations in the radial, transverse and normal (RTN) positions using Kaula's linear satellite theory.

5.5.1 Analytical spectrum from Kaula's linear satellite theory

The geopotential defined in (2.18) must be expressed as function of the orbital elements $(a, e, i, \omega, \Omega, M)$ through the Wigner's theorem[2] for the rotation of spherical harmonics, in order to be used in the Lagrange Planetary Equations. This formulation reads [64, Kaula, 1966]

$$V = \frac{GM_e}{R_e} \sum_{l=0}^{L} \sum_{m=0}^{l} \sum_{p=0}^{l} \sum_{q=-Q}^{Q} \left(\frac{R_e}{a}\right)^{l+1} \bar{F}_{lmp}(i) G_{lpq}(e) A_{lm} \cos(\nu_{lmpq} - \psi_{lm} + \pi_{lm}), \tag{5.13}$$

where $\bar{F}_{lmp}(i)$ are the normalized inclination functions, $G_{lpq}(e)$ the eccentricity functions, $\pi_{lm} = -\frac{\pi}{2} \mod (l+m, 2)$ is a phase correction accounting for the parity of $l+m$, A_{lm} and ψ_{lm} are respectively amplitude and phase in terms of the geopotential Stokes coefficients as

$$A_{lm} = \sqrt{\bar{C}^2_{lm} + \bar{S}^2_{lm}}, \tag{5.14}$$

$$\psi_{lm} = \arctan(\bar{S}_{lm}/\bar{C}_{lm}), \tag{5.15}$$

and ν_{lmpq} is the Kaula phase given by

$$\nu_{lmpq} = (l-2p)\omega + (l-2p+q)M + m(\Omega - \theta_g). \tag{5.16}$$

[2]The Wigner's theorem establishes that a spherical harmonic can be rotated by $R(\alpha, \beta, \gamma)$ as

$$Y_{lp}(\lambda', \phi') = \sum_{k=-l}^{l} D^l_{kp}(\alpha, \beta, \gamma) Y_{lk}(\lambda, \phi), \tag{5.11}$$

where D^l_{kp} are given in terms of the Wigner's coefficients

$$D^l_{kp}(\alpha, \beta, \gamma) = \mathrm{e}^{-\mathrm{i}\, k(\alpha - \pi/2)}\, d^l_{kp}(\beta)\, \mathrm{e}^{-\mathrm{i}\, p(\gamma + \pi/2)}\,. \tag{5.12}$$

The time derivative of (5.16) is the Kaula frequency, function of the satellite secular rates $(\dot{\omega}, \dot{\Omega}, \dot{M})$ and the Earth's rotation rate $\dot{\theta}_g$ as

$$\dot{\nu}_{lmpq} = (l-2p)\dot{\omega} + (l-2p+q)\dot{M} + m(\dot{\Omega} - \dot{\theta}_g). \tag{5.17}$$

Analogously, for the ocean tide case $A^{\pm}_{lm}$ and $\psi^{\pm}_{lm}$ are respectively amplitude and phase in terms of the fully-normalized and adimensional ocean tide harmonic parameters $(\tilde{C}^{\pm}_{\mathbf{k}lm}, \tilde{S}^{\pm}_{\mathbf{k}lm})$, already defined in (3.92) and (3.93), so that

$$A^{\pm}_{lm} = \sqrt{\tilde{C}^{\pm 2}_{lm} + \tilde{S}^{\pm 2}_{lm}}, \tag{5.18}$$

$$\psi^{\pm}_{lm} = \arctan(\tilde{S}^{\pm}_{lm}/\tilde{C}^{\pm}_{lm}), \tag{5.19}$$

Kaula's linear satellite theory ([64] Kaula, 1966) allows the analytical determination of the spectrum of ocean tide perturbations affecting a satellite, both in the orbital elements and in the RTN positions and velocities. In particular, ocean tide perturbations in the radial, transverse and normal positions (Δr, $\Delta\tau$, $\Delta\chi$) are given respectively by [14, Casotto, 1989]

$$\Delta r = \sum_{l=1}^{L}\sum_{m=0}^{l}\sum_{p=0}^{l}\sum_{q=-Q}^{Q}\sum_{\mathbf{k}}\sum_{+}^{-} A^{\pm}_{\mathbf{k}lm} C^{r\pm}_{\mathbf{k}lmpq} \cos(\gamma^{\pm}_{\mathbf{k}lmpq} \mp \psi^{\pm}_{\mathbf{k}lm} + \pi_{lm}), \tag{5.20}$$

$$\Delta\tau = \sum_{l=1}^{L}\sum_{m=0}^{l}\sum_{p=0}^{l}\sum_{q=-Q}^{Q}\sum_{\mathbf{k}}\sum_{+}^{-} A^{\pm}_{\mathbf{k}lm} C^{\tau\pm}_{\mathbf{k}lmpq} \sin(\gamma^{\pm}_{\mathbf{k}lmpq} \mp \psi^{\pm}_{\mathbf{k}lm} + \pi_{lm}), \tag{5.21}$$

$$\begin{aligned}\Delta\chi = \sum_{l=1}^{L}\sum_{m=0}^{l}\sum_{p=0}^{l}\sum_{q=-Q}^{Q}\sum_{\mathbf{k}}\sum_{+}^{-} A^{\pm}_{\mathbf{k}lm} \Big[& C^{\chi^+\pm}_{\mathbf{k}lmpq} \sin(\gamma^{\pm}_{\mathbf{k}(l+1)mpq} \mp \psi^{\pm}_{\mathbf{k}lm} + \pi_{lm}) \\ & - C^{\chi^-\pm}_{\mathbf{k}lmpq} \sin(\gamma^{\pm}_{\mathbf{k}(l-1)mpq} \mp \psi^{\pm}_{\mathbf{k}lm} + \pi_{lm}) \Big],\end{aligned} \tag{5.22}$$

where $\gamma^{\pm}_{\mathbf{k}lmpq}$ is the tidal argument defined in terms of the Kaula phase and the Doodson argument as

$$\gamma^{\pm}_{\mathbf{k}lmpq} = \nu_{lmpq} \pm \Theta_{\mathbf{k}} = \dot{\nu}_{lmpq}(t-t_0) + \nu^{0\pm}_{lmpq} \pm \dot{\Theta}_{\mathbf{k}}(t-t_0) \pm \Theta^0_{\mathbf{k}}, \tag{5.23}$$

where $\nu^{0\pm}_{lmpq}$ and $\Theta^0_{\mathbf{k}}$ are the Kaula phase and the Doodson argument at epoch t_0. The time derivative of the tidal argument in (5.23) represents the tidal perturbation frequency

$$\dot{\gamma}^{\pm}_{\mathbf{k}lmpq} = \dot{\nu}_{lmpq} \pm \dot{\Theta}_{\mathbf{k}} \tag{5.24}$$

which is the combination of the Kaula frequency $\dot{\nu}_{lmpq}$ and the Doodson frequency $\dot{\Theta}_{\mathbf{k}}$ in (2.43) and can not be zero (secular perturbation) for the incommensurability assumption between the satellite and the tidal frequencies. However, tidal secular perturbations exist and they result from the static part ($\mathbf{k} = 055.555$) of the tidal potential, corresponding to the constant term in the zonal TGP.

The functions $C^{r\pm}_{\mathbf{k}lmpq}$, $C^{\tau\pm}_{\mathbf{k}lmpq}$, $C^{\chi^+\pm}_{\mathbf{k}lmpq}$, $C^{\chi^-\pm}_{\mathbf{k}lmpq}$ have the units of a length and are expressed as [103, Rosborough and Tapley, 1987]

$$C^{r\pm}_{\mathbf{k}lmpq} = \sum_{s=-S}^{S} (\dot{\gamma}^{\pm}_{\mathbf{k}lmps})^{-1} \left[H_{q-s} E^{a\pm}_{lmps} + a H'_{q-s} E^{e\pm}_{lmps} + a(q-s) H_{q-s} E^{M\pm}_{lmps} \right], \tag{5.25}$$

$$\begin{aligned}C^{\tau\pm}_{\mathbf{k}lmpq} = a \sum_{s=-S}^{S} (\dot{\gamma}^{\pm}_{\mathbf{k}lmps})^{-1} \Big[& H_{q-s}(E^{\omega\pm}_{lmps} + E^{M\pm}_{lmps} + E^{\Omega\pm}_{lmps} \cos i) \\ & + \sum_{u=-U}^{U} H_{u-s} \left(I'_{q-u} E^{e\pm}_{lmps} + (q-u) I_{q-u} E^{M\pm}_{lmps} \right) \Big],\end{aligned} \tag{5.26}$$

$$C^{\chi^+\pm}_{\mathbf{k}lmpq} = \frac{a}{2}\sum_{s=-S}^{S}\sum_{u=-U}^{U}(\dot\gamma^{\pm}_{\mathbf{k}lmps})^{-1}H_{u-s}(E^{i\pm}_{lmps} - E^{\Omega\pm}_{lmps}\sin i)(R_{q-u+1} + Q_{q-u+1}), \tag{5.27}$$

$$C^{\chi^-\pm}_{\mathbf{k}lmpq} = \frac{a}{2}\sum_{s=-S}^{S}\sum_{u=-U}^{U}(\dot\gamma^{\pm}_{\mathbf{k}lmps})^{-1}H_{u-s}(E^{i\pm}_{lmps} + E^{\Omega\pm}_{lmps}\sin i)(R_{q-u-1} - Q_{q-u-1}). \tag{5.28}$$

It can be noticed that they depend on the excitation functions $E^{\alpha\pm}_{lmps}$ which at the first order are equivalent to E^{α}_{lmps} $\forall\ \alpha \in \{a, e, i, \omega, \Omega, M\}$ [64, Kaula, 1966]

$$\begin{aligned}
E^{a}_{lmpq} &= 2na\left(\frac{R_e}{a}\right)^l F_{lmp}Glpq(l-2p+q),\\
E^{e}_{lmpq} &= n\frac{\sqrt{1-e^2}}{e}\left(\frac{R_e}{a}\right)^l F_{lmp}G_{lpq}[(l-2p+q)\sqrt{1-e^2} - (l-2p)],\\
E^{i}_{lmpq} &= \frac{n}{\sqrt{1-e^2}\sin i}\left(\frac{R_e}{a}\right)^l F_{lmp}G_{lpq}[(l-2p)\cos i - m],\\
E^{\omega}_{lmpq} &= \frac{n}{\sqrt{1-e^2}\sin i}\left(\frac{R_e}{a}\right)^l \left[\frac{1-e^2}{e}F_{lmp}G'_{lpq}\sin i - F'_{lmp}G_{lpq}\cos i\right],\\
E^{\Omega}_{lmpq} &= \frac{n}{\sqrt{1-e^2}\sin i}\left(\frac{R_e}{a}\right)^l F'_{lmp}G_{lpq},\\
E^{M}_{lmpq} &= \frac{n}{\sqrt{1-e^2}\sin i}\left(\frac{R_e}{a}\right)^l F_{lmp}\left[2(l+1)G_{lpq} - \frac{1-e^2}{e}G'_{lpq}\right],
\end{aligned} \tag{5.29}$$

and on the special functions H_n, I_n, Q_n, R_n of order n, written in terms of the Bessel function J_n of the first kind of order n and its first derivative J'_n with respect to the eccentricity. The special functions are given by [103, Rosborough and Tapley, 1987]

$$\begin{array}{lll}
H_0 = 1 + \frac{e^2}{2}, & H_n = H_{-n} = -\frac{e}{n^2}J'_n(ne), & n = 1, 2, ..., \infty\\
R_0 = -e, & R_n = R_{-n} = \frac{(1-e^2)}{e}J_n(ne), & n = 1, 2, ..., \infty\\
Q_0 = 0, & Q_n = -Q_{-n} = \frac{1}{n}\sqrt{(1-e^2)}J'_n(ne), & n = 1, 2, ..., \infty\\
I_0 = 0, & I_n = -I_{-n}, & n = 1, 2, ..., \infty
\end{array} \tag{5.30}$$

where

$$I_n = \frac{1}{n}\left\{J_n(ne) + \sum_{\nu=1}^{\infty}\beta^{\nu}[J_{n-\nu}(ne) + J_{n+\nu}(ne)]\right\}, \qquad \beta = \frac{1-\sqrt{(1-e^2)}}{e}. \tag{5.31}$$

In order to compute spectral analysis of the RTN ocean tide perturbations, the equations in (5.20) must be written in spectral form as [14, Casotto, 1989]

$$\Delta r = \sum_{l=1}^{L}\sum_{m=0}^{l}\sum_{p=0}^{l}\sum_{q=-Q}^{Q}\sum_{\mathbf{k}}\sum_{+}^{-} A^{r\pm}_{\mathbf{k}lmpq}\cos(\dot\gamma^{\pm}_{\mathbf{k}lmpq}(t-t_0) \mp \psi^{r\pm}_{\mathbf{k}lmpq}), \tag{5.32}$$

$$\Delta\tau = \sum_{l=1}^{L}\sum_{m=0}^{l}\sum_{p=0}^{l}\sum_{q=-Q}^{Q}\sum_{\mathbf{k}}\sum_{+}^{-} A^{\tau\pm}_{\mathbf{k}lmpq}\sin(\dot\gamma^{\pm}_{\mathbf{k}lmpq}(t-t_0) \mp \psi^{\tau\pm}_{\mathbf{k}lmpq}), \tag{5.33}$$

$$\begin{aligned}
\Delta\chi = \sum_{l=1}^{L}\sum_{m=0}^{l}\sum_{p=0}^{l}\sum_{q=-Q}^{Q}\sum_{\mathbf{k}}\sum_{+}^{-} \Big[&A^{\chi^+\pm}_{\mathbf{k}lmpq}\sin(\dot\gamma^{\pm}_{\mathbf{k}(l+1)mpq}(t-t_0) \mp \psi^{\chi^+\pm}_{\mathbf{k}(l+1)mpq})\\
&- A^{\chi^-\pm}_{\mathbf{k}lmpq}\sin(\dot\gamma^{\pm}_{\mathbf{k}(l-1)mpq}(t-t_0) \mp \psi^{\chi^-\pm}_{\mathbf{k}(l-1)mpq})\Big],
\end{aligned} \tag{5.34}$$

where $A^{r\pm}_{\mathbf{k}lmpq}$, $A^{\tau\pm}_{\mathbf{k}lmpq}$, $A^{\chi^+\pm}_{\mathbf{k}lmpq}$, $A^{\chi^-\pm}_{\mathbf{k}lmpq}$ are the prograde and retrograde amplitudes of the spectral lines in the radial, transverse and normal directions

$$A^{r\pm}_{\mathbf{k}lmpq} = A^{\pm}_{\mathbf{k}lm} C^{r\pm}_{\mathbf{k}lmpq}, \tag{5.35}$$

$$A^{\tau\pm}_{\mathbf{k}lmpq} = A^{\pm}_{\mathbf{k}lm} C^{\tau\pm}_{\mathbf{k}lmpq}, \tag{5.36}$$

$$A^{\chi^+\pm}_{\mathbf{k}lmpq} = A^{\pm}_{\mathbf{k}lm} C^{\chi^+\pm}_{\mathbf{k}lmpq}, \tag{5.37}$$

$$A^{\chi^-\pm}_{\mathbf{k}lmpq} = A^{\pm}_{\mathbf{k}lm} C^{\chi^-\pm}_{\mathbf{k}lmpq}, \tag{5.38}$$

while $\psi^{r\pm}_{\mathbf{k}lmpq}$, $\psi^{\tau\pm}_{\mathbf{k}lmpq}$, $\psi^{\chi^+\pm}_{\mathbf{k}(l+1)mpq}$, $\psi^{\chi^-\pm}_{\mathbf{k}(l-1)mpq}$ are the corresponding phases, which can be defined separating the frequency part from the phase part of the cosine and sine arguments in (5.32), (5.33), (5.34) as

$$\gamma^{\pm}_{\mathbf{k}lmpq} \mp \psi^{\pm}_{\mathbf{k}lm} + \pi_{lm} = \dot{\nu}_{lmpq}(t-t_0) + \nu^{0\pm}_{lmpq} \pm \dot{\Theta}_{\mathbf{k}}(t-t_0) \pm \Theta^0_{\mathbf{k}} \mp \psi^{\pm}_{\mathbf{k}lm} + \pi_{lm}. \tag{5.39}$$

From this relation it follows that the spectral phases for the radial, transverse and normal components result

$$\psi^{r\pm}_{\mathbf{k}lmpq} = \psi^{\tau\pm}_{\mathbf{k}lmpq} = \psi^{\pm}_{\mathbf{k}lm} \mp \nu^{0\pm}_{lmpq} - \Theta^0_{\mathbf{k}} \mp \pi_{lm}, \tag{5.40}$$

$$\psi^{\chi^+\pm}_{\mathbf{k}(l+1)mpq} = \psi^{\pm}_{\mathbf{k}lm} \mp \nu^{0\pm}_{(l+1)mpq} - \Theta^0_{\mathbf{k}} \mp \pi_{lm}, \tag{5.41}$$

$$\psi^{\chi^-\pm}_{\mathbf{k}(l-1)mpq} = \psi^{\pm}_{\mathbf{k}lm} \mp \nu^{0\pm}_{(l-1)mpq} - \Theta^0_{\mathbf{k}} \mp \pi_{lm}. \tag{5.42}$$

The tide perturbation frequencies defined in (5.24) are chosen to be positive

$$\dot{\gamma}^{\pm}_{\mathbf{k}lmpq} = \begin{cases} \dot{\nu}_{lmpq} \pm \dot{\Theta}_{\mathbf{k}} & \text{if} \quad \dot{\gamma}^{\pm}_{\mathbf{k}lmpq} > 0 \\ -\dot{\nu}_{lmpq} \mp \dot{\Theta}_{\mathbf{k}} & \text{if} \quad \dot{\gamma}^{\pm}_{\mathbf{k}lmpq} < 0 \end{cases} \tag{5.43}$$

so also the phases of the cosine and sine terms in (5.32), (5.33), (5.34) must be changed in sign as

$$\psi^{r\pm}_{\mathbf{k}lmpq} = \psi^{\tau\pm}_{\mathbf{k}lmpq} = \begin{cases} \psi^{\pm}_{\mathbf{k}lm} \mp \nu^{0\pm}_{lmpq} - \Theta^0_{\mathbf{k}} \mp \pi_{lm} & \text{if} \quad \dot{\gamma}^{\pm}_{\mathbf{k}lmpq} > 0 \\ -(\psi^{\pm}_{\mathbf{k}lm} \mp \nu^{0\pm}_{lmpq} - \Theta^0_{\mathbf{k}} \mp \pi_{lm}) & \text{if} \quad \dot{\gamma}^{\pm}_{\mathbf{k}lmpq} < 0 \end{cases} \tag{5.44}$$

$$\psi^{\chi^+\pm}_{\mathbf{k}(l+1)mpq} = \begin{cases} \psi^{\pm}_{\mathbf{k}lm} \mp \nu^{0\pm}_{(l+1)mpq} - \Theta^0_{\mathbf{k}} \mp \pi_{lm} & \text{if} \quad \dot{\gamma}^{\pm}_{\mathbf{k}(l+1)mpq} > 0 \\ -(\psi^{\pm}_{\mathbf{k}lm} \mp \nu^{0\pm}_{(l+1)mpq} - \Theta^0_{\mathbf{k}} \mp \pi_{lm}) & \text{if} \quad \dot{\gamma}^{\pm}_{\mathbf{k}(l+1)mpq} < 0 \end{cases} \tag{5.45}$$

$$\psi^{\chi^-\pm}_{\mathbf{k}(l-1)mpq} = \begin{cases} \psi^{\pm}_{\mathbf{k}lm} \mp \nu^{0\pm}_{(l-1)mpq} - \Theta^0_{\mathbf{k}} \mp \pi_{lm} & \text{if} \quad \dot{\gamma}^{\pm}_{\mathbf{k}(l-1)mpq} > 0 \\ -(\psi^{\pm}_{\mathbf{k}lm} \mp \nu^{0\pm}_{(l-1)mpq} - \Theta^0_{\mathbf{k}} \mp \pi_{lm}) & \text{if} \quad \dot{\gamma}^{\pm}_{\mathbf{k}(l-1)mpq} < 0 \end{cases} \tag{5.46}$$

and, at the same time, the corresponding amplitudes are changed in sign following the general trigonometric relations $\cos(-\alpha) = \cos(\alpha)$ and $\sin(-\alpha) = -\sin(\alpha)$.

At this point, another check is required on the spectral amplitudes to force them to be positive, and in the case of negative amplitudes the sign of the spectral phases must be changed again taking advantage of the trigonometric formulas $\cos(\alpha+\pi) = -\cos(\alpha)$ for the radial case and $\sin(\alpha+\pi) = -\sin(\alpha)$ for the transverse and normal cases. After these algebraic manipulations, all the tide perturbation frequencies and the spectral amplitudes will be positive, balanced by the suitable changes in the corresponding spectral phases.

Now, it is important to notice that different combinations of indices (l, m, p, q) can generate the same tidal perturbation frequency $\dot{\gamma}^{\pm}_{\mathbf{k}lmpq}$. Thus, in order to compute the ocean tide perturbation spectrum, it is necessary to accumulate all the amplitudes and phases which refer to

the same frequency or spectral line. Using a simplified notation and defining each unique tidal perturbation frequency with $\dot{\gamma}^{\pm}_{\mathbf{k}f}$ and each pair of amplitude and phase contributing to the same frequency respectively with ($A^{r\pm}_{\mathbf{k}f}$, $\psi^{r\pm}_{\mathbf{k}f}$), ($A^{\tau\pm}_{\mathbf{k}f}$, $\psi^{\tau\pm}_{\mathbf{k}f}$), ($A^{\chi\pm}_{\mathbf{k}f}$, $\psi^{\chi\pm}_{\mathbf{k}f}$), we can express the prograde and retrograde ocean tide perturbations in the RTN positions for a specified constituent **k** as a Fourier series expansion

$$\Delta r^{\pm}_{\mathbf{k}} = \sum_{f=1}^{\infty}[a^{r\pm}_{\mathbf{k}f}\cos(\dot{\gamma}^{\pm}_{\mathbf{k}f}(t-t_0)) + b^{r\pm}_{\mathbf{k}f}\sin(\dot{\gamma}^{\pm}_{\mathbf{k}f}(t-t_0))], \tag{5.47}$$

$$\Delta \tau^{\pm}_{\mathbf{k}} = \sum_{f=1}^{\infty}[a^{\tau\pm}_{\mathbf{k}f}\cos(\dot{\gamma}^{\pm}_{\mathbf{k}f}(t-t_0)) + b^{\tau\pm}_{\mathbf{k}f}\sin(\dot{\gamma}^{\pm}_{\mathbf{k}f}(t-t_0))], \tag{5.48}$$

$$\Delta \chi^{\pm}_{\mathbf{k}} = \sum_{f=1}^{\infty}[a^{\chi\pm}_{\mathbf{k}f}\cos(\dot{\gamma}^{\pm}_{\mathbf{k}f}(t-t_0)) + b^{\chi\pm}_{\mathbf{k}f}\sin(\dot{\gamma}^{\pm}_{\mathbf{k}f}(t-t_0))], \tag{5.49}$$

where each pair of Fourier coefficients ($a^{r\pm}_{\mathbf{k}f}, a^{r\pm}_{\mathbf{k}f}$), ($a^{\tau\pm}_{\mathbf{k}f}, a^{\tau\pm}_{\mathbf{k}f}$), ($a^{\chi\pm}_{\mathbf{k}f}, a^{\chi\pm}_{\mathbf{k}f}$) results from the combination of all the spectral amplitudes and phase contributing to the same spectral frequency $\dot{\gamma}_{\mathbf{k}f}$. Given the spectral formulation in (5.32), (5.33), (5.34) and following the standard relations for trigonometric products, the pairs of Fourier coefficients for the RTN perturbations are determined respectively as

$$a^{r\pm}_{\mathbf{k}f} = \sum_f A^{r\pm}_{\mathbf{k}f}\cos(\psi^{r\pm}_{\mathbf{k}f}), \qquad b^{r\pm}_{\mathbf{k}f} = \pm\sum_f A^{r\pm}_{\mathbf{k}f}\sin(\psi^{r\pm}_{\mathbf{k}f}), \tag{5.50}$$

$$a^{\tau\pm}_{\mathbf{k}f} = \mp\sum_f A^{\tau\pm}_{\mathbf{k}f}\sin(\psi^{\tau\pm}_{\mathbf{k}f}), \qquad b^{\tau\pm}_{\mathbf{k}f} = \sum_f A^{\tau\pm}_{\mathbf{k}f}\cos(\psi^{\tau\pm}_{\mathbf{k}f}), \tag{5.51}$$

$$a^{\chi\pm}_{\mathbf{k}f} = \sum_f A^{\chi\pm}_{\mathbf{k}f}\sin(\psi^{\chi\pm}_{\mathbf{k}f}), \qquad b^{\chi\pm}_{\mathbf{k}f} = \sum_f A^{\chi\pm}_{\mathbf{k}f}\cos(\psi^{\chi\pm}_{\mathbf{k}f}). \tag{5.52}$$

As a consequence, for each constituent, the total amplitude and the total phase referring to the same spectral line are respectively

$$A^{\pm}_{\mathbf{k}f} = \sqrt{a^{r\pm 2}_{\mathbf{k}f} + b^{r\pm 2}_{\mathbf{k}f}}, \qquad \Psi^{\pm}_{\mathbf{k}f} = \arctan(b^{r\pm}_{\mathbf{k}f}/a^{r\pm}_{\mathbf{k}f}), \tag{5.53}$$

$$A^{\pm}_{\mathbf{k}f} = \sqrt{a^{\tau\pm 2}_{\mathbf{k}f} + b^{\tau\pm 2}_{\mathbf{k}f}}, \qquad \Psi^{\pm}_{\mathbf{k}f} = \arctan(b^{\tau\pm}_{\mathbf{k}f}/a^{\tau\pm}_{\mathbf{k}f}), \tag{5.54}$$

$$A^{\pm}_{\mathbf{k}f} = \sqrt{a^{\chi\pm 2}_{\mathbf{k}f} + b^{\chi\pm 2}_{\mathbf{k}f}}, \qquad \Psi^{\pm}_{\mathbf{k}f} = \arctan(b^{\chi\pm}_{\mathbf{k}f}/a^{\chi\pm}_{\mathbf{k}f}). \tag{5.55}$$

The main resonances of the ocean tide perturbations belong to the short period band and are defined by

$$(l-2p+q)\dot{M} \approx (m \mp s)\dot{\theta}_g, \tag{5.56}$$

being s the tidal species and leading to a resonant harmonic order

$$m \approx k\frac{\dot{M}}{\dot{\theta}_g} \pm s, \tag{5.57}$$

where $k = l - 2p + q$ is the order of the resonance.

Following the mathematical formulation described above, the analytical spectral analysis of ocean tide perturbations on GOCE was computed using, as reference model, the FES2004 model (Lyard et al., 2006) up to degree and order 20×20 for 106 constituents reported in Table 2.3. GOCE mean orbital elements and rates used to compute the spectral analysis are reported in Table 5.4.

The obtained prograde and retrograde radial amplitude spectra are shown in Figures 5.33 and 5.34. The prograde and retrograde transverse amplitude spectra are shown in Figures 5.35 and 5.36. The prograde and retrograde normal amplitude spectra are shown in Figures 5.37 and 5.38.

All the spectra show resonances at frequencies of 16 cyc/day (once-per-rev band) and its multiples and a very strong resonance is especially evident in the normal prograde spectrum. Moreover, the radial amplitude spectrum show large perturbations in the short period band, while the transverse amplitude spectrum is characterized by large long period perturbations.

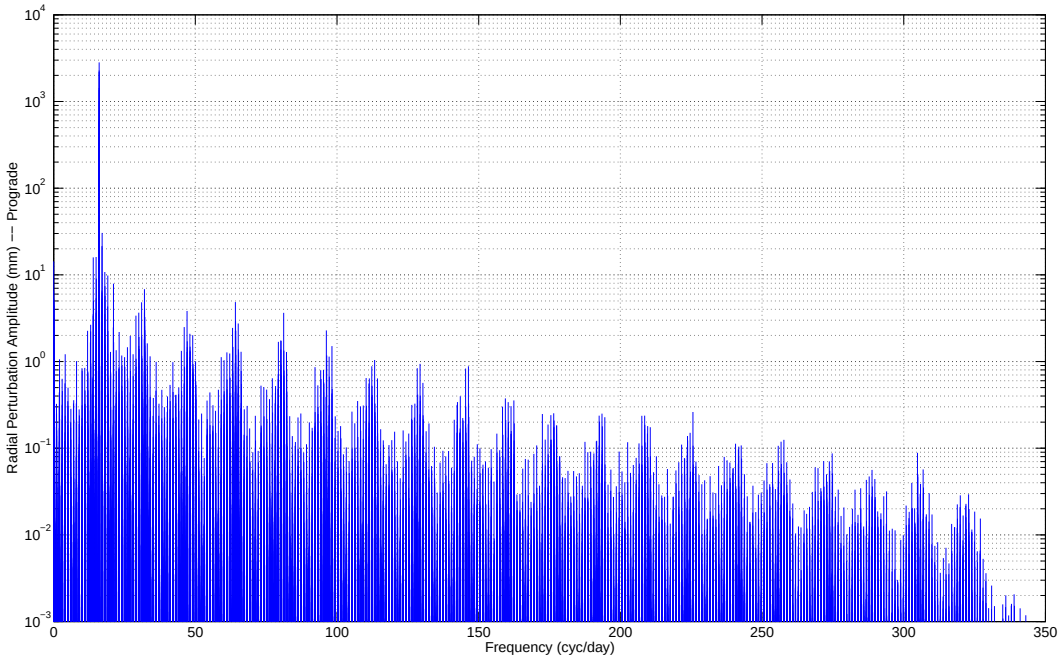

Figure 5.33. Amplitude spectrum of the radial prograde perturbation in position due to ocean tides.

5.5.2 Statistics of ocean tide perturbations by coefficient

The ocean tide perturbations in the RTN positions generated by the prograde and retrograde coefficient (l, m) for a constituent $\mathbf{k}$ can be expressed using the spectral equations (5.32), (5.33), (5.34), where only the summations over the indices (p, q) remain, as

$$\Delta r^{\pm}_{\mathbf{k}lm} = \sum_{p=0}^{l} \sum_{q=-Q}^{Q} A^{r\pm}_{\mathbf{k}lmpq} \cos(\dot{\gamma}^{\pm}_{\mathbf{k}lmpq}(t-t_0) \mp \psi^{r\pm}_{\mathbf{k}lmpq}), \tag{5.58}$$

$$\Delta \tau^{\pm}_{\mathbf{k}lm} = \sum_{p=0}^{l} \sum_{q=-Q}^{Q} A^{\tau\pm}_{\mathbf{k}lmpq} \sin(\dot{\gamma}^{\pm}_{\mathbf{k}lmpq}(t-t_0) \mp \psi^{\tau\pm}_{\mathbf{k}lmpq}), \tag{5.59}$$

$$\begin{aligned} \Delta \chi^{\pm}_{\mathbf{k}lm} = \sum_{p=0}^{l} \sum_{q=-Q}^{Q} \Big[& A^{\chi^+\pm}_{\mathbf{k}lmpq} \sin(\dot{\gamma}^{\pm}_{\mathbf{k}(l+1)mpq}(t-t_0) \mp \psi^{\chi^+\pm}_{\mathbf{k}(l+1)mpq}) \\ & - A^{\chi^-\pm}_{\mathbf{k}lmpq} \sin(\dot{\gamma}^{\pm}_{\mathbf{k}(l-1)mpq}(t-t_0) \mp \psi^{\chi^-\pm}_{\mathbf{k}(l-1)mpq}) \Big]. \end{aligned} \tag{5.60}$$

The mean of the square values of the perturbations by coefficients $< (\Delta r^{\pm}_{\mathbf{k}lm})^2 >$, $< (\Delta \tau^{\pm}_{\mathbf{k}lm})^2 >$, $< (\Delta \chi^{\pm}_{\mathbf{k}lm})^2 >$ depend on the mean of the product between cosine and sine terms, such as $< \cos(\dot{\gamma}^{\pm}_{\mathbf{k}lmpq}(t-t_0) \mp \psi^{r\pm}_{\mathbf{k}lmpq}) \cos(\dot{\gamma}^{\pm}_{\mathbf{k}lmuv}(t-t_0) \mp \psi^{r\pm}_{\mathbf{k}lmpq}) >$, which are not zero only for

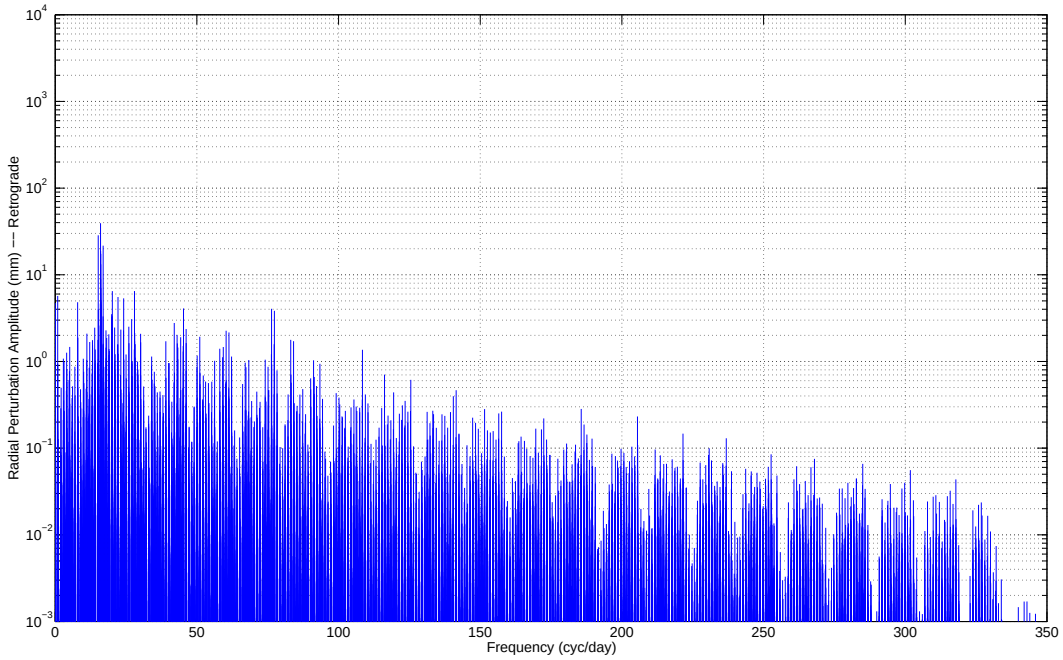

Figure 5.34. Amplitude spectrum of the radial retrograde perturbation in position due to ocean tides.

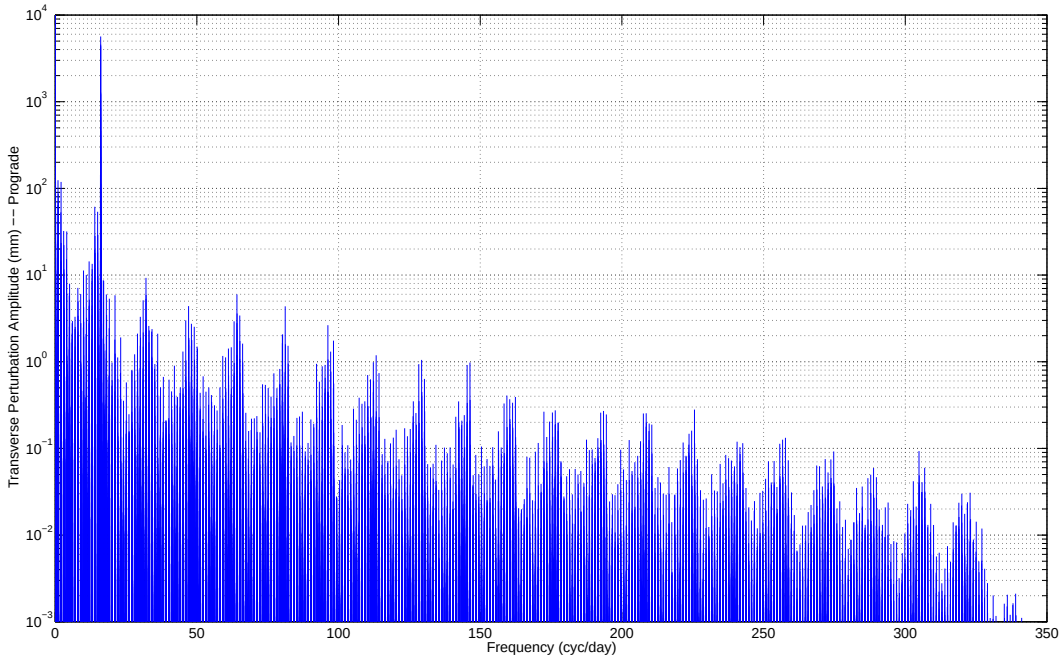

Figure 5.35. Amplitude spectrum of the transverse prograde perturbation in position due to ocean tides.

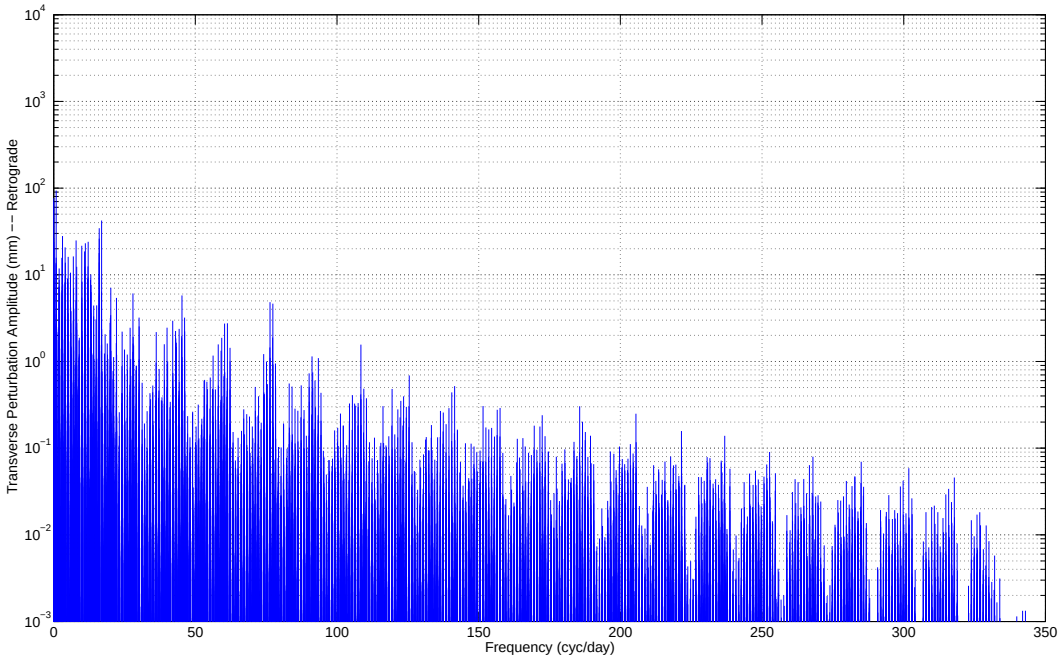

Figure 5.36. Amplitude spectrum of the transverse retrograde perturbation in position due to ocean tides.

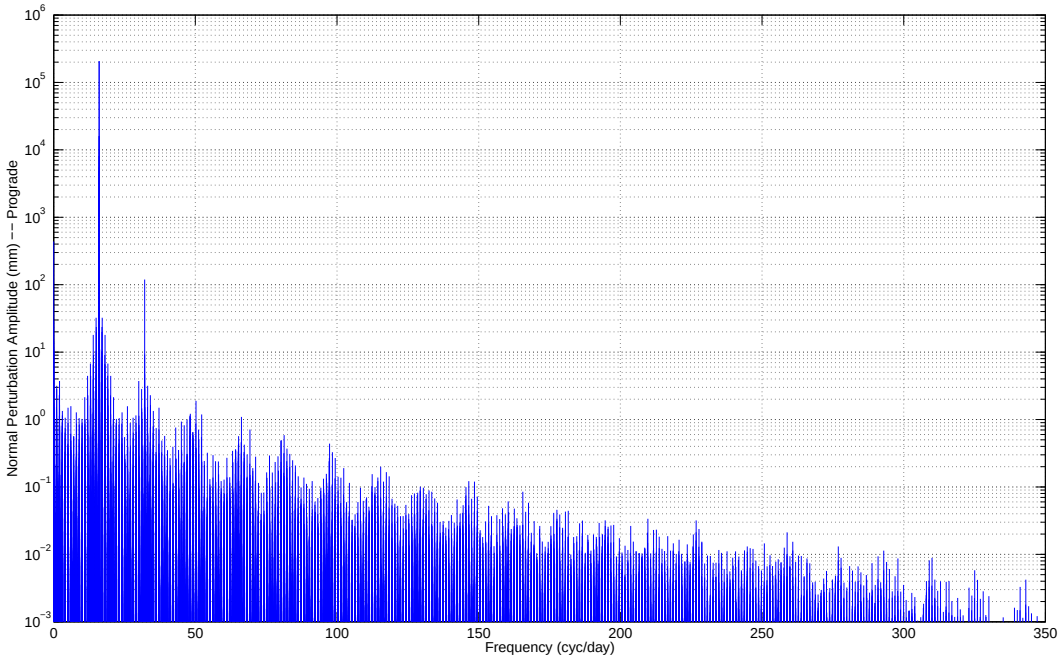

Figure 5.37. Amplitude spectrum of the normal prograde perturbation in position due to ocean tides.

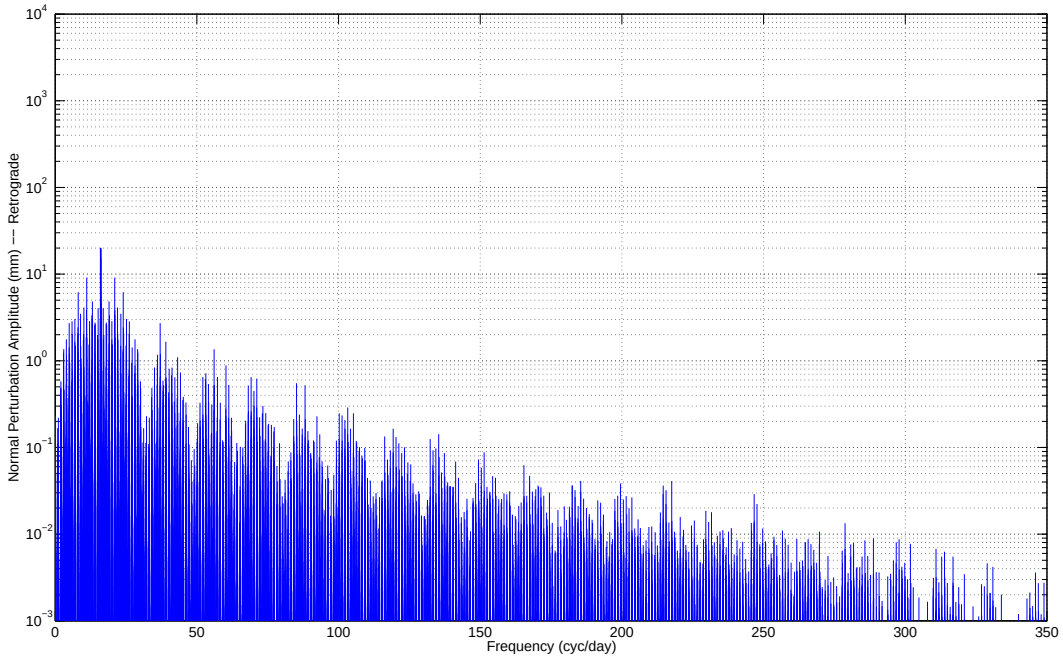

Figure 5.38. Amplitude spectrum of the normal retrograde perturbation in position due to ocean tides.

$\dot{\gamma}^{\pm}_{\mathbf{k}lmpq} = \dot{\gamma}^{\pm}_{\mathbf{k}lmuv}$, leading to

$$< (\Delta r^{\pm}_{\mathbf{k}lm})^2 > = \frac{1}{2} \sum_{p=0}^{l} \sum_{q=-Q}^{Q} (A^{r\pm}_{\mathbf{k}lmpq})^2, \tag{5.61}$$

$$< (\Delta \tau^{\pm}_{\mathbf{k}lm})^2 > = \frac{1}{2} \sum_{p=0}^{l} \sum_{q=-Q}^{Q} (A^{\tau\pm}_{\mathbf{k}lmpq})^2, \tag{5.62}$$

$$< (\Delta \chi^{\pm}_{\mathbf{k}lm})^2 > = \frac{1}{2} \sum_{p=0}^{l} \sum_{q=-Q}^{Q} [(A^{\chi^{+}\pm}_{\mathbf{k}lmpq})^2 + (A^{\chi^{-}\pm}_{\mathbf{k}lmpq})^2]. \tag{5.63}$$

Hence, the prograde and retrograde RMS by coefficients (l, m) in the RTN position perturbations is given for each constituent by

$$RMS_{\Delta r^{\pm}_{\mathbf{k}lm}} = \sqrt{\frac{1}{2} < (\Delta r^{\pm}_{\mathbf{k}lm})^2 >}, \tag{5.64}$$

$$RMS_{\Delta \tau^{\pm}_{\mathbf{k}lm}} = \sqrt{\frac{1}{2} < (\Delta \tau^{\pm}_{\mathbf{k}lm})^2 >}, \tag{5.65}$$

$$RMS_{\Delta \chi^{\pm}_{\mathbf{k}lm}} = \sqrt{\frac{1}{2} < (\Delta \chi^{\pm}_{\mathbf{k}lm})^2 >}, \tag{5.66}$$

while the total (prograde + retrograde) contribution is

$$RMS_{\Delta r_{\mathbf{k}lm}} = \sqrt{\frac{1}{2} \sum_{+}^{-} (RMS_{\Delta r^{\pm}_{\mathbf{k}lm}})^2}, \tag{5.67}$$

$$RMS_{\Delta \tau_{\mathbf{k}lm}} = \sqrt{\frac{1}{2} \sum_{+}^{-} (RMS_{\Delta \tau^{\pm}_{\mathbf{k}lm}})^2}, \tag{5.68}$$

$$RMS_{\Delta \chi_{\mathbf{k}lm}} = \sqrt{\frac{1}{2} \sum_{+}^{-} (RMS_{\Delta \chi^{\pm}_{\mathbf{k}lm}})^2}. \tag{5.69}$$

Finally, the total RMS by coefficients accumulated over the constituents is

$$RMS_{\Delta r_{lm}} = \sqrt{\frac{1}{2}\sum_{\mathbf{k}}(RMS_{\Delta r_{\mathbf{k}lm}})^2}, \tag{5.70}$$

$$RMS_{\Delta \tau_{lm}} = \sqrt{\frac{1}{2}\sum_{\mathbf{k}}(RMS_{\Delta \tau_{\mathbf{k}lm}})^2}, \tag{5.71}$$

$$RMS_{\Delta \chi_{lm}} = \sqrt{\frac{1}{2}\sum_{\mathbf{k}}(RMS_{\Delta \chi_{\mathbf{k}lm}})^2}. \tag{5.72}$$

In Figures 5.39, 5.40, 5.41 the accumulated RMS by coefficient is shown respectively for the radial, transverse and normal ocean tide perturbations. In particular, the maximum RMS for the radial component is about 1.323 m corresponding to the coefficient $(l, m) = (3, 2)$, the maximum RMS for the transverse component is 363.136 m for the coefficient $(l, m) = (2, 2)$ and the maximum RMS for the normal component is 76.241 m for the coefficient $(l, m) = (2, 2)$.

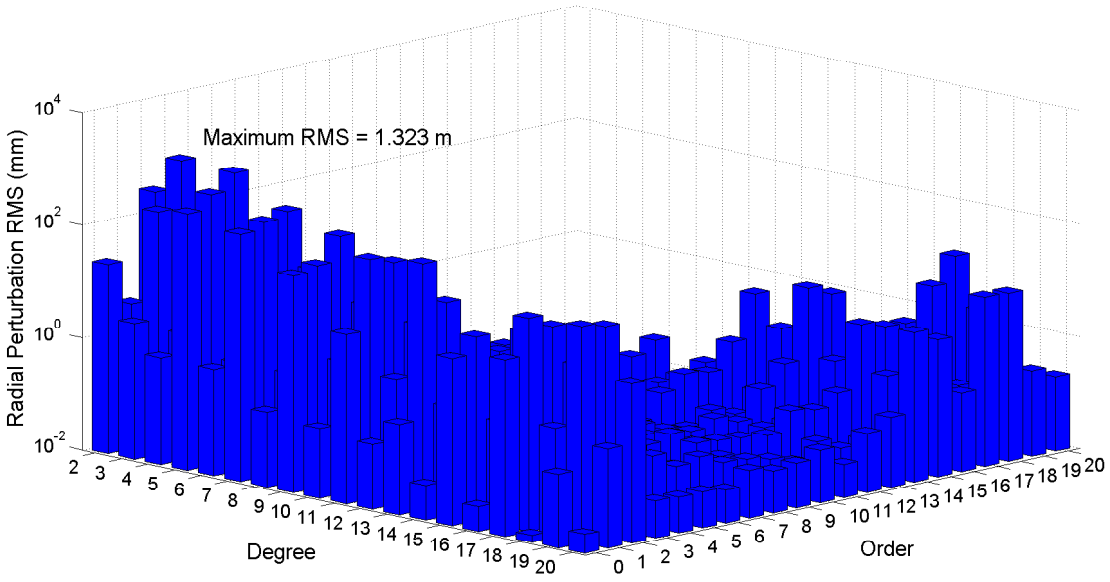

Figure 5.39. Accumulated RMS by coefficient of the radial perturbation in position due to ocean tides.

5.6 Aliasing of the ocean tide constituents for GOCE

GOCE does not monitor the entire global field continually, but samples the static gravity field and its time-varying part only along its orbital path, with a temporal resolution depending on the frequency with which the satellite repeats the same groundtrack, defined by the satellite repeat period.

The exact repeat period is a non-linear function of semimajor axis and inclination of the satellite orbit and, in particular, GOCE orbit has been designed to follow closely a repeat period of 979 revolutions in 61 nodal days (orbital resonance 979:61[3]), in order to achieve a global, dense and uniformly distributed groundtrack coverage for an extremely good spatial sampling of

[3] An orbital resonance R:D happens when the satellite performs exactly R revolutions in D nodal days, R and D being coprime integers.

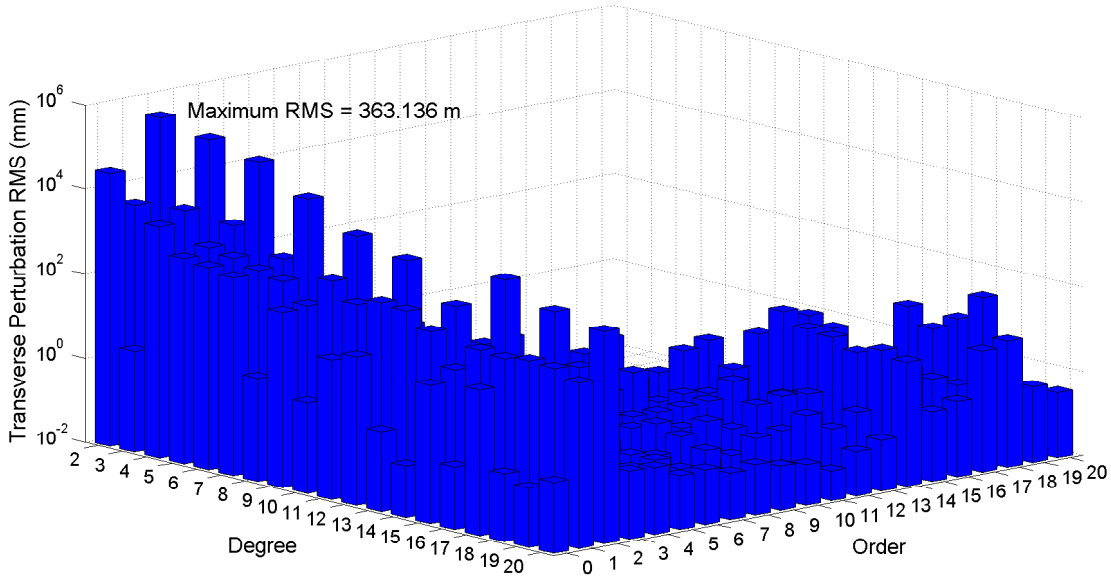

Figure 5.40. Accumulated RMS by coefficient of the transverse perturbation in position due to ocean tides.

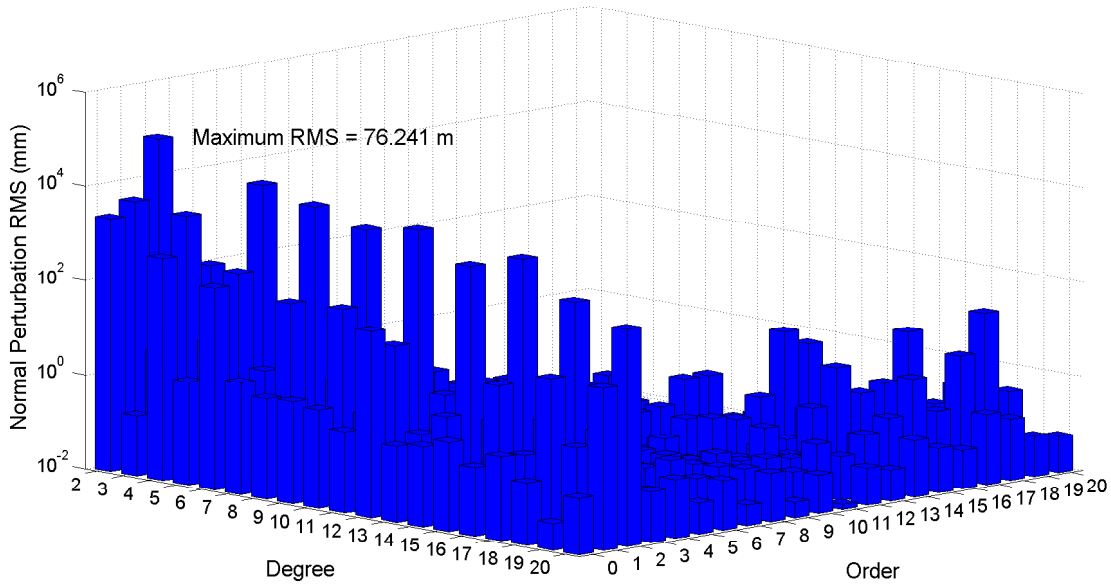

Figure 5.41. Accumulated RMS by coefficient of the normal perturbation in position due to ocean tides.

the static gravity field, guaranteeing an equatorial separation[4] of the ground tracks of less than 0.4 deg or 41 km and a maximum degree of the spherical harmonic expansion of the geopotential equal to about 200[5].

However, for Earth observing satellites, the spatial resolution can not be increased without loosing temporal resolution and vice-versa, causing respectively temporal and spatial aliasing phenomena. To reduce both types of aliasing, more satellites would be necessary. Indeed, the scientific requirements of the GOCE mission ensure a very good spatial coverage, corresponding to a long repeat period, at the expense of temporal resolution, leading to strong temporal aliasing. Many oceanographic signals may suffer the aliasing problem, in particular ocean tide aliasing is a crucial issue and will be discussed in the following.

According to the Nyquist criterion, temporal aliasing occurs when there is a variability in a signal at scales shorter than twice the sampling interval T_s, so that signals with original periods between 0 and $2T_s$ might be aliased to longer periods ranging from $2T_s$ to infinite (non-periodic signals). Analogously, temporal aliasing for ocean tides recovered by a satellite occurs when the period of a tidal constituent is less than twice the orbit repeat period, also called the Nyquist period, which is about 122 days for GOCE; aliasing does not exist for signals with period greater than the Nyquist limit. As a consequence, the minimum alias period is twice the corresponding orbit repeat period and increases linearly with it. The case of infinite alias periods is the worst to recover ocean tide signals, because they could not be completely separated from the Earth's static gravity field, acting as constant terms.

For repeating orbits, the alias periods of the ocean tide constituents can be calculated accurately, because they depend on the satellite exact repeat period T_{rp} and the period $T_{\mathbf{k}}$ of the tide constituent. The principal alias period $T^a_{\mathbf{k}}$ for a tidal frequency can be determined as [95, Parke et al., 1987]

$$T^a_{\mathbf{k}} = \left| \frac{2\pi T_{rp}}{\Delta\phi_{\mathbf{k}}} \right|, \tag{5.74}$$

where $\Delta\phi_{\mathbf{k}}$ is the change of the tidal phase for that constituent over the satellite repeat period

$$\Delta\phi_{\mathbf{k}} = \frac{2\pi T_{rp}}{T_{\mathbf{k}}}, \qquad [-\pi, \pi]\,. \tag{5.75}$$

The principal alias periods for the 106 tidal constituents of the FES2004 model to be recovered by GOCE are reported in Table 5.5.

Table 5.5. Original periods and principal alias periods for the 106 ocean tide constituents of the FES2004 model detected by GOCE. The original periods are the inverse of the Doodson frequency or, equally, of the tidal perturbation frequency with $l = 2p$, $m = 0$, $q = 0$, $p > 0$, being the Kaula frequency zero.

Tidal Constituent	Darwin Symbol	Original Period (days)	Alias Period (days)
165555	K_1	0.997269576	359.595739003
255555	M_2	0.517525054	483.220633707
245655	N_2	0.527431168	179.353774119

[4] For an R:D resonant orbit, the equatorial separation of the ground tracks is expressed as ([6] Bezděk et al., 2010)

$$\Delta\lambda^{deg} = 360^\circ/R \qquad \text{or} \qquad \Delta\lambda^{km} = 2\pi R_e/R. \tag{5.73}$$

[5] For the Nyquist sampling theorem, the maximum degree N of the Stokes coefficients that might be fully recovered by a gravimetric satellite in the resonance R:D is approximately $N \leq R/2$.

Table 5.5 – Continued from previous page

Tidal Constituent	Darwin Symbol	Original Period (days)	Alias Period (days)
145555	O_1	1.075805910	206.170746684
163555	P_1	1.002745417	371.071362978
135655	Q_1	1.119514811	124.435924954
273555	S_2	0.500000000	11627.749505082
275555	K_2	0.498634788	179.797869502
235755	$2N_2$	0.537723914	136.779437965
115855		1.218530090	976.547974398
117655		1.211361065	170.044451432
125745		1.167126164	228.152158399
125755	$2Q_1$	1.166925821	220.743737538
127545		1.160547602	139.803478299
127555	σ_1	1.160349511	142.738917214
135645		1.119699204	126.756135754
137445		1.113643040	274.215020430
137455	ρ_1	1.113460637	285.740962047
145535		1.076146513	194.380512406
145545		1.075976185	200.102106655
145755		1.075089982	236.331270709
147555	τ_1	1.069505562	1598.845342483
153655		1.040614670	161.263687362
155445		1.035539509	670.545087419
155455		1.035381791	743.923616878
155655	M_1	1.034718639	1378.884265940
155665		1.034561171	1729.732641159
157455	χ_1	1.029544743	242.038390802
162556	π_1	1.005505848	184.070555560
163545		1.002893347	351.864955983
164556	S_1	1.000000000	23201.542664760
165545		0.997415895	379.679466512

Table 5.5 – Continued from previous page

Tidal Constituent	Darwin Symbol	Original Period (days)	Alias Period (days)
165565		0.997123299	341.529986719
166554	ψ_1	0.994554120	181.202075576
167555	ϕ_1	0.991853215	122.909960477
173655	θ_1	0.966956486	699.190593115
175455	J_1	0.962436581	159.057737090
175465		0.962300344	155.421284203
183555	SO_1	0.934174078	202.578836659
185355		0.929954783	151.524612746
185555	OO_1	0.929419770	167.207642064
185565		0.929292719	171.424029343
185575		0.929165703	175.858562333
195455	ν_1	0.899093237	404.128041000
195465		0.898974342	429.670780807
217755		0.558046925	193.964176044
219555		0.556538526	156.731300006
225855	$3N_2$	0.548426378	262.817904245
227655	ϵ_2	0.546969472	129.349006550
229455		0.545520286	347.920251529
237555	μ_2	0.536323242	236.692145521
238554		0.535536889	672.450967796
244656		0.528193880	123.772102882
245645		0.527472092	174.743526124
246654		0.526670655	352.389045467
247455	ν_2	0.526083537	1391.260479627
248454		0.525326903	495.287994234
253755	γ_2	0.518829140	144.378311638
254556	α_2	0.518259366	208.019221975
255545		0.517564456	451.151960486
256554	β_2	0.516792821	1496.217682528

Table 5.5 – Continued from previous page

Tidal Constituent	Darwin Symbol	Original Period (days)	Alias Period (days)
263655	λ_2	0.509240578	292.387107133
265455	L_2	0.507984191	696.050893451
265655		0.507824509	486.457851243
265665		0.507786577	453.972509168
272556	T_2	0.500685388	377.102511201
274554	R_2	0.499316486	354.132582885
275565		0.498598216	175.165057365
275575		0.498561650	170.764993360
285455	η_2	0.489771754	136.522276712
285465		0.489736470	139.320163716
293555		0.482345620	129.579830943
295555		0.481074991	312.530538904
295565		0.481040950	327.590957353
135555		1.119902846	129.420277592
155555		1.035050109	966.441267415
175555		0.962149982	151.594964160
235655		0.537813420	142.825712569
245555	O_2	0.527517279	169.921436361
265555		0.507904337	572.679776794
055565	LP	6798.096532971	6798.096532971
056554	S_a	365.256775513	365.256775513
057555	S_{sa}	182.621717375	182.621717375
057565	S_{saa}	177.844172936	177.844172936
058554	S_{ta}	121.749293854	122.262277179
063655	MS_m	31.811877283	740.370341278
065445		27.666726611	297.705469988
065455	M_m	27.554585634	285.215190972
065465		27.443350065	273.730774031
065555		27.321583231	262.080288919

Table 5.5 – Continued from previous page

Tidal Constituent	Darwin Symbol	Original Period (days)	Alias Period (days)
065655		27.092488337	242.416919420
065665		26.984945099	234.070090283
073555	MS_f	14.765290935	463.940412704
075355		13.777292817	142.607595486
075555	M_f	13.660791616	131.040144459
075565		13.633395274	128.561983000
075575		13.606108599	126.175813185
083455		9.613720702	176.629331423
083655	MS_{tm}	9.556848916	159.221120143
083665		9.543432639	155.577278312
085455	M_{tm}	9.132937207	190.281781660
085465		9.120683978	195.761226499
093555	MS_{qm}	7.095791770	151.376635968
093565		7.088392969	154.824183972
095355		6.859397443	571.677084899
095365		6.852483169	624.165468009

Unfortunately, a Sun-synchronous satellite, like GOCE, does not allow the complete estimation of the diurnal and semidiurnal solar tide constituents S_2 and S_1 which have original periods of exactly 12 h and 24 h, because it will always sample both these constituents at the same phase every day. As a consequence, S_2 and S_1 are aliased to almost infinite periods, respectively of about 31 years for S_2 and 63 years for S_1, in the specific case of GOCE, so they represent essentially a bias.

Moreover, the diurnal solar tide constituents K_1 and P_1 are aliased to annual periods, respectively of about 359 and 371 days, while K_2 is aliased to semiannual period of about 179 days.

Another important factor to be accounted for is the capability to separate tidal constituents with neighboring alias periods from each other, expressed by the Rayleigh criterion. The minimum data record length needed for the accurate separation of two tide constituents is called Rayleigh period and is defined as

$$T_{Ray} = \frac{1}{\left|\frac{1}{T_1} - \frac{1}{T_2}\right|}, \tag{5.76}$$

where T_1 and T_2 are the original periods of the two constituents. For the GOCE satellite,

the Rayleigh period necessary to separate respectively the semidiurnal lunar and lunisolar constituents N_2 and K_2 is approximately 199 years, because they are aliased to nearly the same period of about 179 days, so it results quite impossible to resolve them.

Finally, the time series of available GOCE orbital observations must be considered and, for the Nyquist sampling theorem, only ocean tide frequencies with alias periods shorter than twice this period and relatively large amplitudes are detectable. For the available GOCE data record of about 400 days, the maximum alias period beyond which the tidal constituents must be discarded turns out to be $T_{max} = 200$ days.

5.7 Definition of the ocean tide parameters to be estimated

Combining information deriving from the spectral analysis, the perturbation statistics by coefficient, the determination of ocean tide alias periods and resonant coefficients, it is possible to identify the list of the ocean tide parameters to be estimated from GOCE orbital data. Also the total number of parameters must be taken into account, so cutoffs on the RTN perturbation RMS by coefficient must be applied. The following automatic procedure was adopted for both the prograde and retrograde case, which can be treated in parallel and independently from each other.

During the spectral analysis, the principal alias periods were computed according to the relation (5.74) for the ocean tide perturbation frequencies $\dot{\gamma}^{\pm}_{\mathbf{k}lmpq}$ defined by all the combinations of indices (l, m, p, q). In this way, it is possible to discriminate between the partial spectral amplitudes $A^{\pm}_{\mathbf{k}lmpq}$ which are aliased to periods greater than the limit period T_{max} or not. The choice adopted consists in not estimating the coefficient (l, m), if the dominant partial amplitude among all those contributing to the same pair (l, m) is aliased beyond T_{max}, because in that case GOCE would not be able to solve it. As a consequence, in the processing of GOCE data, these parameters will not be estimated, but taken from the reference ocean tide model FES2004 and kept fixed.

Also the resonant prograde/retrograde ocean tide coefficients (l, m) of the short period band, as defined in (5.56), are excluded from the estimation process and the corresponding FES2004 parameters are used instead.

To limit the number of parameters to be estimated with the multiarc approach, three different cutoffs are adopted for the selection of the parameters based on the perturbation RMS by coefficient in the three directions RTN and are reported in Table 5.6, being 5 mm for the radial component, 2 cm for the transverse component and 1 cm for the normal component, both in the prograde and retrograde case. In particular, if at least a RMS by coefficient is above its cutoff in any one of the three directions RTN, the corresponding parameter prograde/retrograde (l, m) is retained for the estimation.

Table 5.6. Cutoffs adopted for the perturbation RMS by coefficient in the radial, transverse and normal directions.

Cutoff R (mm)	**Cutoff T (mm)**	**Cutoff N (mm)**
5	20	10

According to this selection procedure, the ocean tide parameters which will be estimated through the processing of GOCE orbital data are 490 in total, among which 460 are prograde and 30 are retrograde. They are listed in Table 5.7, where constituent, degree and order are indicated and the string *potide* refers to prograde coefficients, *rotide* to retrograde coefficients and *otide* to both types.

Table 5.7. Original periods and principal alias periods for the 106 ocean tide constituents of the FES2004 model detected by GOCE. The original periods are the inverse of the Doodson frequency or, equally, of the tidal perturbation frequency with $l = 2p$, $m = 0$, $q = 0$, $p > 0$, being the Kaula frequency zero.

Parameter Type	**Constituent**	(l, m)
potide	125.755	2 1
potide	125.755	4 1
potide	127.555	2 1
potide	127.555	4 1
potide	135.645	2 1
potide	135.645	4 1
potide	145.545	2 1
potide	145.545	2 2
potide	145.545	3 1
potide	145.545	4 1
potide	145.545	4 2
potide	145.545	5 1
potide	145.545	6 1
potide	145.545	8 1
potide	145.545	10 1
potide	145.545	12 1
potide	145.545	17 17
potide	153.655	4 1
potide	155.655	2 1
potide	155.655	4 1
potide	157.455	2 1
potide	157.455	4 1
potide	162.556	3 1
potide	162.556	4 1
potide	162.556	5 1
potide	162.556	6 1
potide	162.556	7 1
potide	164.556	2 1

Table 5.7 – Continued from previous page

Parameter Type	**Constituent**	(l, m)
potide	164.556	4 1
potide	165.565	6 1
potide	165.565	8 1
potide	165.565	10 1
potide	166.554	3 1
potide	166.554	4 1
potide	166.554	5 1
potide	167.555	2 1
potide	167.555	4 1
potide	167.555	5 1
potide	167.555	7 1
potide	175.455	2 1
potide	175.455	2 2
potide	175.455	4 1
potide	175.455	5 1
potide	175.455	10 1
rotide	175.455	15 15
potide	175.465	2 1
potide	175.465	4 1
potide	183.555	4 1
potide	185.555	2 1
potide	185.555	4 1
rotide	185.555	15 15
potide	185.565	2 1
potide	185.565	4 1
potide	227.655	2 2
potide	227.655	4 2
potide	237.555	2 2
potide	237.555	4 2
potide	237.555	6 2

Table 5.7 – Continued from previous page

Parameter Type	**Constituent**	(l, m)
potide	247.455	2 2
potide	253.755	2 2
potide	253.755	4 2
potide	254.556	2 2
potide	254.556	4 2
potide	265.455	2 2
potide	274.554	2 2
potide	275.565	8 2
potide	275.565	9 2
potide	275.565	10 2
rotide	275.565	15 14
potide	275.565	16 2
potide	275.565	17 2
potide	275.565	19 18
potide	275.575	3 2
potide	275.575	4 2
potide	275.575	5 2
potide	275.575	6 2
potide	285.455	2 2
potide	285.455	4 2
potide	285.455	6 2
potide	285.465	2 2
potide	285.465	4 2
potide	245.555	2 2
potide	245.555	4 2
potide	055.565	2 0
potide	055.565	4 0
potide	055.565	6 0
potide	055.565	12 0
potide	056.554	2 0

Table 5.7 – Continued from previous page

Parameter Type	**Constituent**	(l, m)
potide	057.555	2 0
potide	057.555	4 0
potide	057.555	5 0
potide	057.555	6 0
potide	057.555	7 0
potide	057.555	9 0
potide	057.555	11 0
potide	057.555	15 0
potide	057.555	17 0
potide	057.565	2 0
potide	058.554	2 0
potide	065.455	2 0
potide	065.655	2 0
potide	065.665	2 0
potide	075.355	2 0
potide	075.555	4 0
potide	075.555	5 0
potide	075.555	6 0
potide	075.555	7 0
rotide	075.555	17 16
potide	075.565	4 0
potide	083.655	2 0
potide	085.455	2 0
potide	085.455	4 0
potide	085.465	2 0
potide	093.555	2 0
potide	235.755	2 2
potide	235.755	4 2
potide	235.755	6 2
potide	165.555	3 1

Table 5.7 – Continued from previous page

Parameter Type	**Constituent**	(l, m)
potide	165.555	4 1
potide	165.555	5 1
potide	165.555	6 1
potide	165.555	7 1
potide	165.555	8 1
potide	165.555	10 1
potide	165.555	11 1
potide	165.555	12 1
potide	165.555	13 1
potide	165.555	16 1
potide	165.555	18 1
potide	165.555	19 1
potide	165.555	20 1
potide	255.555	2 2
rotide	255.555	15 14
potide	245.655	2 2
potide	245.655	3 2
potide	245.655	4 0
potide	245.655	4 1
otide	245.655	4 2
potide	245.655	4 3
potide	245.655	4 4
potide	245.655	5 2
potide	245.655	6 0
potide	245.655	6 1
potide	245.655	6 2
potide	245.655	6 4
otide	245.655	6 6
potide	245.655	7 2
potide	245.655	8 1

Table 5.7 – Continued from previous page

Parameter Type	**Constituent**	(l, m)
potide	245.655	8 2
potide	245.655	10 2
potide	245.655	12 2
rotide	245.655	15 14
rotide	245.655	17 14
potide	245.655	18 2
potide	245.655	19 18
potide	145.555	2 0
otide	145.555	2 1
potide	145.555	2 2
potide	145.555	3 1
potide	145.555	3 2
otide	145.555	3 3
potide	145.555	4 0
otide	145.555	4 1
potide	145.555	4 2
potide	145.555	4 3
otide	145.555	4 4
potide	145.555	5 1
potide	145.555	6 0
potide	145.555	6 1
potide	145.555	6 2
potide	145.555	7 1
potide	145.555	8 1
potide	145.555	10 1
potide	145.555	11 1
potide	145.555	12 1
potide	145.555	13 1
potide	145.555	14 1
rotide	145.555	15 15

Table 5.7 – Continued from previous page

Parameter Type	**Constituent**	(l, m)
potide	145.555	16 1
potide	145.555	17 17
potide	145.555	18 1
potide	145.555	18 17
potide	145.555	20 17
potide	163.555	4 1
potide	135.655	2 0
potide	135.655	2 1
potide	135.655	2 2
potide	135.655	3 1
potide	135.655	4 0
potide	135.655	4 1
potide	135.655	4 2
potide	135.655	5 1
potide	135.655	6 1
potide	135.655	10 1
potide	135.655	12 1
potide	273.555	2 2
potide	273.555	3 2
potide	273.555	4 2
potide	273.555	5 2
potide	273.555	6 2
potide	273.555	7 2
potide	273.555	8 2
potide	273.555	9 2
potide	273.555	10 2
potide	273.555	11 2
potide	273.555	12 2
potide	273.555	14 2
potide	273.555	16 2

Table 5.7 – Continued from previous page

Parameter Type	**Constituent**	(l, m)
potide	273.555	17 2
potide	273.555	18 2
potide	273.555	19 2
potide	273.555	19 18
potide	273.555	20 2
potide	275.555	2 2
potide	275.555	3 2
potide	275.555	4 1
potide	275.555	4 2
potide	275.555	4 3
potide	275.555	4 4
potide	275.555	5 2
potide	275.555	6 2
potide	275.555	7 2
potide	275.555	8 2
potide	275.555	9 2
potide	275.555	10 2
potide	275.555	11 2
potide	275.555	12 2
potide	275.555	13 2
potide	275.555	14 2
potide	275.555	15 2
rotide	275.555	15 14
potide	275.555	16 2
potide	275.555	17 2
rotide	275.555	17 14
potide	275.555	18 2
potide	275.555	19 2
rotide	275.555	19 14
potide	275.555	19 18

Table 5.7 – Continued from previous page

Parameter Type	**Constituent**	(l, m)
potide	275.555	20 2

Chapter 6

Preliminary estimation of ocean tide parameters

The GOCE GPS observations are processed in daily orbital arcs using the NAPEOS S/W system (ESA/ESOC), specific for satellite orbit determination and modified to include the partial derivatives with respect to the ocean tide parameters and the ocean tide model inversion capability. For each arc, the satellite state vector at the initial epoch is estimated, together with one solar radiation pressure (SRP) parameter, six empirical accelerations per hour (three CPR along-track and three CPR cross-track) and the ocean tide parameters selected from the sensitivity study of tidal perturbations on GOCE. Ocean tide parameters are then estimated globally through a multiarc solution, combining the normal equations for a specified number of daily arcs. To evaluate the goodness of the obtained results, the GOCE POD was then carried out using the estimated tidal parameters instead of the corresponding FES2004 parameters and the comparison with the POD performed using FES2004 is shown, involving the post-fit RMS of GPS phase observations and the 3D RMS of orbit residuals, the last computed also with respect to the official GOCE R/D PSO.

6.1 GOCE orbital data processing with NAPEOS

NAPEOS (NAvigation Package for Earth Observation Satellites) is a software developed and maintained by ESA/ESOC for Earth Observation satellite missions, providing especially capabilities of orbit determination/prediction and parameter estimation. It is fully written in Fortran90 and is characterized by an object oriented methodology and a highly modular and flexible design. However, the ocean tide model inversion capability was not implemented in the system. As a consequence, it was necessary to extend the S/W system introducing a new data structure within existing satellite global structure, to allow for the estimation of ocean tide parameters through a multiarc solution. A total of eighteen Fortran90 modules of NAPEOS have been modified and the main programs involved in the upgrade were BAHN (orbits and parameters estimator) and MULTIARC (combines normal equations of independent arc runs) [3, Bardella and Casotto, 2012]. Partial derivatives with respect to the ocean tide parameters were entirely implemented in NAPEOS. In particular, the central body structure in BAHN was extended to include the ocean tide parameters characteristics: the tidal constituent, harmonic type (C or S), the harmonic degree and order and the chirality (prograde or retrograde). The MULTIARC upgrade involved essentially the normal equation file output to contain these characteristics.

The sequence of NAPEOS programs defined to process the GOCE orbital data is reported in Figure 6.1. The main input data for the POD/Multiarc processing are:

- GOCE GPS observables in RINEX 2.20 format (file type SST RIN 1b), covering the time

interval from 1st November 2009 (beginning of the operational phase) to 31st May 2011, provided by ESA through EOLI-SA ([43], Earth Observation Link - Stand Alone), an interactive tool to view and order products from ESA's Earth Observation catalogues;

- IGS final GPS orbits and clock solutions ([59]);
- official GOCE R/D PSO as a-priori reference orbits [8, Bock et al., 2011];
- GOCE GPS antenna information in ANTEX (ANTenna EXchange) format [60, Jäggi et al., 2009];
- GOCE radiation cross-section area, aerodynamic cross-section area and attitude information [47, ESA/ESOC].

Each program performs a specific task with specific processing procedures, called modes, and can briefly described as follows:

- ClockUpd, for the merge and conversion of clock files;
- OrbUpd, for the merge of SP3 orbit files with the IGS orbits to get a complete SP3 file;
- Tracksim, for the conversion of SP3 orbits to NTDF files;
- Buildcat, generates an RTDC (RINEX Tracking Data Catalogue) catalogue of RINEX files;
- GnssObs, for RINEX observation pre-processing;
- Bahn, for parameter estimation;
- Multiarc, for normal Equation Stacking;
- CmdLine,

The three principal modes associated to the programs are:

- *ORBIT-FIT*, which characterized the group of programs involved in the generation of a best fitting orbit which serves as a-priori orbit;
- *GOCE-RAW*, which characterized the programs involved in the first data pre-processing and generation of a raw orbit at the meter level using only pseudorange measurements;
- *GOCE*, which characterized the programs involved in the second data pre-processing and parameter estimation, resulting in an accurate orbit at the centimeter level using both pseudorange and phase measurements.

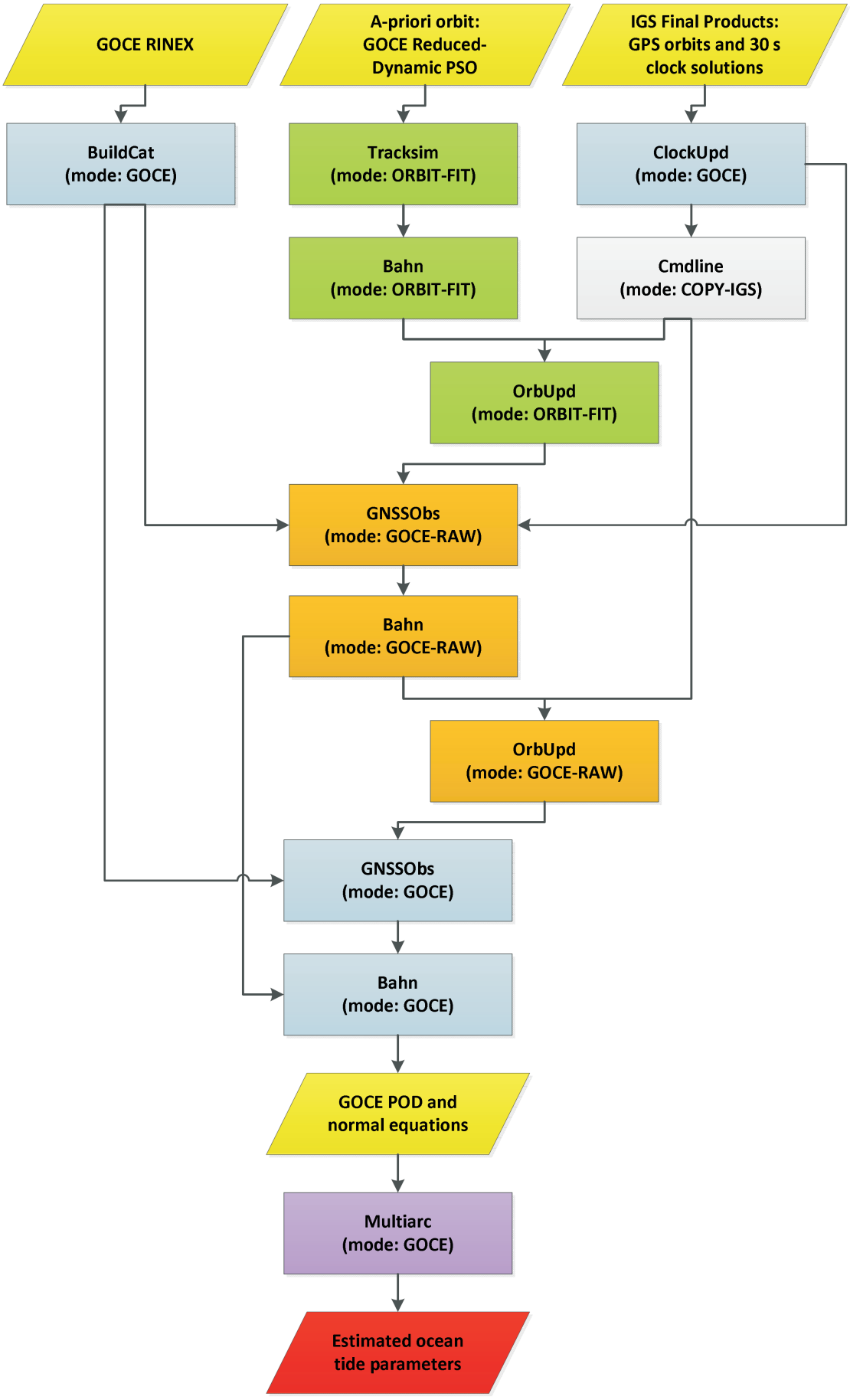

Figure 6.1. Sequence of NAPEOS programs to perform the GOCE fully-dynamic POD and multiarc processing.

The main input data for the POD-Multiarc processing are:

- GOCE GPS observables in RINEX 2.20 format (file type SST RIN 1b), covering the time interval from 1st November 2009 (beginning of the operational phase) to 31st May 2011, provided by ESA through EOLI-SA ([43], Earth Observation Link - Stand Alone), an interactive tool to view and order products from ESA's Earth Observation catalogues;
- IGS final GPS orbits and clock solutions ([59]);
- official GOCE R/D PSO as a-priori reference orbits [8, Bock et al., 2011];
- GOCE GPS antenna information in ANTEX (ANTenna EXchange) format [60, Jäggi et al., 2009];
- GOCE radiation cross-section area, aerodynamic cross-section area and attitude information [47, ESA/ESOC].

For a detailed explanation of the NAPEOS programs refer to the NAPEOS User Manual [45, ESA GMVSA, 2006].

6.1.1 Dynamical model

In order to estimate the ocean tide parameters through a fully-dynamic POD of GOCE, it is necessary to have a complete and accurate dynamical model. However, mismodeling of some perturbations is inevitable and this may lead to high discrepancies of the resulting tidal parameters with respect to the reference tide model.

The Earth's static gravity field considered for the GOCE data processing is the EIGEN-6C model [50, Förste et al., 2011] up to degree and order 200, which combines LAGEOS, GRACE and GOCE satellite measurements, gravity and altimetric data, and can be downloaded from the International Centre for Global Earth Models [58, ICGEM].

The third-body gravitational forces of the Sun, the Moon and the planets are included, together with the indirect oblateness perturbation, consisting in the perturbation due to the J_2 Earth gravity field component on the Moon.

The effect of ocean tides is not distinguishable from that of solid tides and is therefore relative to the particular solid Earth tide model used, which is the IERS-TN32 [82, McCarthy and Petit, 2003] up to degree and order 4 for 71 constituents. On the other hand, the reference ocean tide model accounting for the parameters which are not considered in the list of parameters to be estimated is the FES2004 model [79, Lyard et al., 2006] up to degree and order 50 for 106 constituents.

The correction due to General Relativistic effects caused by the curvature in the time-space generated by the Earth heavy rotating body is included in the dynamical model [82, McCarthy and Petit, 2003].

Three analytical models are implemented in NAPEOS in order to compute the non-gravitational perturbations due to solar radiation pressure (SRP) [82, McCarthy and Petit, 2003], Earth albedo and infrared radiation [2, Arnold and Dow, 1984].

The aerodynamic forces are not considered during the POD process because GOCE is flying in drag-free control via an electric propulsion system used to continuously counteract the atmospheric drag in the direction of the motion.

Finally, one cycle per revolution empirical accelerations are introduce in the radial, along-track and cross-track directions to compensate model omission errors.

Table 6.1 illustrates the force models considered during GOCE fully-dynamic POD process. For the mathematical models and algorithms implemented in NAPEOS refer to [46, ESA/ESOC, 2009].

Table 6.1. Gravitational, non-gravitational and empirical forces adopted for the GOCE fully-dynamic POD process.

Dynamical Models	Description	Reference
Static gravity field	EIGEN-6C 200x200	[50]
Solid Earth tides	IERS-TN32 71 constituents, 3x3	[82]
Ocean tides	FES2004 106 constituents, 50x50	[79]
Ocean loading tides	FES2004, 50x50	[79]
Third body perturbation	Lunar gravity	
	Solar gravity	
	Planetary gravity	
	Indirect oblateness perturbation	
Relativistic correction	Correction according to General Relativity	[82]
Aerodynamic forces	not considered	
Radiation Pressure	Solar Radiation Pressure	[82]
	Albedo radiation pressure	[2]
	Infrared radiation pressure	[2]
Empirical accelerations	Radial, along-, cross-track CPR	[46]

6.1.2 Analyzed GOCE data

GOCE data are processed in daily orbital arcs from the 1st November 2009, corresponding to the beginning of the operational phase, until the 31st May 2011 to perform the fully-dynamic POD. For each arc, the satellite state vector at the initial epoch (at 12 h of each day) is estimated, together with one solar radiation pressure (SRP) parameter (considering a constant GOCE radiation area), six empirical accelerations per hour (three CPR along-track and three CPR cross-track) and the ocean tide parameters selected from the sensitivity study reported in the previous Chapter. The normal equations are accumulated at the end of each arc. The parameters estimated over each daily arc during GOCE fully-dynamic POD process are reported in Table 6.2.

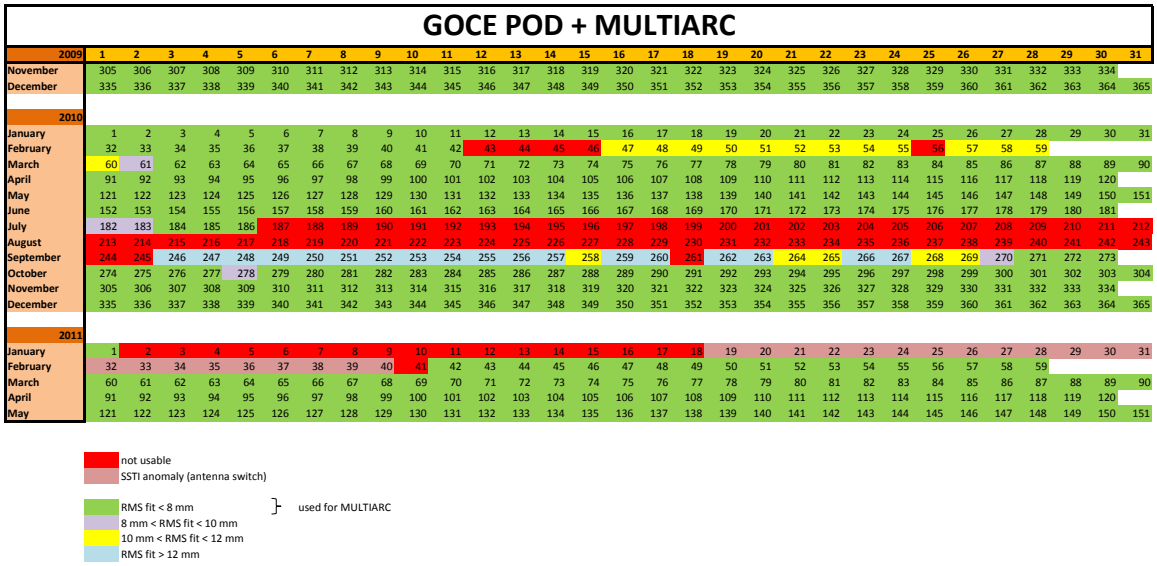

Figure 6.2. Daily report showing GOCE successful processed data for POD with different colors corresponding to different fit RMS values, of which accumulated normal equations are then used for the multiarc solution for ocean tide parameter estimation.

A daily report of the obtained post-fit RMS of the GPS phase observations for the analyzed data is shown in Figure 6.2. GOCE POD was successfully computed for at total of 472 days. Of these, 18 days present a post fit-RMS greater than 12 mm and other 18 days have a post-fit RMS between 10 mm and 12 mm, 5 days show a post-fit RMS between 8 mm and 10 mm, while the remaining 431 days have a post-fit RMS lower than 8 mm with a minimum of about 5 mm.

Only arcs with a post fit RMS of the GPS phase observations residuals lower than 8 mm are considered for the multiarc processing, so a total of 431 days are used to solve for 490 selected ocean tide parameters. Firstly, a pre-elimination of the arc-dependent parameters (satellite state vector, SRP coefficient, CPR coefficients) is performed, without loosing information as described in Chapter 4. Then, the ocean tide parameters are globally estimated through a multiarc solution, combining the normal equations for a specified number of daily arcs, not necessarily

consecutive. In fact, for the estimation of arc-independent (time-independent) parameters, it is not required the condition of continuity of the orbital arcs at the boundaries, because they are global (constant) over all the arcs.

Table 6.2. Estimated and fixed parameters during the GOCE fully-dynamic POD process for each daily arc.

Parameters	Description	Type	Reference
Satellite state vector		estimated (1 per arc at epoch)	
Radiation pressure	Solar Radiation Pressure	estimated (1 per arc)	[82]
	Albedo radiation pressure	fixed, equal to 1	[2]
	Infrared radiation pressure	fixed, equal to 1	[2]
Empirical accelerations	CPR constant along-track	estimated (1 per hour)	[46]
	CPR constant cross-track	estimated (1 per hour)	
	CPR cosine along-track	estimated (1 per hour)	
	CPR cosine cross-track	estimated (1 per hour)	
	CPR sine along-track	estimated (1 per hour)	
	CPR sine cross-track	estimated (1 per hour)	
Ocean tide parameters	490 selected parameters	estimated (once per arc)	

6.2 Preliminary results

All major diurnal, semi-diurnal and long-period tides from harmonic degree 2 to 20, according to the selected list, were included in the estimation process and preliminary results were obtained. In Figure 6.3 the absolute difference of the estimated parameters with respect to the corresponding FES2004 ocean tide parameters is shown. In particular, the 56% of the total number of parameters has a difference below 1 cm from the FES2004 model.

The standard deviation of the estimated parameters is reported in Figure 6.4 and it can be observed that the 36% of the parameters presents a value lower than 1 mm.

In Figure 6.5 the relative error with respect to the FES2004 parameters is illustrated and about the 16% have a relative error lower than 1, meaning that they are of the order of magnitude of the FES2004 parameters.

These preliminary results show quite significant discrepancies if compared with the values of the FES2004 model. However, it must be considered that the FES2004 model results from the assimilation of satellite altimeter data into a hydrodynamic ocean solution with the best combination between physical parameters and model discretization, while the parameters estimated through the POD-Multiarc processing are the result of a densely-parameterized, fully-dynamic orbital solution and tend to absorb errors due to the mismodeling of the force field acting on the satellite.

Certainly, GOCE is the most sensitive satellite to ocean tide perturbations, but there are many difficulties for the tidal recovery from GOCE orbital data. First of all because it is a Sun-synchronous satellite with perfect resonances with the dominant semidiurnal solar tide S_2 and deep resonances with all the other solar tides. Moreover, GOCE long repeat period of 61 days causes strong temporal aliasing of the tidal perturbation frequencies characterized by a period

shorter than about 122 days. An extension of the data set to much longer time-period, together with the inclusion of more satellites, such as GRACE, should allow a substantial improvement of the obtained results.

Further POD-Multiarc runs are certainly necessary, together with the refinement of the list of parameters to be estimated, removing excessively ill-estimated ocean tide parameters (and the correlated ones) and introducing new parameters where appropriate. The model parameter tuning and investigation is essential to adjust the best combination of parameters to be estimated. Indeed, the task has proven very intensive and challenging, but the partial results obtained are encouraging and a motivation for future analysis.

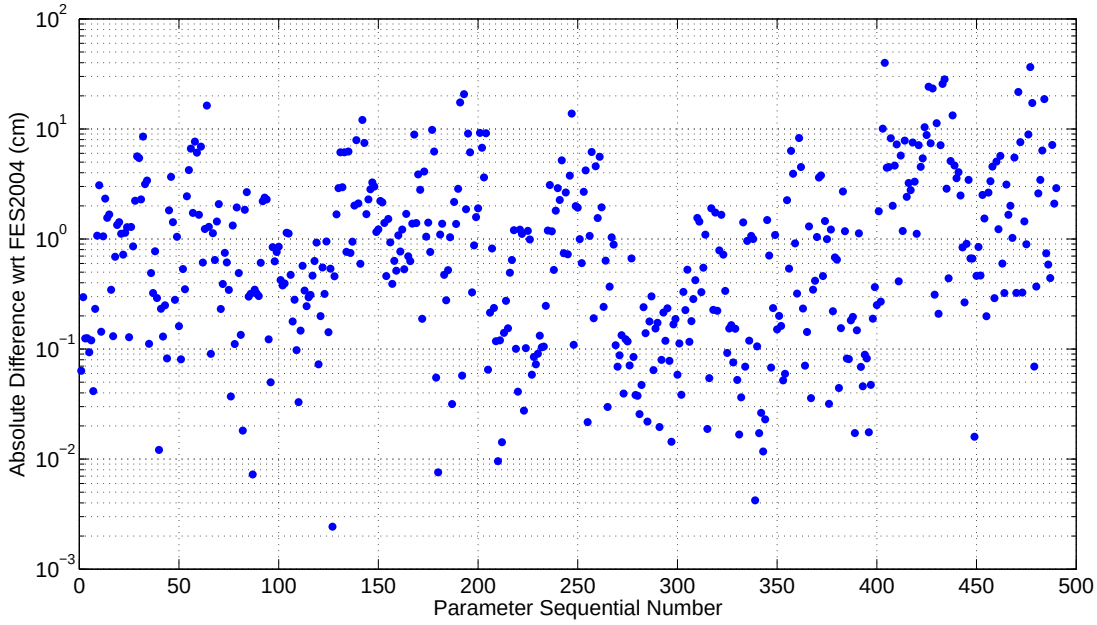

Figure 6.3. Absolute difference of the estimated parameters with respect to the corresponding FES2004 ocean tide parameters.

The correlation matrix of the ocean tide estimated parameters is reported in Figure 6.6.

6.3 Recomputation of GOCE orbit with the estimated parameters

The impact of the estimated parameters on the precise orbit determination of GOCE was evaluated. GOCE orbital data were reprocessed from the 1st November 2009 to the 31st May 2011, initializing the ocean tide model with the estimated parameters, if present, and maintaining otherwise the FES2004 parameters. During this run no ocean tide model estimation is performed. The results are compared with those obtained from the GOCE precise orbit determination using the complete FES2004 model.

Figure 6.7 shows the post-fit RMS of the GPS phase residuals obtained with the new ocean tide model, with a mean value of 6.5 mm. Moreover, Figure 6.8 reports the difference between the post-fit RMS obtained with the FES2004 model and that resulting from the new ocean tide model. A mean improvement of 0.6 mm in the post-fit RMS can be observed for the 96% of the analyzed daily arcs, in particular, the 16% of the arcs shows an improvement greater than 1 mm and few days reach a difference of 2 mm.

The GOCE orbits resulting from the new ocean tide model are then compared with both the official R/D PSO [122, Visser et al. 2009][8, Bock et al., 2011]and the orbits obtained using

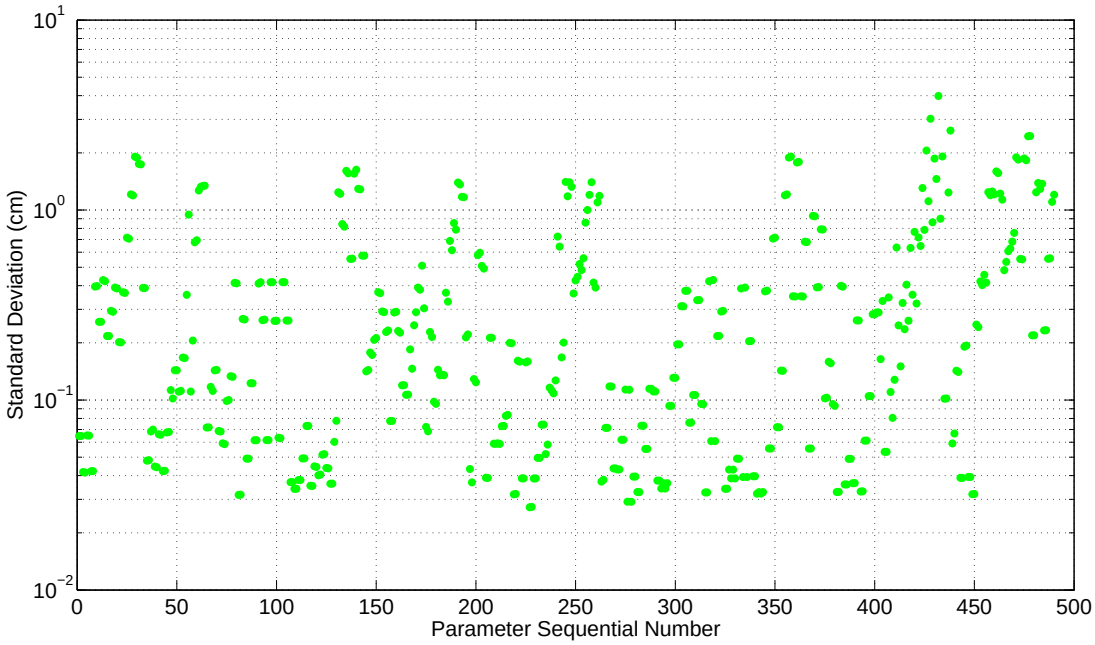

Figure 6.4. Standard deviation of the estimated parameters.

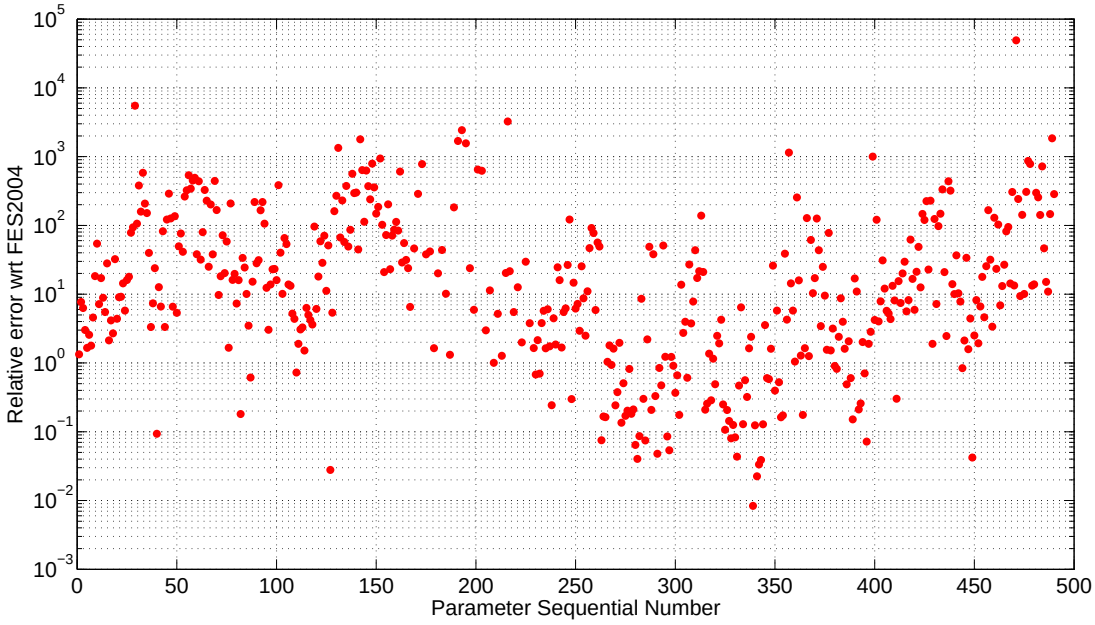

Figure 6.5. Relative error of the estimated parameters with respect to the corresponding FES2004 ocean tide parameters.

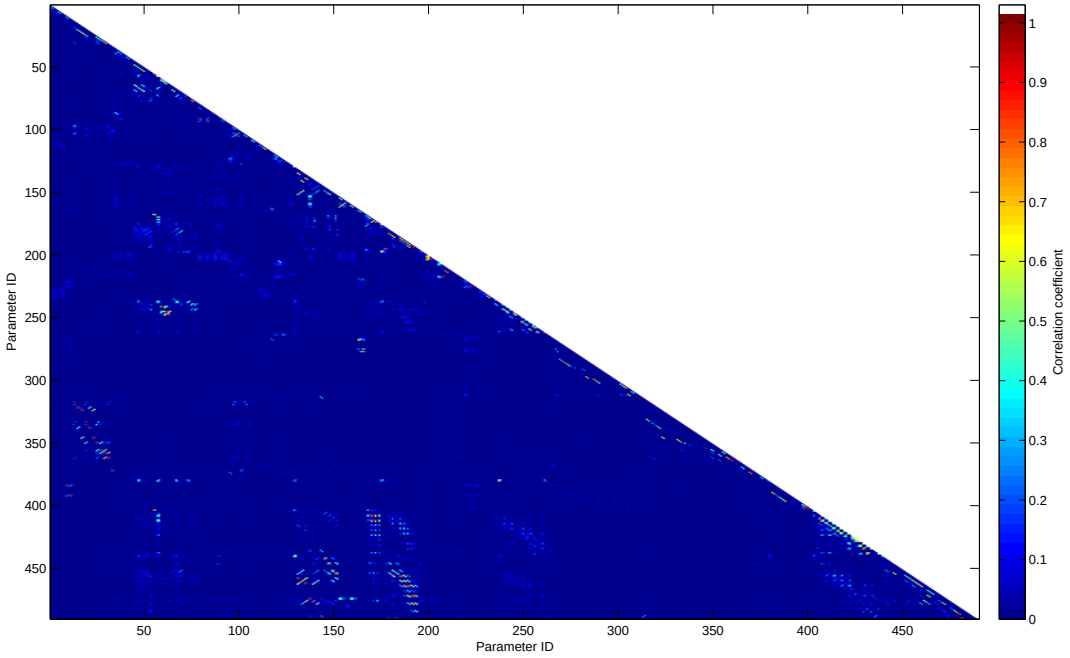

Figure 6.6. Correlation matrix of the estimated parameters.

FES2004 model. In particular, the 3D RMS of the difference between the orbits computed using FES2004 and those recomputed with the new parameters is illustrated in Figure 6.9, showing a mean value of 2.5 cm. Also the 3D RMS of the difference between the official R/D PSO and those recomputed with the new ocean tide model were computed and plotted in 6.10, resulting in an averaged difference of 4.9 cm.

Finally, the difference between the 3D RMS of the orbit residuals between the R/D PSO and the GOCE POD with FES2004 and the RMS of the difference between the GOCE R/D PSO and the GOCE POD with the new parameters is presented in Figure 6.11. It is interesting to notice that only for the 25% of the arcs the POD performed with FES2004 has more agreement with the R/D PSO, with a mean improvement of 0.2 cm. For the remaining arcs, the POD carried out with the model including the estimated parameters shows a mean improvement of 0.9 cm, with several peaks greater than 1 cm.

These results confirm that the estimated ocean tide parameters absorbed unmodeled signal due to omission errors or mismodeling errors deriving from the other models. The improvement in the agreement of the GOCE POD performed with the new ocean tide model is noteworthy and a good premise for further investigations.

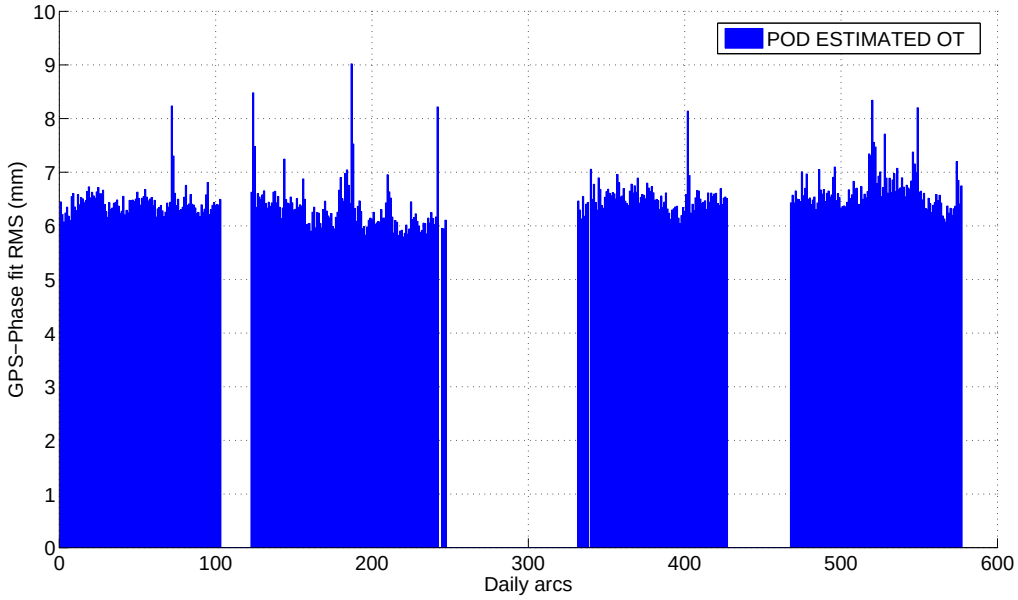

Figure 6.7. Fit RMS of the GPS phase residuals obtained using the new estimated parameters in the ocean tide model, instead of the corresponding FES2004 parameters.

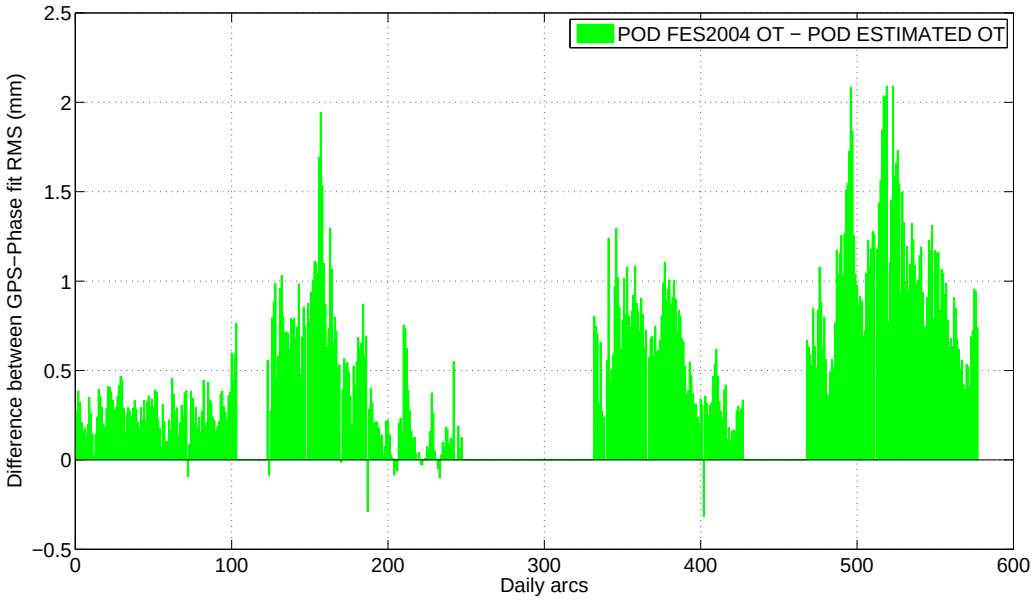

Figure 6.8. Difference between the fit RMS obtained using FES2004 model and the fit RMS obtained with the new estimated ocean tide parameters, instead of the corresponding FES2004 parameters.

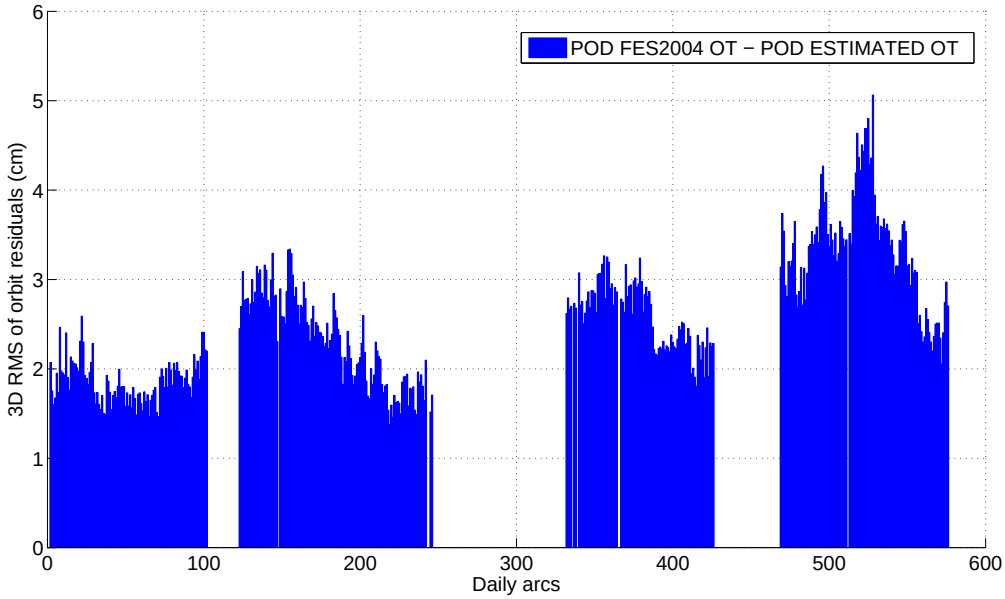

Figure 6.9. 3D RMS of the difference between the GOCE orbits computed using FES2004 and the orbits recomputed with the new parameters substituting the corresponding FES2004.

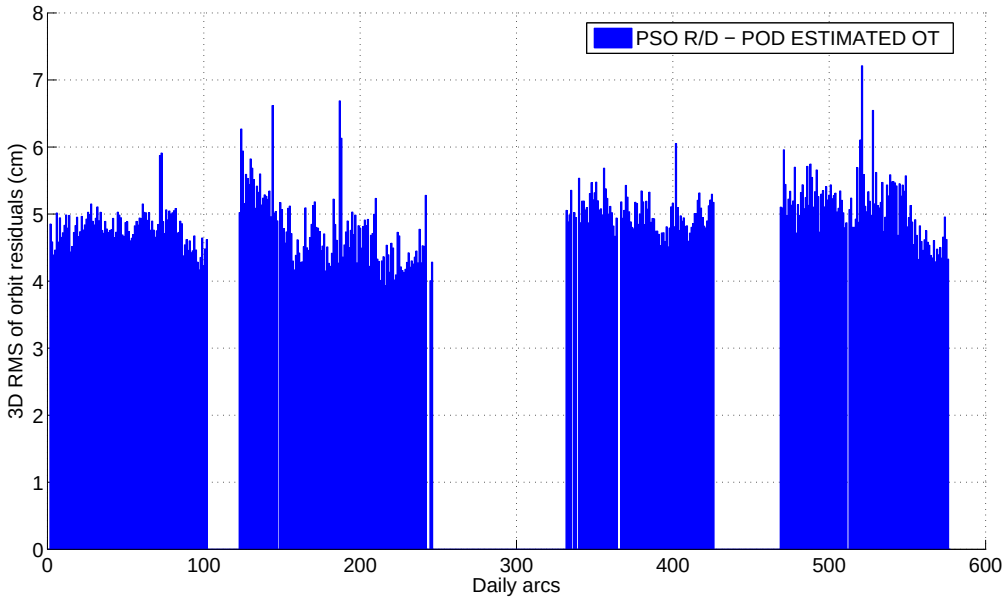

Figure 6.10. 3D RMS of the difference between the GOCE R/D PSO [8, Visser et al. 2009; Bock et al., 2011] and the orbits recomputed with the new parameters substituting the corresponding FES2004.

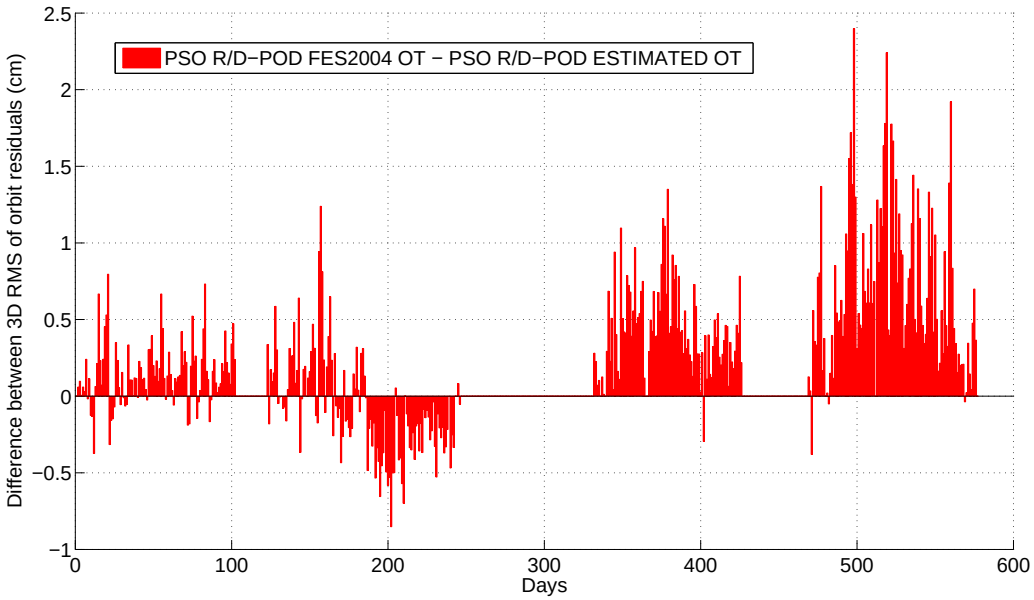

Figure 6.11. Difference between the 3D RMS of the differences between R/D PSO and the GOCE orbits estimated with FES2004 and the RMS of the difference between the GOCE R/D PSO and the orbits recomputed with the new parameters.

Chapter 7

Conclusions and future works

Tides are periodical phenomena affecting both the solid Earth and oceans, caused by the differential gravitational attraction of external perturbing bodies on the Earth's surface, and by the Earth's response to this tide-generating potential, so they represent a time-variable part of the geopotential.

The ocean tide height field was expressed according to different parameterizations, the main being the classical spherical harmonic representation, characterized by a sum of partial tide heights each corresponding to a tidal frequency, and the response analysis, in which the transfer function or impulse response between the tidal forcing and the ocean tide height field is assumed to be linear inside each tidal band. Concerning the orthonormalized formulation of the response method developed by Groves and Reynolds (1975), a new computational algorithm was developed and implemented, with the aim to accurately redetermine diurnal and semidiurnal orthotide constants necessary for the accurate redetermination of the orthotides used as basis functions in the representation of the ocean tide height field. The results show that orthonormality requirements are satisfied with a precision better than 10^{-8} for the diurnal band and better than 10^{-7} for the semidiurnal band up to orthotide order 50.

Tides are often considered as a noise or a correction to be removed from satellite gravity records and from the sea level observed by altimeters, in order to study other oceanic phenomena such as ocean currents. However, ocean tides represent also a signal to be recovered for applications concerning the evaluation of gravitational perturbations acting on the Earth orbiting satellites or for the accurate computation of ocean tide loading deformation and station displacements.

Thanks to its extremely low altitude of about 250 km, the GOCE satellite launched by ESA in 2009 is the most sensitive to ocean tide perturbations and a test-bed for the application of classical orbit perturbation analysis methods to estimate tidal parameters, which is the fundamental topic of this work of research. Among the several processing strategies that can be adopted, the direct fully-dynamic approach was chosen, consisting in performing the fully-dynamic precise orbit determination of GOCE, accumulating the normal equations for each orbital arc and estimating the global ocean tide parameters through a multiarc solution. The tool to perform this type of analysis has been identified in ESA's NAPEOS S/W system, specific for orbit determination and prediction and parameter estimation capabilities for the Earth orbiting satellites. However, it was necessary to upgrade the system with the entire implementation of the partial derivatives with respect to the ocean tide harmonic parameters and the extension of the structure for the inclusion of the ocean tide parameters characteristics: the tidal constituent, harmonic type (C or S), the harmonic degree and order and the chirality (prograde or retrograde).

The principal and quite intensive task in order to accomplish the scientific objective of the study was to define the set of ocean tide harmonic parameters ($\bar{C}^{\pm}_{\mathbf{k}lm}, \bar{S}^{\pm}_{\mathbf{k}lm}$) to which GOCE is more sensitive.

A global and detailed sensitivity study of the ocean tide perturbations on GOCE orbit was carried out using as a reference the FES2004 model. First of all, the effect of several combinations of ocean tide constituents on GOCE orbit was quantified over annual period, obtaining the following results:

- 106 constituents of the ocean tide field FES2004, 50x50, show a total position perturbation reaching a maximum of about 3000 m;
- 8 main constituents $O1$, $P1$, $K1$, $Q1$, $N2$, $M2$, $K2$, $S2$ of the ocean tide field FES2004, 50x50, show a total effect of about 3000 m;
- 6 main constituents $O1$, $P1$, $Q1$, $N2$, $M2$, $K2$ of the ocean tide field FES2004, 50x50 (the two resonant constituents $K1$ and $S2$ have been discarded), show a total effect of about 400 m;
- 103 constituents of the ocean tide field FES2004, 50x50 (the three resonant constituents $K1$, $S1$ and $S2$ have been discarded), show a total effect of about 600 m;
- the main constituent $M2$ of the ocean tide field FES2004, 50x50, shows a total effect of about 600 m.

In addition, over the longest tidal period of 18.6 years regarding the lunar node regression, the effect of 106 constituents of the model FES2004, 50x50, shows a maximum perturbation of about 140 km.

Ocean tides accelerations acting on GOCE orbit were determined over a period of about 70 days using different existent ocean tide models, resulting in an RMS of the order of 10^{-8} m/s^2.

Then, from the evolution of GOCE orbital elements available from a preliminary run of GOCE precise orbit determination with NAPEOS, the mean values of the foronomic elements and the secular rates of the angular elements were estimated through a linear least-square fit, obtaining respectively for the argument of perigee, the longitude of ascending node and mean anomaly values of $\dot{\omega} = -3.764817 \times 10^{-7}$ rad/s, $\dot{\Omega} = 2.022334 \times 10^{-7}$ rad/s, $\dot{M} = 1.167455 \times 10^{-3}$ rad/s.

Using the mean orbital characteristics of GOCE (reported in Table 5.4), the analytical spectral analysis of the radial, transverse and normal ocean tide perturbations affecting GOCE position on orbit was computed using Kaula's linear satellite theory, up to degree and order 20×20 for 106 constituents of the FES2004 model, reported in Table 2.3. The resulting amplitude spectra were plotted for the three directions for both the prograde and the retrograde case in Figures 5.33, 5.34, 5.35, 5.36, 5.37 and 5.38.

Together with the spectral analysis, the perturbation statistics by coefficient was also performed respectively for the radial, transverse and normal ocean tide perturbations, obtaining a maximum RMS for the radial component of about 1.323 m, for the transverse component of 363.136 m and for the normal component of 76.241 m.

Moreover, an investigation concerning the temporal aliasing problem of the tidal perturbation frequencies affecting GOCE was necessary. In fact, GOCE does not monitor the entire global field continually, but samples the static gravity field and its time-varying part only along its orbital path, with a temporal resolution depending on the satellite repeat period. Following closely a repeat period of 979 revolutions in 61 nodal days, the tidal frequencies as felt by GOCE are aliased to periods from 122 days (twice the orbit repeat period) to almost infinite. Unfortunately, GOCE is also a Sun-synchronous satellite, so it does not allow the complete estimation of the diurnal and semidiurnal solar tide constituents S_2 and S_1 which have original periods of exactly 12 h and 24 h, because it will always sample both these constituents at the same phase every day, so they represent essentially a bias.

Combining information deriving from the spectral analysis, the perturbation statistics by coefficient and the determination of ocean tide alias periods, the list of the ocean tide parameters

from harmonic degree 2 to 20 to be estimated from GOCE orbital data was identified. It must be pointed out that the total number of parameters was limited through the application of three different cutoffs on the perturbation RMS by coefficient, respectively equal to 5 mm for the radial component, 2 cm for the transverse component and 1 cm for the normal component, both in the prograde and retrograde case. The resulting total number of parameters, to be estimated through a multiarc solution, is 490 and they are listed in Table 5.7.

GOCE orbital data were processed in daily arcs from the 1st November 2009, corresponding to the beginning of the operational phase, until the 31st May 2011 and the fully-dynamic POD was successfully computed for a total of 472 days (see Figure 6.2). However, only arcs with a post-fit RMS of the GPS phase observations residuals lower than 8 mm were considered for the multiarc processing, so a total of 431 days were used to solve for 490 ocean tide parameters.

The obtained preliminary results show that the 56% of the total number of parameters has a difference below 1 cm from the FES2004 model (see Figure 6.3), while the relative error of the estimated parameters with respect to the corresponding FES2004 parameters lower than 1 for about the 16% of the total (see Figure 6.5), meaning that they are of the order of magnitude of the FES2004 parameters. Though a large part of estimated parameters shows quite significant discrepancies from the values of the FES2004 model, it must be considered that they are recovered differently from the hydrodynamic with assimilation FES2004 model, being the result of a densely-parameterized, fully-dynamic orbital solution and tend to absorb errors due to the mismodeling of the force field acting on the satellite.

Then, the impact of the estimated parameters on the GOCE precise orbit determination was evaluated. GOCE orbital data were reprocessed from the 1st November 2009 to the 31st May 2011, initializing the ocean tide model with the estimated parameters, if present, and maintaining otherwise the FES2004 parameters. The post-fit RMS of the GPS phase residuals obtained with the new ocean tide model has a mean value of 6.5 mm, and it is noteworthy that the difference between the post-fit RMS obtained with the FES2004 model and that resulting from the new ocean tide model indicates a mean improvement of about 0.6 mm in for the 96% of the analyzed arcs and greater than 1 mm for the 16%, few days reach a difference of 2 mm.

Finally, the orbits obtained with the estimated parameters are compared with the orbits obtained employing the FES2004 model and the official GOCE R/D PSO. The 3D RMS of the difference between the orbits computed using FES2004 and those recomputed with the new parameters shows a mean value of 2.5 cm (see Figure 6.9), while the 3D RMS of the difference with respect to the official R/D PSO has a mean value of 4.9 cm. The difference between the 3D RMS of the orbit residuals between the R/D PSO and the GOCE POD with FES2004 and the RMS of the difference between the R/D PSO and the GOCE POD with the new parameters results to have a mean improvement of 0.9 cm (see Figure 6.11).

As a future work, further POD-Multiarc runs are certainly necessary, together with the refinement of the list of parameters to be estimated, removing excessively ill-estimated ocean tide parameters which could wrongly absorb tidal signal, redistributing erroneously the remaining signal on the other parameters, and then introducing new parameters where appropriate. The model parameter tuning and investigation is essential to adjust the best combination of parameters to be estimated. Moreover, an extension of the data set to much longer time-period should allow a substantial improvement of the obtained results. Indeed, the task has proven very intensive and challenging, but the partial results obtained are encouraging and a motivation for future analysis.

Appendix A

Lag index limits and symmetry properties of the orthotide coefficients

The number of unknown coefficients U_{nk} and V_{nk} associated with the orthotide of any order n, as expressed by equation (3.115) in terms of an arbitrary value K of the maximum lag index, is $N = 2(2K + 1)$. However, according to the orthonormality relation (3.116), the number of equations of condition is $(n + 1)$. If we set $K = n = i$ the plot of these two integer functions shown in Figure A.1 reveals that the number of coefficients to be determined is always greater than the number of available equations, i.e., the system to be solved is underdetermined. It is then expedient to use K as a free parameter to limit the number of unknowns depending on the order n of the orthotide in such a manner as to generate a non-overdetermined system of equations $\langle \zeta_n(t)\zeta_m(t) \rangle = \delta_{nm}$, for $m = 0, 1, ..., n$.

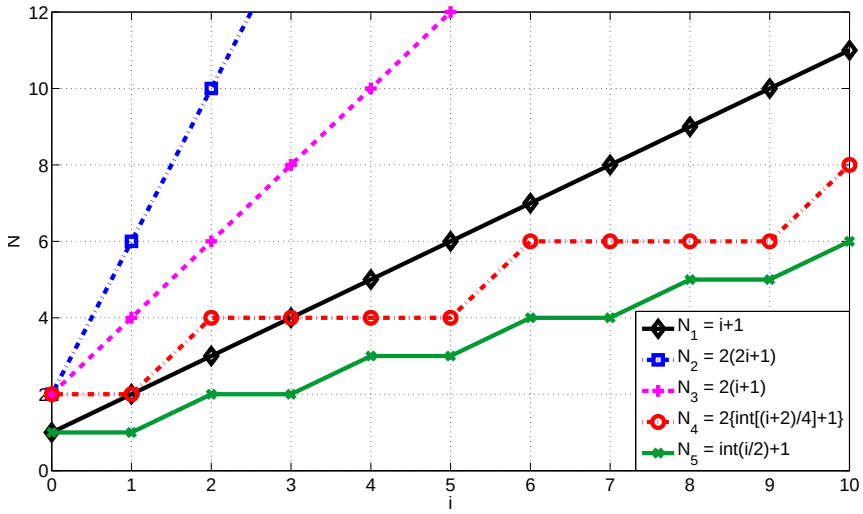

Figure A.1. In black (continuous line with diamond marker): number of equations $N = n + 1$ to be solved for each system of mean displaced products versus the order represented here by the index i; in blue (dash-dot line with square marker): number of coefficients $N = 2(2K + 1)$ free of constraints and comprehensive of negative lag indeces versus the maximum lag index K, here represented by i; in magenta (dashed line with plus sign marker): number of coefficients $N = 2(K + 1)$ to be determined versus the maximum index K, here represented by i, after the imposition of symmetry conditions allowing the exclusion of negative lag indeces; in red (dash-dot line with circle marker): number of coefficients $N = 2(\lfloor (n + 2)/4 \rfloor + 1)$ to be determined versus the order represented by the index i, after the imposition of the constraint (A.69) on K; in green (continuous line with cross marker): number of non-zero coefficients $N = \lfloor n/2 \rfloor + 1$, equivalent to the number of effective equations to be solved for each system of mean orthotide products.

Following Groves and Reynolds (1985), it is convenient to drastically reduce the number of

coefficients to $N = 2(K+1)$ by imposing the following relations of symmetry between orthotide coefficients of opposite parity

$$U_{n,-k} = (-1)^n U_{nk}, \tag{A.1}$$
$$V_{n,-k} = -(-1)^n V_{nk}, \tag{A.2}$$

which effectively eliminate the negative lag indices. Then the expression for the generic orthotide of order n becomes[1]

$$\begin{aligned} \zeta_n(t) &= U_{n0}a(t) + V_{n0}b(t) \\ &\quad + \sum_{k=1}^{K} U_{nk}\left[a(t+k\Delta t) + (-1)^n a(t-k\Delta t)\right] \\ &\quad + \sum_{k=1}^{K} V_{nk}\left[b(t+k\Delta t) - (-1)^n b(t-k\Delta t)\right]. \end{aligned} \tag{A.4}$$

As Figure A.1 shows, the slope of the relation between the number of coefficients and the maximum lag index K is less steep. Now we choose the maximum lag index K in order that is the maximum value allowing for an underdetermined or determined system.

Examining the problem in more detail, we observe that for order $n = 0$ and maximum lag $K = 0$, the system consists of only one equation

$$\langle \zeta_0(t)\zeta_0(t)\rangle = (U_{00}^2 + V_{00}^2)\psi_0 = 1, \tag{A.5}$$

so there must be only one unknown and this implies that either U_{00} or V_{00} must be discarded. We choose to set $V_{00} = 0$ because in the orthotide expression (3.115), V_{nk} terms multiply $b(t+k\Delta t)$ terms, which are built as combination of sine functions, while it can be preferable to have cosine functions. The solution is then $U_{00} = \sqrt{1/\psi_0}$ so that

$$\zeta_0(t) = U_{00}a(t). \tag{A.6}$$

[1]

$$\begin{aligned} \zeta_n(t) &= \sum_{k=-K}^{K}\left[U_{nk}a(t+k\Delta t) + V_{nk}b(t+k\Delta t)\right] \\ &= \sum_{k=0}^{K}\left[U_{nk}a(t+k\Delta t) + V_{nk}b(t+k\Delta t)\right] \\ &\quad + \sum_{k=-K}^{-1}\left[U_{nk}a(t+k\Delta t) + V_{nk}b(t+k\Delta t)\right] \\ &= \sum_{k=0}^{K}\left[U_{nk}a(t+k\Delta t) + V_{nk}b(t+k\Delta t)\right] \\ &\quad + \sum_{k=1}^{K}\left[U_{n,-k}a(t-k\Delta t) + V_{n,-k}b(t-k\Delta t)\right] \\ &= \sum_{k=0}^{K}\left[U_{nk}a(t+k\Delta t) + V_{nk}b(t+k\Delta t)\right] \\ &\quad + \sum_{k=1}^{K}(-1)^n\left[U_{nk}a(t-k\Delta t) - V_{nk}b(t-k\Delta t)\right] \\ &= U_{n0}a(t) + V_{n0}b(t) \\ &\quad + \sum_{k=1}^{K}\left\{U_{nk}\left[a(t+k\Delta t) + (-1)^n a(t-k\Delta t)\right]\right. \\ &\quad \left. + V_{nk}\left[b(t+k\Delta t) - (-1)^n b(t-k\Delta t)\right]\right\}. \end{aligned} \tag{A.3}$$

For order $n = 1$, the system has two equations and the maximum lag index must be $K = 0$ so as to have only two unknowns. In fact, the corresponding system is then

$$\langle \zeta_1(t)\zeta_0(t)\rangle = (U_{10}U_{00} + V_{10}V_{00})\psi_0 = 0, \tag{A.7}$$

$$\langle \zeta_1(t)\zeta_1(t)\rangle = (U_{10}^2 + V_{10}^2)\psi_0 = 1. \tag{A.8}$$

Using the known values of V_{00} and U_{00}, the system simplifies to

$$\sqrt{\psi_0}U_{10} = 0, \tag{A.9}$$

$$(U_{10}^2 + V_{10}^2)\psi_0 = 1, \tag{A.10}$$

which admits the solution $U_{10} = 0$, $V_{10} = \sqrt{1/\psi_0}$. Note that $U_{10} = -V_{00}$ and $V_{10} = U_{00}$. Therefore

$$\zeta_1(t) = V_{10}b(t), \tag{A.11}$$

or

$$\zeta_1(t) = U_{00}b(t). \tag{A.12}$$

For order $n = 2$ we have a system of three equations, and the maximum lag index can be taken as $K = 1$. In this case there are three coefficients and the system

$$\begin{aligned}
\langle \zeta_2(t)\zeta_0(t)\rangle &= U_{00}(U_{20}\psi_0 + 2U_{21}\psi_1 && \text{(A.13)}\\
&\quad + 2V_{21}\chi_1) = 0, && \text{(A.14)}\\
\langle \zeta_2(t)\zeta_1(t)\rangle &= V_{10}V_{20}\psi_0 = 0, && \text{(A.15)}\\
\langle \zeta_2(t)\zeta_2(t)\rangle &= U_{20}^2\psi_0 + 2U_{21}^2(\psi_0 + \psi_2)\\
&\quad + 2V_{21}^2(\psi_0 - \psi_2) + 4U_{20}V_{21}\chi_1 && \text{(A.16)}\\
&\quad + 4U_{20}U_{21}\psi_1 + 4U_{21}V_{21}\chi_2 = 1.
\end{aligned}$$

is well determined. Again, using the previous solutions this simplifies to

$$\sqrt{1/\psi_0}(U_{20}\psi_0 + 2U_{21}\psi_1 + 2V_{21}\chi_1) = 0, \tag{A.17}$$

$$\sqrt{\psi_0}V_{20} = 0, \tag{A.18}$$

$$\begin{aligned}
&U_{20}^2\psi_0 + 2U_{21}^2(\psi_0 + \psi_2)\\
&+ 2V_{21}^2(\psi_0 - \psi_2) + 4U_{20}V_{21}\chi_1 && \text{(A.19)}\\
&+ 4U_{20}U_{21}\psi_1 + 4U_{21}V_{21}\chi_2 = 1.
\end{aligned}$$

The second of these equations is decoupled from the other two and provides $V_{20} = 0$. The other two equations still contain the three unknowns U_{20}, U_{21}, and V_{21}. We eliminate one by setting $V_{21} = 0$. Then U_{20} and U_{21} follow from eqs. (A.17) and (A.19), which now read

$$U_{20}\psi_0 + 2U_{21}\psi_1 = 0, \tag{A.20}$$

$$U_{20}^2\psi_0 + 2U_{21}^2(\psi_0 + \psi_2) + 4U_{20}U_{21}\psi_1 = 1. \tag{A.21}$$

The orthotide[2] of order 2 is then

$$\zeta_2(t) = U_{20}a(t) + U_{21}\left[a(t + \Delta t) + a(t - \Delta t)\right]. \tag{A.23}$$

[2]The general orthotide at $n = 2$ has the expression

$$\begin{aligned}
\zeta_2(t) &= U_{2,-1}a(t - \Delta t) + V_{2,-1}b(t - \Delta t) + U_{20}a(t) + V_{20}b(t)\\
&\quad + U_{21}a(t + \Delta t) + V_{21}b(t + \Delta t)\\
&= U_{21}a(t - \Delta t) - V_{21}b(t - \Delta t)\\
&\quad + U_{20}a(t) + V_{20}b(t) + U_{21}a(t + \Delta t) + V_{21}b(t + \Delta t)\\
&= U_{20}a(t) + V_{20}b(t) + U_{21}\left[a(t + \Delta t) + a(t - \Delta t)\right]\\
&\quad + V_{21}\left[b(t + \Delta t) - b(t - \Delta t)\right]. && \text{(A.22)}
\end{aligned}$$

For order $n = 3$ we keep $K = 1$ and write the following system

$$\langle \zeta_3(t)\zeta_0(t)\rangle = U_{00}U_{30}\psi_0 = 0, \tag{A.24}$$
$$\langle \zeta_3(t)\zeta_1(t)\rangle = V_{10}(V_{30}\psi_0 + 2V_{31}\psi_1 - 2U_{31}\chi_1) = 0, \tag{A.25}$$
$$\langle \zeta_3(t)\zeta_2(t)\rangle = 2U_{31}U_{20}\psi_1 = 0 \tag{A.26}$$
$$\langle \zeta_3(t)\zeta_3(t)\rangle = V_{30}^2\psi_0 + 2V_{31}^2(\psi_0 + \psi_2) + 4V_{30}V_{31}\psi_1 = 1. \tag{A.27}$$

Substitution of known quantities, which we also indicate with the notation $[[]]$, yields

$$\sqrt{1/\psi_0}U_{30} = 0, \tag{A.28}$$
$$\sqrt{1/\psi_0}(V_{30}\psi_0 + 2V_{31}\psi_1 - 2U_{31}\chi_1) = 0, \tag{A.29}$$
$$[[2U_{20}\psi_1]]\, U_{31} = 0 \tag{A.30}$$
$$V_{30}^2\psi_0 + 2V_{31}^2(\psi_0 + \psi_2) + 4V_{30}V_{31}\psi_1 = 1. \tag{A.31}$$

Here, the first and the third equations are decoupled from the others and provide $U_{30} = 0$ and $U_{31} = 0$. Note that we can write $U_{30} = -V_{20}$ and $U_{31} = -V_{21}$. The system then further simplifies to the form

$$V_{30}\psi_0 + 2V_{31}\psi_1 = 0, \tag{A.32}$$
$$V_{30}^2\psi_0 + 2V_{31}^2(\psi_0 + \psi_2) + 4V_{30}V_{31}\psi_1 = 1, \tag{A.33}$$

which is identical with the system (A.20)-(A.21) under the identifications $V_{30} \longleftrightarrow U_{20}$ and $V_{31} \longleftrightarrow U_{21}$. This implies that

$$V_{30} = U_{20}, \tag{A.34}$$
$$V_{31} = U_{21}, \tag{A.35}$$

or that the system of orthotide order 3 has the same solution as the system of order 2 under an appropriate change of variables. Then[3]

$$\zeta_3(t) = V_{30}b(t) + V_{31}\left[b(t+\Delta t) + b(t-\Delta t)\right], \tag{A.37}$$

or

$$\zeta_3(t) = U_{20}b(t) + U_{21}\left[b(t+\Delta t) + b(t-\Delta t)\right]. \tag{A.38}$$

For order $n = 4$ and again $K = 1$ we have

$$\langle \zeta_4(t)\zeta_0(t)\rangle = U_{00}(U_{40}\psi_0 + 2U_{41}\psi_1 + 2V_{41}\chi_1) = 0, \tag{A.39}$$
$$\langle \zeta_4(t)\zeta_1(t)\rangle = V_{10}V_{40}\psi_0 = 0, \tag{A.40}$$
$$\langle \zeta_4(t)\zeta_2(t)\rangle = U_{20}(U_{40}\psi_0 + 2U_{41}\psi_1 + 2V_{41}\chi_1) \tag{A.41}$$

[3] Generically,

$$\begin{aligned}\zeta_3(t) &= U_{3,-1}a(t-\Delta t) + V_{3,-1}b(t-\Delta t) + U_{30}a(t) + V_{30}b(t)\\ &\quad + U_{31}a(t+\Delta t) + V_{31}b(t+\Delta t)\\ &= -U_{31}a(t-\Delta t) + V_{31}b(t-\Delta t)\\ &\quad + U_{30}a(t) + V_{30}b(t) + U_{31}a(t+\Delta t) + V_{31}b(t+\Delta t)\\ &= U_{30}a(t) + V_{30}b(t) + U_{31}\left[a(t+\Delta t) - a(t-\Delta t)\right]\\ &\quad + V_{31}\left[b(t+\Delta t) + b(t-\Delta t)\right].\end{aligned} \tag{A.36}$$

$$+ U_{21}(2U_{40}\psi_1 + 2U_{41}\psi_0 + 2U_{41}\psi_2 \tag{A.42}$$
$$+ 2V_{41}\chi_2) = 0,$$
$$\langle\zeta_4(t)\zeta_3(t)\rangle = 0, \tag{A.43}$$
$$\langle\zeta_4(t)\zeta_4(t)\rangle = U_{40}^2\psi_0 + 2U_{41}^2(\psi_0 + \psi_2)$$
$$+ 2V_{41}^2(\psi_0 - \psi_2) + 4U_{40}U_{41}\psi_1 \tag{A.44}$$
$$+ 4U_{40}V_{41}\chi_1 + 4U_{41}V_{41}\chi_2 = 1.$$

The second equation leads to $V_{40} = 0$. Note that equation (A.43) is identically satisfied, which brings the effective number of equations down by one unit to 3, and this justfies having kept the maximum leg index K to 1. The system[4] of three equations in three unknowns is then

$$U_{40}\psi_0 + 2U_{41}\psi_1 + 2V_{41}\chi_1 = 0, \tag{A.49}$$
$$[[U_{20}]]\,(U_{40}\psi_0 + 2U_{41}\psi_1 + 2V_{41}\chi_1)$$
$$+ [[U_{21}]]\,(2U_{40}\psi_1 + 2U_{41}\psi_0 + 2V_{41}\chi_2) = 0, \tag{A.50}$$
$$U_{40}^2\psi_0 + 2U_{41}^2(\psi_0 + \psi_2) + 2V_{41}^2(\psi_0 - \psi_2)$$
$$+ 4U_{40}U_{41}\psi_1 + 4U_{40}V_{41}\chi_1 + 4U_{41}V_{41}\chi_2 = 1, \tag{A.51}$$

where we have eliminated U_{00}, U_{20} and U_{21} being known quantities. The solution then provides values for U_{40}, U_{41}, V_{41}.

The orthotide of order 4 is then[5]

$$\zeta_4(t) = U_{40}a(t) + U_{41}\left[a(t+\Delta t) + a(t-\Delta t)\right]$$
$$+ V_{41}\left[b(t+\Delta t) - b(t-\Delta t)\right]. \tag{A.53}$$

For order $n = 5$ we can still keep $K = 1$. The corresponding system is

$$\langle\zeta_5(t)\zeta_0(t)\rangle = U_{00}U_{50}\psi_0 = 0, \tag{A.54}$$
$$\langle\zeta_5(t)\zeta 1(t)\rangle = V_{10}(V_{50}\psi_0 + 2V_{51}\psi_1$$
$$- 2U_{51}\chi_1) = 0, \tag{A.55}$$
$$\langle\zeta_5(t)\zeta_2(t)\rangle = 0, \tag{A.56}$$
$$\langle\zeta_5(t)\zeta_3(t)\rangle = V_{30}(V_{50}\psi_0 + 2V_{51}\psi_1 - 2U_{51}\chi_1)$$

[4]

$$\sqrt{1/\psi_0}(U_{40}\psi_0 + 2U_{41}\psi_1 + 2V_{41}\chi_1) = 0, \tag{A.45}$$
$$\sqrt{1/\psi_0}V_{40}\psi_0 = 0, \tag{A.46}$$
$$U_{20}(U_{40}\psi_0 + 2U_{41}\psi_1 + 2V_{41}\chi_1)$$
$$+ U_{21}(2U_{40}\psi_1 + 2U_{41}\psi_0 + 2U_{41}\psi_2 + 2V_{41}\chi_2) = 0, \tag{A.47}$$
$$U_{40}^2\psi_0 + 2U_{41}^2(\psi_0 + \psi_2) + 2V_{41}^2(\psi_0 - \psi_2) + 4U_{40}U_{41}\psi_1$$
$$+ 4U_{40}V_{41}\chi_1 + 4U_{41}V_{41}\chi_2 = 1. \tag{A.48}$$

[5] In general,

$$\begin{aligned}\zeta_4(t) &= U_{4,-1}a(t-\Delta t) + V_{4,-1}b(t-\Delta t) + U_{40}a(t)\\ &\quad + V_{40}b(t) + U_{41}a(t+\Delta t) + V_{41}b(t+\Delta t)\\ &= U_{41}a(t-\Delta t) - V_{41}b(t-\Delta t) + U_{40}a(t) + V_{40}b(t)\\ &\quad + U_{41}a(t+\Delta t) + V_{41}b(t+\Delta t)\\ &= U_{40}a(t) + V_{40}b(t) + U_{41}\left[a(t+\Delta t) + a(t-\Delta t)\right]\\ &\quad + V_{41}\left[b(t+\Delta t) - b(t-\Delta t)\right].\end{aligned} \tag{A.52}$$

$$+ V_{31}(2V_{50}\psi_1 + 2V_{51}\psi_0 + 2V_{51}\psi_2 \quad (A.57)$$
$$- 2U_{51}\chi_2) = 0,$$
$$\langle\zeta_5(t)\zeta_4(t)\rangle = 0, \quad (A.58)$$
$$\langle\zeta_5(t)\zeta_5(t)\rangle = V_{50}^2\psi_0 + 2V_{51}^2(\psi_0 + \psi_2) + 2U_{51}^2(\psi_0 - \psi_2)$$
$$+ 4V_{50}V_{51}\psi_1 - 4V_{50}U_{51}\chi_1 \quad (A.59)$$
$$- 4U_{51}V_{51}\chi_2 = 1.$$

The first equation leads to $U_{50} = 0$. Note that we can write $U_{50} = -V_{40}$. The third and the fifth equations are actually identities and thus lower the number of equations by 2. Using the previous solutions the system reduces to

$$V_{50}\psi_0 + 2V_{51}\psi_1 - 2U_{51}\chi_1 = 0, \quad (A.60)$$
$$V_{30}(V_{50}\psi_0 + 2V_{51}\psi_1 - 2U_{51}\chi_1) \quad (A.61)$$
$$+ V_{31}(2V_{50}\psi_1 + 2V_{51}\psi_0 + 2V_{51}\psi_2 - 2U_{51}\chi_2) = 0,$$
$$V_{50}^2\psi_0 + 2V_{51}^2(\psi_0 + \psi_2) + 2U_{51}^2(\psi_0 - \psi_2)$$
$$+ 4V_{50}V_{51}\psi_1 - 4V_{50}U_{51}\chi_1 - 4U_{51}V_{51}\chi_2 = 1. \quad (A.62)$$

Now this is a system of 3 equations in the three unknowns U_{51}, V_{50} and V_{51}. The system is identical with the system of order 4 (A.49)-(A.51) under the identifications $U_{51} \longleftrightarrow -V_{41}$, $V_{50} \longleftrightarrow U_{40}$ and $V_{51} \longleftrightarrow U_{41}$. Therefore we deduce that

$$U_{51} = -V_{41}, \quad (A.63)$$
$$V_{50} = U_{40}, \quad (A.64)$$
$$V_{51} = U_{41}. \quad (A.65)$$

The system of order $n = 5$ therefore has the same solution as the system of order $n = 4$ under an appropriate change of variables. This again justifies having kept the maximum lag index K fixed to 1. In fact, the maximum lag index K remains the same until all the coefficients U,V available with that K are used to determine the coefficients of subsequent odd orders. When all the coefficients of an even order have been used to determine the coefficients of the subsequent odd order, the maximum lag index K must be increased by 1 and, consequently, also the number of coefficients to be determined.

The orthotide of order 5 is then[6]

$$\zeta_5(t) = V_{50}b(t) + U_{51}[a(t+\Delta t) - a(t-\Delta t)]$$
$$+ V_{51}[b(t+\Delta t) + b(t-\Delta t)], \quad (A.67)$$

or

$$\zeta_5(t) = U_{40}b(t) - V_{41}[a(t+\Delta t) - a(t-\Delta t)]$$
$$+ U_{41}[b(t+\Delta t) + b(t-\Delta t)]. \quad (A.68)$$

[6] In general terms,

$$\begin{aligned}\zeta_5(t) &= U_{5,-1}a(t-\Delta t) + V_{5,-1}b(t-\Delta t) + U_{50}a(t)\\ &\quad + V_{50}b(t) + U_{51}a(t+\Delta t) + V_{51}b(t+\Delta t)\\ &= -U_{51}a(t-\Delta t) + V_{51}b(t-\Delta t) + U_{50}a(t) + V_{50}b(t)\\ &\quad + U_{51}a(t+\Delta t) + V_{51}b(t+\Delta t)\\ &= U_{50}a(t) + V_{50}b(t) + U_{51}[a(t+\Delta t) - a(t-\Delta t)]\\ &\quad + V_{51}[b(t+\Delta t) + b(t-\Delta t)]. \quad (A.66)\end{aligned}$$

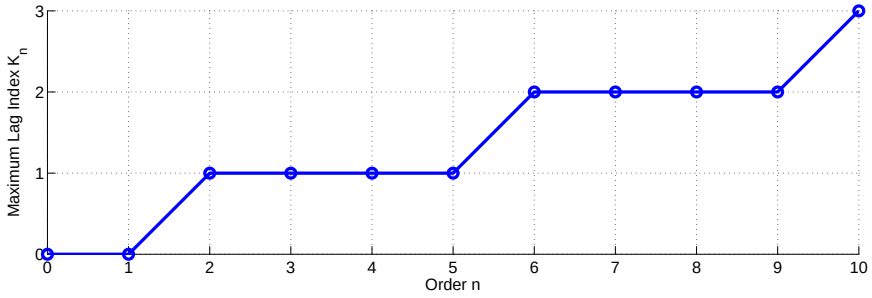

Figure A.2. Relation between the maximum lag K and the orthotide order n.

The analysis can be continued[7] for $n = 6$ (where the maximum lag index increases to $K = 2$) and beyond, but we can already draw the fundamental conclusions. We can state in fact that

1. The maximum lag index K is a function K_n of the orthotide order n. It starts at 0 for $n = 0$, increases by 1 for $n = 2, 6, 10, ...$ and (see Figure A.2) is thus given by

$$K_n = \lfloor (n+2)/4 \rfloor . \tag{A.69}$$

K_n is the minimum value such that the number $N = 2(K_n + 1)$ of coefficients at order n is compatible with a non-overdetermined system of equations (recall that the order of the system is equal to the number of available equations of constraint). It follows that the total number of coefficients (both zero and non-zero) at orthotide order n is

$$N = 2\left(\left\lfloor \frac{n+2}{4} \right\rfloor + 1\right). \tag{A.70}$$

2. At each order n there are $\lfloor (n+1)/2 \rfloor$ products of opposite parity and they all generate either identities, or trivial equations (i.e., equations directly implying either $U_{2n+1,0} = 0$ or $V_{2n,0} = 0$). Thus the number N_e of effective equations (those generating the non-zero coefficients) becomes

$$N_e = (n+1) - \left\lfloor \frac{n+1}{2} \right\rfloor = \left\lfloor \frac{n}{2} \right\rfloor + 1; \tag{A.71}$$

3. It has been observed that at each odd order the solution can be directly expressed in terms of the previous, even order, i.e., we can express the orthotide coefficients of order $2n+1$ as a function of the orthotide coefficients of order $2n$ as

$$V_{2n+1,k} = U_{2n,k}, \tag{A.72}$$

$$U_{2n+1,k} = -V_{2n,k}. \tag{A.73}$$

Then orthotides are always of even order and they assume the expression, for $n = 0, 1, ...$

$$\begin{aligned} \zeta_{2n}(t) &= U_{2n,0}a(t) + V_{2n,0}b(t) \\ &\quad + \sum_{k=1}^{K} U_{2n,k}\left[a(t+k\Delta t) + a(t-k\Delta t)\right] \\ &\quad + \sum_{k=1}^{K} V_{2n,k}\left[b(t+k\Delta t) - b(t-k\Delta t)\right]. \end{aligned} \tag{A.74}$$

$$\zeta_{2n}(t) = U_{2n,0}a(t) + V_{2n,0}b(t)$$

[7] For order $n = 6$, the maximum lag is $K = 2$ and the system consists of four equations which can be solved for the coefficients U_{60}, U_{61}, U_{62}, V_{61}, while $V_{60} = 0$ and V_{62} is discarded.

$$+\sum_{k=1}^{K} U_{2n,k}\, a_k^+(t) + \sum_{k=1}^{K} V_{2n,k}\, b_k^-(t)\,, \tag{A.75}$$

where

$$a_k^+(t) = a(t+k\Delta t) + a(t-k\Delta t)\,, \tag{A.76}$$

$$b_k^-(t) = b(t+k\Delta t) - b(t-k\Delta t)\,. \tag{A.77}$$

4. Recalling that we set $V_{00} = 0$, these relations can also be used to write that, for each orthotide order $n \geq 0$,

$$U_{2n+1,0} = V_{2n,0} = 0. \tag{A.78}$$

5. Examination of the results obtained for the solutions of orders $n = 2, 4$ and beyond establishes the property according to which the V functions either terminate at maximum lag index K_n or at the previous index $K_n - 1$, respectively for orthotides of order $n = 4i$, $i = 1, 2, ...$ and orthotides of order $n = 4i - 2$, $i = 1, 2, ...$ This means, in practice, that the ordered sequence of U and V coefficients associated with (even) orthotide orders n alternately terminates with the pair U_{nK_n}, V_{nK_n} for $n = 4, 8, ...$, or with the single coefficient U_{nK_n} for $n = 2, 6, ...$, the coefficient V_{nK_n} being identically zero in this case.

Bibliography

[1] Alcock, G. A., Cartwright, D. E. (1978): Some experiments with orthotides, *Geophysical Journal of the Royal Astronomical Society*, **54**, 681-696.

[2] Arnold, S. J., Dow, J. M. (1984): Models for spacecraft acceleration due to Earth albedo and infrared radiation, OAD WP n. 265.

[3] Bardella, M., Casotto, S. (2012): Extending ESA's NAPEOS S/W System for Ocean Tide Parameter Recovery, 23rd International Symposium on Space Flight Dynamics, October 29 - November 2, 2012, Pasadena, CA, USA.

[4] Barthelmes, F. (2009): *Definition of functionals of the geopotential ad their calculation from spherical harmonic models*, Theory and formulas used by the calculation service of the International Centre for Global Earth Models (ICGEM), Scientific Technical Report STR09/02, GFZ Helmholtz-Zentrum, Potsdam.

[5] Bezděk, A., Klokočnik, J., Kostelecky, J., Floberghagen, R., Gruber, C. (2009): Simulation of free fall and resonances in the GOCE mission, *Journal of Geodynamics*, **48**, 47-53.

[6] Bezděk, A., Klokočnik, J., Kostelecky, J., Floberghagen, R., Sebera, J. (2010): Some aspects of the orbit selection for the measurement phases of GOCE, *Proceedings of the ESA Living Planet Symposium*, Bergen, Norway, 28 June - 2 July, ESA SP-686.

[7] Bock, H., Jäggi, A., Svehla, D., Beutler, G., Hugentobler, U., Visser, P. (2007): Precise orbit determination for the GOCE satellite using GPS, *Advances in Space Research*, **39**, 1638-1647.

[8] Bock, H., Jäggi A., Meyer, U., Visser, P., van den IJssel, J., van Helleputte, T., Heinze, M., Hugentobler, U. (2011): GPS-derived orbits for the GOCE satellite, *Journal of Geodesy*, **85**, 807-818, DOI 10.1007/s00190-011-0484-9.

[9] Carrere, L., Lyard, F., Guillot, Cancet, M., Roblou, L. (2012): FES2012: A new tidal model taking advantage of nearly 20 years of altimetry measurements, OSTST 2012, 22-29 September, Venice, Italy.

[10] Cartwright, D. E., Tayler, R. J. (1971): New computations of the tide-generating potential, *Geophysical Journal of the Royal Astronomical Society*, **23**, 45-74.

[11] Cartwright, D. E., Edden, A. C. (1973): Corrected tables of tidal harmonics, *Geophysical Journal of the Royal Astronomical Society*, **33**, 253-264.

[12] Cartwright, D. E., Ray, R. D. (1990): Oceanic tides from Geosat altimetry, *Journal of Geophysical Research*, **95**(C3), 3069-3090.

[13] Cartwright, D. E., Ray, R. D. (1991): Energetics of Global Ocean Tides From Geosat Altimetry, *Journal of Geophysical Research*, **96**(C9), 16,897-16,912.

[14] Casotto, S. (1989): Nominal ocean tide models for TOPEX precise orbit determination, Center for Space Research, University of Texas, Austin, Texas.

[15] Casotto, S. (1991): Spectral decomposition of geopotential, Earth and ocean tidal perturbations in linear satellite theory, *Celestial Mechanics and Dynamical Astronomy*, **50**, 125-141.

[16] Casotto, S. (1993): The mapping of Kaula's solution into the orbital reference frame, *Celestial Mechanics and Dynamical Astronomy*, **55**, 223-241.

[17] Casotto, S., Biscani, F. (2008): An algebraic manipulator for application to orbital mechanics, *The Byron Tapley Symposium*, Austin, Texas, February 1, 2008.

[18] Casotto, S., Fantino, E. (2009): Gravitational gradients by tensor analysis with application to spherical coordinates, *Journal of Geodynamics*, **83**, 621-634, DOI:10.1007/s00190-008-0276-z.

[19] Casotto, S., Bardella, M. (2010): On the numerical propagation of perturbations with respect to a secularly precessing elliptical orbit, New Trends in Astrodynamics and Applications VI, June 6-8, New York University, New York.

[20] Cazenave, A., Daillet, S., Lambeck, K. (1977): Tidal studies from the perturbations in satellite orbits, *Philosophical Transactions of the Royal Society of London, Ser.A*, **284**, 595-606.

[21] Crustal Dynamics Data Information System (CDDIS): http://cddis.nasa.gov/

[22] Celes Track: http://celestrak.com/

[23] Cesare, S., Sechi, G., Bonino, L., Sabadini, R., Marotta, A. M., Migliaccio, F., Reguzzoni, M., Sansò, F., Milani, A., Pisani, M., Leone, B., Silvestrin, P. (2006): Satellite-to-satellite laser tracking mission for gravity field measurement, 1° International Symposium of IGFS, 28 August - 1 September, Istanbul, Turkey.

[24] Chapman, S., Lindzen, R. (1970): *Atmospheric Tides: thermal and gravitational*, D. Reidel Publishing Company, Dordrecht, Holland.

[25] Chen, J. L., Wilson, C. R., Seo, K. W. (2009): S_2 tide aliasing in GRACE time-variable gravity solutions, *Journal of Geodynamics*, **83**, 679-687, DOI:10.1007/s00190-008-0282-1.

[26] Cheng, M. K., Tapley, B. D., Casotto, S. (1995): A new method for computing the spectrum of the gravitational perturbations on satellite orbits, *Celestial Mechanics and Dynamical Astronomy*, **62**, 117-143.

[27] Cheng, M. K. (2002): Gravitational perturbation theory for intersatellite tracking, *Journal of Geodesy*, **76**, 169-185, DOI:10.1007/s00190-001-0233-6.

[28] Cox, C. M., Chao, B. F. (2002): Detection of a large-scale mass redistribution in the terrestrial system since 1998, *Science*, **297**, 831-832.

[29] Daillet, S. (1981): Oceanic tide studies and satellite orbit perturbations, *Annales de Geophysique*, **37**, 113-118.

[30] Dahlen, F. A. (1993): Effect of the Earth's ellipticity on the lunar tidal potential, *Geophysical Journal International*, **113**(1), 250-251.

[31] Desai, S. D., Wahr, J. M. (1995): Empirical ocean tide models estimated from TOPEX/POSEIDON altimetry, *Journal of Geophysical Research*, **100**, C12, 25,205-25,228.

[32] Desai, S. D., Yuan, D. N. (2006): Application of the convolution formalism to the ocean tide potential: results from the Gravity Recovery and Climate Experiment (GRACE)*Journal of Geophysical Research*, **111**, C06023, DOI:10.1029/2005JC003361.

[33] Dickey, J. O., Marcus, S. L., De Viron, O., Fukumori, I. (2002): Recent Earth oblateness variations: unraveling climate and postglacial rebound effects, *Science*, **298**, 1975-1977, DOI:10.1126/science.1077777.

[34] Ditmar, P., Visser, P., Klees, R. (2003): On the joint inversion of SGG and SST data from the GOCE mission, *Advances in Geosciences*, **1**, 87-94.

[35] Doodson, A. T. (1921): The harmonic development of the tide-generating potential, *Proceedings of the Royal Society of London, Series A*, **100**, 305-329.

[36] Doodson, A. T., Warburg, H. D. (1941): *Admiralty manual of tides*, Her Majesty's Stationery Office, London.

[37] Driscoll, J. R., Healy, D. M. (1994): Computing Fourier transforms and convolutions on the 2-sphere, *Advances in Applied Mathematics*, **15**, 202-250.

[38] Eanes, R. J., Schutz, B. E., Tapley, B. D. (1983): Earth and ocean tide effects on Lageos and Starlette, *Proceedings of the Ninth International Symposium on Earth Tides*, 239-249.

[39] Eanes, R. J., Bettadpur, S. V. (1995): *The CSR 3.0 global ocean tide model: Diurnal and Semi-diurnal ocean tides from TOPEX/POSEIDON altimetry*, CRS-TM-96-05, University of Texas, Centre for Space Research, Austin, Texas.

[40] Egbert, G.D., Erofeeva, S.Y. (2002): Efficient inverse modeling of barotropic ocean tides, *Journal of Atmospheric and Oceanic Technology*, **19**(2), 183-204.

[41] Ekman, M. (1988): Impacts of geodynamic phenomena on systems for height and gravity, *Journal of Geodesy*, **63**(3), 281-296, DOI:10.1007/BF02520477.

[42] Ekman, M. (1996): The permanent problem of the permanent tide: what to do with it in geodetic reference systems?, *Marees terrestre: bulletin d'informations*, **125**, 9508-9513.

[43] EOLI-SA 9.1.7 User Guide: Interacting with Earth Observation Data, Telespazio France, 2012, available at the web site http://earth.esa.int/EOLi/EOLi.html

[44] ESA SP-1233(1) (1999): *Gravity field and steady-state ocean circulation mission. Reports for mission selection. The four candidate Earth explorer core missions*, SP-1233(1), available at http://esamultimedia.esa.int/docs/goce_sp1233_1.pdf

[45] GMVSA (2006): NAPEOS software user manual, 20224/06.

[46] ESA/ESOC (2009): NAPEOS - Mathematical models and algorithms, DOPS-SYS-TN-0100-OPS-GN.

[47] ESOC ftp: ftp://dgn6.esoc.esa.int/napeos

[48] Fantino, E., Casotto, S. (2009): Methods of harmonic synthesis for global geopotential models and their first-, second- and third-order gradients, *Journal of Geodynamics*, **83**, 595-619, DOI:10.1007/s00190-008-0275-0.

[49] Farrell, W. E. (1972): Deformation of the Earth by surface loads, *Reviews of Geophysics and Space Physics*, **10**(3), 761-797.

[50] Förste, C., Bruinsma, S., Shako, R., Marty, J-C, Flechtner, F., Abrikosov, O., Dahle, C., Lemoine, J.-M., Neumayer, K.H., Biancale, R., Barthelmes, F., König, R., Balmino, G. (2011): EIGEN-6 - A new combined global gravity field model including GOCE data from the collaboration of GFZ-Potsdam and GRGS-Toulouse; *Geophysical Research Abstracts*, Vol. 13, EGU2011-3242-2, EGU General Assembly, 2011.

[51] Groves, G. W., Reynolds, R. W. (1975): An orthogonalized convolution method of tide prediction, *Journal of Geophysical Research*, **80**(30), 4131-4138, DOI:10.1029/JC080i030p04131.

[52] Han, S.-C., Ray, R. D., Luthcke, S. B. (2007): Ocean tidal solutions in Antarctica from GRACE inter-satellite tracking data, *Geophysical Research Letters*, **34**(L21607), 1-6, DOI:10.1029/2007GL031540.

[53] Hartmann, T., Wenzel, H.-G. (1994): The harmonic development of the Earth tide generating potential due to the direct effect of the planets, *Geophysical Research Letters*, **21**(18), 1991-1993.

[54] Hartmann, T., Wenzel, H.-G. (1995): The HW95 tidal potential catalogue, *Geophysical Research Letters*, **22**(24), 3553-3556.

[55] Harwood, N. M., Swinerd, G. G. (1997): Ocean-tide parameters from the simultaneous long-period analysis of the orbits of Starlette and Stella, *Annales Geophysicae*, **15**, 263-271.

[56] Hobbs, D., Bohn, P. (2006): Precise Orbit Determination for Low Earth Orbit satellites, *Annals of the Marie Curie Fellowships*, **4**, 128-135.

[57] Hofmann-Wellenhof, B., Moritz, H. (2005): *Physical Geodesy*, Springer Verlag, Vienna.

[58] International Centre for Global Earth Models (ICGEM): http://icgem.gfz-potsdam.de/ICGEM/

[59] International GNSS Service (IGS): http://igscb.jpl.nasa.gov/

[60] Jäggi, A., Dach, R., Montenbruck, O., Hugentobler, U., Bock, H., Beutler, G. (2009): Phase center modeling for LEO GPS receiver antennas and its impact on precise orbit determination, *Journal of Geodesy*, **83**, 1145-1162, DOI:10.1007/s00190-009-0333-2.

[61] Jarecki, F., Müller, J., Petrovic, S., Schwintzer, P. (2004): Temporal gravity variations in GOCE gradiometric data, *Gravity, Geoid and Space Missions*, GGSM 2004, IAG International Symposium, 30 August - 3 September, Porto, Portugal, International Association of Geodesy Symposia, Vol. 129, C. Jekeli, L. Bastos and J. Fernandes Editors, Springer.

[62] Jekeli, C. (1999): The determination of gravitational potential differences from satellite-to-satellite tracking, *Celestial Mechanics and Dynamical Astronomy*, **75**, 85-101.

[63] Jekeli, C. (2006): *Geometric reference systems in Geodesy*, Division of Geodesy and Geospatial Science, School of Earth Sciences, Ohio State University.

[64] Kaula, W. M. (1966): *Theory of Satellite Geodesy, Applications of Satellites to Geodesy*, Dover Publications, Inc., Mineola, New York.

[65] Kaula, W. M. (1983): Inference of variations in the gravity field from satellite-to-satellite range rate, *Journal of Geophysical Research*, **88**(B10), 8345-8349.

[66] Kang, Z., Tapley, B., Bettadpur, S., Ries, J., Nagel, P. (2006): Precise orbit determination for GRACE using accelerometer data, *Advances in Space Research*, **38**, 2131-2136.

[67] Kantha, L. H., Clayson, C. A. (2000): *Numerical models of oceans and oceanic processes*, International Geophysics Series, Vol. 66, Academic Press.

[68] Kudryavtsev, S. M. (2003): Advanced harmonic development of the Earth tide generating potential, *Proceedings of the International Association of Geodesy IAG General Assembly, Sapporo, Japan, June 30 - July 11, 2003*, 465-470.

[69] Kudryavtsev, S. M. (2004): Improved harmonic development of the Earth tide-generating potential, *Journal of Geodesy*, **77**, 829-838, DOI:10.1007/s00190-003-0361-2.

[70] Lambeck, K., Cazenave, A., Balmino, G. (1974): Solid Earth and ocean tides estimated from satellite orbit analysis, *Reviews of Geophysics and Space Physics*, **12**(3), 621-634.

[71] Lambeck, K. (1980): *The Earth's variable rotation: geophysical causes and consequences*, Cambridge University Press.

[72] Lambert, A. (1974): Earth tide analysis and prediction by the Response Method, *Journal of Geophysical Research*, **79**(32), 4952-4960.

[73] Leick, A. (1995): *GPS satellite surveying*, Second Edition, Wiley-Interscience.

[74] Lemoine, F. G., Luthcke, S. B., Rowlands, D. D., Chinn, D. S., Klosko, S. M., Cox, C. M. (2005): The use of mascons to resolve time-variable gravity from GRACE, *International Association of Geodesy Symposia*, Vol.130, Dynamic Planet, 231-236, Springer Berlin Heidelberg, DOI:10.1007/978-3-540-49350-1_35.

[75] Le Provost, C., Genco, M. L., Lyard, F., Vincent, P., Canceil, P. (1994): Spectroscopy of the ocean tides from a finite element hydrodynamic model, *Journal of Geophysical Research*, **99**(C12), 24777-24797.

[76] Le Provost, C. (2001): Chapter 6 - Ocean tides, Satellite Altimetry and Earth Sciences, *International Geophysics*, **69**, 267-303.

[77] Lindzen, R. S. (1979): Atmospheric tides, *Annual Review of Earth and Planetary Sciences*, **7**, 199-225.

[78] Lorenzini E. (2006): *Astrodynamic*, Lecture Notes of Astrodynamic.

[79] Lyard, F., Lefevre, F., Letellier, T., Francis., O. (2006): Modelling the global ocean tides: modern insights from FES2004, *Ocean Dynamics*, **56**, 394-415, DOI:10.1007/s10236-006-0086-x.

[80] Luthcke, S. B., Arendt, A. A., Rowlands, D. D., McCarthy, J. J., Larsen, C. F. (2008): Recent glacier mass changes in the Gulf of Alaska region from GRACE mascon solutions, *Journal of Glaciology*, **54**(88), 767-777.

[81] Maybeck, P. S. (1982): *Stochastic models, estimation, and control*, Mathematics in Science and Engineering, Vol. 141-1,2,3, Academic Press.

[82] McCarthy, D. D., Petit, G. (2003): *IERS Conventions (2003), Technical Note 32*, Verlag des Bundesamts für Kartographie und Geod¨asie, Frankfurt, Germany, ISBN 3-89888-884-3.

[83] Petit, G., Luzum, B. (2010): *IERS Conventions (2010), Technical Note 36*, Verlag des Bundesamts für Kartographie und Geodäsie, Frankfurt, Germany, ISBN 3-89888-884-3.

[84] Matsumoto, K., Ooe, M., Sato, T., Segawa, J. (1995): Ocean tides model obtained from TOPEX/POSEIDON altimeter data, *Journal of Geophysical Research*, **100**, 25319-25330.

[85] Matsumoto, K., Takashi, T., Masatsugu, O. (2000): Ocean Tide Models Developed by Assimilating TOPEX/POSEIDON Altimeter Data into Hydrodynamical Model: a Global Model and a Regional Model around Japan, *Journal of Oceanography*, **46**, 567-581.

[86] McGuirk, J. M., Foster, G. T., Fixler, J. B., Snadden, M. J., Kasevich, M. A. (2002): Sensitive absolute gravity gradiometry using atom interferometry, *Physical Review A*, **65**, DOI:10.1103/PhysRevA.65.033608.

[87] Meeus, J. (1998): *Astronomical Algorithms*, Second Edition, Willmann-Bell, Inc., Richmond, Virginia, USA.

[88] Merson, R. H. (1967): A brief survey of satellite orbit determination, *Philosophical Transactions of the Royal Society of London, Ser.A, Mathematical and Physical Sciences*, **262**(1124), 71-78.

[89] Montenbruck, O., Gill, E. (2000): *Satellite Orbits*, Springer-Verlag Berlin Heidelberg.

[90] Moyer, T. D. (2000): *Formulation for observed and computed values of deep space network data types for navigation*, Monograph 2, Deep Space Communications and Navigation Series, Issued by the Deep Space Communications and Navigation Systems, Jet Propulsion Laboratory, California Institute of Technology, Joseph H. Yuen, Editor-in-Chief.

[91] Munk, W. H., MacDonald, G. J. F. (1960): *The rotation of the Earth. A geophysical discussion*, Cambridge University Press, London.

[92] Munk, W. H., Cartwright, D. E. (1966): Tidal spectroscopy and prediction, *Philosophical Transactions of the Royal Society of London, Ser.A*, **259**(1105), 533-581.

[93] National Geophysical Data Centre (NGDC): http://www.ngdc.noaa.gov/ngdc.html

[94] NRC (National Research Council) (1997): *Satellite Gravity and the Geosphere: contributions to the study of the solid Earth and its fluid envelope*, National Academy Press, Washington D.C., USA.

[95] Parke, M. E., Stewart, R. H., Farless, D. L., Cartwright, D. E. (1987): On the Choice of Orbits for an Altimetric Satellite to Study Ocean Circulation and Tides, *Journal of Geophysical Research*, **92**(C11), 11693-11707, DOI:10.1029/JC092iC11p11693.

[96] Poutanen, M., Vermeer, M., Mäkinen, J. (1996): The permanent tide in GPS positioning, *Journal of Geodesy*, **70**, 499-504.

[97] Press, W. H., Teukolsky, S. A., Vetterling, W. T., Flannery, B. P. (2007): *Numerical Recipes - The Art of Scientific Computing*, Third Edition, Cambridge University Press.

[98] Quarteroni, A., Sacco, R., Saleri, F. (2000): *Numerical Mathematics*, Springer Verlag, New York.

[99] Ray, R. D. (1999): *A global ocean tide model from TOPEX/POSEIDON altimetry: GOT99.2*, NASA Technical Memorandum 209478, National Aeronautics and Space Administration, Goddard Space Flight Centre, Greenbelt, MD, USA.

[100] Ray, R. D., Rowlands, D. D., Egbert, G. D. (2003): Tidal models in a new era of satellite gravimetry, *Space Science Reviews*, **108**, 271-282.

[101] Ray, R. D., Luthcke, S. B., Boy, J.-P. (2009): Qualitative comparisons of global ocean tide models by analysis of intersatellite ranging data, *Journal of Geophysical Research*, **114**(C09017), DOI:10.1029/2009JC005362.

[102] Roosbeek, F. (1996): RATGP95: a harmonic development of the tide-generating potential using an analytical method, *Geophysical Journal International*, **126**, 197-204.

[103] Rosborough, G. W., Tapley, B. D. (1987): Radial, transverse and normal satellite position perturbations due to the geopotential, *Celestial Mechanics*, **40**, 409-421.

[104] Rowlands, D. D., Luthcke, S. B., Klosko, S. M., Lemoine, F. G. R., Chinn, D. S., McCarthy, J. J., Cox, C. M., Anderson, O. B. (2005): Resolving mass flux at high spatial and temporal resolution using GRACE intersatellite measurements, *Geophysical Research Letters*, **32**, L04310, DOI:10.1029/2004GL021908.

[105] Rummel, R. (1986): *Satellite gradiometry*, Fourth International Summer School in the Mountains on Mathematical and Numerical Techniques in Physical Geodesy, Lecture Notes in Earth Sciences, Vol.7, 317-365, Springer Verlag.

[106] Sansò, F., Rummel, R. (1989): *Theory of Satellite Geodesy and Gravity Field Determination*, Lecture Notes in Earth Sciences, Springer Verlag, Berlin, Heidelberg, New York.

[107] Schubert, G. (2007): *Treatise on Geophysics*, Geodesy, Vol.3, Elsevier.

[108] Schureman, P. (1940): *Manual of harmonic analysis and prediction of tides*, U.S. Coast and Geodetic Survey, Special Publication No. 98, Washington, D.C., U.S. Govt. Print. Off.

[109] Schwiderski, E. W. (1980): On charting global ocean tides, *Reviews of Geophysics and Space Physics*, **18**(1), 243-268.

[110] Schwiderski, E. W. (1980): Ocean tides, part I: Global ocean tidal equations, *Marine Geodesy*, **3**, 161-217.

[111] Shum, C. K., Woodworth, P. L., Andersen, O. B., Egbert, G. D., Francis, O., King, C., Klosko, S. M., Le Provost, C., Li, X., Molines, J-M., Parke, M. E., Ray, R. D., Schlax, M. G., Stammer, D., Tierney, C. C., Vincent, P., Wunsch, C. I. (1997): Accuracy assessment of recent ocean tide models, *Journal of Geophysical Research*, **102**(C11), 25,173-25,194.

[112] Simon, J. L., Bretagnon, P., Chapront, J., Chapront-Touzè, M., Francou, G., Laskar, J. (1994): Numerical expressions for precession formulae and mean elements for the Moon and the planets, *Astronomy and Astrophysics*, **282**, 663-683.

[113] Sneeuw, N. (1994): Global spherical harmonic analysis by least-squares and numerical quadrature methods in historical perspective, *Geophysical Journal International*, **118**(3), 707-716, DOI:10.1111/j.1365-246X.1994.tb03995.x.

[114] Sneeuw, N., Bun, R. (1996): Global spherical harmonic computation by two-dimensional Fourier methods, *Journal of Geodesy*, **70**(4), 224-232, DOI:10.1007/s001900050011.

[115] Sneeuw, N. (2000): *A semi-analytical approach to gravity field analysis from satellite observations*, PhD Thesis, Institut für Astronomische und Physikalische Geodäsie, Technischen Universität München, Germany.

[116] Sneeuw, N., Schaub, H. (2004): Satellite clusters for future gravity field missions, *Gravity, Geoid and Space Missions*, GGSM 2004, IAG International Symposium, 30 August - 3 September, Porto, Portugal, International Association of Geodesy Symposia, Vol. 129, C. Jekeli, L. Bastos and J. Fernandes Editors, Springer.

[117] Tamura, Y. (1987): A Harmonic development of the Tide-Generating Potential, Bulletin d'Informations Marees Terrestres, **99**, 6813-6855.

[118] Tapley, B. D., Schutz, B. E., Born, G. H. (2004): *Statistical Orbit Determination*, Elsevier Academic Press.

[119] Vallado, D. A. (2007): *Fundamentals of Astrodynamics and Applications*, Third Edition, Space Technology Library.

[120] Visser, P. N. A. M. (1999): Gravity field determination with GOCE and GRACE, *Advances in Space Research*, **23**(4), 771-776, DOI:10.1016/S0273-1177(99)00154-4.

[121] Visser, P. N. A. M. (2005): Low-low satellite-to-satellite tracking: a comparison between analytical linear orbit perturbation theory and numerical integration, *Journal of Geodesy*, **79**, 160-166, DOI:10.1007/s00190-005-0455-0.

[122] Visser, P. N. A. M., van den IJssel, J., van Helleputte, T., Bock, H., Jäggi A., Beutler, G., Svehla, D., Hugentobler, U., Heinze, M. (2009): Orbit determination for the GOCE satellite, *Advances in Space Research*, **43**, 760-768.

[123] Wahr, J. (1981): Body tides on an elliptical, rotating, elastic and oceanless Earth, *Geophysical Journal of the Royal Astronomical Society*, **64**(3), 677-703.

[124] Wenke, S., Sjöberg, L. E. (2001): Permanent components of the crust, geoid and ocean depth tides, *Journal of Geodynamics*, **31**, 323-339.

[125] Wenzel, H. G. (1997): Tide-generating potential for the Earth, *Lecture Notes in Earth Sciences*, **66**, 9-26, DOI: 10.1007/BFb0011455.

[126] Wilhelm, H. (1983): Earth's flattening effect on the tidal forcing field, *Journal of Geophysics*, **52**, 131-135.

[127] Xi, Q. W. (1987): A new complete development of the tide generating potential for the epoch J2000.0, *Bulletin d'Informations Marees Terrestres*, **99**, 6786-6812.

[128] Xu, G. (2003): *GPS - Theory, Algorithms and Applications*, Springer Verlag.

[129] Xu, P. (2008): Position and velocity perturbations for the determination of geopotential from space geodetic measurements, *Celestial Mechanics and Dynamical Astronomy*, **100**, 231-249, DOI:10.1007/s10569-008-9117-x.

[130] Zahran, K. H., Jentzsch, G., Seeber, G. (2006): Accuracy assessment of ocean tide loading computations for precise geodetic observations, *Journal of Geodynamics*, **42**, 159-174.